1994 Annual Report

Volume 5, No. 1
June 1994

Table of Contents

Transmission and Reflection Tomography

Migration and CLP Imaging

Forward Modeling

Diffraction Tomography and Inversion

STP Information

PAPER A

INTEGRATED CROSSWELL IMAGING: REFLECTION TOMOGRAPHY– SYNTHETIC EXAMPLES

Mark A. Van Schaack

ABSTRACT

Last year I introduced a proposal to integrate the processing of crosswell reflection imaging and traveltime tomography. I have modified this scheme to allow an interpretation of the reflection image to be used to guide the picking of reflection traveltimes. This requires an ability to map reflection data using the 2-D traveltime tomogram and to inverse map, or forward model, the interpreted reflections.

I am currently working on programming the various processors required in the integrated iterative inversion. A program allowing the simultaneous inversion of reflection and direct arrival traveltime picks is now complete. Traveltime inversions run on synthetic data show that including reflections in the traveltime inversion improves the imaging ability at the top and bottom of the surveyed zone where ray coverage is typically poor for direct arrivals. Also, reflection tomography improves the vertical resolution midway, between the wells. This improvement in resolution is required to reduce the "dog bone" and "football" artifacts which occur as a result of bowed interfaces.

INTRODUCTION

An approach to integrating crosswell reflection imaging and traveltime tomography was presented by Van Schaack and Lazaratos (1993). As observed by Lazaratos (1993), inaccuracies in the velocity model used in the XSP-CDP mapping technique result in lateral and vertical mispositioning of reflection events. These mispositioning errors cause destructive interference when stacked and result in a loss of resolution in the reflection image. An inversion was proposed which perturbs the velocity model to minimize these errors. Although this inversion is similar in philosophy to surface seismic velocity analysis it is better described as crosswell reflection traveltime tomography (CRTT). It utilizes both direct and reflected arrival traveltimes in a single inversion for the velocity field.

There are a number of different ways in which CRTT can be parameterized and solved. It would be preferable to solve for "everything", e.g., a finely-gridded, fully 3-dimensional anisotropic velocity distribution including the location and orientation of arbitrarily defined reflectors. Unfortunately, even a simple 2-dimensional isotropic velocity inversion may end up being underdetermined if care is not taken in defining the gridding. To optimize a solution, the parameterization should be made to reduce the number of variables wherever possible. An example of this in CRTT is a parameterization developed by Michelena (personal comm.) which solves for the location and dip of linear interfaces and the velocity of homogeneous isotropic layers. In a geology where layers can be accurately described as constant velocity, this parameterization might be ideal.

In this paper I review a philosophy of integrated reflection and tomographic inversion. This philosophy determines the parameterization of the reflection traveltime inversion. A number of synthetic examples are presented to illustrate the potential of including reflections in crosswell traveltime tomography. Finally, I discuss the next steps required to apply this technique to real data.

PHILOSOPHY OF THE INTEGRATED CROSSWELL INVERSION

Background

A large number of the published crosswell studies have been of areas where the geologic structure is predominantly flat or mildly dipping (homocline). Examples of this are: Amoco/Conoco's North Cowden study, West Texas (Lines et al., 1993), Stanford/Chevron's McElroy study, West Texas (Harris et al., 1992), Exxon's Friendswood test site, Texas (Chen et al., 1990) and BP's Devine test site, West Texas (Harris, 1988). Areas with simple geologic structure are ideal for CRTT since structural interpretation of the reflection image is relatively straightforward and easily checked against the well log interpretation. If reflectors can be found, and their orientations determined manually, the reflection tomography problem is much simpler.

If the structure is simple, what is the benefit of crosswell imaging? There are several potential uses of crosswell imaging in simple structures. One application is reservoir characterization. Even when the basic structure of the geology is simple, stratigraphic variations within layers can exist. These stratigraphic variations may result from primary depositional processes, or from secondary infilling or enlargement of the pore space. Secondary processes are occasionally the direct result of oil production and injection programs. These variations may be measured seismically as small velocity perturbations. A

second application is monitoring. The injection of fluids in a reservoir may be monitored directly with crosswell imaging if the injected fluid results in a seismic velocity change.

Both of the above applications, reservoir characterization and monitoring, benefit from the highest resolution, most accurate information available. One of the advantages of integrating reflection imaging and traveltime tomography is that resolution and accuracy are added to both. In this paper I will describe an approach to integrated inversion using CRTT. This approach is designed to work optimally when the basic geologic structure is simple and the crosswell reflection images can be interpreted in a straightforward manner.

Simple structures

The definition of simple structure that I have used in the design of the integrated inversion is subject to several conditions:

1) Reflectors must be interpretable from the crosswell reflection image

2) Each interpreted reflector must intersect both wells

3) Each interpreted reflector must expressible as a function of horizontal, interwell offset

These conditions are required to define the position of each reflector in terms of a simple equation. For the i'th reflector, the depth of that reflector is defined as a function of offset,

$$z_i = f_i(x) \tag{1}$$

In this equation, z_i is the reflector depth, and x is the horizontal offset. The $f_i(x)$ is a function describing the i'th reflector which is determined from the interpreted reflection image.

THE INTEGRATED INVERSION

Data preparation

Figure 1 is a schematic of the integrated crosswell imaging procedure. Prior to the iterative imaging process the crosswell data are processed in a standard fashion. First, direct arrival traveltimes are picked from the raw waveforms. The next step is wavefield separation and reflector enhancement. Typically traveltime picks are used to design filters to perform this processing (Rector, 1994). The results of these steps, the direct arrival traveltimes and the processed wavefield, are passed to the iterative integrated inversion.

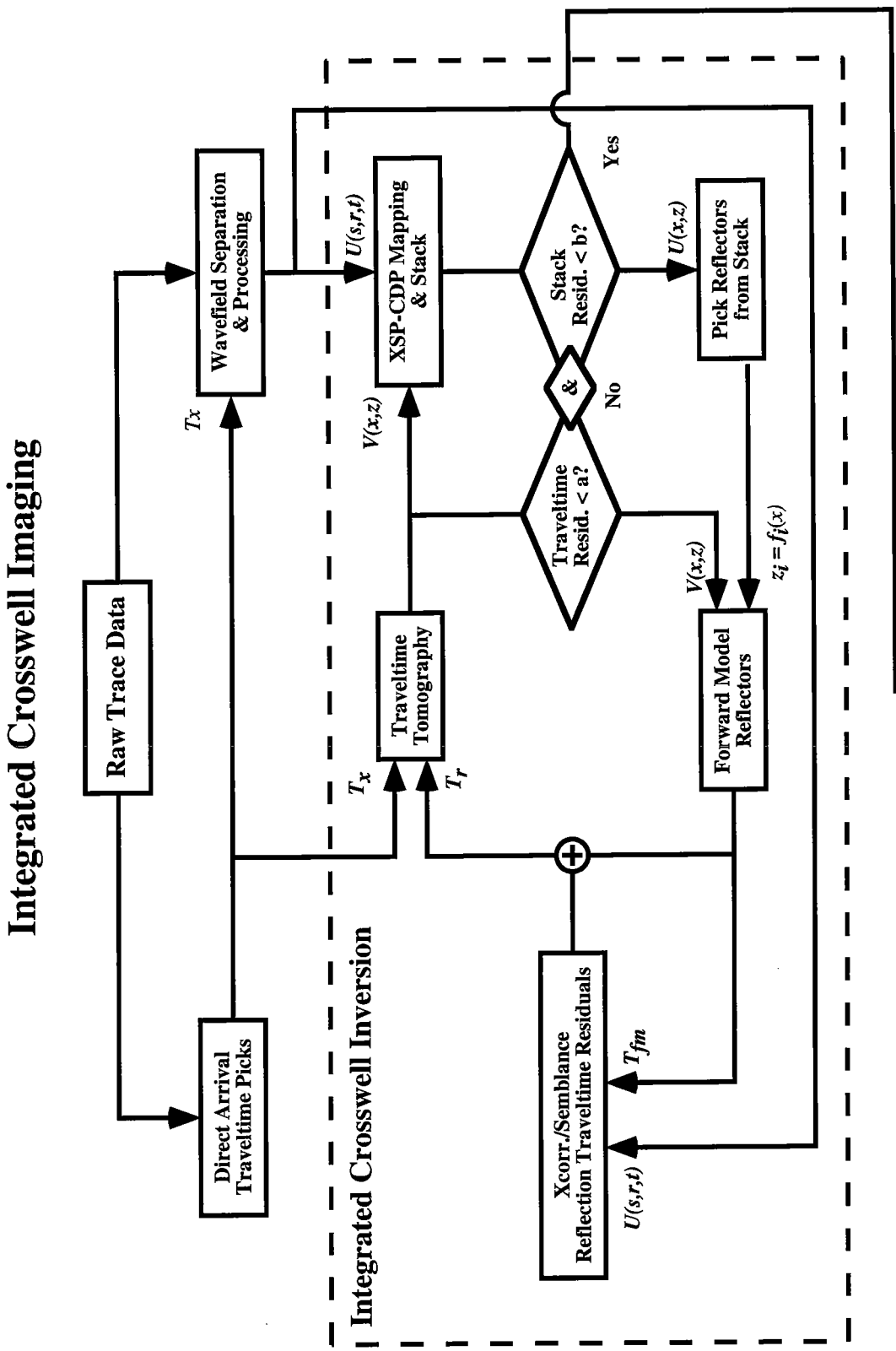

Figure 1: This schematic outlines a processing technique which integrates crosswell traveltime and reflection data in a single inversion. This technique is iterative and requires interpretation of the reflection image after each mapping to define reflector locations and orientations.

Iterative Inversion: Step 1 – Direct Arrival Tomography and Reflection Imaging

The first step in the iterative inversion is direct arrival traveltime tomography. The traveltime inversion is run in a standard fashion to calculate a 2-D velocity model. The result of the velocity inversion, a velocity map, $v(x,z)$, is passed to the mapping routine. The mapping and stacking process is performed in a similar manner to that described by Lazaratos (1993). There are two differences to Lazaratos' technique. First, a fully 2-D mapping algorithm is used to accommodate the 2-D traveltime tomogram. Second, the "residual statics" step, used to line up reflection events prior to stacking, is not required.

The purpose of residual statics processing is to align reflections prior to stacking to ensure an optimal stack. The use of the residual statics technique was originally justified by several reasons (Lazaratos, 1993). The XSP-CDP mapping algorithm used by Lazaratos was designed to use only a 1-dimensional velocity models. Also, corrections were not made for well deviations. The McElroy data processed using this technique were collected in a setting where the geology was primarily layer-cake and well deviations were mild. The validity of the 1-D and straight well assumptions was supported by the observation that the mispositioning of the reflection events, prior to stacking, was also rather mild. Nevertheless, Lazaratos found that additional resolution could be obtained in the reflection image by "forcing" the reflectors to align. This technique is similar to "non-surface consistent statics", which is used occasionally in surface seismic data processing. Since I intend to use a 2-D mapping algorithm, which will also correct for well deviations, the residual statics technique should not be necessary.

Iterative Inversion: Step 2 – Convergence test

These decision boxes, seen in Figure 1, following the traveltime tomography and reflection imaging, test the images for convergence. Acceptable limits for convergence are primarily subjective and the number of iterations performed may be determined, in reality, by available computer and human resources. If the convergence criteria are met, the velocity tomogram and reflection image are judged acceptable and the processing is finished.

Iterative Inversion: Step 3 – Reflector picking from stacked reflection image

In this step the two reflection images, upgoing and downgoing, are interpreted. Although nothing prohibits the use complex dipping structures the algorithm has been designed to use reflectors defined as single-valued functions of offset. This is done to

simplify several steps: the definition of the reflector, inverse mapping (not yet discussed), and raytracing. Equation (1) provides the mathematical description of the reflection events. Any phase can be used to define the reflector: peaks, troughs, zero crossings, or an intermediate phase. The important point is that this same phase must be used to identify the reflections in the space-time domain.

The reflection events are picked separately from the upgoing and downgoing sections. In practice, the downgoing section is typically the best at the top of the surveyed zone and the upgoing section is the best at the bottom. Past experience suggests that the number of events that are imaged by both up and downgoing events is not that large. The small number of these twice imaged reflections, plus the difficulty of ensuring that the events picked actually are the same reflection, suggests that the inversion is best parameterized without them.

Iterative Inversion: Step 4 – Inverse mapping reflection events

The traveltime tomogram and picked reflection events are next input to the inverse mapping routine. Inverse mapping, as it is used here, is essentially forward modeling. For a given source-receiver-reflector combination, and an assumed velocity model (the traveltime tomogram), a traveltime is calculated. This time is calculated using an energetic-arrival finite-differences eikonal solver (Mo, 1994). This solver is used to calculate two traveltime maps using the traveltime tomogram as the velocity model. One map is calculated using the source's location and another map is calculated using the receiver's location. These two maps are then added together. The resulting combined traveltime map defines the traveltime from every point on the image to the source and receiver. Described another way, the traveltime from the source, to a point, to the receiver, is stored at the location of that point.

For a particular reflector, the reflection traveltime can be found on the combined traveltime map as the minimum time on that reflector's trajectory. This approach is an application of Fermat's principle. Forward modeled traveltimes for each source-receiver-reflector combination are calculated and stored for both upgoing and downgoing images.

Iterative Inversion: Step 5 – Reflection traveltime residuals

Step 4, inverse mapping/forward modeling, calculates the traveltimes of reflected events using with the traveltime tomogram as the velocity model. If the traveltime tomogram is "correct", in other words, accurately reflects the true velocities of the medium, several observations can be made:

1) The traveltime residual of the tomographic inversion will be zero (or a minimum)

2) There will be no misalignments of reflection events in the pre-stack, mapped reflection data

3) The reflection traveltimes calculated in step 4, forward modeling, will equal the observed reflection traveltimes

Since step 5 is reached by failing the convergence test, step 2, observations 1 and 2 are not true. The failure of the convergence test also ensures that observation 3 will be untrue.

In step 5 the residual error, r, is calculated. The residual error is the difference between the forward-modeled reflection traveltimes and the observed reflection traveltimes. This can be expressed as

$$r = t_{obs} - t_{calc} \tag{2}$$

The observed traveltime used in the tomographic inversion, can be calculated by adding the residual to the calculated traveltime. This indirect approach to obtaining the true reflection traveltimes is necessitated by the fact that reflections are normally very difficult to see even in the processed data. By calculating the reflection traveltimes as a perturbation of a predicted set of times, the search window can be focused, minimizing errors.

There are several approaches to obtaining the reflection traveltime residuals. The most direct approach, although very labor intensive, is to manually correct the traveltimes in the space-time domain. This produces the observed traveltimes directly. By perturbing the forward-modeled times the residual is added in one step. The disadvantage of this technique is that it is so labor intensive that it would be difficult to process a large number of reflectors in a reasonable time. The advantage is that this technique allows the human operator to interpret and reject noise that might overwhelm other techniques.

A more automated approach is to use a semblance, correlation, or maximum coherency technique. Each of these has its own advantages and disadvantages which are currently under study. The primary motivation for research in this area is that a robust automated traveltime picker will allow a large number of reflectors to be processed.

Iterative Inversion: Step 6 – Completing the iteration with CRTT

The final step of the combined iterative inversion is to use both reflection and direct arrival traveltimes in a single tomographic inversion. Mathematically, the combined inversion is identical to the inversion using only direct arrivals. For each source-receiver-reflector combination where a traveltime is obtained, a raypath can be computed and a

traveltime calculated. The difference between observed and calculated traveltimes is then backprojected along the raypath. This is done for all reflection and direct arrival traveltimes and iterated until a convergence criteria is met. The output velocity model is then passed along to the mapping routine for processing and the entire process is repeated again.

CROSSWELL REFLECTION TOMOGRAPHY — SYNTHETIC EXAMPLES

Introduction

There are several algorithms to build in order to implement the integrated crosswell inversion. In this section I show the results of two synthetic crosswell reflection traveltime inversions. The algorithm used in these crosswell inversions uses a SIRT inversion scheme parameterized with orthogonal pixels describing a 2-D velocity image. Raytracing is performed with an initial value ray tracer described by Harris (1992).

These inversions simulate the final iteration of the integrated inversion process. In the final iteration, reflector geometries are known and the reflection traveltimes are considered accurate. With accurate direct arrival and reflection traveltimes, the traveltime inversion is run to convergence to obtain the optimum velocity image. The results of these inversions show the potential of a combined reflection and direct traveltime inversion.

Simulation 1 — A simple 3-layer model

Figure 2 shows the simple 3-layered model used in the first simulation. The data set for this model consists of 101 source by 101 receiver locations. Reflection traveltimes are modeled for 4 reflectors: one at the top of the surveyed zone, one at 200 ft, one at 300 ft, and one at 500 ft, the bottom of the surveyed zone. Both upgoing and downgoing reflection traveltimes are calculated for each reflector.

Examples of the traveltime picks used in the inversion are shown in Figure 3. The direct arrival picks are displayed (Figure 3a) with the receiver elevation on the horizontal axis and source elevation on the vertical axis. The reflection traveltime picks for the 200 ft reflector are shown in Figure 3b. The same display is used for these picks. Note that a large part of the receiver pick map is zero valued. These null values occur at source and receiver positions that straddle the reflector. One of these pick maps is required for each reflector used in the traveltime inversion.

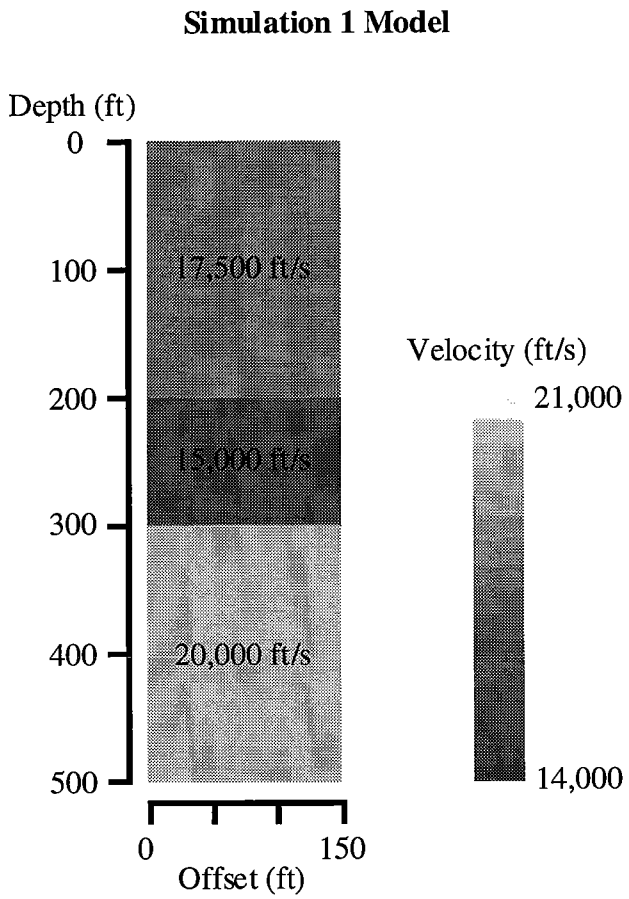

Figure 2: A simple 3-layered model used to generate traveltime data for a combined direct arrival and reflected arrival traveltime inversion. The shooting geometry is 101 sources by 101 receivers evenly spaced every 5 ft down the sides of the model.

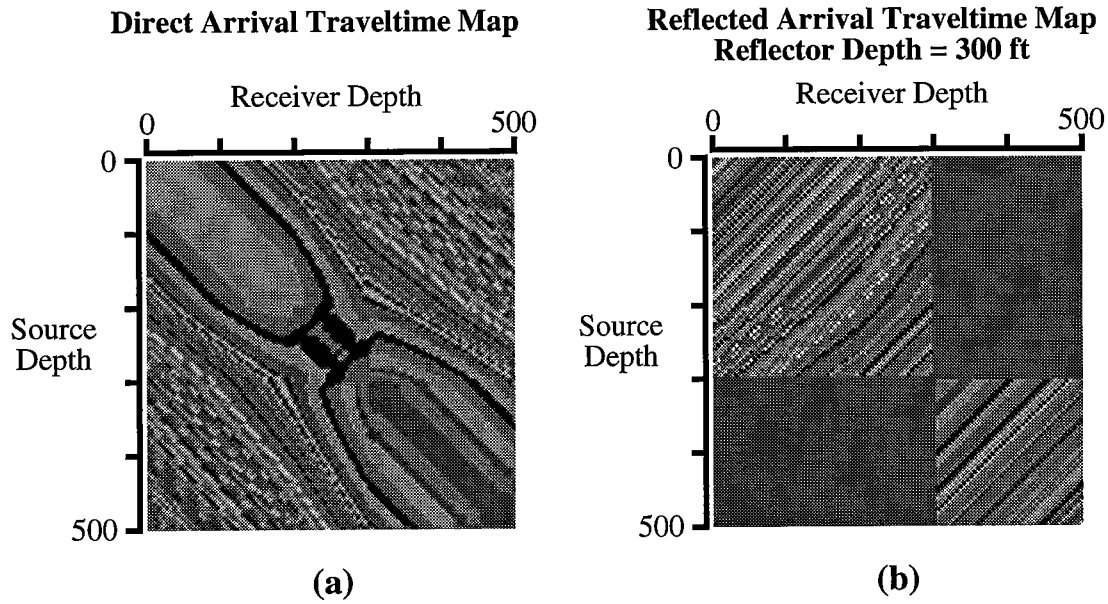

Figure 3: Direct arrival (a) and reflected arrival (b) traveltime maps. These images are displayed using a "random" colortable to accentuate the isochron contours of the pick images. Figure 3b is an example of reflected arrival traveltime picks for a horizontal reflector at 300 ft. The homogeneous gray areas of the map are null picks. This occurs when the source and receiver locations straddle the reflector and no reflection is possible. Both up and downgoing reflection picks are present on this image.

The results of the traveltime inversions are shown in Figure 4. Figure 4a is the model used to create the traveltime data. Figure 4b is the final image of a traveltime inversion using only direct arrivals . Figure 4c is the final image of the traveltime inversion using both direct and reflected arrivals. Both of these inversion were run in an identical manner: 10 iterations with 4 backprojections for each inversion.

The most obvious improvements seen in the reflection traveltime tomogram can be found in the vicinity of the interfaces located at 200 and 300 ft. The bowing in the interfaces seen in Figure 4b, a common artifact in crosswell traveltime inversions, is virtually eliminated by including the reflection traveltimes. Lateral variations in the top and bottom layers in Figure 4b are also absent in the reflection traveltime tomogram.

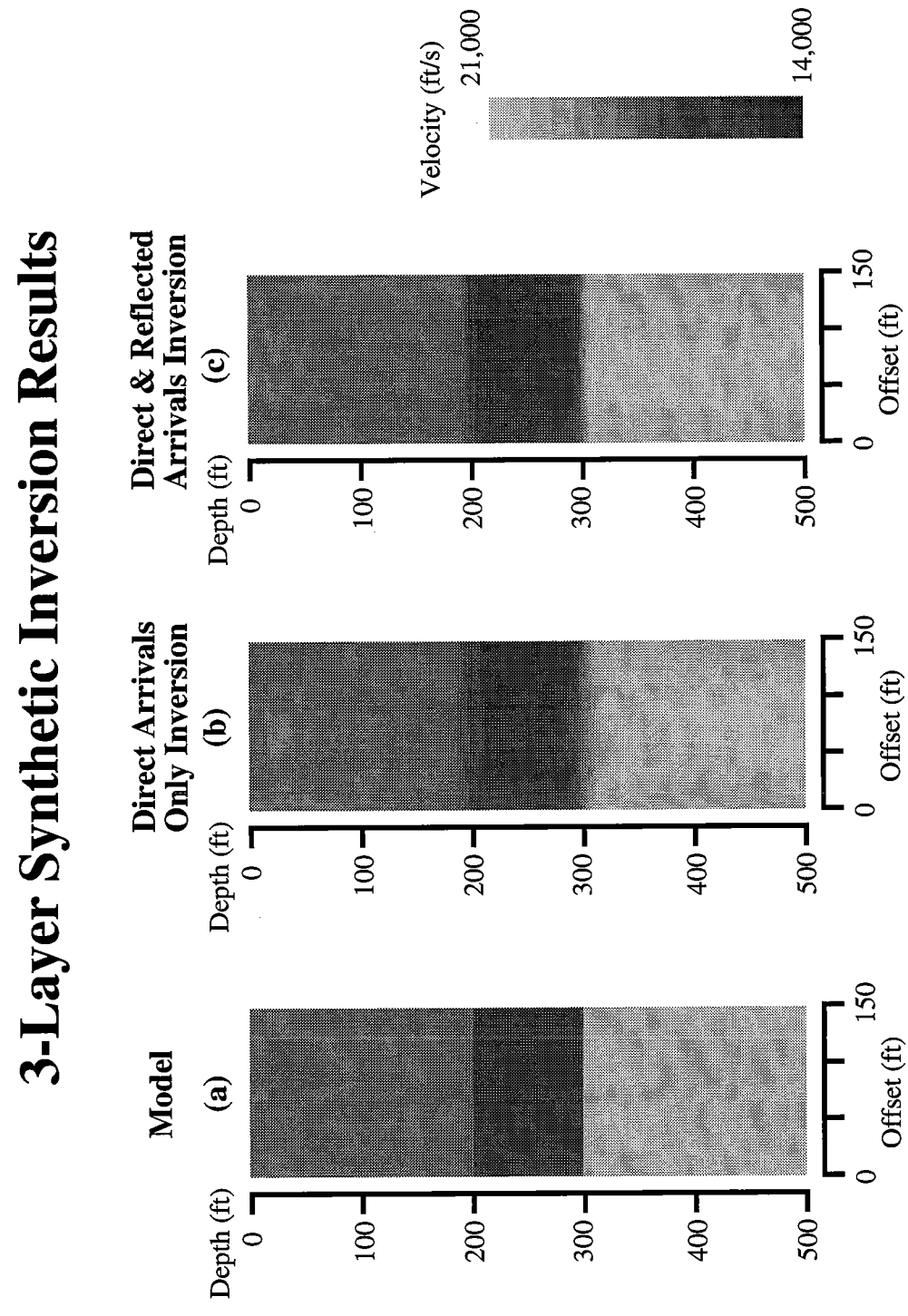

Figure 4: The above results provide a comparison of an inversion calculated with both direct and reflected traveltime arrivals (c), and an inversion run using only direct arrivals (b). Both inversions were run identically: 10 iterations, 4 backprojections each iteration.

Simulation 2 — A 7-layer model

Figure 5a shows the model used in the second simulation. This model includes 7 layers and reflection traveltime picks were used for all 8 interfaces, which includes the top and bottom of the model. Traveltime inversions were run using only direct arrival picks and combined direct arrival and reflected arrival picks. Again, the inversions were run identically. In this test, 10 iterations were calculated with 20 backprojections for each iteration. The source and receiver geometries are identical to the first simulation: 101 source by 101 receiver locations spaced evenly every 5 ft.

The results of simulation 2 are shown in Figures 5b and 5c. The improvements offered by the combined inversion are essentially the same as seen in simulation 1. The artifacts in Figure 5b are comparatively larger than those seen in Figure 4b. This is a result of the interfaces near the top and bottom edges of the model where ray coverage and resolution are poor.

CONCLUSIONS

Integrated iterative inversion of crosswell reflection and traveltime data can potentially lead to improvements in the resolution obtainable in crosswell imaging. In this paper I outline a scheme by which these data can be simultaneously processed. Nearly all of the programs required to accomplish this processing are in place. The next step will be to write a general 2-D mapping program which corrects for well deviations and to automate reflection traveltime picking so that large numbers of reflections can be processed.

The combined reflection and traveltime inversion offers improvements in the resolution of interfaces near the middle of the surveyed region. Also, improvements in resolution are seen at the top and bottoms of the surveyed zone where transmission traveltime tomography fails due to poor ray coverage.

ACKNOWLEDGMENTS

I would like to thank Bob Langan, Le-Wei Mo, and Spyros Lazaratos for their useful discussions on the topic of reflection imaging and traveltime tomography. I would also like to thank the corporate sponsors of the Stanford Tomography Project for their continued support.

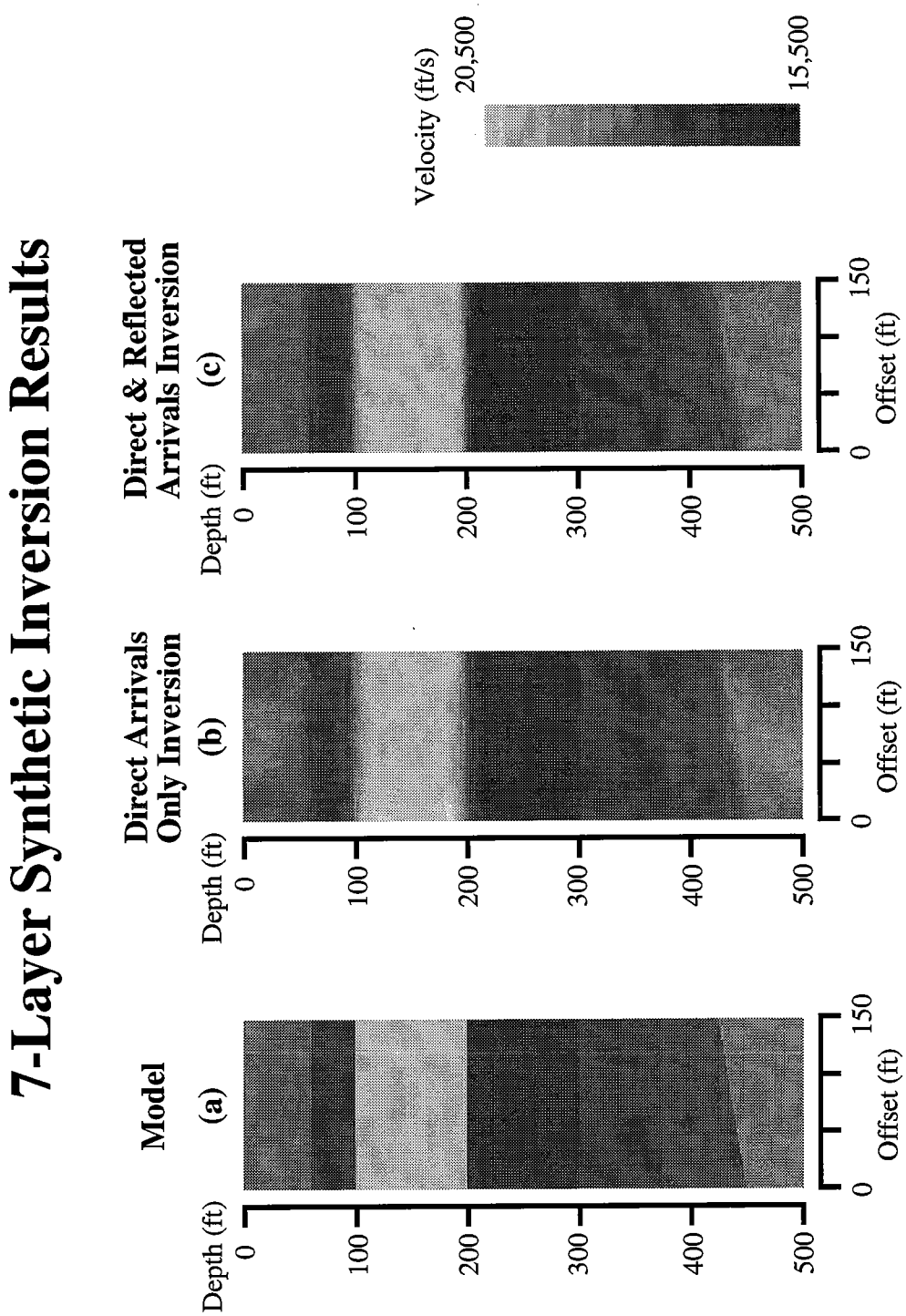

Figure 4: The above results for the more complex 7-layer model provide another comparison of an inversion calculated with both direct and reflected traveltime arrivals (c), and an inversion run using only direct arrivals (b). Both inversions were run identically: 10 iterations, 20 backprojections each iteration.

References

Chen, S.T., Zimmerman, L.J. and Tugnait, J.K., 1990, Subsurface imaging using reversed vertical seismic profiling and crosshole tomographic methods: Geophysics, **55**, 1478-1487.

Harris, J.M., 1992, Initial value raytracing in smoothly varying heterogeneous media: STP-**3**, paper I.

Harris, J.M., Nolen-Hoeksema, R., Rector, J.W., Van Schaack, M.A., and Lazaratos, S.K., 1992, High resolution cross-well imaging of a West Texas carbonate reservoir: Part 1. Data acquisition and project overview: 62nd Ann. Internat'l Mtg., Soc. Expl. Geophys., Expanded Abstracts, 35-39.

Harris, J.M., 1988, Cross-well seismic measurements in sedimentary rocks: 58th Ann. Internat'l Mtg., Soc. Expl. Geophys., Expanded Abstracts, 147-150.

Lazaratos, S.K., 1993, Cross-well reflection imaging: Ph.D. thesis, Stanford University.

Lines, L., Tan, H., Treitel, S., Beck, J., Chambers, R., Eager, J., Savage, C., Queen, J., Rizer, W., Buller, P., Cox, D., Ballard, J., Kokkoros, G., Sinton, J., Guerendel, P., Track, A., Harris, J., Lazaratos, S., Van Schaack, M., 1993, Integrated reservoir characterization: Beyond Tomography: 63rd Ann. Internat'l Mtg., Soc. Expl. Geophys., Expanded Abstracts, 298-303.

Mo., L.W., 1994, Calculation of direct arrival traveltimes by the eikonal equation: STP-**5**, paper K.

Rector, J.W., Harris, J.M., Lazaratos, S.K., and Van Schaack, M.A., 1994, Multidomain analysis and wavefield separation of cross-well seismic data: Geophysics, **59**, 27-35.

Van Schaack, M.A. and Lazaratos, S.K., 1993, An approach to interval velocity analysis for crosswell reflection imaging using reflection traveltimes: STP-**4**, paper F.

PAPER B

SEISMIC ATTENUATION TOMOGRAPHY USING THE FREQUENCY SHIFT METHOD: PRACTICAL CONSIDERATIONS AND APPLICATIONS

Youli Quan

ABSTRACT

This paper focuses on the implementation and application of seismic attenuation tomography based on the central frequency shift method. The frequency shift method uses the central frequency difference between incident and transmitted waves as the data to calculate the attenuation coefficient. The central frequency of transmitted waves can be measured from recorded seismograms, but the central frequency of incident waves may not be directly obtained. We suggest an approach which includes this frequency as an unknown in the inversion problem. This method is applied to 1-D geological structure (Devine data) and 2-D geological structure (King Mountain data).

INTRODUCTION

We have introduced the central frequency shift method to seismic wave attenuation tomography. Quan and Harris (1993) presented the basic theory with verification tests. In this paper we discuss more problems related to implementation of the method, and give more crosswell real data examples of 1-D and 2-D cases. Integrated geological interpretation with attenuation tomograms is in process.

BRIEF OF THE THEORY

We use a Gaussian spectrum as an example to briefly review the basic idea of the central frequency shift method. We assume that an incident wave has a spectrum of Gaussian distribution:

$$|S(f)| = \exp[-\frac{(f-f_s)^2}{2\sigma_s^2}], \qquad (1)$$

and the attenuation response of the medium is given by

$$|H(f)| = \exp[-f \int_{ray} \alpha_o df] , \tag{2}$$

where α_o is attenuation coefficient. Then the wave spectrum recorded at a receiver still has a Gaussian shape which is represented as

$$|R(f)| = |S(f)||H(f)| = A \exp[-\frac{(f - f_R)^2}{2\sigma_S^2}], \tag{3}$$

where,

$$A = \exp[-\frac{f_S^2 - f_R^2}{2\sigma_s^2}]$$

and

$$f_R = f_S - \sigma_s^2 \int_{ray} \alpha_o df . \tag{4}$$

Equation (4) can be rewritten as a tomographic inversion equation

$$\int_{ray} \alpha_o df = \frac{(f_S - f_R)}{\sigma_s^2} . \tag{5}$$

where $(f_S - f_R)$ is the central frequency difference between incident and transmitted waves, and $1/\sigma_s^2$ acts as a scaling factor. (Note that Eqn (4) in Quan & Harris (1993) had a typing error).

PRACTICAL CONSIDERATIONS

Static Correction Of Source Frequency f_S

Eqn (5) is the basic equation used for attenuation tomography which can be written in a discrete form as

$$\sum_j \alpha_{oj}^i l_j^i = \frac{f_S - f_R^i}{\sigma_s^2} . \tag{6}$$

Here index i represents the ith ray and j is for the jth pixel of the medium, l_j^i is the ray length within the jth pixel. In practice we can measure f_R from recorded seismograms, but may not directly obtain the source central frequency f_S and variance σ_s^2. From Eqns (1) and (3) we understand that the source spectrum $|S(f)|$ and receiver spectrum $|R(f)|$ exhibit the same variance σ_s^2, under the conditions given in Eqns (1) and (2). Therefore, we can choose the average of variances σ_R^2 at receivers as σ_s^2. We include the source spectral frequency f_S as an unknown in addition to α_j^i. By solving simultaneous equations we obtain attenuation coefficients α_j^i as well as f_S. Let

$$f_S = \bar{f}_S + \Delta f, \tag{7}$$

where $\bar{f}_S = \max\{ f_R^i \}$ is an initial estimation of f_S, and Δf is static correction. Then

$$\frac{f_S - f_R^i}{\sigma_s^2} = \frac{\bar{f}_S + \Delta f - f_R^i}{\sigma_s^2} = \frac{\bar{f}_S - f_R^i}{\sigma_s^2} + \frac{\Delta f}{\sigma_s^2}. \tag{8}$$

Eqn (6) can be written as

$$\sum_j \alpha_j^i l_j^i - \frac{\Delta f}{\sigma_s^2} = \frac{\bar{f}_S - f_R^i}{\sigma_s^2}, \tag{9}$$

where α_j^i and Δf are unknowns to solve. We need to properly scale the coefficients of these simultaneous equations to make the numerical calculation stable, since coefficients l_j^i and $1/\sigma_s^2$ have different dimensions.

Data Processing

We first pick and align the direct wave. Then we mix traces to reduce scattering interference, and perform FFT to the direct wave which is covered by a short time window. The central frequency f_R and variance σ_s^2 are calculated by the following formulas:

$$f_R = \frac{\int f|R(f)|df}{\int |R(f)|df},$$

$$\sigma_s^2 = \frac{\int (f - f_R)^2 |R(f)| df}{\int |R(f)| df}.$$

If we treat $(\bar{f}_S - f_R^i)/\sigma_S^2$ as "travel time", α_j^i as "slowness", and add one more term $-\Delta f / \sigma_s^2$ into the system of equations, then we can slightly modify the techniques and programs for travel time tomography to do the attenuation tomography.

APPLICATIONS

Devine Data Survey 2

Quan and Harris (1993) took a test on the Devine crosswell data set. We here apply the modified inversion method and program based on Eqn (9) to the same data again. To run the program, we only need to input travel time picks, central frequency picks and spectral variances. The program selects the average variance, the initial model and the source frequency, and then calculates the velocity tomogram and attenuation tomogram with source frequency static correction. Figure 1 shows data picks and inversion results for this data set. Figure 1a displays the central frequency picks which are used to inverse the P-wave attenuation coefficient α_o. We use straight rays and a 1-D model for the inversion. The model in vertical direction is divided into 300 pixels. Figure 1c gives the calculated α_o which is displayed in the form of $1/\alpha_o$. Figure 1b shows travel time picks which are used to inverse P-wave velocity displayed in Figure 1f. In Figure 1d we convert attenuation α_o and velocity v to Q-values by the definition

$$Q = \frac{\pi}{v\alpha_o}. \tag{10}$$

The geological structure and a well log are shown in Figures 1e and 1g which exhibit an excellent agrement with the inversion results. structure.

King Mountain Data

The geological structure in the King Mountain survey is complicated. We use a 2-D model for this crosswell data set. The model is divided into 30 (horizontal) by 60 (vertical). pixels. The central frequency picks of this data range from 600 - 1000 Hz. Figure 2 shows the 2-D P-wave velocity and attenuation tomograms which exhibit good correlation.

CONCLUSIONS

The frequency shift method can be used to estimate seismic attenuation, even in a complicated medium. The source frequency static correction this method makes the attenuation estimation relatively unique and stable.

ACKNOWLEDGMENTS

The inversion program was originally written by Feng Yin for velocity tomography. Feng Yin also helped to modify this program for attenuation tomography. The author also would like to thank Nicholas Smalley for editing this paper.

REFERENCE

Quan, Y. and Harris, J. M., 1993, Seismic attenuation tomography based on centroid frequency shift: Expanded Abstract of the 63rd SEG annual meeting (See also STP Annual Report, Vol. 4, No. 1, 1993

PAPER C

CALCULATING FRESNEL ZONES FOR CROSSWELL TOMOGRAPHY

Mark A. Van Schaack

ABSTRACT

Ray-theoretic tomography relies on the high frequency approximation of ray theory. Using ray theory, the traveltime from a source to a receiver is simply the line integral of slowness along the raypath. In practical applications the high frequency assumption of ray theory is often incorrect. In these cases the traveltime should be calculated as a function of the slowness within a wavepath.

The first step in wavepath tomography is defining the wavepath. This can be a difficult task in a general 2-dimensional medium. I define the Fresnel volume wavepaths numerically using an energetic-arrival finite-differences eikonal solver. Traveltime maps calculated in a 2-dimensional medium for the source and receiver are added together and any traveltime on this combined map falling within $1/2T$ of the energetic arrival defines a point lying within the Fresnel volume. Here, T is the period of the source wavelet. The advantage of using the energetic arrival solver is that critically refracted energy is ignored in the wavepath and traveltime calculations. This is a useful feature because forward-modeling critical refractions is inherently inaccurate in the non-linear traveltime tomography inversion. The use of the energetic arrival eikonal solver provides a fast, robust technique to calculate Fresnel wavepaths.

I use these wavepaths in a simple tomographic application. In this application the wavepaths are used as the basis for backprojecting over an area rather than a line. This builds a smoothing criterion into the tomographic inversion.

INTRODUCTION

The technique most commonly used to process crosswell seismic data is traveltime tomography. Seismic traveltime tomography uses the source-to-receiver propagation times for multiple source and receiver positions to estimate the velocity structure of a surveyed zone. The general approach to solving this inversion problem is to perturb an assumed

velocity model to minimize the difference between the traveltimes calculated using the assumed model and the observed traveltimes. There are two particularly important parts in this inversion. First is the forward modeling step, e.g., calculating traveltimes through the assumed model. Second is the backprojection technique. The backprojection technique is the formulation used to update the velocity model to minimize the difference between the calculated and observed traveltimes.

The most popular method used for calculating traveltimes through the velocity model is "ray-tracing". The use of ray-tracing implies a fundamental assumption of high frequency and invokes Snell's law along the path to calculate a ray trajectory. To satisfy the infinite frequency assumption, the spatial variation of velocity must be small compared with the wavelength of the seismic source. The "mathematical ray" resulting from the infinite frequency assumption of ray theory is a trajectory with zero volume, and the source-to-receiver traveltime is the line integral of slowness along this trajectory.

Often the high frequency assumption is not valid for a particular experiment. A typical approach in this situation is to apply a smoothing criterion to solve for only the part of the velocity field that does satisfy the high frequency assumption. The smoothing can be applied to the velocity model between iterations (Nemeth et al., 1993), or it can be built into the solution of the linear set of equations with techniques such as "convolutional quelling" (Meyerholtz et al., 1989) and damped least squares (Menke, 1984). A different approach is to apply the smoothing in the parameterization of the inverse problem. In this case the model is parameterized in terms of smooth basis functions (Michelena and Harris, 1991).

Woodward (1989) and Harlan (1990) have followed the idea of *wavepaths* based on Fresnel regions. Woodward, following work done by Hagedoorn (1954), replaces raypaths used in tomography with wavepaths calculated using the Rytov approximation. The calculation of these wavepaths is not always straightforward since it requires solutions for Green's functions in a 2-dimensional medium. Harlan estimates wavepaths by solving for all paths within a model for a given source-receiver geometry which do not exceed the minimum Fermat time by more than half a temporal wavelength. This technique has the advantage that it is easy to conceptualize and implement.

In this paper I describe a technique similar to Harlan's for determining wavepaths. The advantage of this technique is that it uses a finite-differences eikonal solver designed to calculate the traveltimes of *energetic* arrivals (Mo, 1994). Calculating only the energetic arrivals avoids problems which can result when the traveltimes of critical refractions, or head waves, are used. To illustrate one potential application, I use of the wavepaths as a smoothing function in a crosswell traveltime tomographic inversion.

DEFINING FRESNEL WAVEPATHS

The principle of Huygens-Fresnel states that any path, from source to receiver, that has a traveltime within half the period of the source wavelet of the minimum path time, contributes to the first arrival. This principle is just another way of expressing the idea that a wave traveling along the trajectory of a raypath is influenced not only by the velocities along that path, but also by the velocities in the near vicinity. I will use this idea as a basis to define wavepaths for use in backprojection in the crosswell tomographic inversion.

I introduce one difference into the wavepath definition: the minimum path time used is for the energetic travel path. Typically the minimum, or Fermat, traveltime is used in tomography. This is done because it is much easier to uniformly identify first arrivals in a crosswell data set than direct arrivals. Unfortunately, this philosophy can lead to several problems when high velocity contrasts lead to first arrival traveltimes from critical refractions.

Critical refractions typically result from raypaths which are at some point defined by an interface of fast and slow media. Crosswell transmission traveltime tomography, in general, lacks the resolution required to define these interfaces. For this reason the forward-modeled raypath will seldom be correct. Another related problem results from the inherent non-linearity of the traveltime inversion problem. The raypath is required to estimate the traveltime through the model and to define the path of backprojection. Unfortunately, this raypath is a function of the velocity model that is being calculated. As with many non-linear problems, the system is linearized by using an estimate of the velocity model to determine the raypaths and calculated traveltimes. This estimated model is improved and used in the next iteration as the new velocity estimate. Hopefully, the velocity model eventually converges to an accurate solution. However, until this velocity structure is found with a fair degree of accuracy, the conditions required to trace the refracted path will not be present. Another ambiguity lies in whether any particular critically refracted event comes from above or below the receiver.

For all these reasons I focus on using only the direct arrival traveltimes. One drawback of this philosophy is that it requires interpreting the data while picking traveltimes to avoid picking the traveltimes of critically refracted events. With the aid of local geologic knowledge, model based pick estimates, and personal expertise (acquired through practice), this is not an impossible problem. In my implementation, the Fresnel wavepath is the region defined by a set of point meeting the following criterion: a point falls within the Fresnel wavepath if the traveltime of a wave traveling from the source to that point, plus the

traveltime from that point to the receiver, is less than or equal to the minimum direct arrival traveltime plus one half the period of the source wavelet.

CALCULATING FRESNEL WAVEPATHS

The key to efficiently computing the Fresnel wavepaths is the energetic-arrival finite-differences eikonal solver (Mo, 1994). This solver is similar to the one developed by Vidale (1988) except that it computes the arrival times of the direct arriving energy and ignores critically refracted waves. Details of how this algorithm works can be found in Paper K, this volume.

Operationally, the eikonal solver runs using a 2-D gridded slowness model and a starting location, or source point. The solver then produces a traveltime map with the same dimensions as the original slowness map except that each node of the map represents the traveltime from the starting point to that node instead of the local slowness.

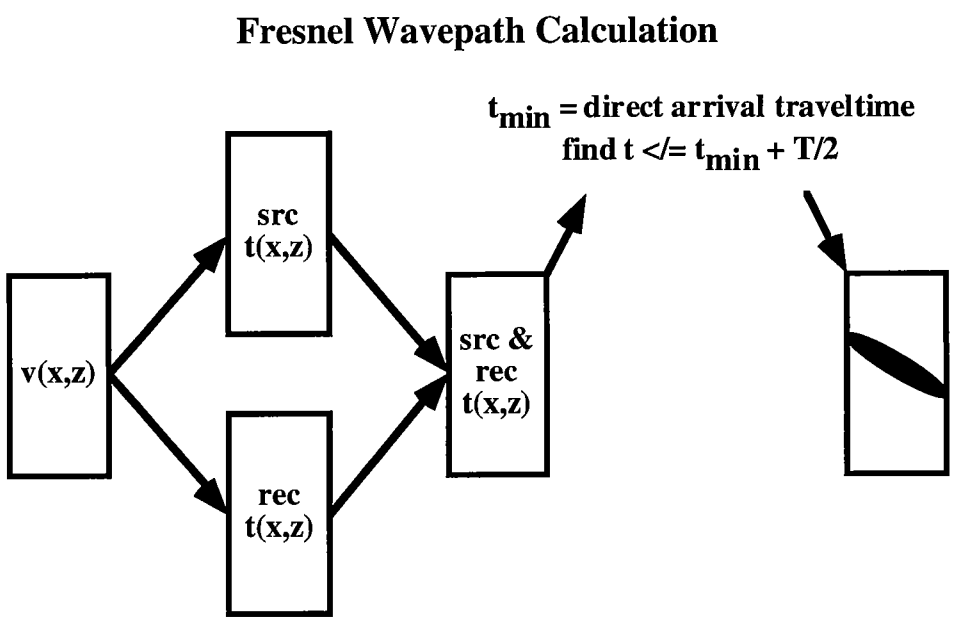

Figure 1: A schematic of the Fresnel wavepath calculation. Traveltime maps are calculated for the source and receiver positions from an input velocity model. The traveltime maps are calculated with a energetic-arrival finite-differences eikonal solver. These velocity maps are then added. A filter is applied to the combined map identifying all traveltimes falling within the direct arrival time and that time plus T/2, 1/2 the period of the source signal. The result of this filter is the Fresnel volume wavepath.

The procedure used to calculate the Fresnel wavepath is shown in Figure 1. To better illustrate this procedure I will go through the steps using the velocity model shown in Figure 2. The source location is at zero offset and at adepth of 175 ft. The receiver is located at an offset of 150 ft and a depth of 375 ft. The first step in calculating the Fresnel

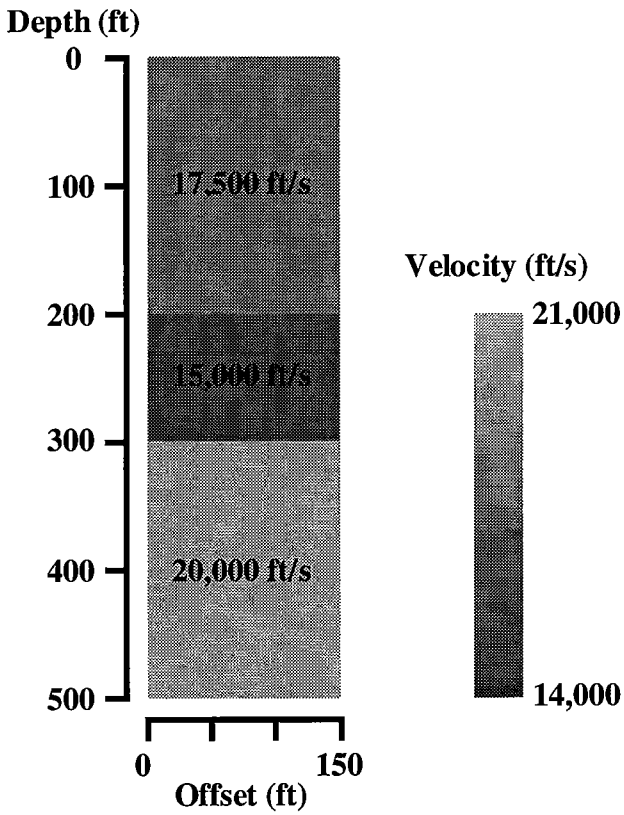

Figure 2: A simple 3 layer velocity model used to illustrate the technique used to calculate the Fresnel wavepath.

wavepath is to run the eikonal solver to create two traveltime maps, one where the source location is the starting point and another where the receiver location is the starting point. The results of these calculations are shown in Figure 3. The images in Figure 3 are displayed with a "random" colortable to accentuate the isochrons. Notice in the near vicinity of the starting point in each traveltime map that the isochrons are essentially circular in shape. This is expected where the velocity is constant. The isochrons deform at the interfaces due to the refraction of the transmitted energy.

The next step is to add the traveltime images of Figure 3. The result of this step is shown in Figure 4. This figure is also plotted using a "random" colortable. This combined traveltime map exhibits several interesting features. First, the isochrons represent

trajectories where the traveltime from the source, to the isochron, to the receiver is constant. These isochrons are equivalent to Kirchoff migration ellipses. Second, the central dark-gray area, which includes the source and receiver locations, is representative of the Fresnel wavepath. Although it is not within the resolution of this colortable, the central path, connecting the source to the receiver, is the "mathematical" raypath. All points falling on this path will have the same value, equivalent to the source-to-receiver traveltime.

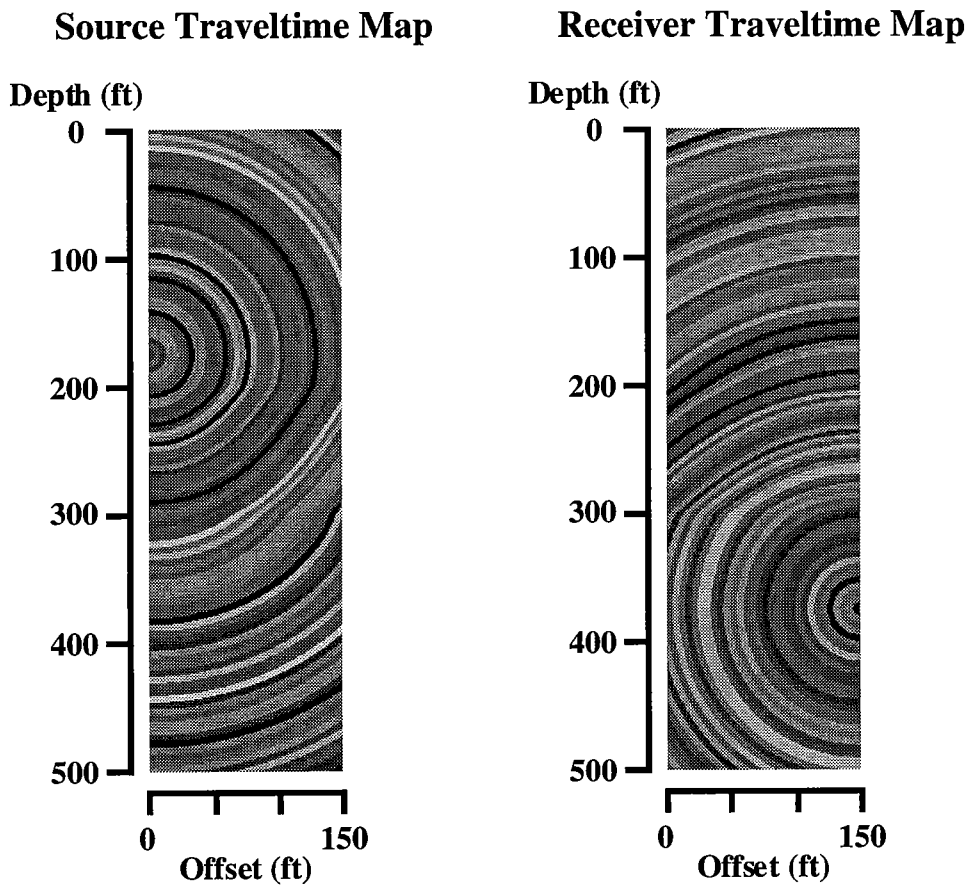

Figure 3: The above illustrations are eikonal traveltime maps for the source (left) and receiver (right). The traveltime maps are displayed with a "random" colortable to accentuate the isochrons of the traveltime maps.

Another potential application of this map is the determination of reflection points. The point at which the minimum traveltime is found along a line (e.g. reflector) drawn arbitrarily through this map, is the reflection point for that line. That minimum traveltime is also the reflection traveltime. If there is no possible reflection point along the line, the minimum time will be found at one of the two points where the line goes off the traveltime map.

These reflection points and times are useful in the calculation of XSP-CDP mapping trajectories.

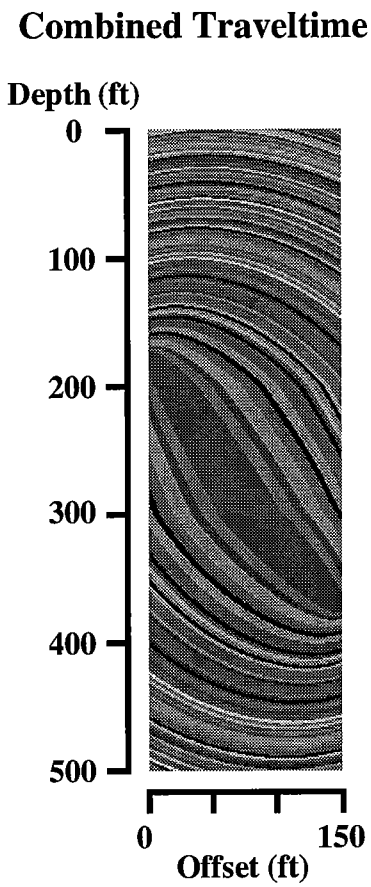

Figure 4: The above figure is the result of adding the source and receiver traveltime maps shown in Figure 3. A "random" colortable is used to highlight the traveltime contours. Notice the equi-colored contours are essentially equivalent to Kirchoff migration ellipses. Although the central "wavepath" is representative of the shape of the Fresnel wavepath the actual wavepath is determined by traveltime values falling between the direct arrival time, and the direct time + 1/2T. (one half the period of the source wavelet).

Finally, to determine the Fresnel wavepath, all times in Figure 4 are found which fall between the direct arrival traveltime, to this time plus one half the period of the source wavelet (inclusive). These points constitute the Fresnel wavepath. For this example I assume a source wavelet with a period of 1 ms which corresponds to a center frequency of 1000 Hertz. Therefore, the window used in determining the Fresnel wavepath is from 14.7 ms (the direct arrival traveltime) to 15.2 ms (14.7 ms + 1.0/2.0 ms). The Fresnel wavepath for this example is shown in Figure 5. The Fresnel wavepath in a homogeneous medium is

defined by an ellipse. The wavepath shown in Figure 5 is deformed due to the velocity contrasts in the model and is clipped where the wavepath extends outside the model.

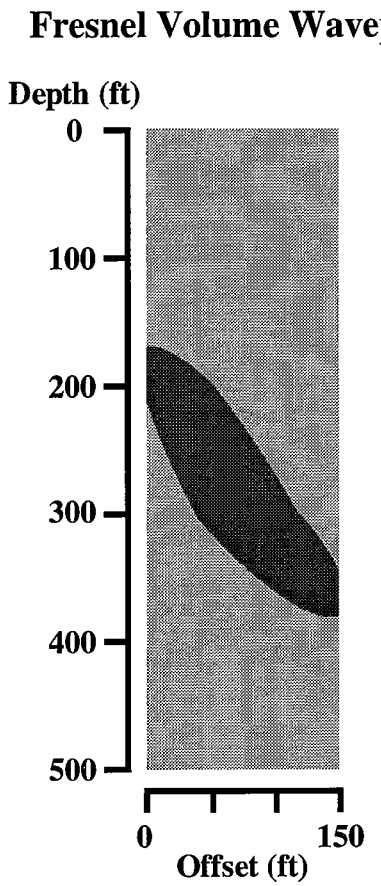

Figure 5: The Fresnel wavepath for the example shown in Figure 2. This wavepath includes all paths which have traveltimes within 0.5 ms of the direct arrival traveltime . The 0.5 ms window represents the appropriate value for a source wavelet with a period of 1 ms.

USING FRESNEL WAVEPATHS IN TRAVELTIME TOMOGRAPHY

Backprojection using volumeless rays

Using the high frequency ray approximation, the traveltime along path l, in a medium where the slowness is defined by $S(x,z)$, can be written as

$$t = \int_l S(x,z)dl \qquad (1)$$

Typically, the raypath is a function of the slowness field, $S(x,z)$, and a traveltime inversion must be performed in a sequence of linearized steps. Linearization is accomplished by using a slowness estimate, $S'(x,z)$, as the starting point of the inversion. This estimate defines the raypath, l', and is updated in the inversion to minimize the difference between t, the measured traveltime, and t', the traveltime calculated through the estimate $S'(x,z)$. One of the approximations made in the linearization is that the l' equals l. Equation (1) in terms of these new parameters is

$$t = \int_{l'} S'(x,z)dl' + R \tag{2}$$

where R, the traveltime residual, is defined by

$$R = t - t' \tag{3}$$

and t' is the traveltime measured through slowness field $S'(x,z)$:

$$t' = \int_{l'} S(x,z)dl' \tag{4}$$

To include the residual term inside the integral, multiply and divide R by $\int_{l'} dl'$ and rewrite the equation,

$$t = \int_{l'} (S'(x,z) + \frac{R}{l'})dl' \tag{5}$$

Equation (5) shows a method to use the traveltime residual to modify the continuous slowness field S' along the raypath so that the calculated traveltime matches the measured traveltime. This process is referred to as "backprojection". A single linear step in a tomographic inversion is called an "iteration". In an iteration the raypaths are defined by the estimated velocity model $S'(x,z)$ and do not change. The backprojection step is performed for all the raypaths and the final correction to $S'(x,z)$ is the average of the residual corrections. This process is the simultaneous iterative reconstruction technique (SIRT) (Dines and Lytle, 1979).

Backprojection using Fresnel wavepaths

Backprojection across Fresnel wavepaths is similar to backprojection along raypaths. In the case of wavepaths, the backprojection is done over an area instead of along a line. In this application I will use the Fresnel wavepaths to define an area to be used for backprojection. This formulation is still ray-theoretic in nature since the calculated traveltime used to calculate the residual is the energetic arrival eikonal time. To fully utilize the wavepath in a wave-theoretic traveltime inversion a formulation must be developed which uses all the information within the wavepath. In this formulation all the velocities within the wavepath contribute to the final calculated traveltime and perturbing any of these velocities would result in perturbing the calculated traveltime. Although a wave-based formulation would be superior to a ray-based formulation, the research on calculating wave-based traveltimes is still in progress.

The simple technique I describe utilizes the wavepath as a smoother. In this case the residual calculated using the ray-theoretic traveltime is backprojected over the entire wavepath. The advantage offered by this simple application is that the smoothing typically required in any ray-based inversion is defined honoring the wave nature of the data rather than in an ad hoc manner.

The wavepath backprojection formulation

Similar to equation (1) above, the Fresnel volume traveltime can be written as

$$t = G\iint_a w(x,z)S(x,z)da \tag{6}$$

In this equation $w(x,z)$ is a weighting factor and G is a geometric factor used to scale the contributions to obtain a traveltime measurement. I determine G empirically by forward-modeling. The first step in computing G is to rewrite the equation replacing the weighted slowness terms by the average of the weighted slowness terms. Equation (6) becomes

$$t = G\iint_a S_{avg}da \tag{7}$$

where S_{avg} is defined as

$$S_{avg} = \frac{\iint_a w(x,z)S(x,z)da}{\iint_a w(x,z)da} \tag{8}$$

These equations are now used to define G. This is done using the direct arrival eikonal time through the estimated slowness field $S'(x,z)$. This traveltime, t', was calculated when the wavepath was defined. Rewriting equation (7) using the estimated slowness field and the calculated traveltime,

$$t' = G\iint_a S'_{avg}\, da \tag{9}$$

In equation (9), G is the only unknown. Solving for G

$$G = \frac{t'}{S'_{avg}} \tag{10}$$

Now a backprojection formulation can be written starting with equation (7) using the same philosophy as applied in equations (2)–(5). First, rewrite equation (7) in terms of the observed traveltime, the geometric factor, the estimated slowness model, and the traveltime residual:

$$t = G\iint_a S'_{avg}\, da + R \tag{11}$$

The residual term, R, is defined by equation (3). Now include R inside the integral. To do this expand S_{avg} and multiply and divide R by an integral form to provide a common denominator. This expression is

$$t = G\iint_a \frac{\iint_a w(x,z)S'(x,z)da'}{\iint_a w(x,z)da'} da + R\frac{\dfrac{G\iint_a da'}{\iint_a w(x,z)da'}}{\dfrac{G\iint_a da'}{\iint_a w(x,z)da'}} \tag{12}$$

Rearranging terms and putting R inside the integral,

$$t = \frac{G}{\iint_a w(x,z)da'}\iint_a \left(\iint_a w(x,z)S'(x,z) + \frac{R\iint_a w(x,z)da'}{G\iint_a da'} da' \right) da \tag{13}$$

Implementation

Although equation (13) appears complicated it is fundamentally the same as equation (5). To implement equation (13) in an inversion algorithm the slowness model is dicretized as a finely meshed grid. In this parameterization the areas of integration become a summation over the nodes. Equation (13) can now be written in its discretized form,

$$t = \frac{G}{\sum_{i,j} w_{i,j}} \sum_{i',j'} \left(w_{i',j'} S_{i',j'} + \frac{R \sum_{i,j} w_{i,j}}{GN} \right) \tag{14}$$

If the weighting function is assumed to be unitary within the Fresnel volume then the summation of the weighting function is equal to the number of grid points within the Fresnel volume, *N*. This further simplifies the equation,

$$t = \frac{G}{N} \sum_{i',j'} \left(S_{i',j'} + \frac{R}{G} \right) \tag{15}$$

FRESNEL VOLUME BACKPROJECTION EXAMPLE

I have run a traveltime inversion using the Fresnel volume backprojection formulation on a synthetic data set. The simple model used is seen in Figure 2. The data set includes 101 sources by 101 receivers evenly spaced along the sides of the model every 5 ft. In my inversion I implemented equation (14) to utilize the weighting function. I designed a simple function that linearly ramps the wavepath's weight from a value of one on the axis of the Fresnel volume to zero at the edge. Starting with a homogeneous model, four iterations were run using a SIRT-type algorithm. Each iteration was run for 20 backprojections.

The results of the inversion are shown in Figure 6. The inversion has converged reasonably well towards the solution. Some artifacts are seen near the interfaces and at the top and bottom of the image. Although the Fresnel wavepaths might provide additional stability, the inversion still contains artifacts typical of inversions which use the high frequency ray assumption. The forward modeled traveltime used in my inversion is calculated using the eikonal solver with its ray-theoretic assumptions. The wavepath is used simply to provide a smoothing criterion. The results of the wavepath inversion suggest that

developing a formulation where the traveltime is calculated from the wavepath might provide improved results.

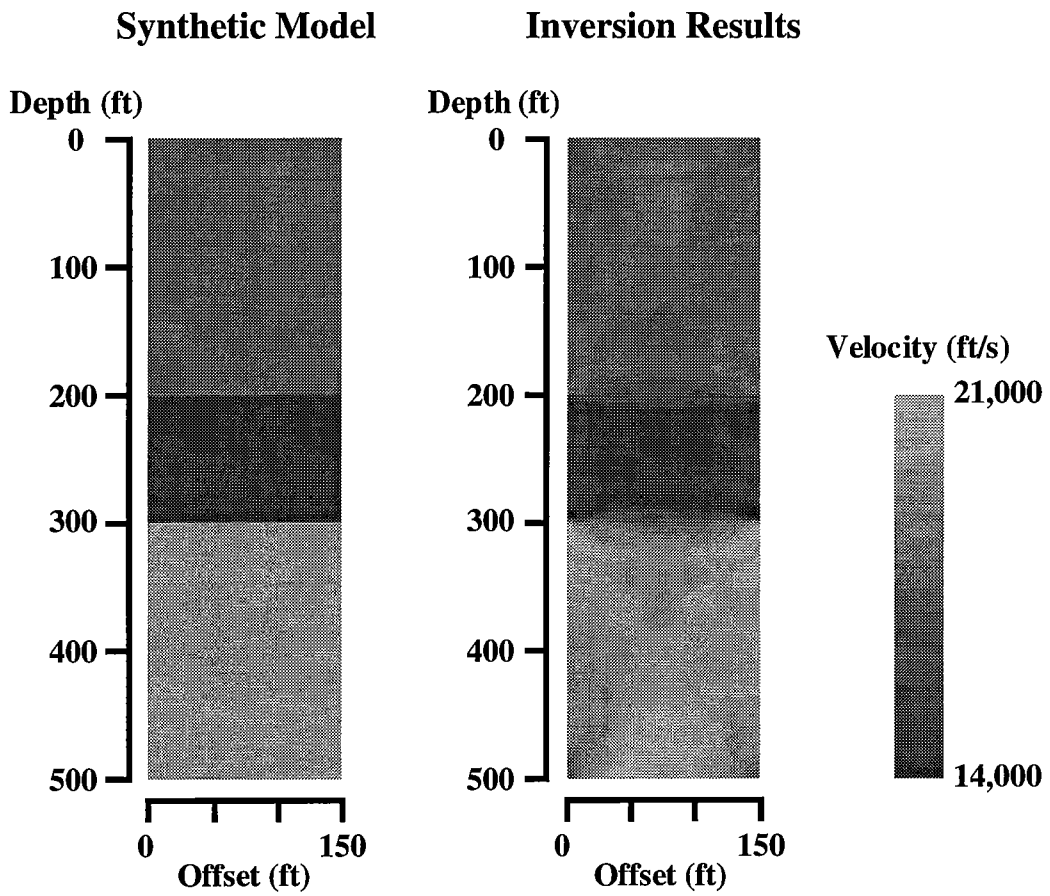

Figure 6: The results of the Fresnel wavepath inversion. In this inversion the Fresnel wavepaths were used to provide a basis for smoothing the inversion. This smoothing is accomplished during backprojection. This inversion consisted of 4 iterations of 20 backprojections each. The starting model was homogeneous.

DISCUSSION

I have described a technique by which energetic arrival Fresnel volumes can be easily calculated. A simple application was designed to use these wavepaths as a smoothing criterion in a crosswell traveltime inversion. The results of this inversion do not show much improvement in speed or accuracy compared with more standard smoothing techniques. The ease with which these wavepaths are calculated might be more fully utilized if the

wavepaths are applied in a fullwave inversion formulation. They might also be used as a basis set in a "fat ray" formulation such as that described by Michelena and Harris (1991).

ACKNOWLEDGMENTS

I would like to thank Reinaldo Michelena, Bob Langan, and Le-Wei Mo for their useful discussions on the topic of Fresnel zones. I would also like to thank the corporate sponsors of the Stanford Tomography Project for their continued support.

References

Dines, K.A., and Lytle, R.J., 1979, Computerized geophysical tomography: Proc. IEEE, **67**, 1065–1073.

Hagedoorn, J.G., 1954, A process of seismic reflection interpretation: Geophys. Prosp.., **2**, 85–127.

Harlan, B., 1990, Tomographic estimation of shear velocities from shallow cross-well seismic data: 60th Ann. Internat. Mtg., Soc. Expl. Geophys., Expanded Abstracts, 86–89.

Menke, W., 1984, Geophysical data analysis: discrete inverse theory: Academic Press Inc.

Meyerholtz, K.A., Pavlis, G.L., Szpakowski, S.A., 1989, Convolutional quelling in seismic tomography: Geophysics, **54**, 570–580.

Michelena, R.J., and Harris, J.M., 1991, Tomographic inversion using natural pixels: Geophysics, **56**, 635–644.

Mo., L.W., 1994, Calculation of direct arrival traveltimes by the eikonal equation: STP-**5**, paper K.

Nemeth, T., Fuhao, Q., and Normark, E., 1993, Dynamic smoothing in crosswell tomography: 63rd Ann. Internat. Mtg., Soc. Expl. Geophys., Expanded Abstracts, 118–121.

Vidale, J., 1988, Finite-difference calculation of traveltimes: Bull. Seis. Soc. Am., **78**, no. 6, 2062–2076.

Woodward, M.J., 1989, Wave equation tomography: Ph.D. thesis, Stanford University.

PAPER D

AN APPROACH TO ADAPTIVE GRIDDING FOR TRAVELTIME TOMOGRAPHY

Jerry M. Harris

ABSTRACT

This short paper summarizes the recent development and application of a node-based tomography inversion algorithm. The node model provides adaptive gridding to address the problems of non-uniform ray coverage and inhomogeneous resolution. The spacing or density of nodes are adaptively selected to provide more uniform ray density per node or to match the geometrical pattern of the geological structure being imaged. In this way, reconstruction artifacts associated with non-uniform coverage may be reduced while velocity estimates are made more reliably. Also, "unknowns' are not wasted on homogeneous zones but may be concentrated in heterogeneous regions of the image. If no information is available to adapt the grid, the node model may be run as a regular spaced lattice.

THE MODEL

The motivation for this model was introduced last year (Harris, 1993). Consider velocity inversion from traveltime data. For the forward problem, the velocity is specified at irregularly spaced nodes. See Figure 1. The forward model traveltime is obtained from the discrete summation:

$$t_j = \sum_{m=1}^{M_j} \hat{S}_{jm} \Delta\ell \qquad (1)$$

where $\hat{S}_{jm}$ are "interpolated" slowness values for points along the jth ray path and M_j is the number of equi-spaced steps of length $\Delta\ell$ along the ray. The slowness values $\hat{S}_{jm}$ are interpolated from the nodes using an N-term interpolation scheme:

$$\hat{S}_{jm} = \sum_{i=1}^{N} d_{ijm} S_i , \qquad (2)$$

where the S_i's are the values of slowness at the N nodes of the model and the d_{ijm}'s are the interpolation coefficients. In practice, I use bi-linear interpolation from the four nearest nodes, i.e, N=4. The interpolation coefficients are determined in closed form following identification of the locations of the four surrounding nodes. See Figure 2.

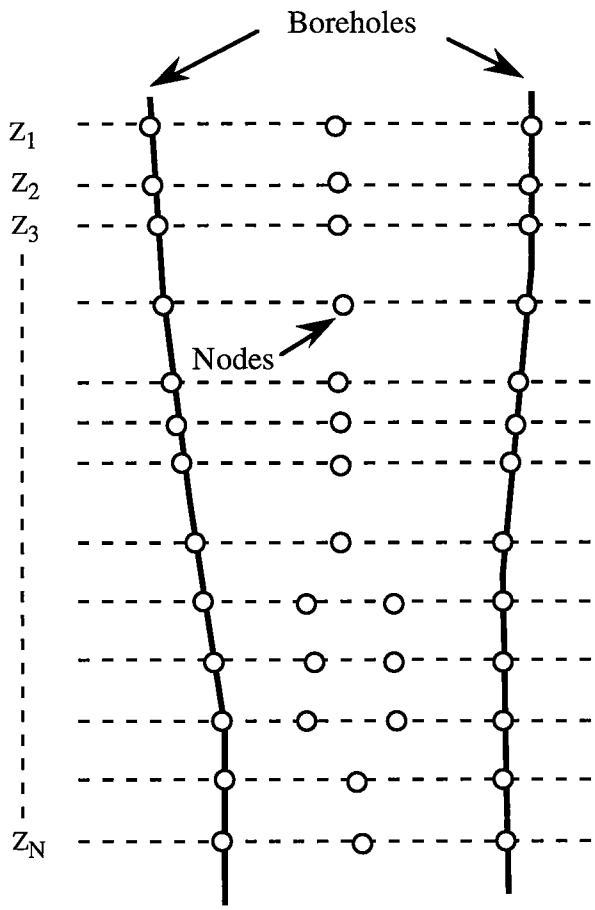

Figure 1. The density and pattern of nodes are adapted by the user to fit the geological structure or other criteria such as ray density. The location of the nodes is given by its depth and offset coordinates. For many geological situations, its is appropriate to begin with nodes only along the profile of the wellbores.

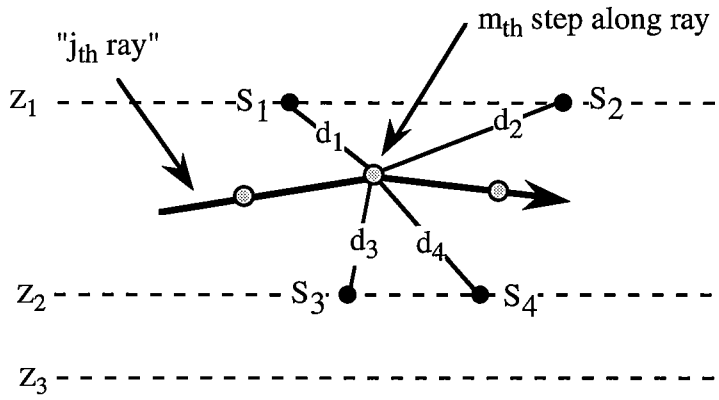

Figure 2. Slowness along the ray path is calculated by interpolating values from the four neighboring nodes. When node spacing is small and uniform, i.e., a lattice, a nearest neighbor approximation can be used and the node model reduces to the string model.

Because the nodes are irregularly spaced, computer time is spent finding the four nodes surrounding the interpolation point. This effort can be reduced when the nodes are regularly spaced and can be indexed for a fast search. During forward modeling, the slowness is known and the bi-linear coefficients are used to calculate the slowness at the interpolation point. During inversion, for example using SIRT, the bi-linear coefficients are used to weight the distribution of traveltime residual to the four contributing nodes.

EXAMPLES

The first example is the synthetic model shown in Fig. 3a. This model is mostly 1-D with a dipping feature near the bottom of the survey. The result of a SIRT inversion using straight rays is shown in Fig. 3b. Fig. 3b was then used as the background for the curved ray result shown in Fig. 3c. These results were obtained for two nodes per depth level. The two nodes are located along the right and left boundaries of the model at uniform depth intervals.

The second example, Figs. 4a through 4c, uses real field data taken from a Gulf Coast site. This result illustrates how complex interwell variations are handled by only two lateral nodes.

REFERENCES

Harris, J. M., 1993. Lattice parameterization for tomography, STP Annual Rpt, vol. 4, no.1, Paper E.

PAPER E

CROSSWELL COMMON LATERAL POINT REFLECTION IMAGING

Nicholas Smalley

ABSTRACT

A new method of crosswell reflection imaging is introduced in this paper. It uses previously described gathers (Smalley, 1992) and crosswell reflection velocity analysis (Smalley, 1993), (Smalley, 1994) along with a point to point imaging procedure described in this paper. A high resolution real data reflection image result is shown.

INTRODUCTION

Crosswell reflection imaging is a relatively new field in the crosswell seismology experiment. Some excellent results have already been obtained in crosswell reflection imaging (Lazaratos, et. al, 1992). The objective in this paper is to improve on the XSP-CDP mapping procedure by developing an algorithm that uses the reflection data itself to obtain the velocity model that is used to image the reflection data and therefore takes into account 2-D variation in the medium. The algorithm described in this paper is the Common Lateral Point (CLP) imaging method (Smalley, 1992). The benefits of using this method is that we take into account 2-D variation in the velocity structure which is particularly important as we go to wider well separations, and avoid use of tomogram velocities which may not be the best velocities for reflection imaging. However, the CLP reflection imaging method does keep the point to point mapping procedure of the XSP - CDP imaging algorithm (i.e. the same impulse response). This is important to enable signal to noise separation, particularly in dealing with the shear wave and converted arrivals.

WAVEFIELD SEPARATION

Before full wave form data can be imaged for reflections, it first has to be optimized for reflections. Crosswell data contain many different modes. While the data itself is very complicated, we can go through a fairly simple procedure to separate other wave modes from the reflections. The raw data is sorted into source and receiver gathers. Even though the imaging procedure used to image the reflections will involve sorting the data into different sorts of gathers, the source and receiver gathers provide a good domain in which to enhance the reflections. We aim to do three things to separate the reflections from the raw data:

1) Remove the direct arrival

2) Enhance all upgoing or downgoing events

3) Remove noise such as converted arrivals and tube wave noise.

Removal of the direct arrival requires:

1) Picking the direct arrival travel time from the raw data

2) Alignment of the direct arrival

3) Subtracting off the direct arrival through a trace mix.

Enhancement of the reflections requires:

1) f-k filter to separate upgoing and downgoing reflections.

2) f-k filter to filter addition noise.

While the f-k filter is a powerful tool it should always be used cautiously. The pass of the filter should be made as wide as possible while still filtering out the undesired noise. A pass that is too narrow can artificially mix the data. Converted arrivals are the biggest source of noise in reflection data, and should be the primary objective of the second f-k filter after upgoing and downgoing wavefield separation.

INPUT TO THE CLP REFLECTION IMAGING ALGORITHM

The input to the CLP reflection imaging algorithm consists of

1) Wavefield separated data optimized for reflections

2) A set of imaging HNMO and VLMO stacking velocities at control points in space.

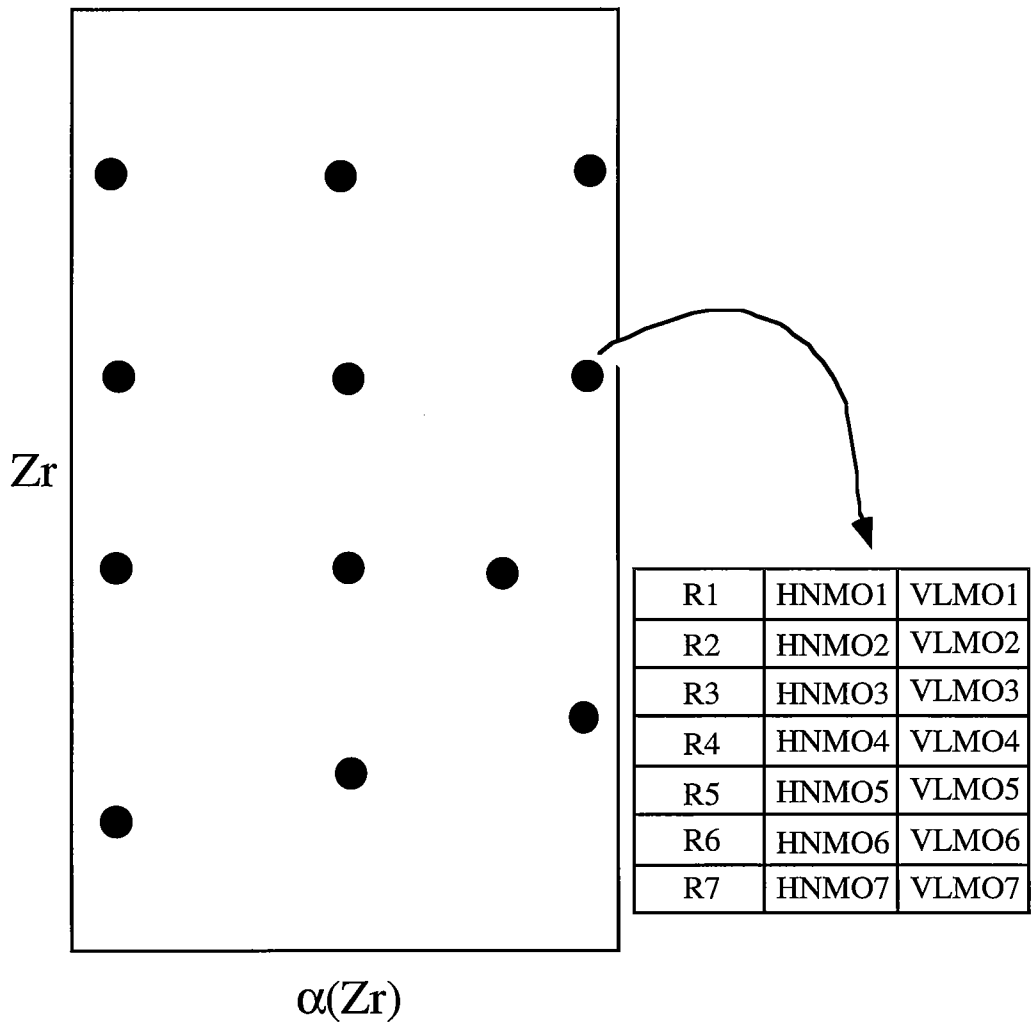

Figure 1. A grid of control points obtained from depth conversion and velocity analysis. At each control point is a 3 by N set of radial distances, HNMO and VLMO stacking velocities.

The procedure for wavefield separation was discussed previously. The control point locations and their corresponding HNMO and VLMO velocities (Smalley, 1992), (Smalley, 1993) are from the depth conversion and velocity analysis procedure in another paper in this volume. The set of control points make up a grid in [α(Zr),Zr] space (Smalley, 1992) (Figure 1). At each one of these control points is a 3 by N matrix of radial distances, HNMO and VLMO stacking velocities (Figure 1). In order to obtain a stacking velocity for all input traces that will be included in the final stack, interpolation between the control points is necessary.

CLP IMAGING PROCEDURE

The CLP imaging algorithm is shown below:

```
Reflection Depth Zr {

   Input traces {

      calculate polar coordinates [ α(Zr), r(Zr) ]

      interpolate radial distance bounds[ r(Zr) ]  {input from velocity analysis}

      if r(Zr) > min r(Zr) and r(Zr) < max r(Zr) {

         calculate incidence angle θ(Zr)

         Interpolate appropriate HNMO and VLMO stacking velocities
         {input from velocity analysis}

         HNMO correction

         VLMO correction

         Extract sample at t=0

      }
```

convert $\alpha(Zr)$ to $x(Zr)$

}

}

stack over $r(Zr)$

This is similar to the procedure described in a previous paper (Smalley, 1992). The differences are

1) the determination of the radial distance bounds for a trace and testing to see if the input trace has a radial distances within the given bounds.

2) interpolation of HNMO and VLMO stacking velocities between control points.

The velocity analysis procedure will indicate over which radial distances we can get a coherent summation of signal over a CLP point. The interpolation of HNMO and VLMO stacking velocities is a linear interpolation in the order of:

1) radial distance $r(Zr)$

2) assumed reflection depth Zr

3) the angular coordinate $\alpha(Zr)$ in the polar coordinate system - representing the lateral location.

As stated previously, the CLP imaging procedure has the same impulse response as the XSP-CDP imaging algorithm (point to point mapping), but has a different way of sorting the data and obtainment of velocities for imaging. The comparison between the CLP and XSP-CDP algorithms are:

CLP imaging		**XSP - CDP**
Reflection depth	**parameterization of input traces**	Source or receiver gather
polar coordinates [$\alpha(Zr)$, $r(Zr)$]	**sorting of input traces**	Receiver or source number
2 - D reflection velocity analysis	**source of velocities for imaging**	1 - D travel time tomography
HNMO and VLMO stacking velocities	**velocities used for imaging**	Tomogram interval velocities
2 - D interpolation between velocity analysis control points	**accounting for velocity variation of imaging region**	1 - D raytracing based on tomogram interval velocities
Common ratio or lateral point gathers (Common $\alpha(Zr)$)	**CDP stacking**	1 - D raytracing based on tomogram interval velocities
Point to point mapping	**imaging operator or impulse response**	Point to point mapping

The differences can be highlighted as:

1) sorting of the data as it is processed through the algorithm

2) use of stacking velocities that have 2-D variation for CLP imaging as opposed to a set of 1-D interval velocities for XSP-CDP imaging.

ACCOUNTING FOR 2-D VELOCITY VARIATION: VELOCITY ANALYSIS VERSUS RAYTRACING

In order to do cross-reflection imaging we need algorithms that take into account that there will be variation in the velocity of the medium within the survey; both 1-D and 2-D. The XSP-CDP algorithm takes into account velocity variation by 1-D raytracing. The CLP imaging algorithm takes into account velocity variation by 2-D velocity analysis. Fermat's principle of minimum travel time and stationary ray paths says that a change in the velocity will have a greater effect on the travel time of the ray path than on the actual location of the ray path. Raytracing takes into account the deviation in the ray path due to velocity variation by use of a 1-D tomogram. The CLP imaging algorithm takes into account velocity variation by correcting the traveltime misfit by use of 2-D velocity analysis.

REAL DATA RESULTS

The preceding theory was applied to West Texas data site. In order to attenuate noise primarily due to converted arrivals, we can do an additional sort of the gathers according to incidence angle (Lazaratos, 1992). This is also shown previously in the CLP algorithm description. The angle domain has many properties for signal and noise separation (Lazaratos, 1992). We f-k filter in this domain to eliminate steeply dipping noise. We also needed to choose the appropriate spatial bandpass to optimize the signal. The choice for the appropriate f-k filtering is determined globally while the bandpass filtering is done on a more localized scale. The final results are shown in figure 2. We see excellent detail of the reservoir region (depths 2850 - 2950 ft.) as well as an unconformity at the bottom of the image.

CONCLUSIONS AND FUTURE WORK

We have described a new method for doing crosswell reflection imaging and have shown its potential on a real data set. In the future we want to standardize the velocity analysis so that we can get immediate feedback on the choice of velocities for imaging. Essentially we want to make the velocity analysis procedure automated on the same level as surface seismic imaging.

ACKNOWLEDGMENTS

The author thanks Jerry Harris for his support, Youli Quan for providing the well logs, and Mark Van Schaack for providing the traveltime picks. The author thanks the sponsors of the STP project at Stanford for their support.

REFERENCES

Lazaratos, S., Rector, J.W., Harris, J.M., and Van Schaack, M., 1992, High Resolution Imaging Of a West Texas Carbonate Reservoir: STP vol. 3 No.1 Paper E

Smalley, N., 1992, Crosswell Pre-Stack Partial Migration (Theory): STP vol. 3 No. 1, Paper M.

Smalley, N., 1993, Crosswell Reflection Velocity Analysis: STP vol. 4 No. 1 Paper G.

Smalley, N., 1994, Crosswell Reflection Depth and Velocity Analysis, Paper F, this volume.

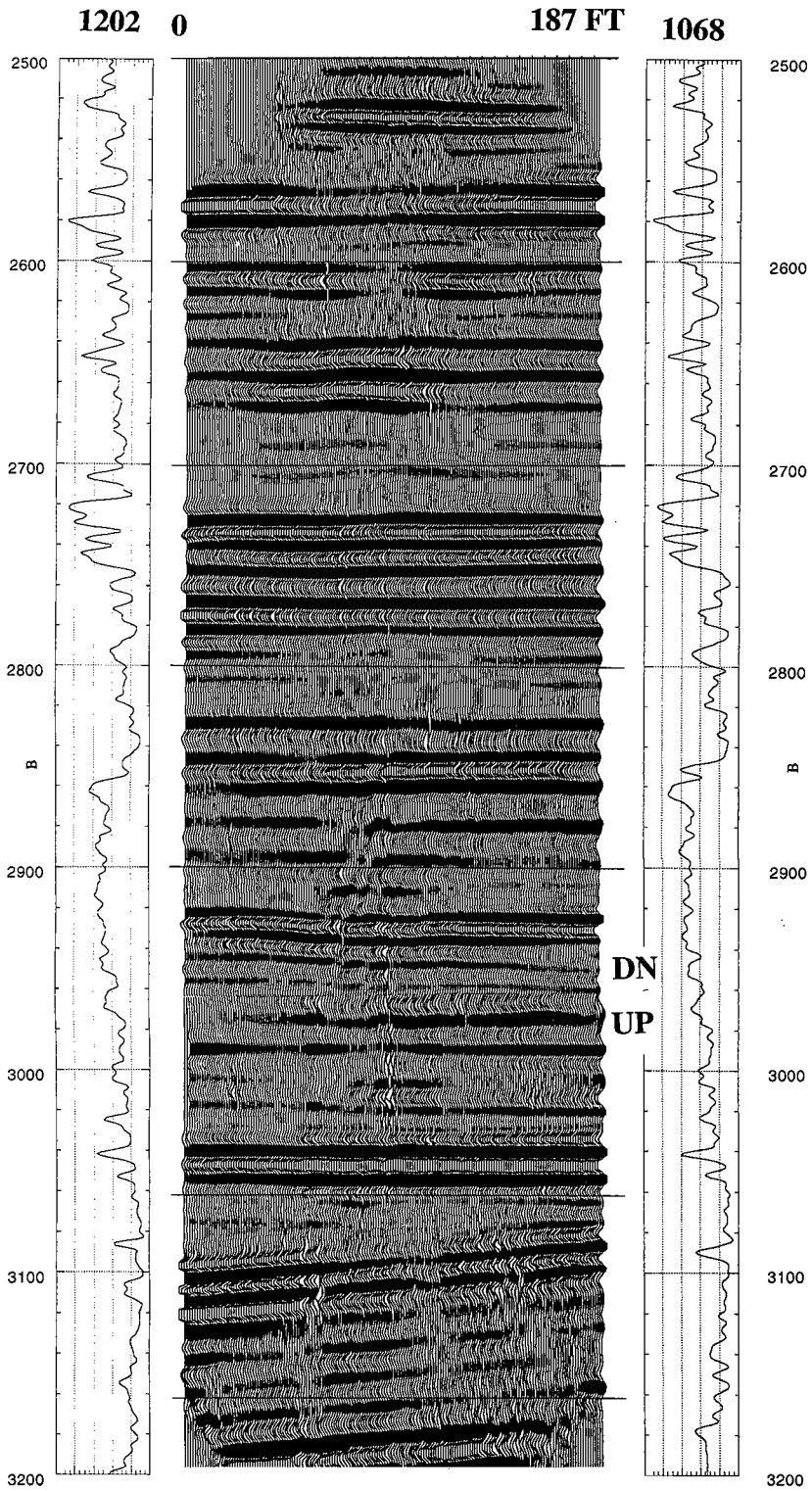

Figure 2. Composite Reflection Image

PAPER F

CROSSWELL REFLECTION DEPTH AND VELOCITY ANALYSIS

Nicholas Smalley

ABSTRACT

A method is described for estimating depths of reflections in crosswell data. The depth determination allows for accurate velocity analysis to find the HNMO and VLMO stacking velocities. These velocities are used in the CLP reflection imaging algorithm described in another paper in this volume (Smalley, 1994). It is use of these velocities that allow us to maximize the coherency in the stacking of reflection data and to take into account 2 - D variation in the velocity of the medium.

INTRODUCTION

Recently a method was introduced to obtain stacking velocities from crosswell reflection data (Smalley, 1993). It was shown that these stacking velocities could improve the coherency of individual reflections. This paper shows how the CLP-VLMO domain (Common Lateral Point gather after the VLMO correction (Smalley, 1993)) is used to estimate the depth of the reflection, which allows for subsequent velocity analysis. By allowing for variation in the lateral location of the reflection point as well as reflection depth when we do velocity analysis we can obtain a 2-D sampling of the medium (Figure 1). This 2-D sampling allows us to account for 2-D variation in velocity when doing cross-well reflection imaging. This is particularly important as we go towards wider well offsets.

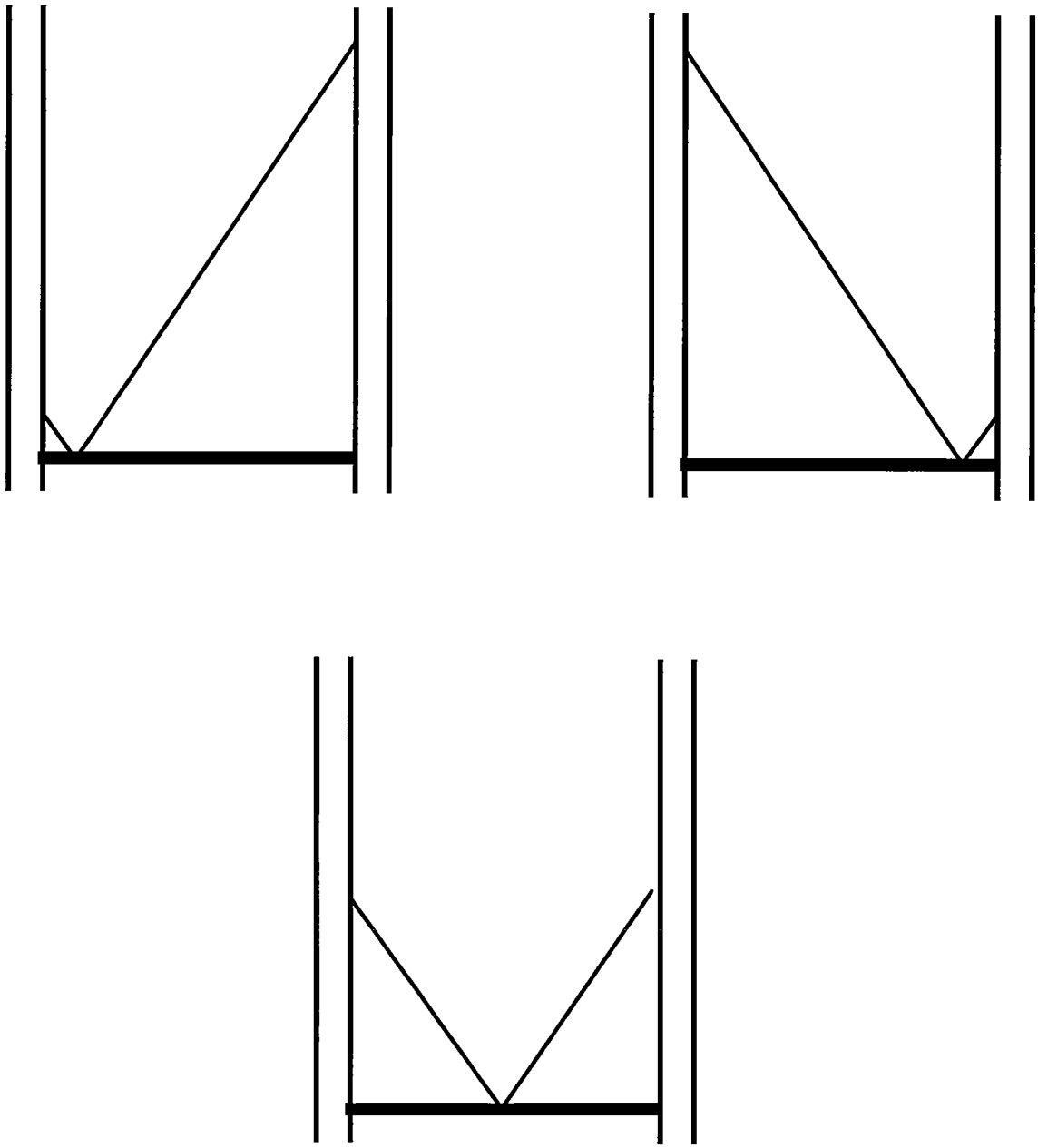

Figure 1. By doing velocity analysis for different reflection points on for a given reflection depth we obtain a 2-D sampling of the medium.

REFLECTION DEPTH AND VELOCITY DETERMINATION

Estimation of Reflection Depth

Before we can determine the HNMO and VLMO stacking velocities for reflections we have to accurately estimate the reflection depth. In a previous paper (Smalley, 1993) we showed that we could use the CLP-HNMO gather to estimate the depth of the reflection upon which we want to do velocity analysis. The disadvantage of this domain is that we were looking for a residual hyperbolic moveout at small radial distances or large angles of incidence. Also, while we were looking for non-linear moveout, the slope of the linear moveout that we needed to see was unknown since it depended on the velocity. By using the CLP - VLMO gather (Smalley, 1993) we can more easily separate the depth - velocity ambiguity. In this domain the desired moveout is zero or a perfectly flat event. Before we estimate the HNMO and VLMO stacking velocity vectors we can apply constant velocity HNMO and VLMO corrections for a set of assumed reflection depths. The velocities and reflection depth pair that yield the least deviation from zero moveout gives us the depth of the reflection. Therefore we choose a lateral location of the reflection point and determine the reflector's depth. This gives us a 2-D location of a control points at which to do reflection velocity analysis.

Velocity Analysis - Determination of HNMO and VLMO stacking velocities

Once we have determined the depth of the reflections we can then align it to zero moveout by use of the HNMO and VLMO corrections. A previous paper described how to align reflections with combinations of HNMO and VLMO stacking velocities in the CLP-VLMO gather (Smalley, 1993). A real data example after depth conversion and velocity analysis is shown in figure 2. The reflector depth was determined to be 2950 ft, and the lateral points are 4, 6, and 8 feet from the source well where the total well offset is 187 ft. A set of the HNMO and VLMO stacking velocities as a function of the radial distance r(Zr) is shown in figure 3 for the lateral point 6 feet from the well. We allowed the HNMO and VLMO stacking velocities to be the same which is a very good approximation except when there is very large changes in velocity (> 50%).

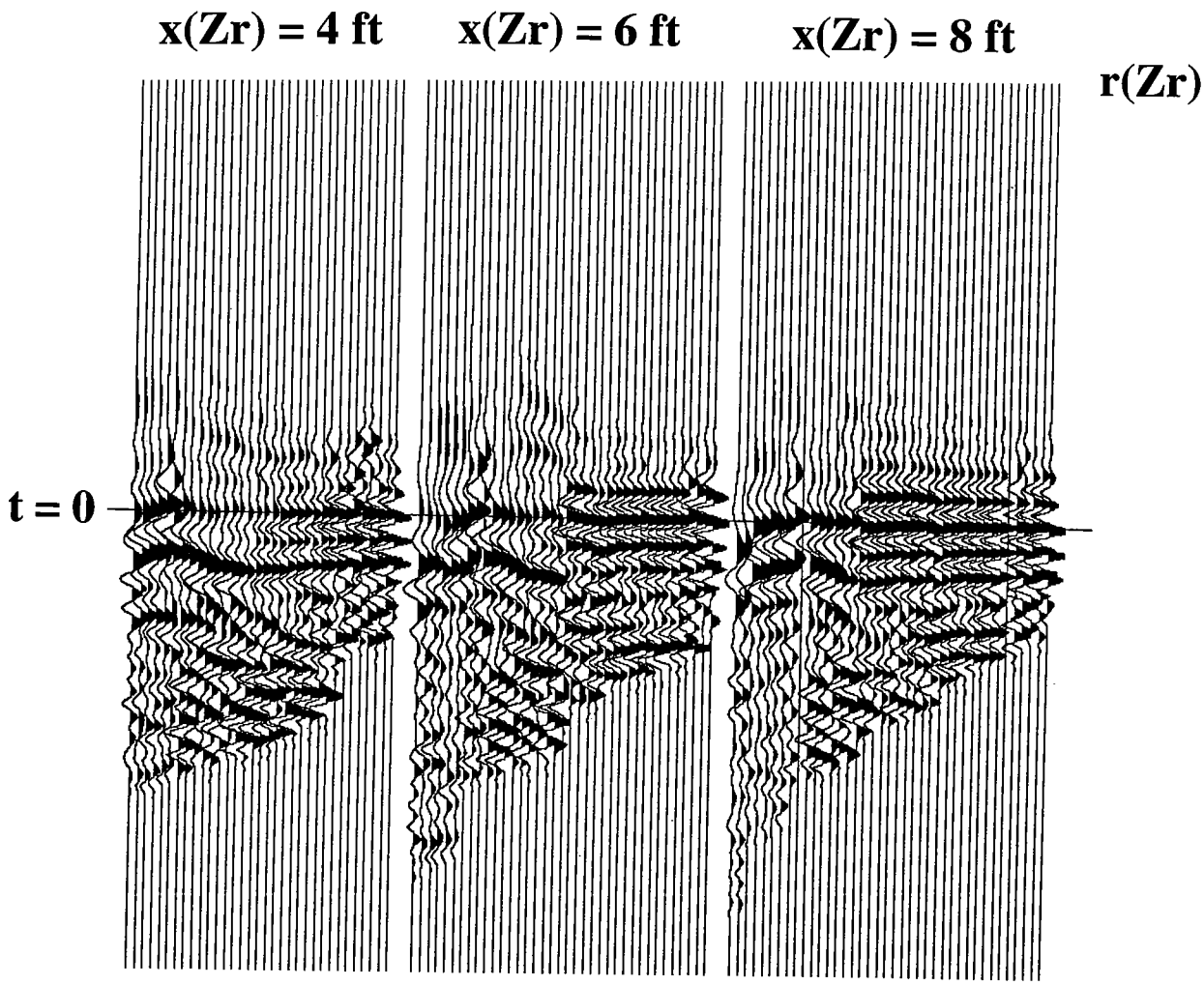

Figure 2. CLP - VLMO after depth estimation and velocity analysis for three reflection lateral points at locations 4, 6, and 8 feet from the source well. The depth of the event at t = 0 was determined to be 2950 ft.

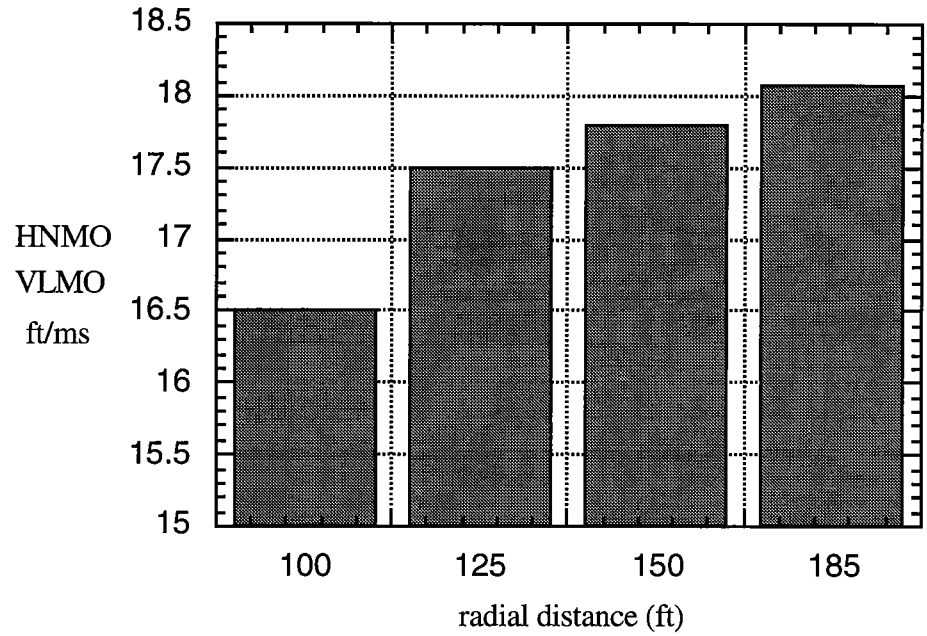

Figure 3. HNMO and VLMO stacking velocites for a lateral point near the source - well

CONCLUSIONS AND FUTURE WORK

We have presented an improved method for depth estimation of reflection data which allows for accurate velocity analysis. Future work involves automating the velocity analysis to the level of surface seismic work so that we can more closely tie it with the reflection imaging procedure.

ACKNOWLEDGMENTS

The author thanks Jerry Harris for his support, and the sponsors of the Seismic Tomography Project at Stanford University.

REFERENCES

Lazaratos, S., Rector, J.W., Harris, J.M., and Van Schaack, M., 1992, High Resolution Imaging Of a West Texas Carbonate Reservoir: STP vol. 3 No.1 Paper E

Smalley, N., 1992, Cross-well Pre-Stack Partial Migration (Theory): STP vol. 3 No. 1, Paper M.

Smalley, N., 1993, Cross-well Reflection Velocity Analysis: STP vol. 4 No. 1 Paper G.

Smalley, N., 1994, Common Lateral Point (CLP) Reflection Imaging, Paper E, this volume.

PAPER G

ANALYSIS AND ATTENUATION OF TUBE WAVES: IN CROSSWELL SEISMIC SURVEYS

Le-Wei Mo

ABSTRACT

Seismic data collected in a crosswell survey often contain strong tube waves that have parts of their travel paths along wells where the sources and receivers are positioned. Tube waves can be excited by the source and propagate along the source well, and then radiate as body waves propagating to the receiver well to be recorded. This is called the source well tube wave. Tube waves can also be excited by passing body waves and propagate along the receiver well, and are recorded. This is called the receiver well tube wave. By the principle of reciprocity, source and receiver well tube waves have similar characteristics and can be analyzed by the same method. Owing to the slow propagation velocity of the tube waves, they are usually spatially aliased in practical records in either common shot gathers (CSG) or common receiver gathers (CRG). While receiver well tube waves are aliased in CSG, they are well sampled and predictable in CRG, and vice versa for source well tube waves. Tube waves that have travel paths in both the source and receiver wells are also predictable. I predict and attenuate source well tube waves in CSG, and predict and attenuate receiver well tube waves in CRG.

INTRODUCTION

Seismic data recorded in a crosswell survey often contain strong tube waves. These tube waves can be stronger than any body waves being recorded. Most explorationists view the tube waves as undesirable coherent noise because they are superimposed on reflection signals and prevent optimum imaging of stratigraphic and structural conditions in the subsurface. Thus, attenuation of tube waves has been the topic of extensive current research. One method to attenuate tube waves is to apply special equipment in field data recording (Pham et al., 1993). Even though tube waves are attenuated in field data recording, tube waves are still recorded, and then one has to resort to numerical processing techniques. Cai and Schuster (1993) aligned tube waves along their traveltime picks in

common shot gathers and common receiver gathers and applied a median filter to predict tube waves. Finally, the predicted tube waves are subtracted from the field data. In this method, tube wave traveltimes must be picked precisely and upgoing and downgoing tube waves are processed separately. A serious problem with this method is to deal with the data within a polygonal shape after the tube waves are aligned. These are the factors that limit the effectiveness of this method.

In this paper, I first analyze the generation and propagation of tube waves in a crosswell experiment. Then I predict and attenuate source well tube waves in CSG, and predict and attenuate receiver well tube waves in CRG. My method is shown to be effective in attenuating tube waves in a field dataset.

ANALYSIS OF CROSSWELL TUBE WAVES

In crosswell seismic surveying using a downhole source, the source excites body waves, and it also excites a tube wave propagating along the borehole fluid called the source well tube wave. When the tube wave passes through an impedance contrast in the source well, it excites body waves that propagate to the receiver well to be recorded. Common impedance contrasts in a borehole are radius changes, junction points between casing and noncasing, perforation, and the top and bottom of the borehole. And according to numerical calculations and field data, body waves excited by tube waves at these impedance contrasts can often be stronger than the body waves directly excited by the source (Balch and Lee, 1984).

When body waves from the source well impinge the receiver well, they are recorded by the receivers. At the same time, strong tube waves are excited at impedance contrasts to propagate along the receiver well. The excitation and propagation of various waves in a crosswell experiment is schematically illustrated in Figure 1 for the recording of a common shot gather. Figure 2 is a synthetic CSG obtained by ray tracing with the experimental geometry of Figure 1(a).

Figure 3 schematically illustrates the wave propagation and the traveltime trajectories within a common receiver gather. By the principle of reciprocity, a common receiver gather can be considered as a common shot gather. And this can be realized by reversing the wave propagation directions (the directions the arrows point) in Figure 3(a). Thus, source and receiver well tube waves have similar characteristics and can be analyzed by the same method. Figure 4 is a synthetic CSG with the experimental geometry of Figure 3(a).

Owing to the slow propagation velocity of the tube waves, the receiver (source) well tube waves have steep slopes in the common shot (receiver) gathers. In discretely sampled field data, these steep events are usually spatially aliased. However, in the other domain, they are well sampled and predictable. For the source (receiver) well tube waves in a CSG (CRG), they are well sampled and predictable. For those tube waves that have propagation paths in both the source and receiver wells, even though they are aliased, they are also predictable.

In neighboring CSG's, the source well tube waves 2 and 22 in Figure 1 and Figure 2 vary by a time delay, the time that the source well tube wave propagates between neighboring source positions. Likewise, in neighboring CRGs, the receiver well tube waves 12 and 22 in Figure 3 and Figure 4 vary by a time delay, the time that the receiver well tube wave propagates between neighboring receiver positions.

ATTENUATION OF CROSSWELL TUBE WAVES

When the source is at a location that excites source well tube waves, the source direct arrival and source well tube waves are time coincident. For a source located away from the location that excites source well tube waves, there is a time delay that the tube wave takes to propagate from the source location to the source well tube wave excitation point. Since one can predict the time trajectory of source well tube waves in CSG's, one can use the relationship between neighboring CSG's to estimate the arrivals of source well tube waves. When the estimated source well tube waves are subtracted from the original CSG's data, source well tube waves are then attenuated.

A CSG data can be modeled as

$$D_i = S_i + T(t - t_0) \tag{1}$$

where i is the index of the CSG, D_i are the whole CSG data, T is source well tube wave (events 2 and 22 in Figure 1 and Figure 2), t is recording time, $t0$ is the first break time trajectory by this analysis, S_i is the portion of the data other than T. A neighboring CSG can be modeled as

$$D_j = S_j + T(t - t_0 + \delta t) \tag{2}$$

where T is the same as in equation (1) except a time shift δt. Cross-correlation D_i with D_j around t_0 and picking the maximum correlation value can determine the time shift δt. Cross-correlation can be carried out for the whole CSG, or for individual traces.When the source well is straight and vertical, the tube wave time delay δt is trivial to predict geometrically, but when the well deviates or curves,one has to resort to a cross-correlation procedure to estimate it.

Then neighboring CSG's are shifted to place the source well tube waves in phase and are stacked to estimate the source well tube waves.

$$\hat{T} = \frac{1}{2n+1} \sum_{i=-n}^{n} D_i(t - \delta t) \tag{3}$$

where n is the number of chosen CSG's on each side of the designated CSG. In the following field data example, I choose n to be 5 so that the events other than the tube waves to be estimated are attenuated by an order of magnitude in the stacking. The estimated source well tube wave $\hat{T}$ is then subtracted from the CSG data.

In practice, source well tube waves are excited at an identifiable finite number of points of impedance contrasts. Source well tube waves excited at these points are each estimated and attenuated. Finally, the data are sorted into CRG's, and estimation and attenuation of receiver well tube waves (events 12 and 22 in Figure 3 and Figure 4) are carried out by the same method as outlined above, invoking the principle of reciprocity.

EXAMPLES

I apply the above method to a field crosswell dataset, which has 201 CSG's and 203 CRG's. Figure 5 is an unprocessed CSG, Figure 6 an unprocessed CRG (Depth 0 in the following Figures refers to the top of the survey, instead of the Earth surface). The borehole source excites both compressional (P-) and shear (S-) waves, as does the source well tube wave. In this dataset, both the source and receiver well tube waves are much stronger than the body waves. Figure 7 is the estimated source well tube wave on the CSG data in Figure 5. Figure 8 is the result after subtracting the source well tube wave in Figure 7 from Figure 5. After all the CSG's are processed, the data are sorted into CRG's.

Figure 9 is the new CRG of the CRG in Figure 6. Figure 10 is the estimated receiver tube wave on the CRG data in Figure 9. Figure 11 is the result after subtracting the receiver

well tube wave in Figure 10 from Figure 9. After all the CRG's have been processed, Figure 12 is the new CSG of the CSG in Figure 8. Comparing data in Figure 5 and 6 to the processed data in Figure 11 and 12, it is obvious that after attenuation of crosswell tube waves, the direct arrival and reflection of body waves stand out clearly.

CONCLUSIONS

The linear time delay relationship of tube wave excited body waves in neighboring data gathers has been used to estimate and attenuate tube waves. I predict and attenuate source well tube waves in common shot gathers, and then predict and attenuate receiver well tube waves in common receiver gathers. Application of the method has shown that it is effective in attenuating tube waves in a crosswell seismic experiment. After attenuation of tube waves, body waves stand out clear, otherwise difficult to identify.

REFERENCES

Balch, A. H., and Lee, M. W., 1984, Vertical seismic profiling: techniques, application, and case histories: International Human Resources Development Corporation.

Cai, W., and Schuster, G. T., 1993,Processing Friendswood cross-well seismic data for reflection imaging: 63rd Ann. Internat. Mig., Soc. Expl. Geophys., Expanded Abstracts,92-94.

Pham, L. D., Krohn, C. E., Murray, T. J., and Chen, S. T., 1993, A tube wave suppression devices for cross-well application: 63rd Ann. Internat. Mig., Soc. Expl. Geophys., Expanded Abstracts,17-20.

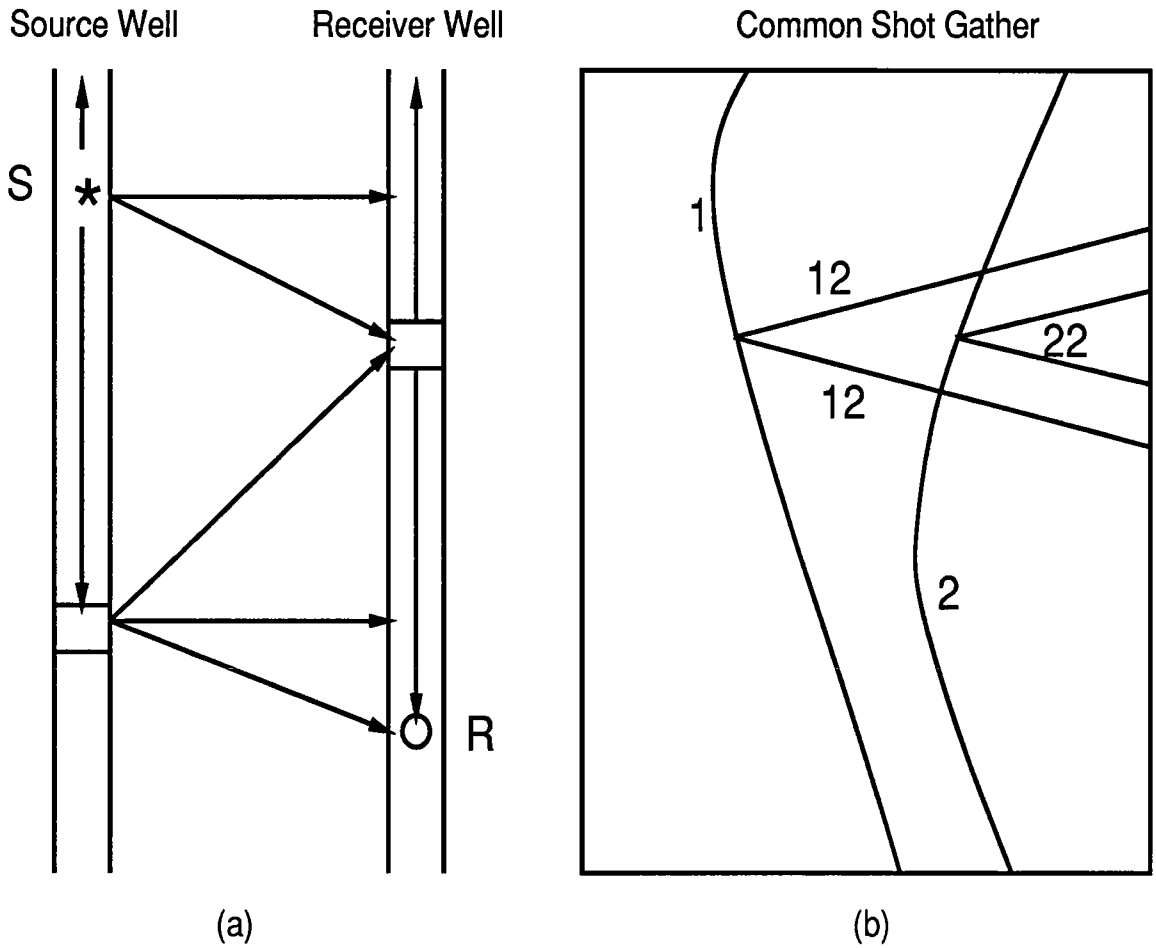

Figure 1 (a) is the crosswell experimentsetup. (b) is the traveltime trajectory of a common shot gather. In (b), 1 is the direct arrival, 2 is the body wave excited by the source well tube wave, 12 (22) is the receiver well tube wave excited by 1 (2).

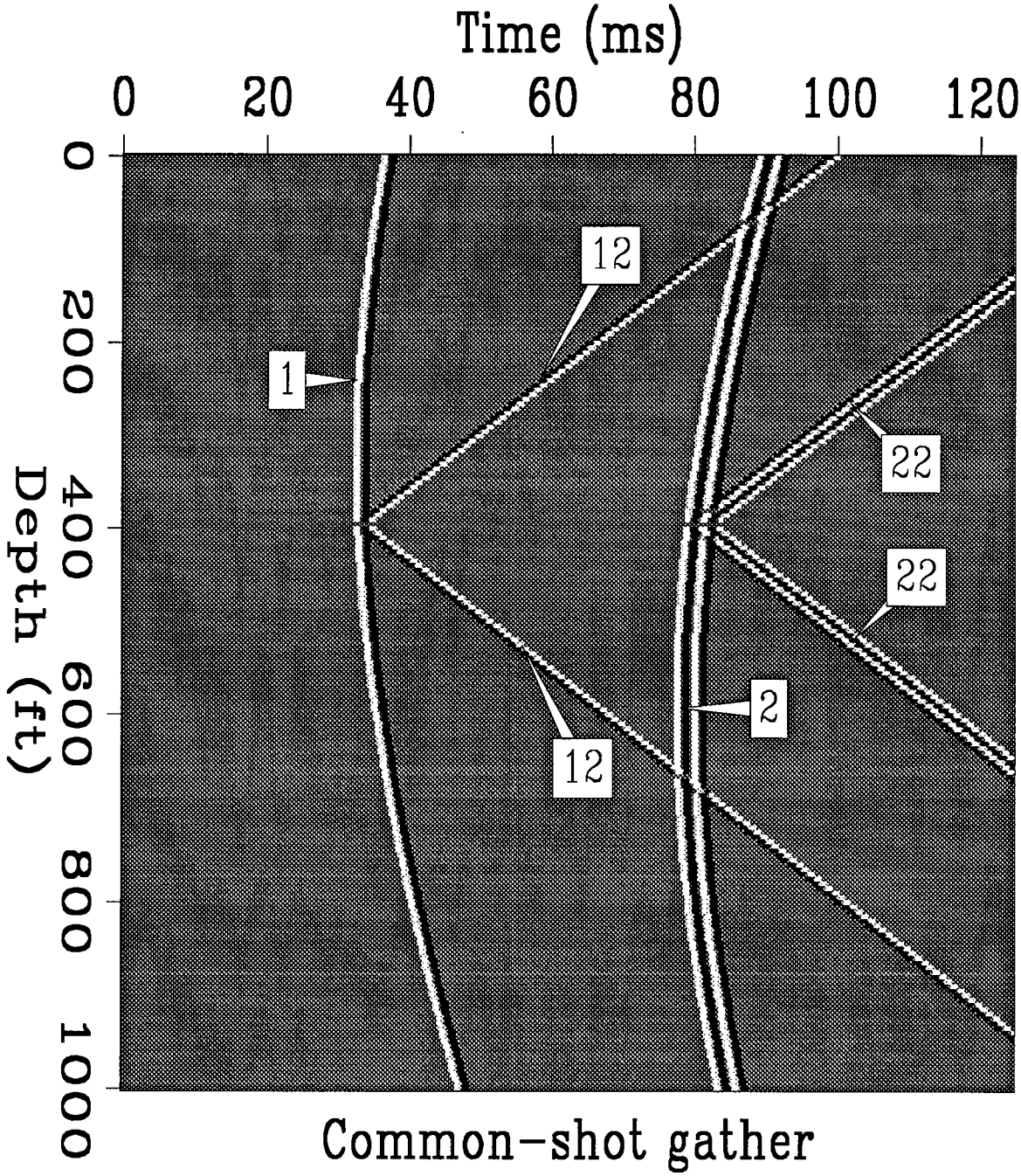

Figure 2 A synthetic common shot gather. Events 1, 2, 12, and 22 have the same descriptions as in Figure 1(b).

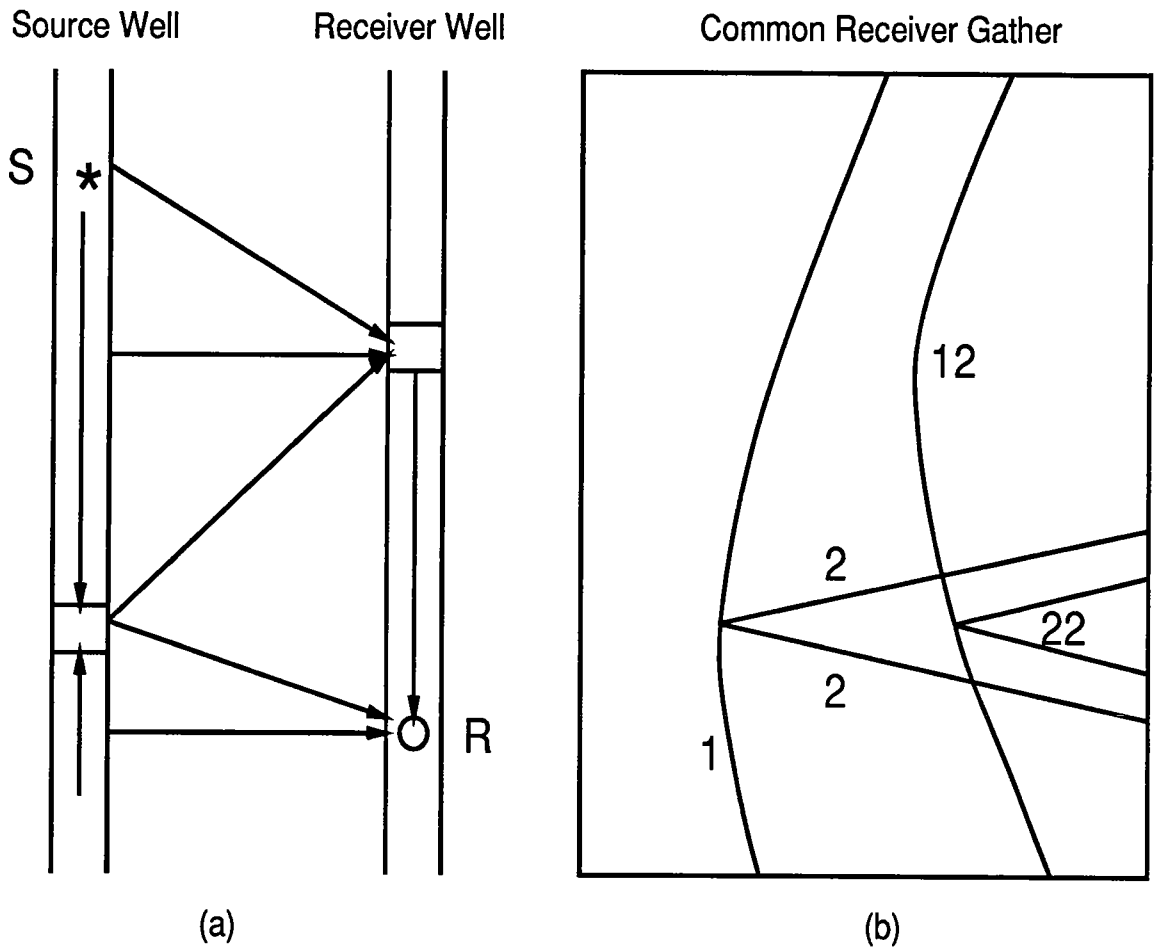

Figure 3 (a) is the crosswell experimentsetup. (b) is the traveltime trajectory of a common receiver gather. In (b), 1 is the direct arrival, 2 is the body wave excited by the source well tube wave, 12 (22) is the receiver well tube wave of 1 (2), as in Figure 1.By the principle of reciprocity, 1 can be considered as the first arrival excited by the receiver, 12 is the body wave excited by tube wave in the receiver well, 2 (22) is the source well tube wave excited by 1 (12).

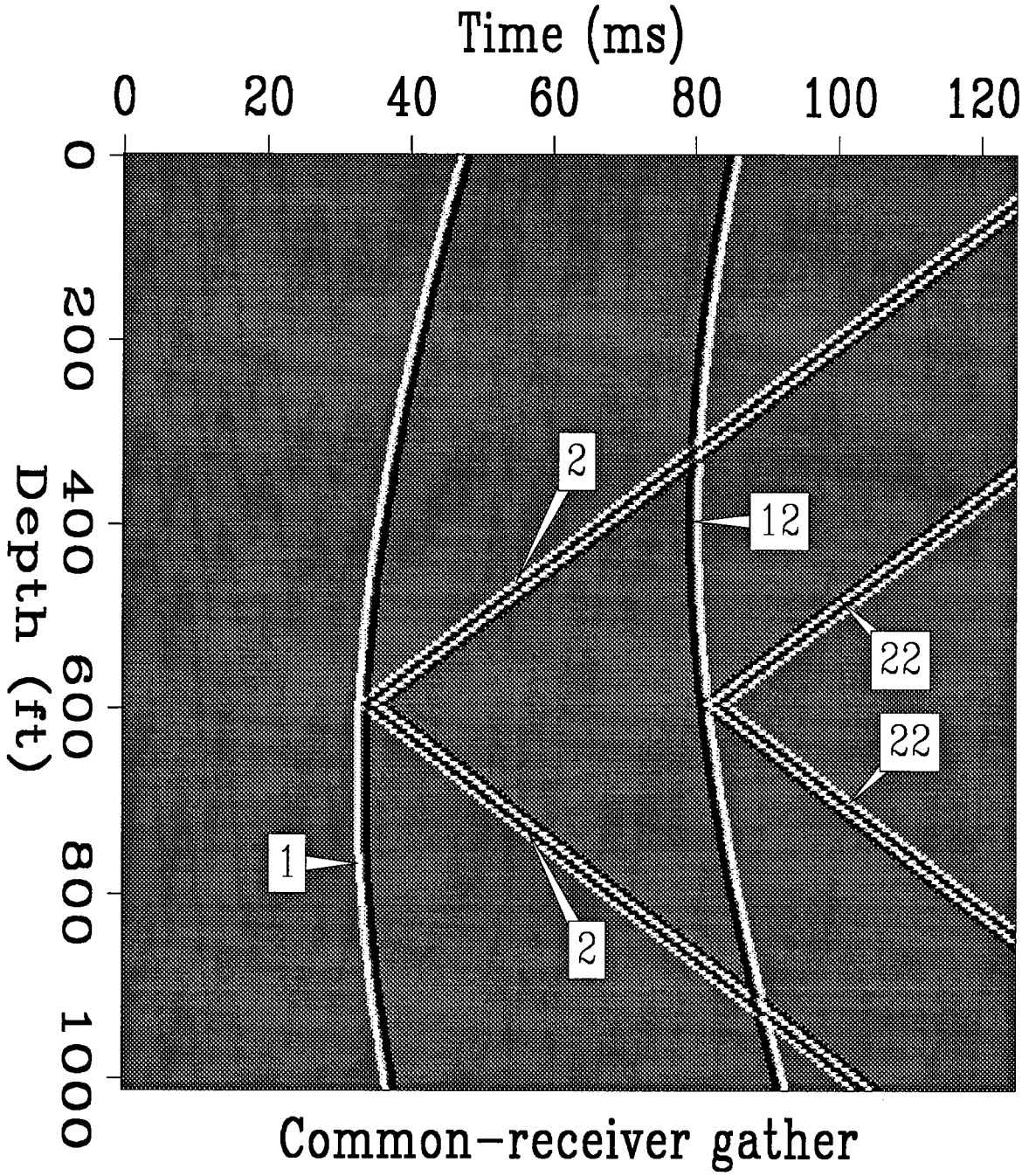

Figure 4 A synthetic common receiver gather. Events 1, 2, 12, and 22 have the same descriptions as in Figure 3. Polarities help to identify the corresponding events between Figure 2 and Figure 4.

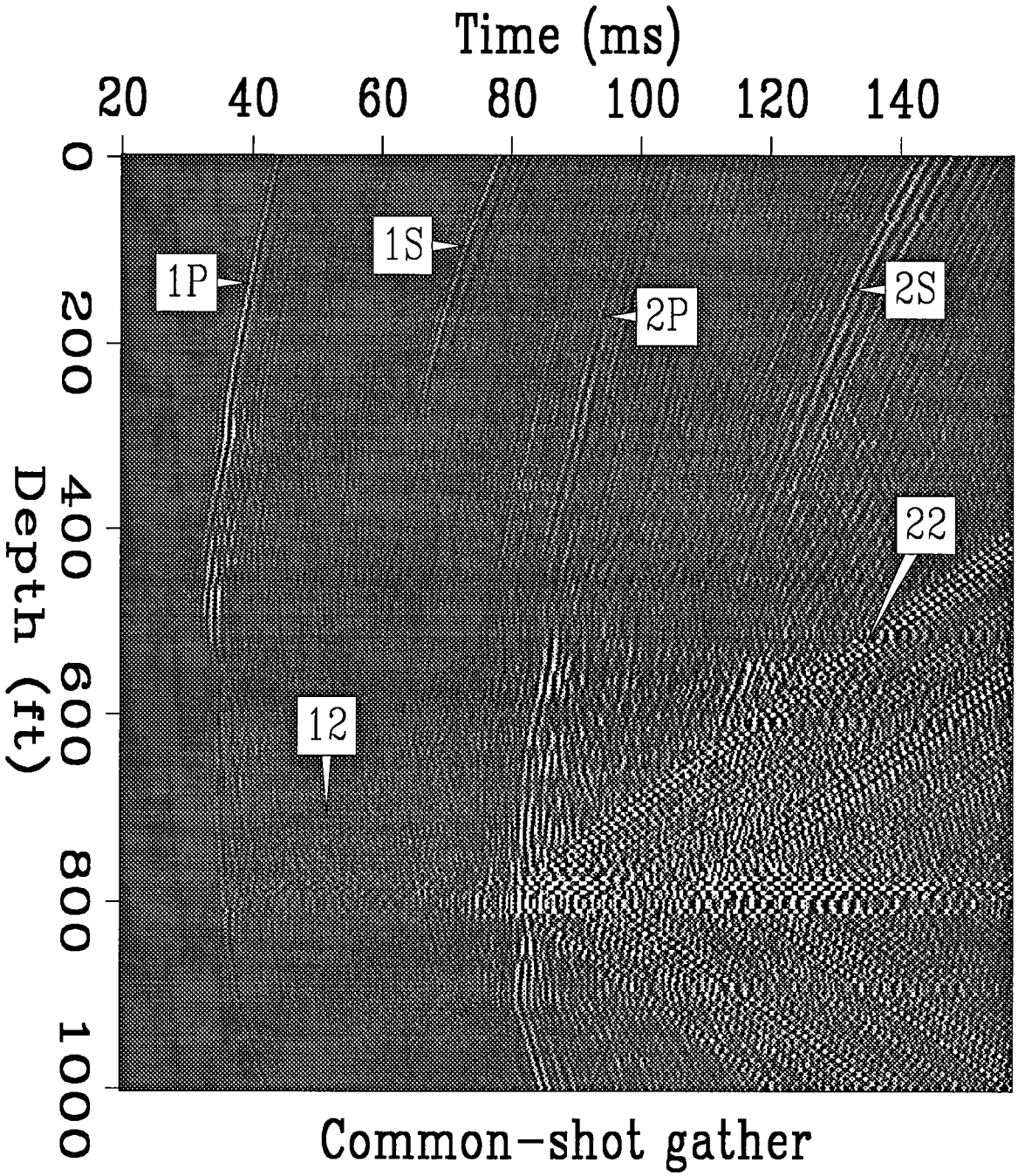

Figure 5 An unprocessedcommon-shot gather. Events 1, 2, 12, and 22 have the same descriptions as in Figure 1 and Figure 2. P (S) stands for P-wave (S-wave). Strong source well tube waves (events 2 and 22) are excited at the depth of 800 ft.

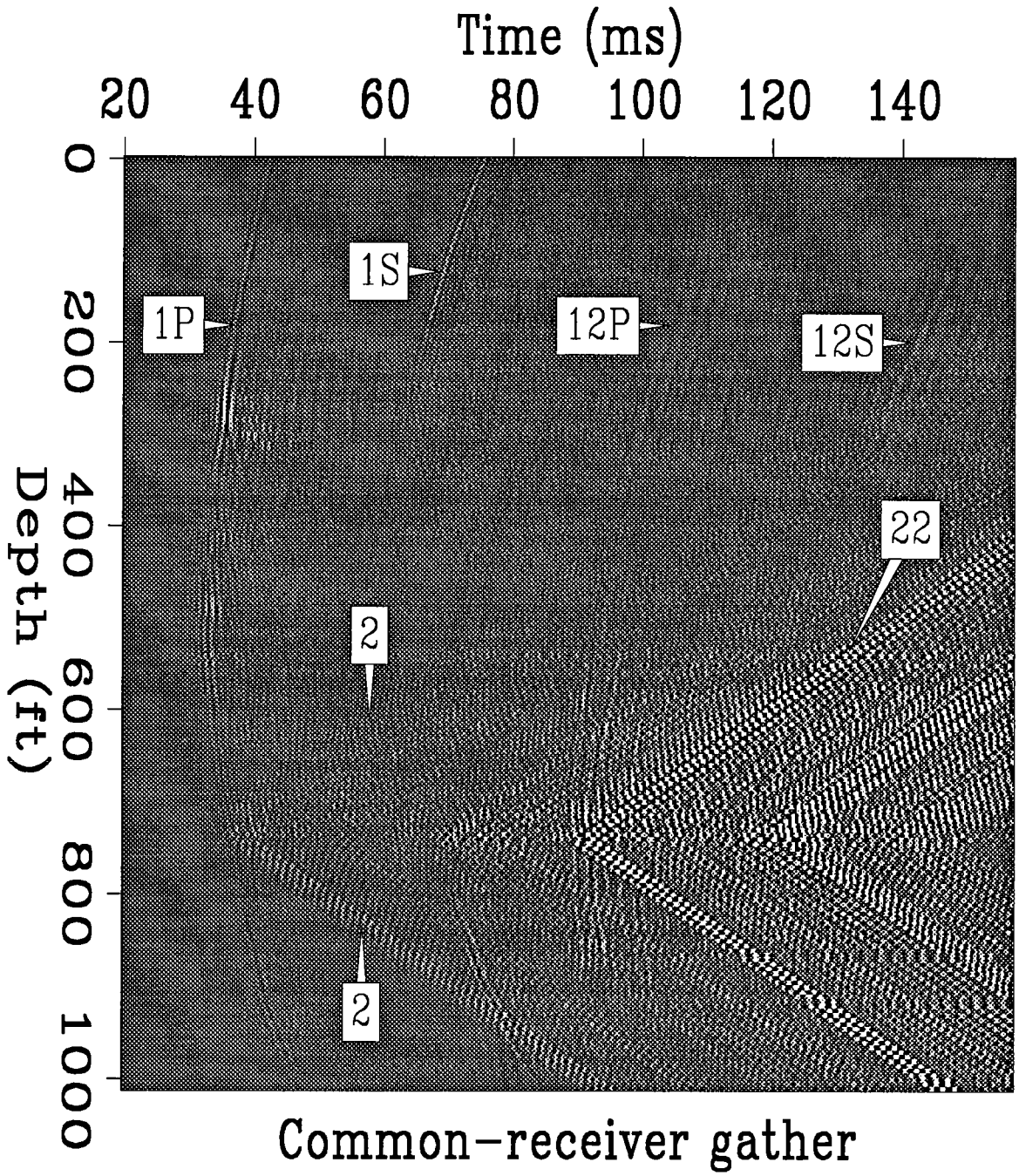

Figure 6 An unprocessedcommon-receiver gather. Events 1, 2, 12, and 22 have the same descriptionsas in Figure 3 and Figure 4. P (S) stands for P-wave (S-wave).Strong receiver well tube waves (events 12 and 22)are excited at the depth of 730 ft.

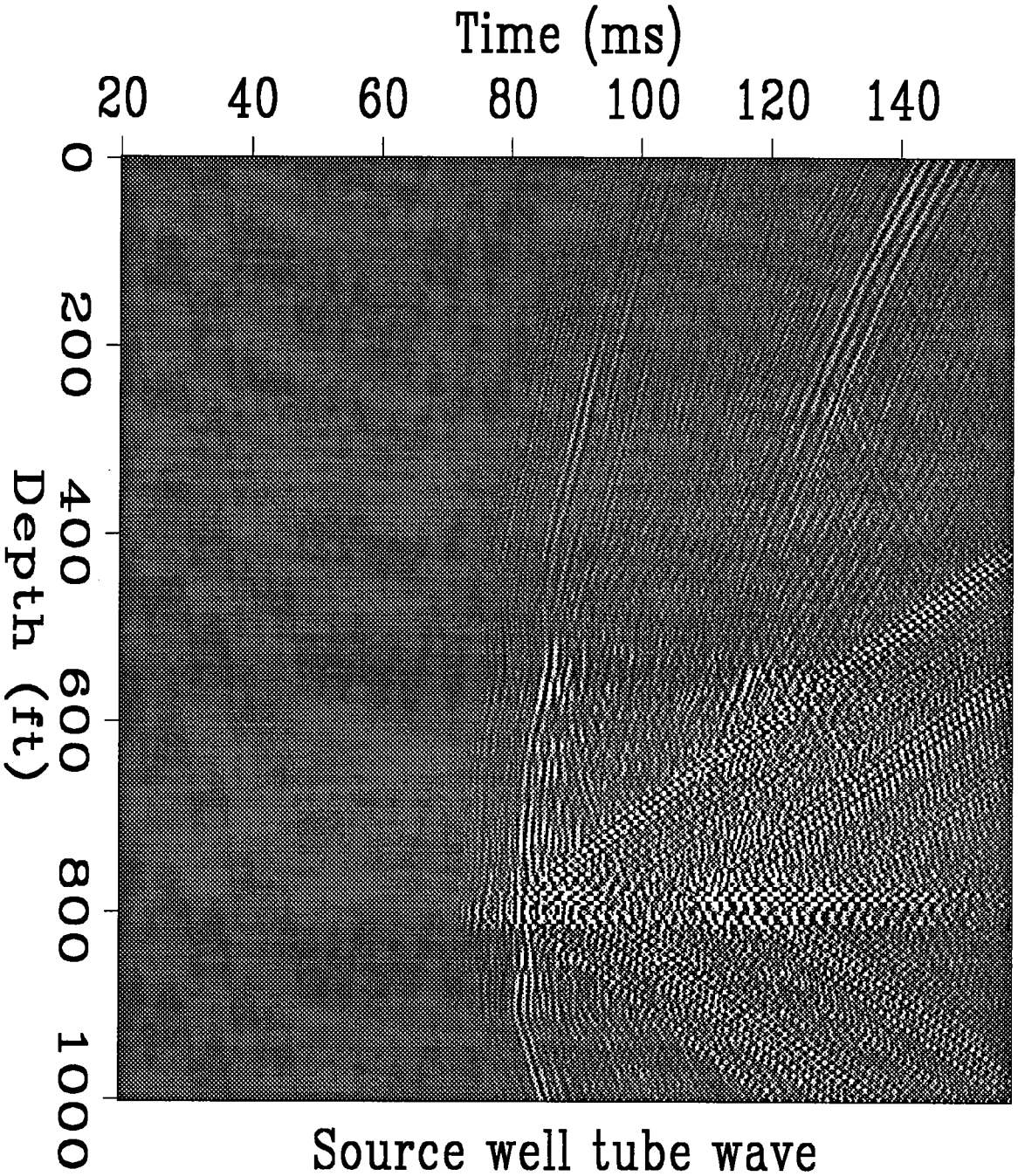

Figure 7 Estimated source well tube wave on the CSG data of Figure 5.

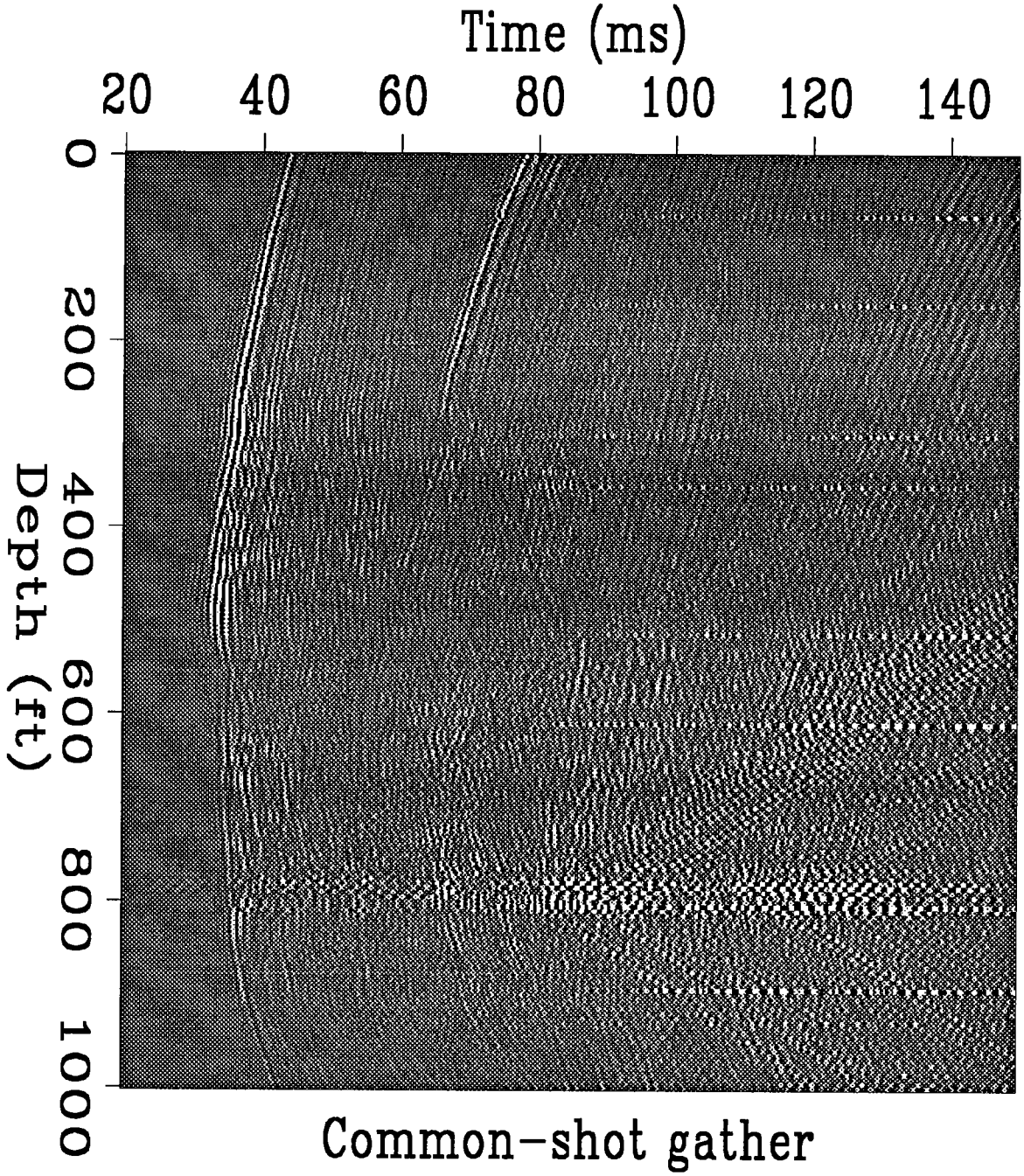

Figure 8 Common-shot gather of Figure 5. Source well tube waves have been attenuated.

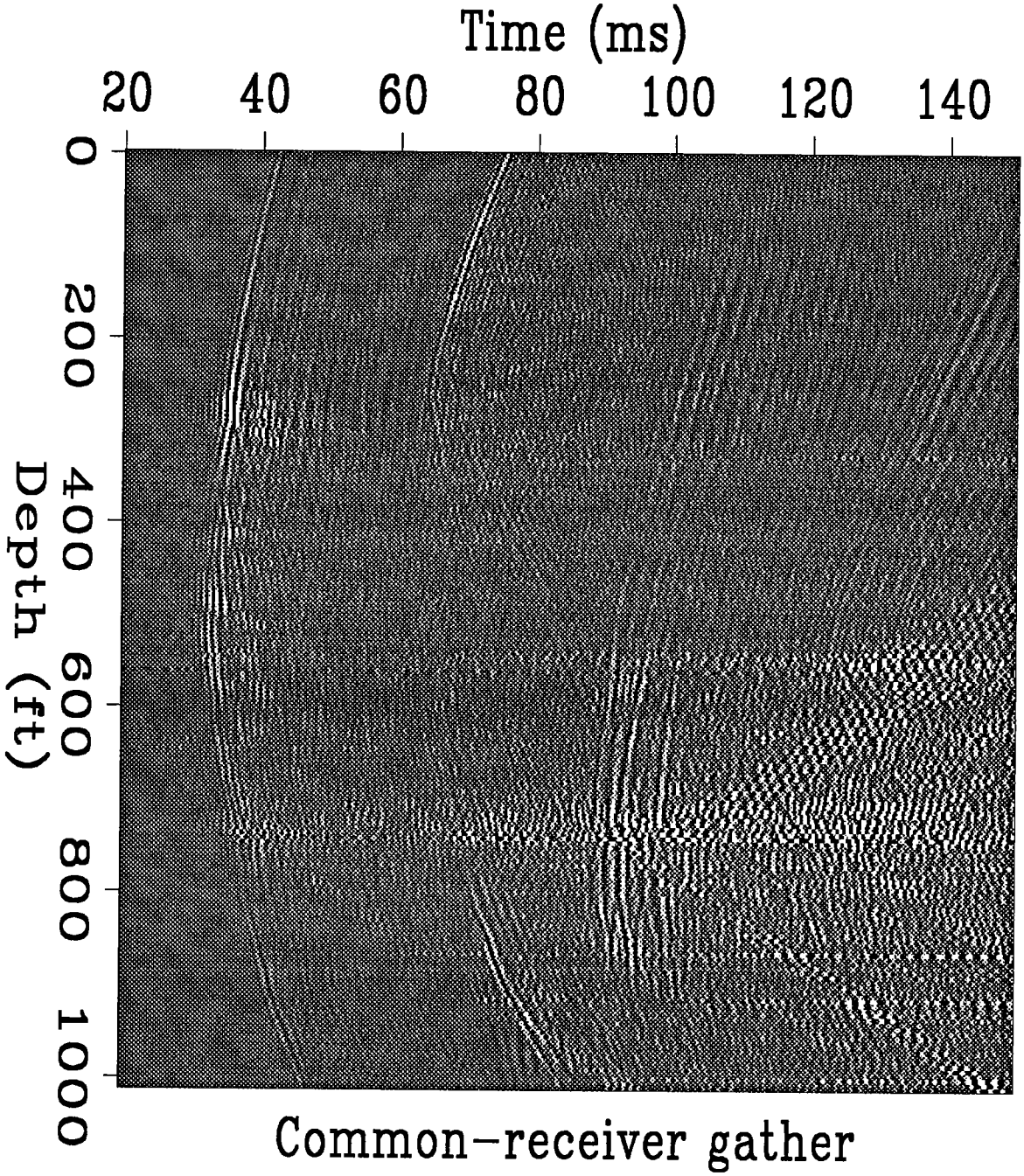

Figure 9 Common-receiver gather of Figure 6. Source well tube waves have been attenuated.

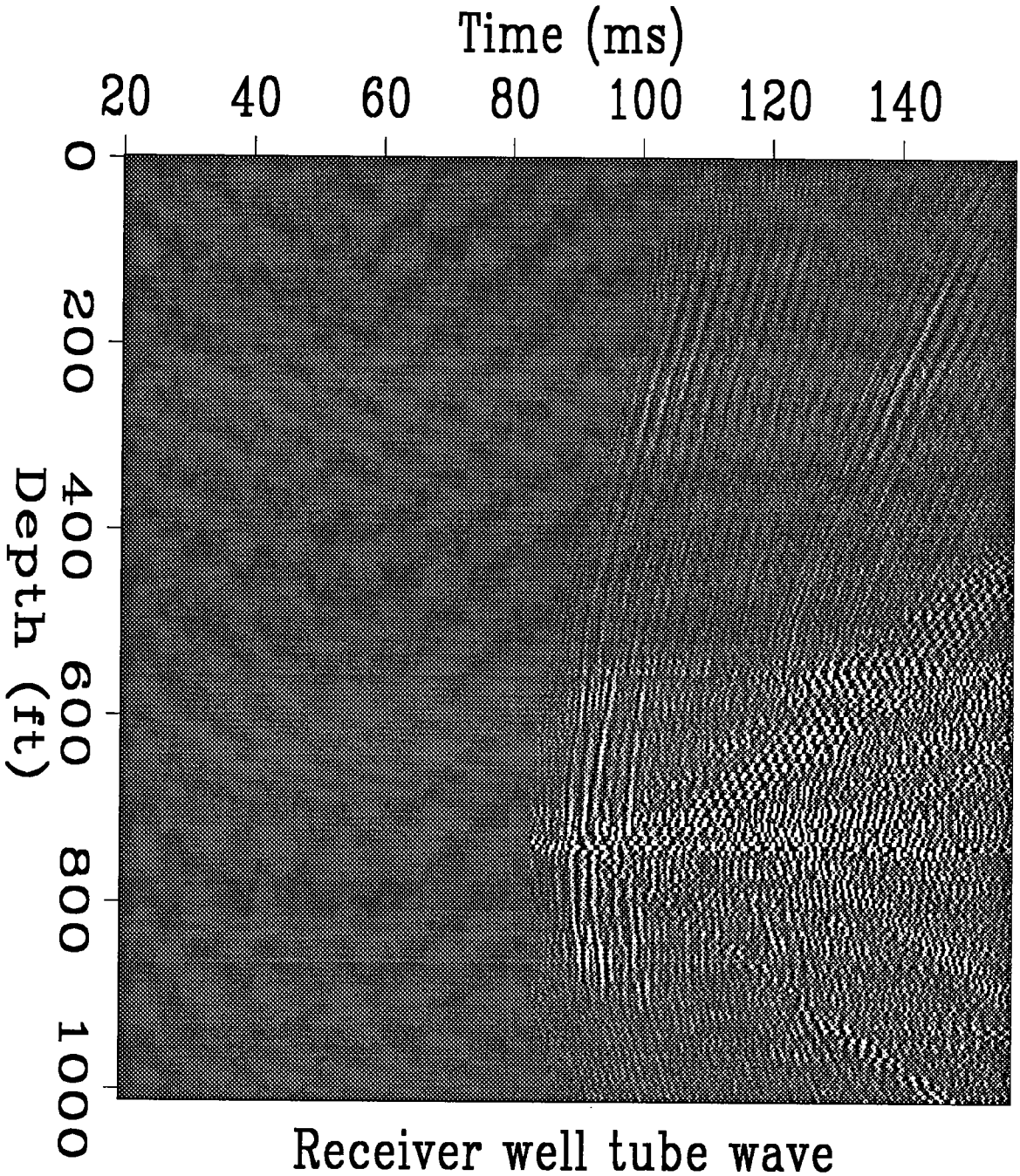

Figure 10 Estimated receiver well tube wave on the CRG data of Figure 9.

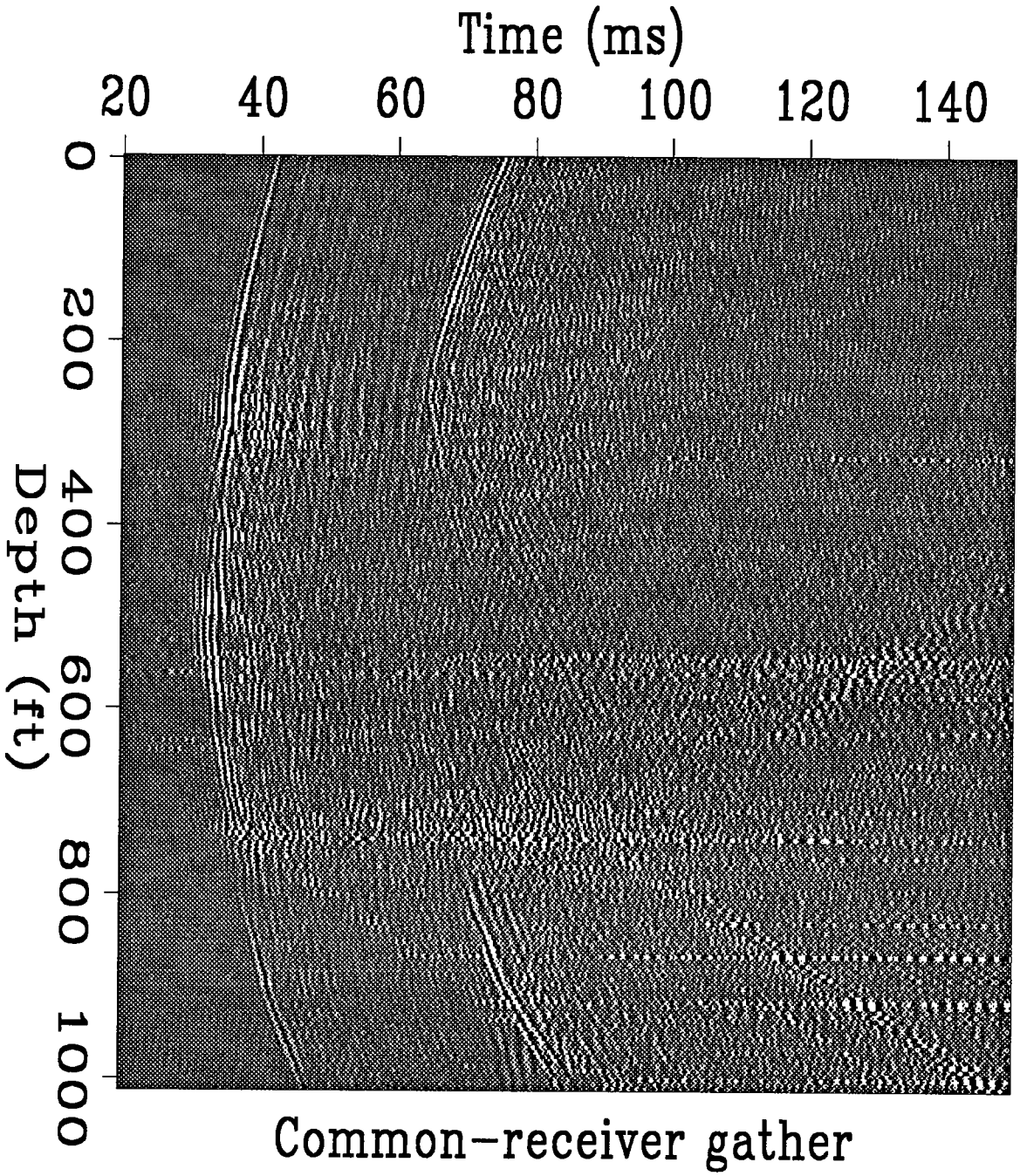

Figure 11 Common-receiver gather of Figure 9. Receiver well tube waves have been attenuated.

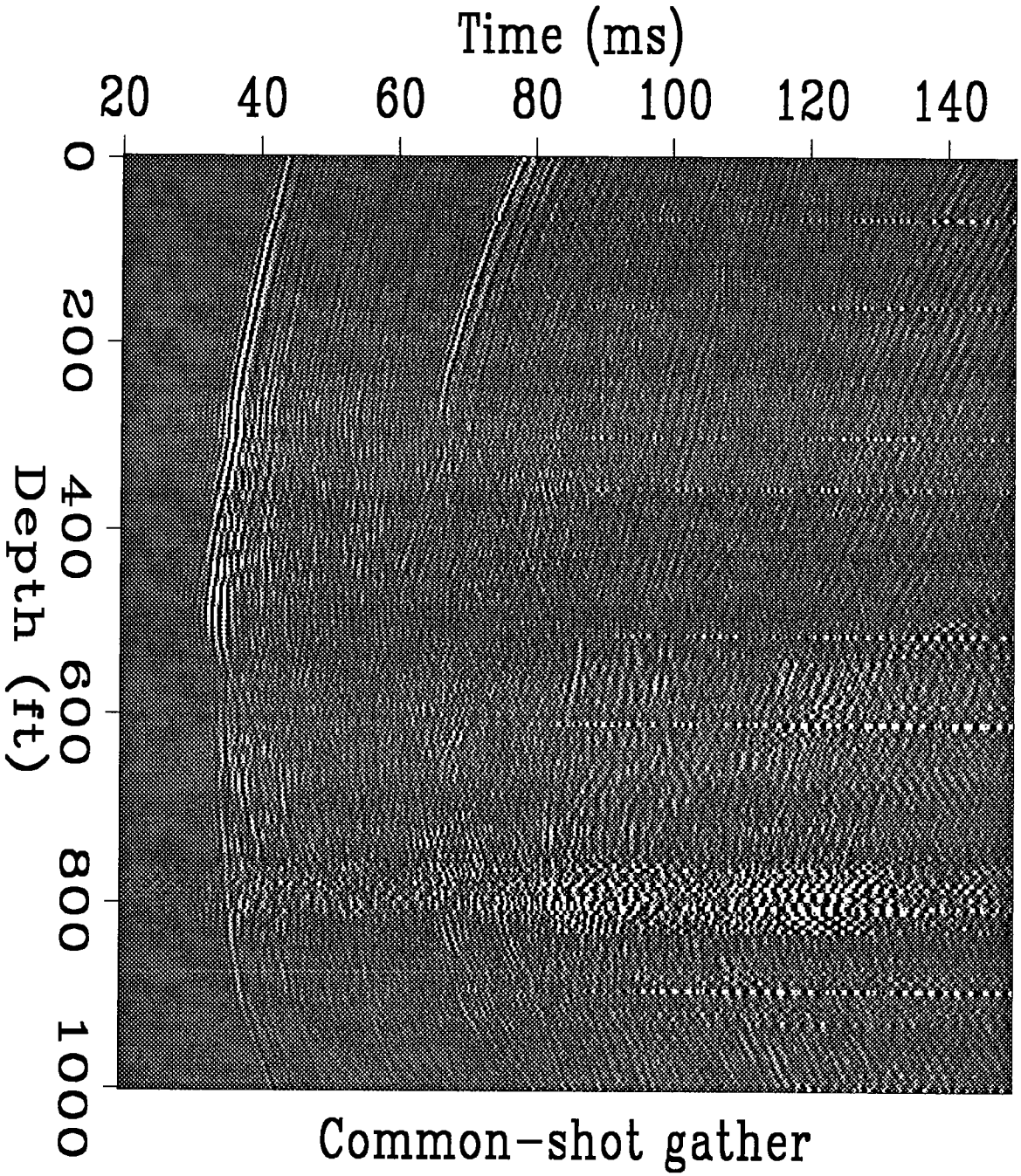

Figure 12 Common-shot gather of Figure 8. Receiver well tube waves have been attenuated.

PAPER H

RELATIONSHIPS BETWEEN MATERIAL PROPERTIES AND ANGLE-DEPENDENT REFLECTIVITY

Steven R. Bacharach

ABSTRACT

An elastic wave incident on an interface between two solid half-spaces produces reflected and transmitted waves with amplitudes dependent upon the solids' properties and the angle of incidence and amplitude of the incident wave. Reflectivity is defined as the ratio of the amplitude of a reflected wave to that of the incident wave. *P*-wave to *P*-wave reflectivities (*PP*) obtained from high incident angles are often used to estimate lower half-space compressional velocity by a process known as CDP trace stacking. For this process, it is assumed that using reflectivity values averaged from large incidence angles in the place of the reflectivity value at normal incidence will result in little error in the velocity estimation. Because several variables simultaneously determine reflectivity, analyzing the effect on reflectivity of changing a single one is difficult. However, assuming that the density and the ratio of *S*-wave velocity to *P*-wave velocity are the same in both media, I plot the change of two different ratios of velocity against each other to outline regions corresponding to material properties in which this CDP velocity inversion will be successful to within 5%. If the average reflectivity is approximately equal to the value for normal incidence or near to zero itself, then one can invert for velocity in the lower half-space with little error if densities and upper half-space *P*-wave velocity are known. Assuming constant density across the interface leads, in some cases, to a better velocity inversion; in others inversion is less accurate. So, the accuracy of accounting for density differences is ambiguous.

A compressional wave incident on a solid from a liquid yields, in general, a reflected *P*-wave, a transmitted *P*-wave, and a transmitted *S*-wave. While discrete *PP* values provide little information toward inferring solid properties, an examination of the relationship between the solid's shear velocity and that pre-critical incident angle that yields the maximum *PP* is useful and has possible applications in the field of non-destructive testing. The ratio of the solid density to the liquid density, appears to have little bearing on the relationship between the ratio of shear velocity in the solid and

An elastic wave striking the interface between a solid half-space and a vacuum is a much easier problem to model than the two previous cases. The vacuum has no density and cannot propagate any waves. Therefore, wave reflectivity at the boundary depends only on the ratio of elastic velocities within the solid and the angle which the incident wave makes with the interface. This simplification yields a functional relationship between the velocity ratio in the solid and the angle of incidence, if non-converted wave reflectivity equals zero. This relationship might be useful as a check on sonic log measurements or as a qualitative measurement of isotropy, homogeneity, or elasticity.

For the three previous cases, solid-solid, liquid/solid, and vacuum/solid, I make several assumptions. I calculate reflectivity from equations describing elastic wave propagation and boundary conditions at elastic interfaces and only examine pre-critical incident angles. Also, amplitudes, and therefore reflectivity coefficients, are measured in the direction of wave propagation. So, a geophone, situated above the reflector and measuring a single component of displacement, would have to be corrected according to which component of displacement, horizontal or vertical, it is measuring. Below the reflector, the geophone measurement, after the geometric correction, would be the negative of the value calculated from the equations I use. Another assumption is that all incident and scattered waves are in a plane perpendicular to the interface and are time-harmonic dependent. I also examine only homogeneous waves, such that the phase and energy velocities are equal in direction and magnitude. By relaxing the restrictions on the wave and interface types by looking at inhomogeneous waves interacting with viscoelastic interfaces, several differences from elastic theory appear. Seismic velocities and the quality factor, Q, depend on frequency; phase velocity travels in a different direction than energy velocity, dependent on incident angle

SOLID-SOLID INTERFACE

At the boundary between two solid half-spaces, a *P*-wave, in general, yields a reflected *P*-wave, a transmitted *P*-wave, a reflected *SV*-wave, and a transmitted *SV*-wave [Aki and Richards 1980] (Figure 1). This simple two-layer model is analogous to surface seismic and crosswell survey geometries. Waves are generated at the surface with receivers placed at different offsets (angles) in the former case; in the latter situation, shots and receivers are both downhole, and incidence angle changes according to their vertical locations within the well and the depth of the reflector. These waves'

shots and receivers are both downhole, and incidence angle changes according to their vertical locations within the well and the depth of the reflector. These waves' propagation directions are described by Snell's Law and amplitudes by the Zoeppritz equations. The reflectivity of this interface is the amplitude of a reflected wave divided by that of the incident wave. The reflectivity varies according to the angle of incidence of the wave and the densities and elastic wave velocities of the half-spaces (See Appendix A). The reflectivity from an incident *P*-wave reflecting a *P*-wave is known as *PP*.

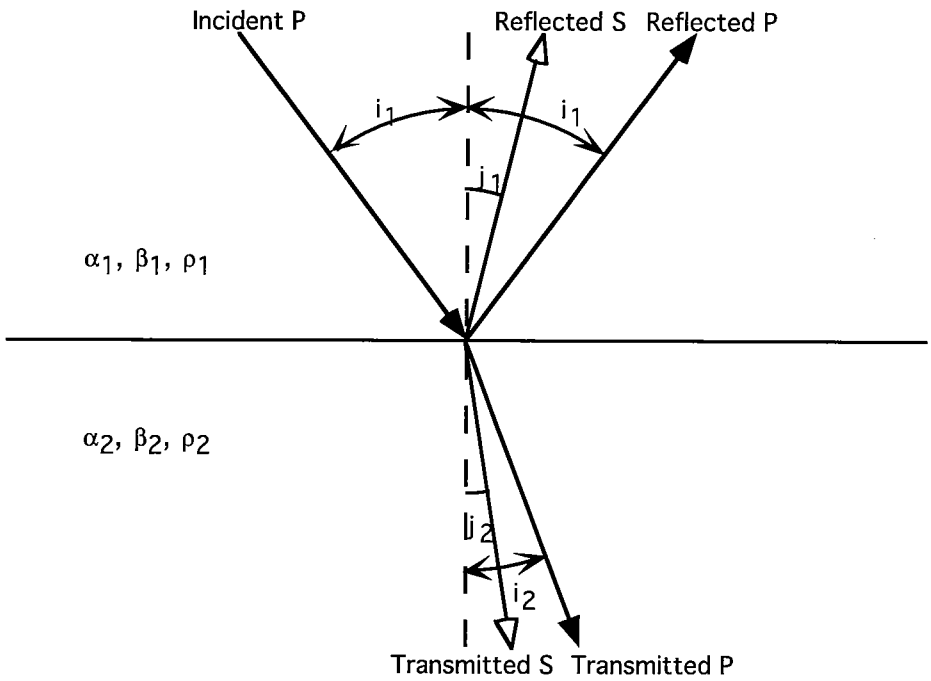

Figure 1: Reflection, transmission, and conversion of a *P*-wave incident on a solid-solid interface. α, β, and ρ are compressional velocity, shear velocity and density, respectively ($\alpha_1 > \alpha_2$) [Tooley *et al.* 1965].

Velocity Inversion from PP Reflectivity and CDP Stacking

Much of the velocity inversion performed today is based on common depth point (CDP) stacking. Shots and receivers are placed at successive intervals along the surface to record the traces of several waves' bouncing off a single reflector point (Figure 2).

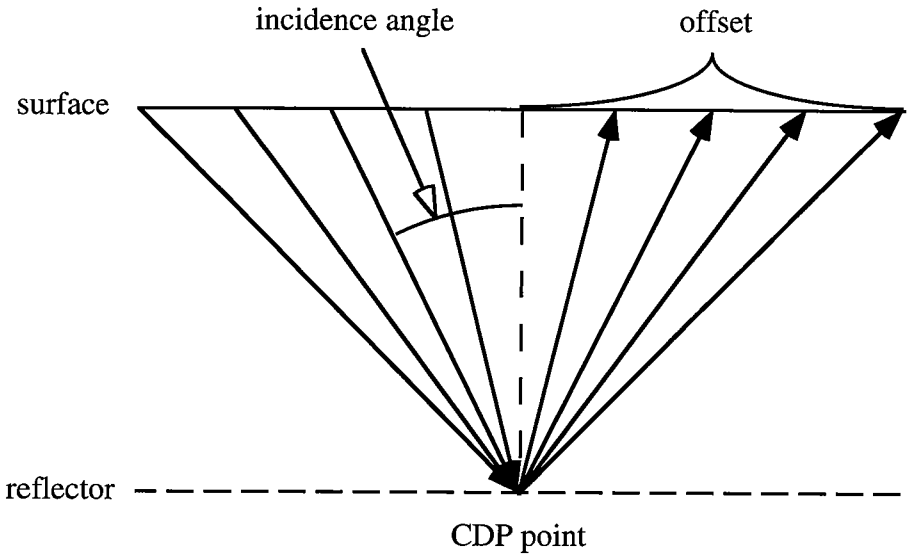

Figure 2: A surface seismic CDP survey - rays emanate from shots on the surface on the left and are reflected to receivers at the surface on the right.

Using an NMO correction, individual traces are moved up to equalize the different pathlengths the waves took to generate them (Figure 3). Traces are then collapsed horizontally to a point on the surface directly above the CDP in a process known as trace stacking.

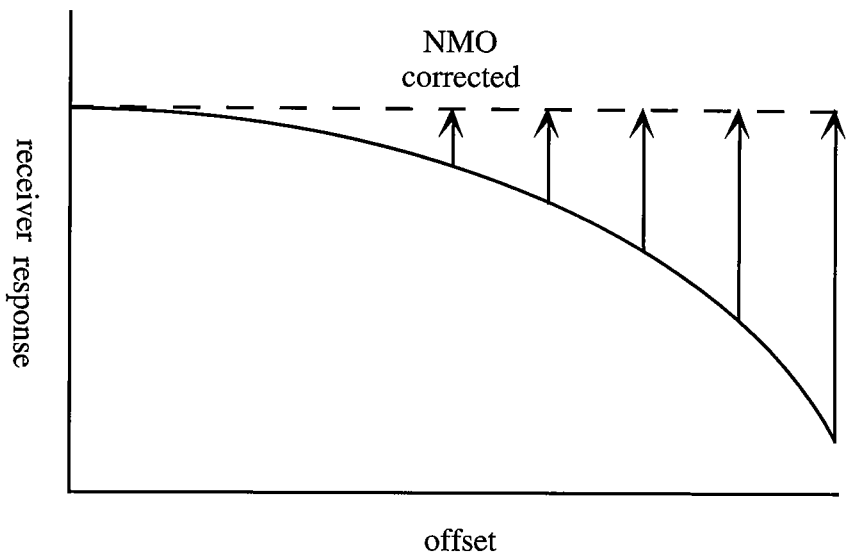

Figure 3: A normal moveout correction adjusts the traces from far offsets according to the distance the ray traveled that created that trace. In this way, traces from nonnormal angles of incidence are used to image a reflector point.

Reflectivity values from nonnormal incident angles are averaged in the stacking process and used as an approximation for *PP* at zero incidence. To study the validity of this approximation, I try to develop relationships between average reflectivity and material properties. Later, I will show that *PP* reflectivities averaged in this way from high angles of incidence will not invert correctly for lower layer compressional velocity, except under certain conditions. Therefore, some of the simple velocity inversion work practiced today, which does not treat reflectivity at nonnormal incidence in a rigorous fashion, is imprecise.

Effect on Reflectivity of Varying a Single Variable

In figures to follow I use velocity and density ratios from a synthetic shale/sandstone contact [Turcotte and Schubert 1982] and from McElroy well logs (West Texas carbonate) at approximately 2845 ft. depth. These ratios are derived from the following velocities and densities:

Synthetic (control): shale - density = 2.60 g/cm3 $\alpha = 4.08$ km/s $\beta = 2.45$ km/s
sand - density = 2.42 g/cm3 $\alpha = 4.12$ km/s $\beta = 2.54$ km/s

McElroy well logs: upper - density = 2.85 g/cm^3 $\alpha = 6.20$ km/s $\beta = 3.55$ km/s
lower - density = 2.71 g/cm^3 $\alpha = 5.84$ km/s $\beta = 3.27$ km/s

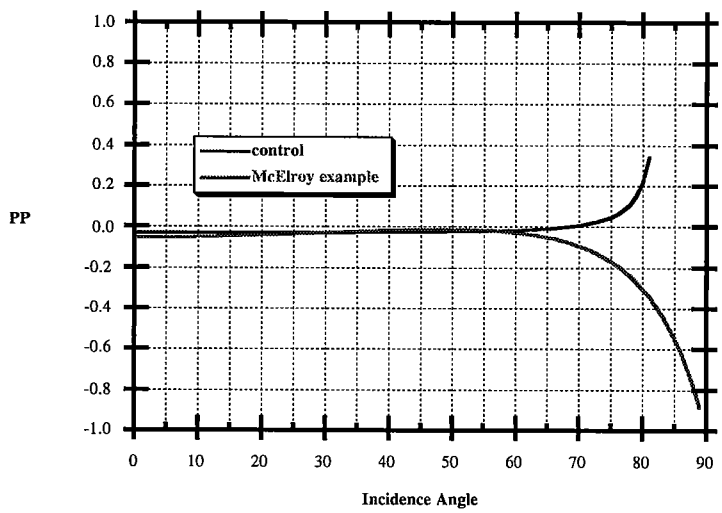

Figure 4: *PP* reflectivity versus angle from the shale overlying sandstone contact and from an interface within the McElroy field. The control curve does not reach 90 degrees, because a critical angle exists at about 81 degrees for this case.

In field seismic surveys, reflectivity is often measured as an average over a range of angles. For surface seismic geometries this range is approximately 0 to 50 degrees, while for crosswell it is approximately 20 to 70 degrees. If the average *PP* does not change appreciably over a wide range of angles, then one can use the value at higher incidence as an estimate for *PP* at normal incidence. Now, at normal incidence the equation for *PP* is much less complicated than the general Zoeppritz equation, because there are no converted waves [Levin 1986]. Assuming constant density, this simplification leads to an inversion scheme for velocity in the lower half-space, given the velocity in the upper half-space and the reflectivity at the interface.

Average Reflectivity

Because reflectivity equations are ratios of a scattered ray property to an incident ray property, they are unitless. Therefore, absolute values for material densities or velocities are meaningless, while using ratios of these values as inputs to the equations is simpler and easier to interpret. I name these input ratios as follows:

$$a=\frac{\alpha_2}{\alpha_1}, \qquad b=\frac{\beta_1}{\alpha_1}, \qquad c=\frac{\beta_2}{\alpha_1}, \qquad r=\frac{\rho_2}{\rho_1}. \tag{1}$$

Using the properties from the synthetic shale/sandstone contact, I vary the separate velocity and density ratios to examine the individual effect each one has on the *PP* reflectivity averaged over a 50 degree window (Figures 5-8). I also examine the average reflectivity data calculated from the McElroy field logs (Figure 9).

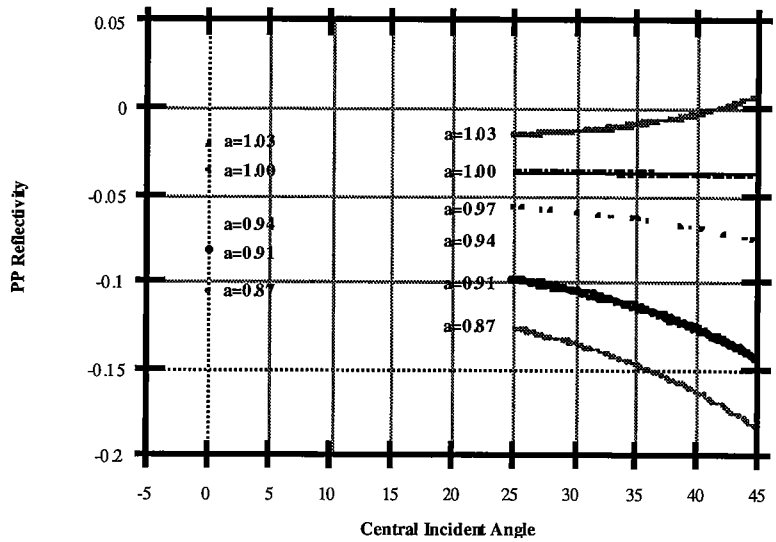

Figure 5: *PP* averaged over a 50 degree window, varying only the *a* ratio. Normal incidence values are dependent on *a* and so are shown to the left of the majority of data points. (shale/sandstone contact: $b = .600$; $c = .623$; $r = .931$)

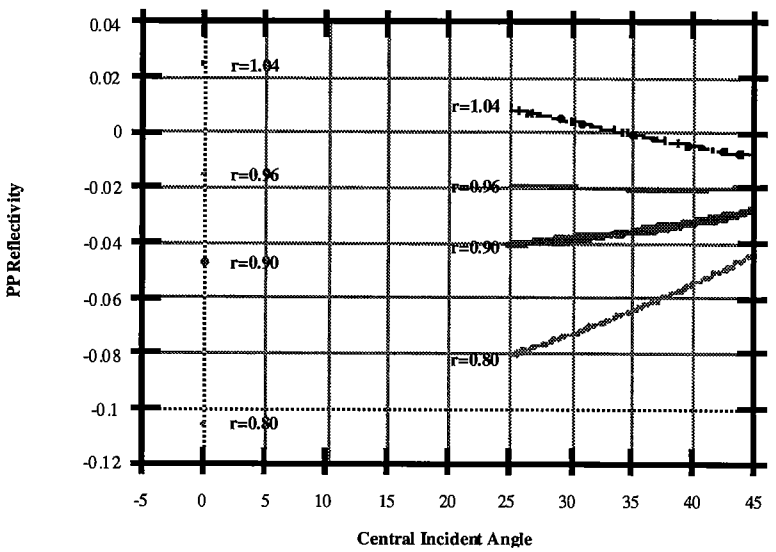

Figure 6: *PP* averaged over a 50 degree window, varying only the *r* ratio. Normal incidence values are dependent on *r* and are shown to the left of the majority of data points. (shale/sandstone contact: $a = 1.010$; $b = .600$; $c = .623$)

In Figure 5, as the range of angles over which *PP* is averaged increases, that average diverges for the different values of *a*, α_2. At the surface seismic end, central incident angle of 25 degrees, only four values of *a*, 0.94, 0.97, 1.00, and 1.03, are close enough to

their respective normal incidence values to be considered candidates for velocity inversion. At the crosswell end, central incident angle of 45 degrees, only the values 1.00 and 1.03 are near enough.

The opposite effect is seen in Figure 6 as central incident angle increases. Now, the average *PP* converges for different density ratios. This effect makes sense since velocity and density have reciprocal effects in the reflectivity equations.

Both Figures 5 and 6 show that normal incidence reflectivity can change sign even if the compressional velocity ratio, *a*, and the density ratio, *r* , do not cross unity. This makes sense because the important quantity determining reflectivity is not either of these values alone, but the impedance, the product of velocity and density. Normal incidence reflectivity in terms of impedance is:

$$PP = \frac{Z_2 - Z_1}{Z_2 + Z_1} . \qquad (2)$$

If the impedances are replaced by the corresponding velocity and density ratios, then

$$PP = \frac{\mathbf{ar} - 1}{\mathbf{ar} + 1} . \qquad (3)$$

Figures 7 and 8 illustrate changes in average *PP* due to changing the *b* and *c* ratios, the shear velocity values. In these cases, both graphs diverge toward higher angles, so velocity inversion for crosswell geometries would be less likely than for surface seismic ones. However, as *b*, or β_1, increases, reflectivity goes up, whereas a similar increase in β_2 causes reflectivity to drop.

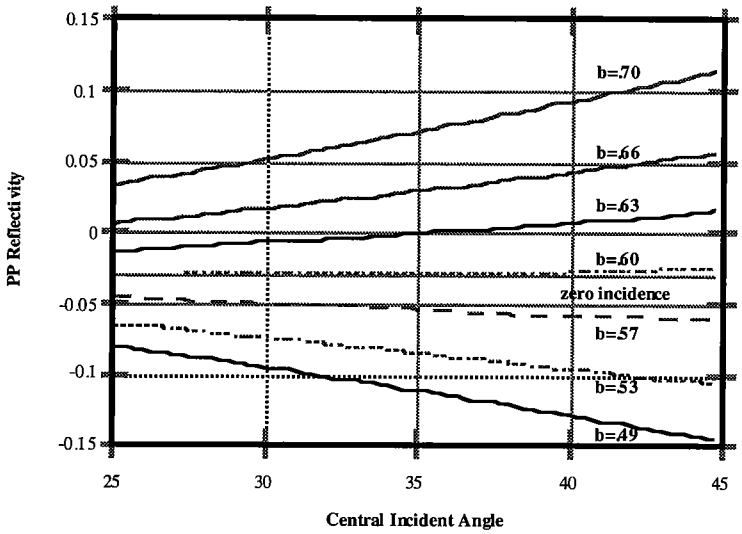

Figure 7: *PP* averaged over a 50 degree window, varying only the *b* ratio. Normal incidence is flat because it is independent of *b*. (shale/sandstone contact: a = 1.010; c = .623; r = .931)

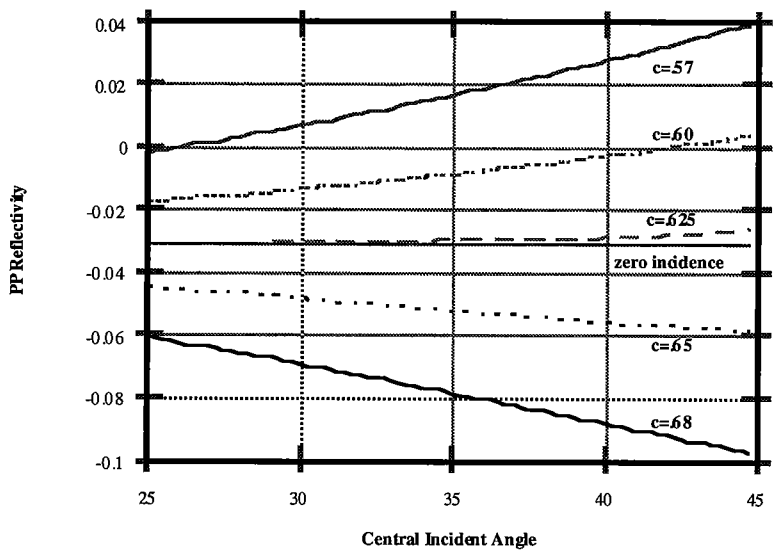

Figure 8: *PP* averaged over a 50 degree window, varying only the *c* ratio. Normal incidence is flat because it is independent of *c* . (shale/sandstone contact: a = 1.010; b = .600; r = .931)

Figure 9 indicates that differences between the McElroy angular average and the McElroy normal incidence seem much too great (> 50%) for velocity inversion to be feasible according to this single ratio analysis. However, as will be shown later, McElroy log numbers do invert very accurately for lower compressional velocity. Accounting for

density and *P*-wave velocity differences simultaneously leads to better velocity estimates. Also, because the absolute values of normal incidence and averaged *PP* are both near zero, reflectivity is "damped" in the formula for α_2.

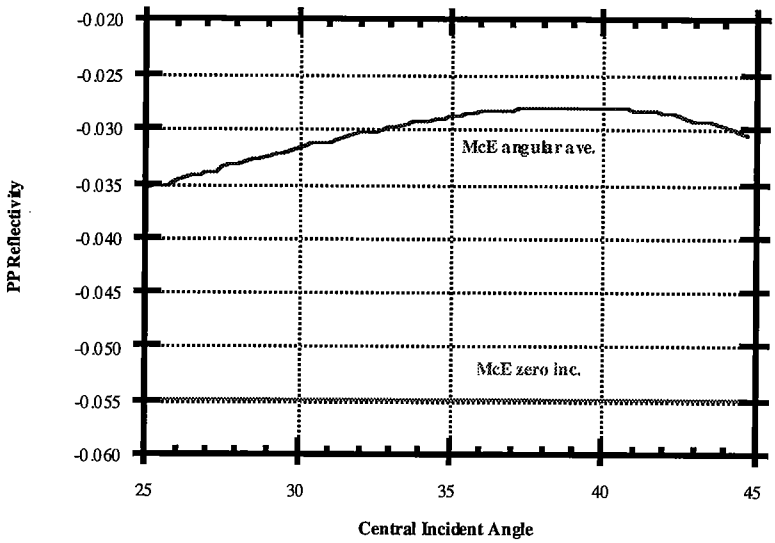

Figure 9: *PP* averaged over a 50 degree window using ratios from a McElroy log. McE zero inc. is the McElroy reflectivity at normal incidence.

The individual velocity and density ratios are too coupled within the Zoeppritz equations, making the interpretation of changing a single ratio meaningless. In fact, the equation for the calculation of PP involves so many factors that the only meaningful assumption resulting in a significant simplification is normal incidence. Other assumptions, such as constant density and Poisson solids, $\alpha/\beta = (3)^{1/2}$, are not sufficient to obtain a simple relationship for velocity ratios as a function of incidence angle.

Using smaller angular windows does not help to constrain the variability of average *PP* with respect to angle. In fact, smaller windows yield average *PP* values that vary more, because they are smoothed from fewer angles. Larger windows could make average *PP* curves slightly flatter, but windows much larger than 50 degrees in the field are rare, and would not flatten average *PP* curves significantly anyway.

I also examine *PP* averages using my control numbers and the McElroy numbers over different angular ranges from zero degrees (Figure 10). Unfortunately, the following figure does not indicate that either case exhibits behavior in a regular pattern that could lead to an inversion scheme.

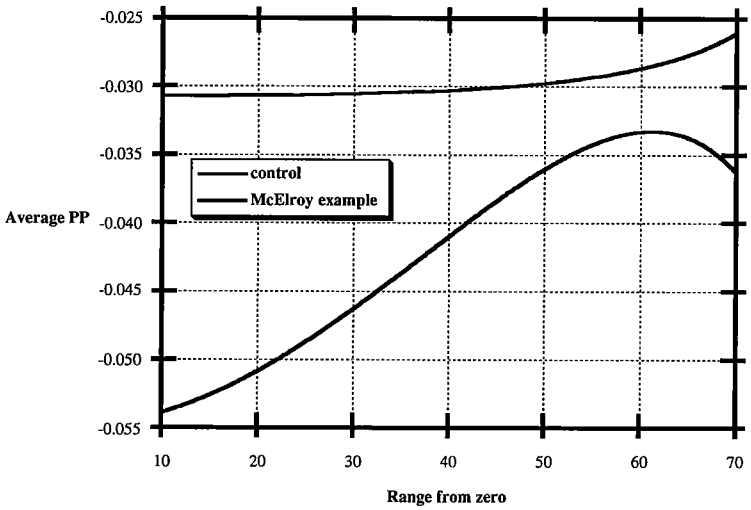

Figure 10: *PP* reflectivity averaged over increasing angular ranges beginning at normal incidence and ending at the angle indicated on the horizontal axis.

A single variable study of the effect on reflectivity, averaged over a moving 50 degree window or a lengthening window starting at normal incidence, is not very enlightening. A two or three ratio model is more appropriate to delineate the range of velocity ratios such that the average angular *PP* remains within a certain tolerance level compared to normal incidence reflectivity *PP* (Figure 11).

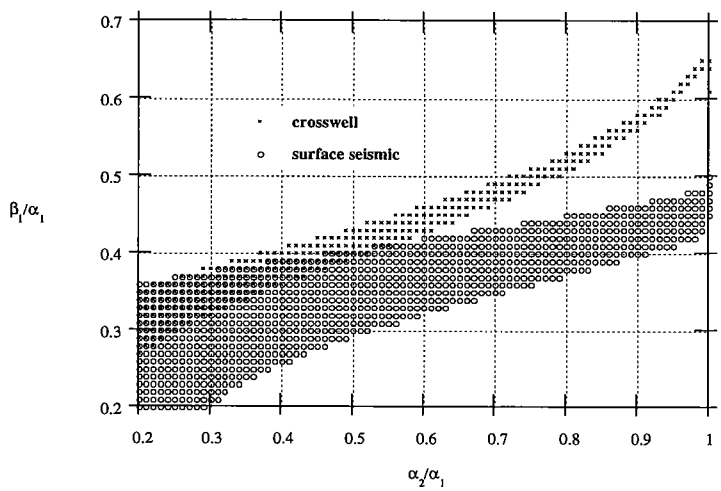

Figure 11: Shaded areas show values of β_1/α_1 and α_2/α_1 such that the average angular *PP* and normal incidence *PP* differ by less than 5% (crosswell is averaged from 20 to 70 degrees; surface seismic is averaged from 0 to 50 degrees).

Velocity Inversion

Inputting the *PP* value averaged from higher angles into the formula for reflectivity perpendicular to the boundary, I can solve for compressional velocity in the lower medium analytically:

$$PP(i=0°)=\frac{\rho_2\alpha_2-\rho_1\alpha_1}{\rho_2\alpha_2+\rho_1\alpha_1}, \tag{4}$$

where i is angle of incidence, can be solved for α_2 if we assume that $\rho_1=\rho_2$. This assumption yields:

$$\alpha_2=-\alpha_1\left(\frac{PP+1}{PP-1}\right). \tag{5}$$

I use two different methods to make envelopes of error in the estimation of α_2. First, I directly compare α_2 using the average angular *PP* in Eqn. (5) to the original value. The second method is a mathematical construction in which I introduce a small error into the estimate of *PP* and deduce the size of the resulting error in α_2 (Appendix B). The following two error envelopes are designed using two constraints. I assume, as in Eqn. (5), that r = 1. Also, to simplify the problem to two variables from three, I assume that $(\beta_1/\alpha_1) = (\beta_2/\alpha_2)$, or $c = a \times b$.

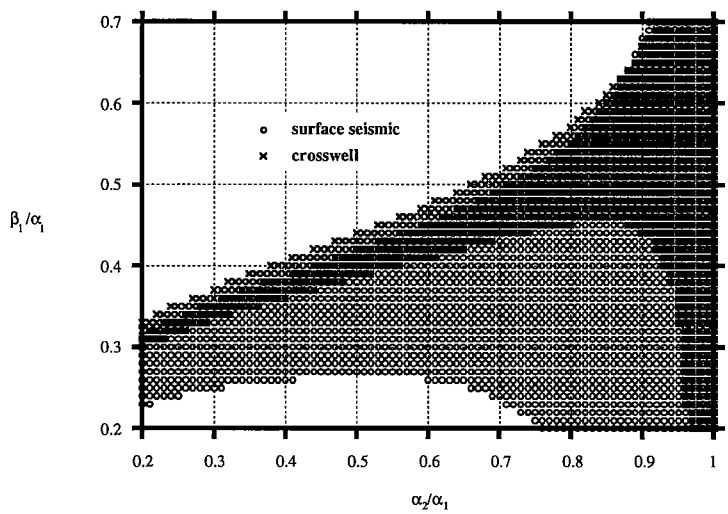

Figure 12: Shaded areas denote values of β_1/α_1 and α_2/α_1 such that α_2 estimated from average angular *PP* and actual α_2 differ by less than 5%.

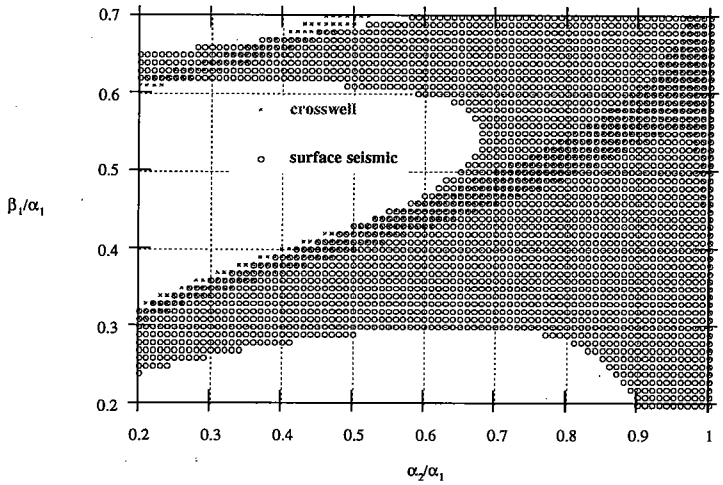

Figure 13: Shaded areas denote values of β_1/α_1 and α_2/α_1 such that error of average angular *PP* from normal incidence *PP* yields a less than 5% error in α_2 from the actual value (Appendix B).

Figures 12 and 13 are shaded mostly on the right. This region corresponds to near equal *P*-wave velocities. With α_1 near α_2, acoustic impedance is small for all incident angles and so reflectivity is as well. Therefore, even if the averaged *PP* differs from the normal incidence *PP* by a large percentage, velocity inversion will still be accurate since *PP* is added to and subtracted from unity in Eqn. (5). This observation makes sense because if compressional velocities are nearly equal, then mathematical interpolation that relates one *P*-wave velocity to the other should be more stable than if the velocities were very different.

The crosswell region on the figures is smaller than the surface seismic region, because the latter is averaged from angles closer to normal incidence, therefore the corresponding reflectivities and estimated velocities are more accurate.

Other Reflectivity Types

I focus on *PP* average reflectivities not only because of their wider use in the field, but also because other average reflectivities and reflectivity zeroes do not provide a useful inversion. Although the equation for *SH*-wave reflectivity,

$$SH = \frac{\rho_2\beta_2 \cos j_2 - \rho_1\beta_1 \cos j_1}{\rho_2\beta_2 \cos j_2 + \rho_1\beta_1 \cos j_1} \qquad (6)$$

is much like Eqn. (4), one can not invert for lower half-space shear velocity using reflectivities from higher angles in the equation for normal incidence. The residuals between the normal incidence *SH* and the angular averages of *SH* are too high to provide a plausible inversion, and *SH* is only near zero at normal incidence, which is trivial.

Attempts at linking *PP* and *SV*-wave reflectivity zeroes with rock properties were also fruitless. The number of velocity and density ratios involved in their calculation is too great to define discrete, meaningful relationships between their values and the behavior of zeroes.

Simple zero incidence reflectivity/velocity èquations, like Eqn. (4), do not exist for converted waves and *SV*- to *SV*-wave reflections. Converted wave reflectivities, *PS* and *SP*, can not be used for inversion in the above manner, because they are always zero perpendicular to the interface. Little can be learned from the behavior of *PS* and *SP* zeroes, because they depend upon too many variables simultaneously.

DISCUSSION

Because of the interdependency of the input ratios in the Zoeppritz equations, studying the effect on reflectivity of changing a single ratio is a wasted effort. However, a multi-variable examination provides some insight toward devising an inversion scheme from average reflectivity. I can use the two variable velocity inversion method as a self-consistency check, by solving for α_2 and β_2 from *PP*, α_1, and β_1, and by comparing with other velocity estimation techniques such as sonic logs or traveltimes.

If I know upper half-space velocities, I can read off a corresponding range of a values from the error envelope and estimate a range for $\alpha_2 = a \times \alpha_1$. I can then solve for α_2 directly from the *PP* velocity inversion formula and compare the two methods to see if the method works for that particular layering scheme.

A possible application of this method is as an estimate of degree of inhomogeneity, anisotropy, and viscoelasticity. If I have upper half-space velocities that fall within a small error envelope, I can then make confident estimates of lower half-space velocities, under the same assumptions from which the original Zoeppritz equations were derived. The difference between my estimates of α_2 and β_2 and those calculated from a sonic log, traveltime, or some other means might be able to give me an idea of how much these assumptions of isotropy, homogeneity, and elasticity are violated in the media.

Figure 12, which shows the velocity ratio regions that yield an inversion within 5% of the true velocity, demonstrates the importance of shear wave velocity information for making an inversion at a common depth point. Estimates of α_2 will be often be incorrect if large offset reflectivity (averaged or discrete angles) is substituted for normal incidence reflectivity.

Check of Velocity Inversion Error

I use the synthetic layering numbers and McElroy log numbers to check the error in velocity estimation associated with them. For the synthetic case the estimated *PP* averaged from typical crosswell incidence angles results in an α_2 value that is about 5 percent too low, while for the McElroy simulation, the estimated velocity is within 1% of the original value. These two layering models do not demonstrate serious problems associated with the use of large offset *PP*, possibly because α_1 and α_2 are about the same. From Figure 10, one can see that for α_2/α_1 ratios near unity, velocity error is minimal.

The assumption I make to arrive at Eqn. (5), namely $\rho_1=\rho_2$, is not normally appropriate. If density is not constant, then Eqn. (5) becomes

$$\alpha_2 = -\alpha_1\left(\frac{\rho_1}{\rho_2}\right)\left(\frac{PP+1}{PP-1}\right). \qquad (7)$$

The density ratio sometimes acts as a correctional factor, as in the synthetic case. Using the density factor, estimated α_2 is only 1% above its true value. Using density,

though, can lead to problems in other situations. Another two layer model, approximating a carbonate over a sand, with properties,

upper layer (1) - density = 2.80 g/cm3 $\alpha = 6.20$ km/s $\beta = 3.50$ km/s
lower layer (2) - density = 2.20 g/cm3 $\alpha = 4.10$ km/s $\beta = 2.50$ km/s

actually works better if densities are assumed to be equal. Using Eqn. (5) to solve for α_2 from *PP* averaged from typical crosswell angles yields a value of 4.09 km/s, an excellent result. Conversely, if Eqn. (7) is used, the value is 5.21 km/s. Therefore, contrary to intuition, accounting for the density differential across the interface is not always more accurate.

There are three cases to consider when trying to calculate lower compressional velocity in a system of two flat, elastic layers. If α_1 is approximately equal to α_2, then, as I have shown, inversion using *PP* reflectivity averages is reliable, because reflectivities are small. If α_1 is less than α_2, then α_2 can be solved using the travel times from head waves through the lower medium. Finally, if α_1 is appreciably greater than α_2, head waves do not exist so reflectivity analysis would be an option. However, if the average reflectivity is not near zero or the normal reflectivity value, then caution must be used to avoid errors when analytically solving for α_2.

LIQUID-SOLID INTERFACE

A *P*-wave incident on a liquid-solid boundary from the liquid will, except at normal or grazing incidence, yield a reflected *P*-wave, a transmitted *P*-wave, and a transmitted *S*-wave [Bourbie 1982] (Figure 14). This seismic wave geometry corresponds to marine surveys in which shots emanate from the water and reflect off the sea floor, or to the non-destructive testing of a material immersed in a liquid using scanning beams. The reflectivity varies according to the angle of incidence of the wave, the elastic wave velocities of the materials, and their relative densities (Appendix C).

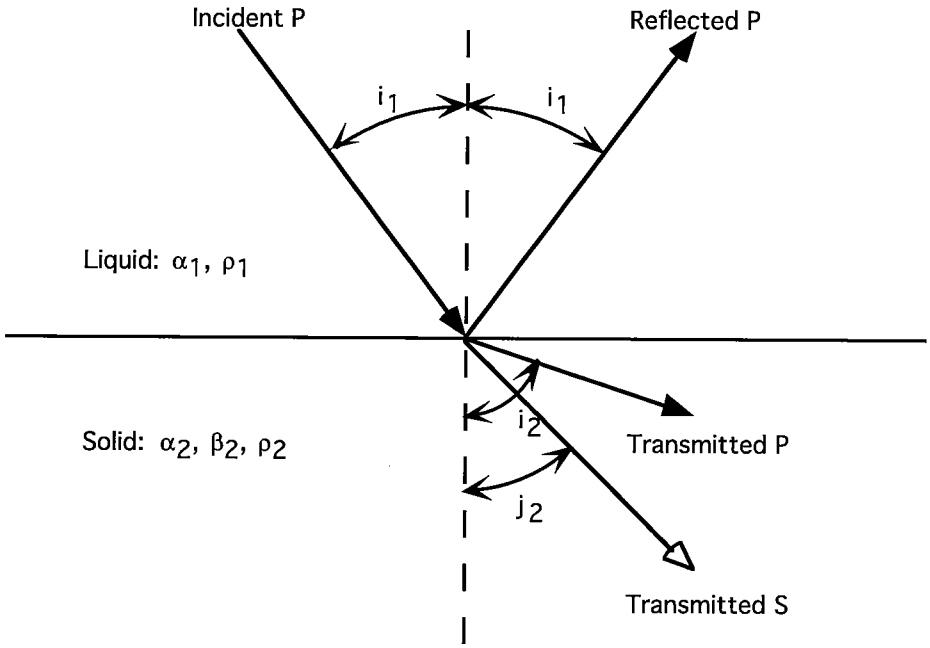

Figure 14: Reflection, transmission, and conversion of a *P*-wave incident on a liquid-solid interface ($\alpha_2 > \beta_2 > \alpha_1$).

Use of Maximum PP

Reflectivity values can indicate, in a non-intrusive manner, some properties of the solid. Although an examination of individual *PP* values does not provide much help in developing a relationship between reflectivity and material properties, maximum *PP* values do show promise. Because there are no *S*-waves in the liquid, the *b* value, β_1/α_1, is not relevant for this type of interface. Remaining are the ratios that concern density, α_2, and β_2. Given the α_2/α_1 values of 2, 4, and 6, the following three figures depict those points where *PP* reflectivity is a maximum for pre-critical incident angles.

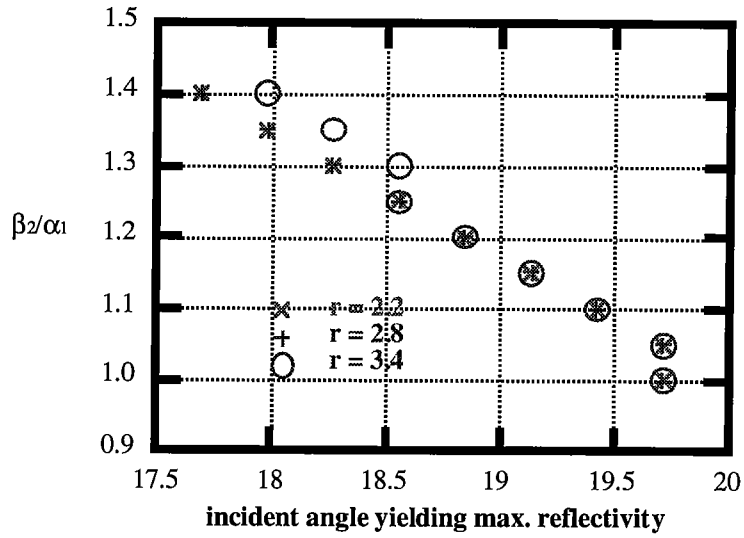

Figure 15: Points indicate the *P*-wave incident angle (on the solid from the liquid) and the ratio β_2/α_1 that yield the highest *PP* reflectivity. For this case, $\alpha_2/\alpha_1 = 2$.

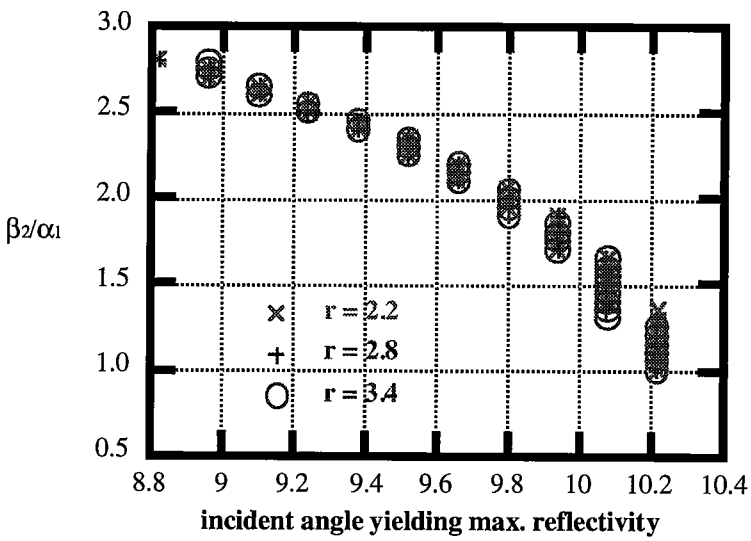

Figure 16: Points indicate the *P*-wave incident angle and the ratio β_2/α_1 that yield the highest *PP* reflectivity. For this case, $\alpha_2/\alpha_1 = 4$.

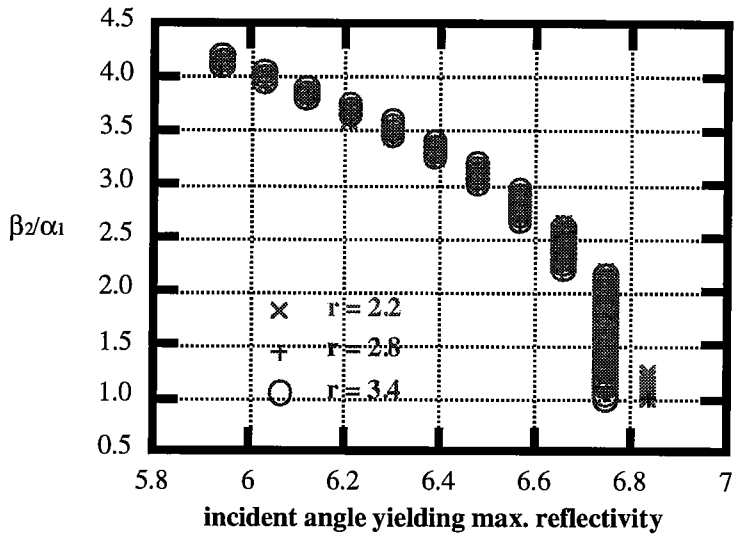

Figure 17: Points indicate the *P*-wave incident angle and the ratio β_2/α_1 that yield the highest *PP* reflectivity. For this case, $\alpha_2/\alpha_1 = 6$.

DISCUSSION

Points corresponding to different densities lie either on top of each other or so close together that distinguishing them individually is very difficult. Therefore, Figures 15-17 clearly show that r, the ratio of the solid density to the liquid density, has little bearing on the relationship between β_2/α_1 and the incident angle which yields the largest amplitude reflected *P*-wave. The vertical axis of β_2/α_1 increases as α_2/α_1 increases, because if α_2 is higher, then β_2, which must be less than the product of $(.5)^{1/2}$ and α_2 for elastic waves, can be higher. The range of pre-critical angles yielding the maximum reflection coefficient decreases with increasing α_2/α_1, because the critical angle decreases sharply.

The relationships illustrated in Figures 15-17 could be useful in determining elastic properties of solids. From preliminary lab measurements one can find values for liquid and solid densities and α_1. Then, measuring reflected amplitudes from the solid-liquid interface, that angle which produces maximum reflectivity can be recorded. The critical angle can be found as well. These angles provide values for β_2/α_1 and α_2/α_1, respectively, which, in turn, give values for elastic velocities within the solid. Once these are known, calculation of elastic constants such as bulk or shear modulus is elementary.

FREE-SOLID INTERFACE

At the interface between a solid half-space and a vacuum, a *P*-wave yields, except at normal incidence, a reflected *P*-wave and a reflected *SV*-wave [Aki and Richards 1982] (Figure 18). This seismic wave geometry usually describes earthquake waves that travel from the hypocenter to the surface and reflect off it. The free-solid interface is also applicable to crosswell though. Waves originating in one well bounce at different angles off the free surface and are detected by receivers in the other well. The reflectivity of the two scattered waves is their amplitude divided by that of the incident wave. The reflectivity varies according to the angle of incidence of the wave and the elastic wave velocities of the solid (Appendix D).

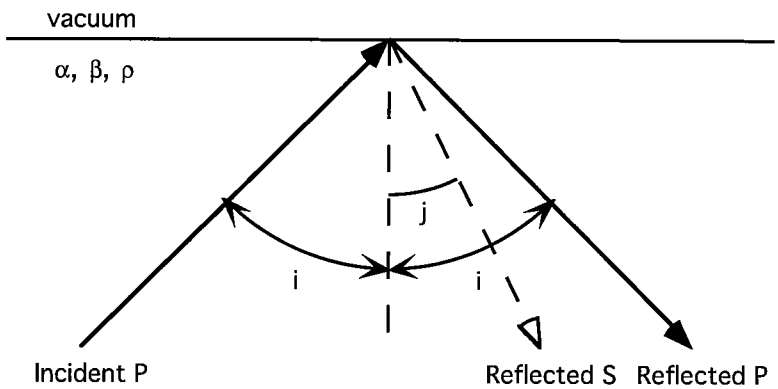

Figure 18: Reflection and conversion of a *P*-wave incident on a free-solid interface [Ewing *et al.* 1957].

Examining the relationship between incidence angle and elastic velocity ratios can provide more than just the solution to a mathematical curiosity. This relationship could be used in materials studies and sonde calibration. In particular, those angles where reflectivity is zero yield information on velocity properties of the solid.

Zero Reflectivity

Because waves cannot transmit through the interface, PP reflectivity is only a function of the angle i and the quantity β/α. If PP is equal to zero, which can be

recognized on seismograms by changes in polarity, then a given incidence angle determines a solid velocity ratio (Appendix D).

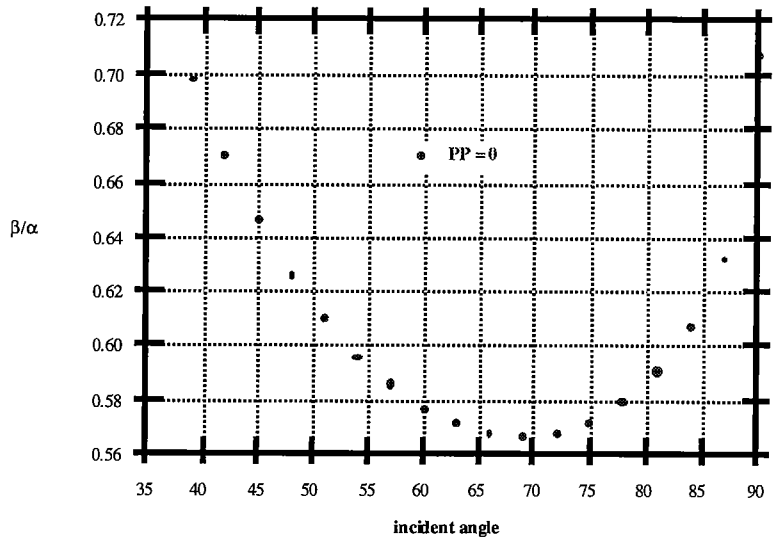

Figure 19: If *PP = 0*, then for a known angle of incidence, a corresponding velocity ratio of the solid can be found. The minimum of the scatter plot is at about 69 degrees, (β/α)=.565.

DISCUSSION

Figure 19 also describes the relationship between i and β/α for incident/reflected *SV*-waves [Aki and Richards 1982]. Reflectivities for converted waves, *PS* and *SP*, equal zero only at normal incidence and grazing incidence (i = 90 degrees). *SH*-wave reflectivity is also not a useful quantity; no wave conversions or transmissions take place so reflectivity should be independent of solid properties. Previously, I did not examine reflectivity zeroes for the solid/solid or liquid/solid cases as I did here, because the number of interdependent velocity and density ratios made finding a relationship such as Eqn. (D3) prohibitive.

A few applications of the i to β/α relationship might exist. Although this section concerns waves incident on the interface from within the solid, if a conjugate relationship exists for those impinging from the other side, then that function could provide a means of non-destructive testing using transducers at the interface. Figure 19 might also have applicability as a check on sonic log measurements. Finally, since the reflectivity equations used in this study assume isotropy, homogeneity, and a flat, elastic interface,

measured residuals from predicted β/α values indicate qualitatively the degree to which those assumptions have failed.

ANELASTICITY

If the materials through which the incident and scattered waves propagate are modeled as anelastic instead of elastic, much of the physics is altered, which affects calculations of reflectivity. Borcherdt (1982) examined the interactions of waves in linear viscoelastic media, at anelastic interfaces. There are a few similarities with the elastic cases, and several differences. As in the elastic case, *P*-waves only convert to *SV*-waves and vice versa as long as the waves are all in the same plane perpendicular to the interface; also, homogeneous waves incident at pre-critical angles will reflect homogeneous waves at the same angle [Borcherdt 1986]. However, Borcherdt (1986) found that transmitted waves will be inhomogeneous for all incident angles, pre- and post-critical, except normal incidence (Figure 20). Intrinsic absorption at a viscoelastic interface causes several other effects not predicted by elasticity theory:

i) phase velocity, indicated by the propagation vector, and energy velocity, indicated by the attenuation vector, propagate with different speeds and directions (Figure 20);

ii) α, β, and the quality factor, Q, which is a measure of attenuation, are all frequency dependent;

iii) phase velocity is dependent on travel path and therefore on incident angle;

iv) energy is transmitted to the lower half-space at post-critical angles due to the interaction of the incident and reflected wavefields and the decrease in the amount of energy transmission is not as abrupt as for the elastic case [Borcherdt 1982,1986].

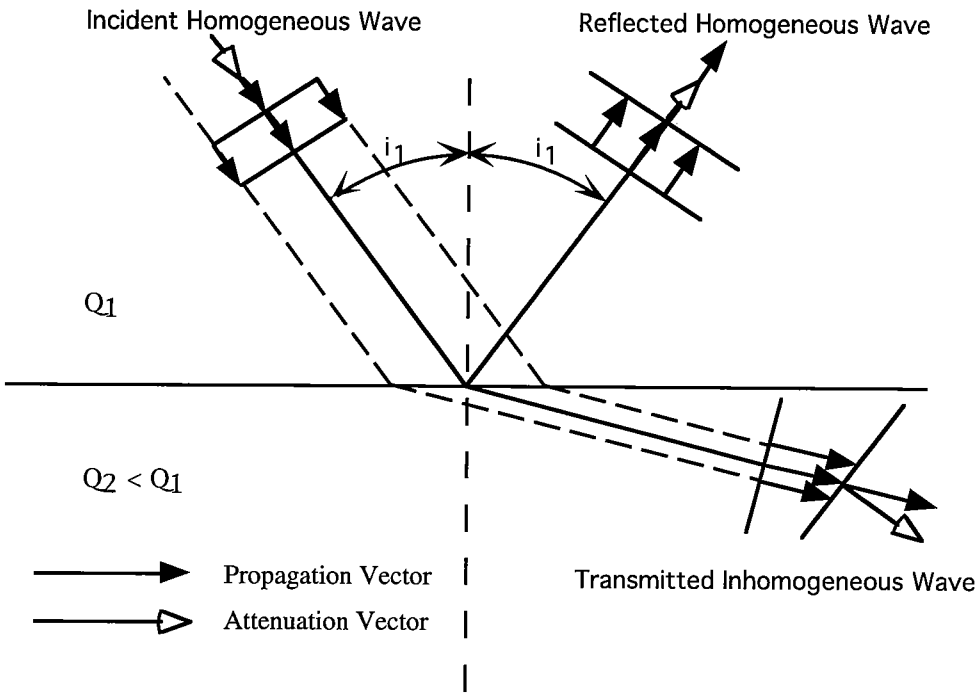

Figure 20: Reflection and transmission of a homogeneous plane wave on an interface between two viscoelastic solids. The propagation vector is perpendicular to planes of constant phase. The attenuation vector is perpendicular to planes of constant amplitude. (Bourbie 1982).

Another effect of anelasticity is particular to a wave within a viscoelastic solid striking a free-surface. Borcherdt (1982) shows that unless $Q_s = Q_p$, an incident *P*-wave will never have a zero reflection coefficient, making the use of Fig.19 problematical.

ACKNOWLEDGMENTS

I would like to thank Jerry Harris and all members of the Seismic Tomography Project for assistance with the conception of this study. I would also like to recognize Mark Van Schaack's invaluable computer support. Funding for this study was provided by Stanford's Seismic Tomography Project Consortium.

REFERENCES

Aki, K. and Richards, P.G., Quantitative Seismology, Theory and Methods, Vol.1. W.H. Freeman and Company, 1980.

Borcherdt, R.D., 1982, Reflection-refraction of general P- and type-I S-waves in elastic and anelastic solids: Geophys. J. R. astr. Soc., 70, p.621-638.

Borcherdt, et al., 1986, Influence of Welded Boundaries in Anelastic Media on Energy Flow, and Characteristics of P, S-I, and S-II Waves: Observational Evidence for Inhomogeneous Body Waves in Low-Loss Solids: J. Geophys. Res., 91, B11, p.11503-11518.

Bourbie, T., Effects of Attenuation on Reflections, PhD Dissertation, Stanford University, 1982.

Ewing, W.M., Jardetzky, W.S., Press, F., Elastic Waves in Layered Media. McGraw-Hill Book Company, Inc., 1957.

Levin, F.K., 1986, When reflection coefficients are zero: Geophysics, 51, p. 736-741.

Tooley, R.D., Spencer, T.W., Sagoci, H.F.,, 1965, Reflection and transmission of plane compressional waves: Geophysics, 30, p. 552-562.

Turcotte, D.L. and Schubert, G., Geodynamics, John Wiley and Sons, Inc., 1982.

APPENDIX A

PP Reflectivity from an Elastic Solid/Solid Interface (Aki and Richards 1982)

The reflection coefficients I use are in terms of displacement amplitudes rather than energy. Displacement amplitude is measured positive in the direction of wave propagation. Seismic receivers generally measure signal only in one direction, vertical or horizontal, but the measured amplitudes can easily be corrected by multiplying by a sine or cosine depending on which component is desired.

Assuming the four possible incident waves, P and S from above and below, and the four scattered waves, the waves' displacement amplitudes are combined with the interface boundary conditions giving a set of four coupled equations. Incident wave displacement amplitudes are $\dot{P}_1$, $\dot{S}_1$, P_2', and S_2'. Scattered wave displacement amplitudes are P_1', S_1', $\dot{P}_2$, and $\dot{S}_2$. The boundary conditions are continuity of displacement and traction in both the parallel and perpendicular directions. The coupled equations are

$$\sin i_1(\dot{P}_1 + P_1') + \cos j_1(\dot{S}_1 + S_1') = \sin i_2(\dot{P}_2 + P_2') + \cos j_2(\dot{S}_2 + S_2'),$$

$$\cos i_1(\dot{P}_1 - P_1') - \sin j_1(\dot{S}_1 - S_1') = \cos i_2(\dot{P}_2 - P_2') - \sin j_2(\dot{S}_2 - S_2'),$$

$$2\rho_1\beta_1^2 p\cos i_1(\grave{P}_1 - P_1') + \rho_1\beta_1\left(1-2\beta_1^2p^2\right)(\grave{S}_1 - S_1')$$
$$= 2\rho_2\beta_2^2 p\cos i_2(\grave{P}_2 - P_2') + \rho_2\beta_2\left(1-2\beta_2^2p^2\right)(\grave{S}_2 - S_2'),$$

$$\rho_1\alpha_1\left(1-2\beta_1^2p^2\right)(\grave{P}_1 + P_1') - 2\rho_1\beta_1^2 p\cos j_1(\grave{S}_1 + S_1')$$
$$= \rho_2\alpha_2\left(1-2\beta_2^2p^2\right)(\grave{P}_2 + P_2') - 2\rho_2\beta_2^2 p\cos j_2(\grave{S}_2 + S_2'), \qquad \text{(A1)}$$

where $p = \dfrac{\sin i_1}{\alpha_1} = \dfrac{\sin i_2}{\alpha_2} = \dfrac{\sin j_1}{\beta_1} = \dfrac{\sin j_2}{\beta_2}$, the ray parameter. This is also a mathematical equation describing Snell's Law.

Putting scattered waves on the left and incident waves on the right, we obtain

$$M\begin{pmatrix} P_1' \\ S_1' \\ \grave{P}_2 \\ \grave{S}_2 \end{pmatrix} = N\begin{pmatrix} \grave{P}_1 \\ \grave{S}_1 \\ P_2' \\ S_2' \end{pmatrix}. \qquad \text{(A2)}$$

The complete scattering matrix becomes $M^{-1}N = \begin{pmatrix} \grave{P}P' & \grave{S}P' & P'P' & S'P' \\ \grave{P}S' & \grave{S}S' & P'S' & S'S' \\ \grave{P}\hat{P} & \grave{S}\hat{P} & P\hat{P} & S\hat{P} \\ \grave{P}\hat{S} & \grave{S}\hat{S} & P\hat{S} & S\hat{S} \end{pmatrix}$ (A3)

We are only concerned with the top left term:

$$\grave{P}P' = \frac{\left(B\dfrac{\cos i_1}{\alpha_1} - C\dfrac{\cos i_2}{\alpha_2}\right)F - \left(A + D\dfrac{\cos i_1}{\alpha_1}\dfrac{\cos j_2}{\beta_2}\right)Hp^2}{EF + GHp^2} \qquad \text{(A4)}$$

where

$$\mathrm{A} = \rho_2\left(1-2\beta_2{}^2\mathrm{p}^2\right) - \rho_1\left(1-2\beta_1{}^2\mathrm{p}^2\right),$$
$$\mathrm{B} = \rho_2\left(1-2\beta_2{}^2\mathrm{p}^2\right) + 2\rho_1\beta_1{}^2\mathrm{p}^2,$$
$$\mathrm{C} = \rho_1\left(1-2\beta_1{}^2\mathrm{p}^2\right) + 2\rho_2\beta_2{}^2\mathrm{p}^2,$$
$$\mathrm{D} = 2\left(\rho_2\beta_2{}^2 - \rho_1\beta_1{}^2\right),$$
$$\mathrm{E} = \mathrm{B}\frac{\cos \mathrm{i}_1}{\alpha_1} + \mathrm{C}\frac{\cos \mathrm{i}_2}{\alpha_2},$$
$$\mathrm{F} = \mathrm{B}\frac{\cos \mathrm{j}_1}{\beta_1} + \mathrm{C}\frac{\cos \mathrm{j}_2}{\beta_2},$$

$$G = A - D\frac{\cos i_1}{\alpha_1}\frac{\cos j_2}{\beta_2},$$
$$H = A - D\frac{\cos i_2}{\alpha_2}\frac{\cos j_1}{\beta_1},$$

APPENDIX B

Solving for Error Limitation of α_2 from Error of *PP*

If the two solid half-spaces have equal density, then for normal incidence,

$$\alpha_2 = -\alpha_1\left(\frac{PP+1}{PP-1}\right). \tag{B1}$$

With error in angularly averaged *PP* from normal incidence *PP*, this becomes

$$\alpha_2 = -\alpha_1\left(\frac{PP+\Delta+1}{PP+\Delta-1}\right). \tag{B2}$$

Rearranging,

$$\frac{\Delta}{PP} = \frac{E\left(\frac{1}{PP} - PP\right)}{E(PP+1)+2} \tag{B3}$$

equals the percentage error of *PP*, where E is the percent allowable error of α_2.

Now if $E << \frac{2}{PP+1}$,

$$\frac{\Delta}{PP} = \frac{E\left(1-PP^2\right)}{2PP}, \tag{B4}$$

which is the expression I used to construct Figure 11.

APPENDIX C

PP Reflectivity from an Elastic Liquid/Solid Interface (Bourbie, 1982)

Starting with *P*- and *S*-wave potentials for incident and scattered waves,

$$\Phi_i = A_i \exp\left[ik_{\alpha_1}\left(x\sin i_1 + z\cos i_1\right) - i\omega t\right]$$
$$\Phi_r = A_r \exp\left[ik_{\alpha_1}\left(x\sin i_1 - z\cos i_1\right) - i\omega t\right]$$
$$\Phi_t = A_t \exp\left[ik_{\alpha_2}\left(x\sin i_2 + z\cos i_2\right) - i\omega t\right]$$
$$\psi_t = B_t \exp\left[ik_{\beta_2}\left(x\sin j_2 + z\cos j_2\right) - i\omega t\right], \tag{C1}$$

$$k_\nu = \frac{\omega}{\nu},$$

and combining with boundary conditions of displacement,

$$u_{1_z} = u_{2_z}, \tag{C2}$$

and stress,

$$\begin{aligned} \sigma'_{zx} &= 0 \\ \sigma_{1zz} &= \sigma_{2zz}. \end{aligned} \tag{C3}$$

yields the expression for PP reflectivity from an incident P-wave on a liquid-solid interface:

$$PP = \frac{\rho_2\alpha_2 \cos i_1 \left\{ \left(1-2\sin^2 j_2\right)^2 + \frac{4\beta_2^3}{\alpha_1^2\alpha_2} \sin^2 i_1 \cos i_2 \cos j_2 \right\} - \rho_1\alpha_1 \cos i_2}{\rho_2\alpha_2 \cos i_1 \left\{ \left(1-2\sin^2 i_2\right)^2 + \frac{4\beta_2^3}{\alpha_1^2\alpha_2} \sin^2 i_1 \cos i_2 \cos j_2 \right\} + \rho_1\alpha_1 \cos i_2}. \tag{C4}$$

APPENDIX D

Derivation of Incidence Angle/Velocity Ratio Relationship for a Vacuum/Solid Interface

The boundary conditions for the free surface/solid interface are discontinuity of both displacement and traction. Also, no waves can propagate in the vacuum, and, of course, the vacuum has no density. Combining these conditions with the wave potentials,

$$\begin{aligned} \frac{\partial\psi_x}{\partial x} + \frac{\partial\psi_z}{\partial z} &= 0 \\ \frac{\partial\psi_x}{\partial z} - \frac{\partial\psi_z}{\partial x} &= 0, \end{aligned} \tag{D1}$$

reflectivity can be solved for in terms of the amplitude of the reflected wave divided by the amplitude of the incident wave.

$$PP = \frac{-\left(\frac{1}{\beta^2} - 2p^2\right)^2 + 4p^2 \frac{\cos i}{\alpha} \frac{\cos j}{\beta}}{+\left(\frac{1}{\beta^2} - 2p^2\right)^2 + 4p^2 \frac{\cos i}{\alpha} \frac{\cos j}{\beta}} \text{ ,(Aki \& Richards p.140)} \tag{D2}$$

where $p = \frac{\sin i}{Vp} = \frac{\sin j}{Vs}$. (D3)

If PP is set to zero then the following relationship results:

$$b^8 + \left(\frac{-1}{\sin^2 i} - 1\right)b^6 + \left(\frac{1.5}{\sin^2 i}\right)b^4 + \left(\frac{-.5}{\sin^4 i}\right)b^2 + \left(\frac{1}{16\sin^6 i}\right) = 0, \tag{D4}$$

where $b = \frac{\beta}{\alpha}$.

PAPER I

THE MOMENT METHOD UTILIZING GREEN'S FUNCTIONS OF STRATIFIED MEDIA: SCATTERING SIMULATIONS

Guan Y. Wang

ABSTRACT

An efficient numerical solution to the two-dimensional scattering problem is achieved by decomposing the original 2-D problem into a layered medium and relatively small scatterers embedded in it. The moment method is applied to solve the scattering from the small scatterers with the Green's function of a layered medium. The layered Green's function is calculated with Fourier transforms. The computational examples show that the proposed method is more efficient than that of directly applying the moment method, especially when large scale problems are involved.

INTRODUCTION

Many imaging problems are carried out in the frequency domain and often require intensive forward modeling computation. Thus, there is a need to be able to efficiently calculate the wave field directly in the frequency domain. Furthermore, for large spatial scale problems, the costs of the finite difference methods increase dramatically, so that it is limited in many real applications. Two-dimensional scattering from inhomogeneous bodies in an unbound uniform medium has been studied extensively with the moment method (Richmod, 1965). However, the method is effective only for small scatters and uniform host medium. The objective of this paper is to develop an efficient numerical solution to the 2-D scattering problem for the scatters embedded in a layered background medium. We calculate layered Green's function first and then apply it to the moment method. The efficiency is achieved by only discretizing the scatters embedded in the layered background.

The paper is organized into three sections. In the first section, the approach of the analysis is outlined in terms of the supposition principle. Section two is a brief review of the moment method. Section three is an analysis of the computation of the Green's

function for layered medium. Finally, we employ the layered Green's function in the moment method to show the effectiveness of the proposed method. In the end of each of the sections, we show some numerical examples to ensure that the implementation of the algorithm is valid.

THE APPROACH OF THE ANALYSIS

For reservoir imaging problems, the low spatial frequency components can often be obtained via prior geological information, or traveltime tomography or other means as indicated in Figure 1.

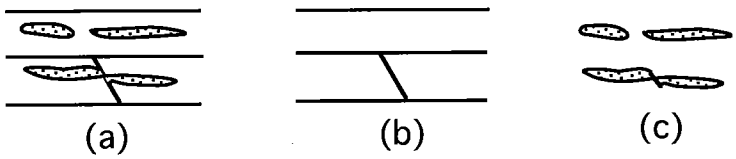

Fig. 1 For a common reservoir imaging problem, the velocity structure illustrated in (a), can be decomposed into low components (b) and high spatial frequency components (c).

In order to image high frequency components, it is necessary to be able to efficiently calculate the wave field of the slowly varying background. Since the background variation is relatively simple, in many practical situations, it can be described by stratified structure with some additional local features, as shown in Figure 2. Therefore, the problem can be analyzed separately as a layered medium with small scatterers embedded in it.

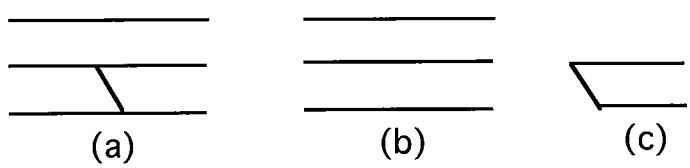

Fig. 2 A 2-D structure (a) can be separate as a 1-D background and a relatively small and isolated 2-D body.

For a two-dimensional scalar Homholtz equation

$$\{\frac{\partial^2}{\partial x^2}+\frac{\partial^2}{\partial z^2}+k^2(x,z)\}u=-\delta(x-x')\delta(z-z'), \tag{1}$$

the corresponding integral equation can be written as

$$u(s,g)=u^i(s,g)-\int u(r',s)f(r')G^0(g,r')d^2r', \tag{2}$$

where $G^0(g,r')$ is the Green's function for a uniform background, and $f(r')$ is the scattering potential relative to that background. The same problem can also written as

$$u(s,g)=u^i(s,g)-\int u(r',s)e(r')G^l(g,r')d^2r', \tag{3}$$

where $G^l(g,r')$ is the Green's function for layered background medium. The function $e(r')$ is the scattering potential relative to the layered background. For most realistic situations, the distribution of the function $e(r')$ is more isolated and weaker than that of $f(r')$. Consequently, solving equation (3) with the moment method is much easier than solving equation (2), since a relatively small area needs to be discretized. However, we have to solve following differential equation in order to obtain the Green's function for the layered background:

$$\{\frac{\partial^2}{\partial x^2}+\frac{\partial^2}{\partial z^2}+k_l^2(z)\}G^l=-\delta(x-x')\delta(z-z'). \tag{4}$$

Fortunately, we can almost solve the above equations analytically with the Fourier transform. We will discuss this in more detail in the following sections.

THE MOMENT METHOD

The moment method is often applied in the calculation of the scattered field from a two dimensional inhomogeneity (Bath, 1982, Chew, 1990). The scattered field is described by following equation:

$$u(r)=u^i-\int u(r')e(r')G(r,r')d^2r'. \tag{5}$$

The method is straightforward and efficient when the size of the scatterer is small. The relatively small and isolated region we separated from the layered background is divided into N square cells. Then, the scattering potential and wave field are represented as a summation of basis functions over the N cells, i.e.,

$$e(r) = \sum_{j,k} e(r_{jk}) b_{jk}(r)$$

$$u(r) = \sum_{j,k} a_{jk} b_{jk}(r)$$

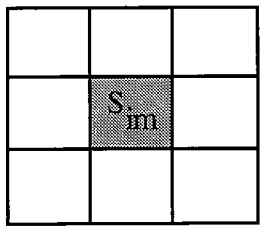

Fig. 3. Scattering potential is divided up into N square cells

where $b_{jk}(r)$ is the basis function, $e(r_{jk})$ and a_{jk} represent the coefficients describing the scattering potential and wave field over the basis function. We choose the same pulse basis function $b_{jk}(r)$ to discretize equation (5), where

$$b_{jk}(r) = \begin{cases} 1 & r \in s_{jk} \\ 0 & r \notin s_{jk} \end{cases}.$$

Applying the point-matching procedure, equation (5) can be written as a linear algebraic system

$$u_{jk} + \sum_{i,m} g(j,k,i,m) f(r_{im}) u_{im} = G(r_{jk}), \qquad (6)$$

where $g(j,k,i,m) = \int_{s_{im}} G(r_{jk}) d^2 r$.

We implemented the above algorithm for the homogeneous background. With the model shown in Figure 4, the scattered and total field both in the time and frequency domains are calculated. Similar to finite difference method, the dimension of the cell is chosen approximately as one tenth wavelength at the lowest velocity in the calculations. The results are displayed in Figure 5 and 6 and it is obvious that the forward scattering is stronger in the forward direction, as expected.

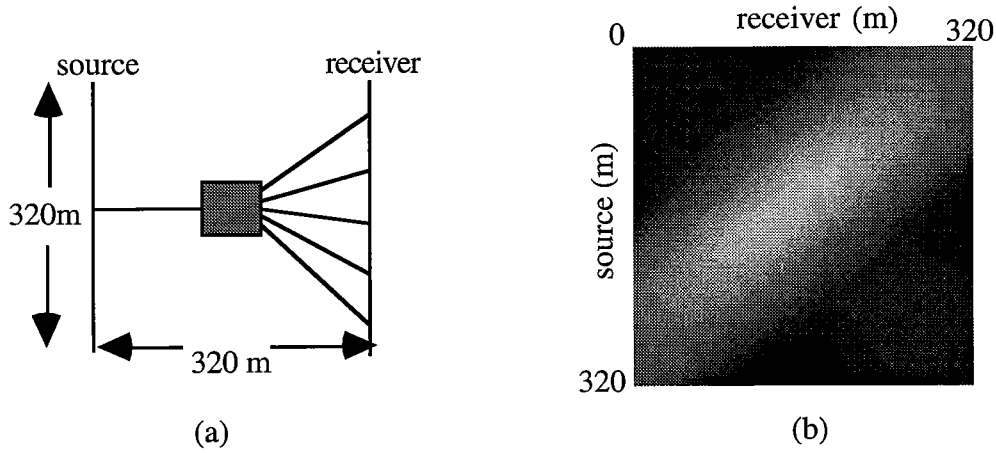

Fig. 4. (a) Forward scattering model for computation with moment method.
(b) The amplitude of the calculated scattered field (Frequency= 400Hz).

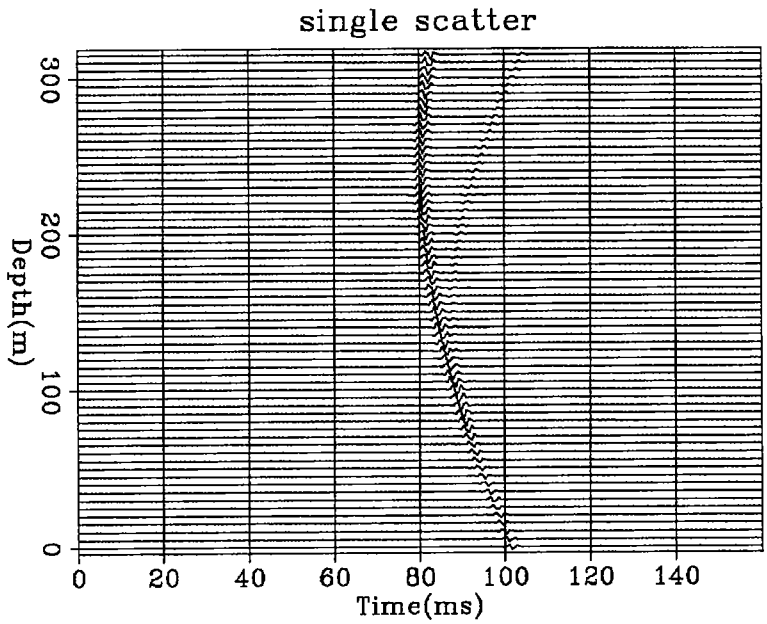

Fig. 5 Forward scattering modeling with moment method.
Total field time signal with a source at the depth of 250m.

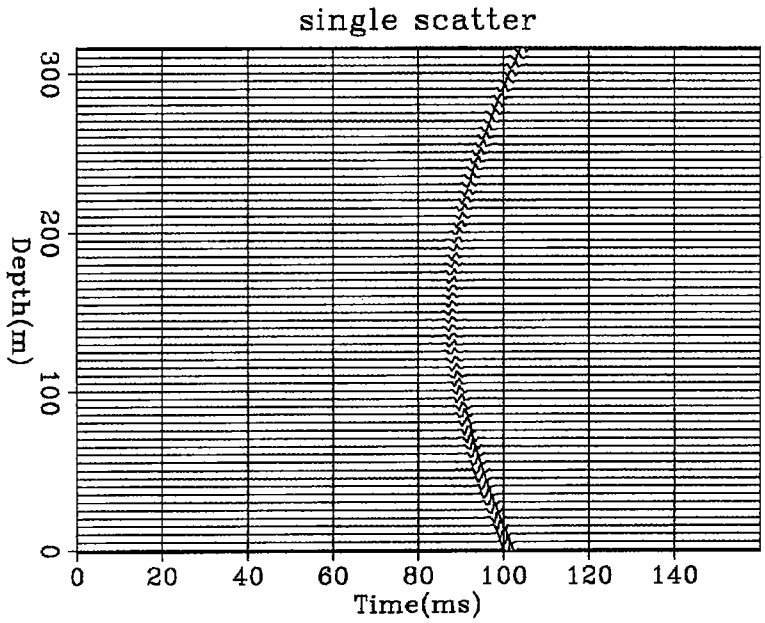

Fig. 6 Forward scattering modeling with moment method.
Time domain scattered field which is stronger in forward direction.

GREEN'S FUNCTIONS FOR THE LAYERED MEDIUM

We calculate the Green's function of the stratified medium through the Fourier transform (Brekhovskikh, 1982). Since the medium is 1-D, we take the Fourier transform of the Holmholtz equation (4) along the horizontal direction and obtain

$$[\frac{\partial^2}{\partial z^2}+k^2(z)-\xi^2]G(\xi,z,z')=-\delta(z-z')e^{i\xi x'}, \qquad (7)$$

where ξ is horizontal wave number. The solution of this equation $G(\xi,z,z')$ is the one-dimensional Green's function and satisfies appropriate boundary conditions. Recall that $G(\xi,z,z')$ is continuous everywhere in the interval of definition and dG/dz is continuous everywhere in the interval except at $z=z'$. At the source depth z',

$$\lim_{\varepsilon\to 0}\int_{z'-\varepsilon}^{z'+\varepsilon}\delta(z-z')dz=1,$$

and

$$\lim_{\varepsilon\to 0}\int_{z'-\varepsilon}^{z'+\varepsilon}\gamma^2(z)U(\xi,z,z')dz=0,$$

which is true, if $\gamma(z)$ and $G(\xi,z,z')$ are continuous. Here, $\gamma(z)$ is vertical wave number. From the above analysis, we can see that the delta function creates an artificial layer or interface for our problem. The eigen-equation of equation (7) is

$$[\frac{\partial^2}{\partial z^2}+\gamma^2(z)]\psi=0. \tag{8}$$

The solution to equation (7) can be constructed with two linearly independent solutions of the eigen equation (8), i.e.,

$$G=\begin{cases} a\psi_1 & z\le z' \\ b\psi_2 & z\ge z' \end{cases}.$$

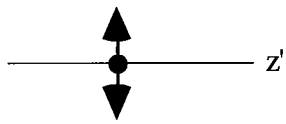

Fig. 7 at the source depth the derivative of the Green's function is discontinuous

With the constrains of the conditions discussed above, we have

$$a\psi_1(z')=b\psi_2(z')$$

and $$a\psi'_1(z')-b\psi'_2(z')=-e^{ik_x x'}.$$

Therefore, the unknown coefficients a and b can be solved. Notice that the solutions ψ_1 and ψ_2 are for arbitrary stratified medium. For a layered medium, ψ_1 and ψ_2 are plane waves in each layer, i.e.,

$$\begin{aligned} &Ae^{-i\gamma_1(z-z_1)} \\ &Be^{i\gamma_2(z-z_1)}+Fe^{-i\gamma_2(z-z')} \\ &Ee^{i\gamma_2(z-z')}+Ce^{-i\gamma_2(z-z_2)} \\ &De^{-i\gamma_2(z-z_2)}. \end{aligned} \tag{8}$$

The conditions at interface are:

i. The wave field is continuous.

ii. The derivative of the wave field is continuous (for constant density).

iii. The wave field at the source depth is continuous.

iv. The derivative of the wave field across the source depth is discontinuous.

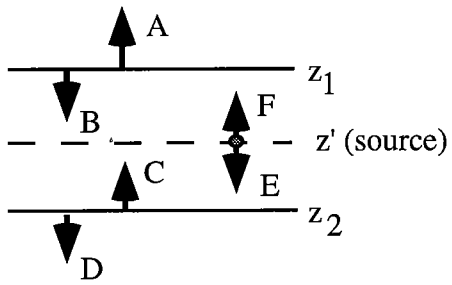

Fig. 8, In each layer the solution to the eigen-equation
is a plane wave. Source depths are treated as artificial interfaces.

With these conditions we can solve for the unknown coefficients of the plane waves in each layer. The Green's function of the layered medium is obtained by taking the inverse Fourier transform of $G(\xi,z,z')$.

The computation of the Sommerfeld-type integral encountered in the spectral representation of Green's function has a well-known difficulty of their numerical evaluation, namely the oscillatory behavior of the integrand due to the function $e^{i\xi(x-x')}$ and the presence of singularities contributed by $G(\xi,z,z')$. These include poles and branch points that result from the dispersion relation

$$\gamma^2 = \frac{\omega^2}{v^2} - \xi^2.$$

It is possible to leave the pole out and take the Cauchy principle value, a common procedure for dealing with improper integrals. However, there is no need to proceed in this way, because all propagating wave systems are naturally dampened and any amount of dampening takes the poles and moves it off the real axis. The integral then becomes proper and can be evaluated without ambiguity. After including a small amount of attenuation, the dispersion relation becomes

$$\gamma^2 = \frac{(\omega + i\varepsilon)^2}{v^2} - (\xi_r + i\xi_i)^2. \qquad (9)$$

From $\mathrm{Im}\,\gamma = 0$ we have

$$\gamma_r \gamma_i = -2\xi_r \xi_i + 2\varepsilon \frac{\omega}{v^2} = 0.$$

Therefore, the curves on which the branch points lie are

$$\xi_r \xi_i = \varepsilon \frac{\omega}{v^2} > 0, \tag{10}$$

as shown in Figure (10). Since z is positive, we can not have $\mathrm{Im}\,\gamma < 0$ on the physical sheet of the complex function $e^{i\gamma z}$, since that would lead to an exponential solution which is unnatural.

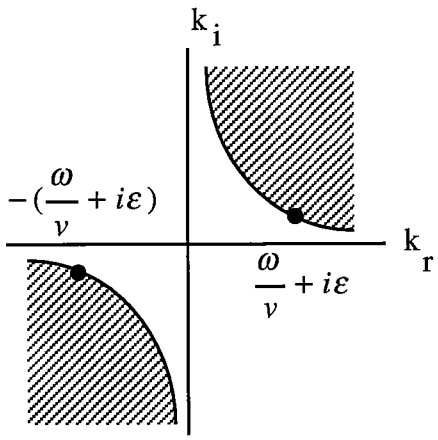

Fig. 9, Branch cut and branch points

We implemented the above algorithm of Green's function for layered medium. The results are shown in Figures 10, and 11. In figure 10 (b) the pattern of the frequency response agrees with those results calculated using the finite difference method. The reflection and transmission events in the figure 11 are consistent with those of events from theoretical analysis. With the verification of Green's function for layered background we are ready to apply the solution obtained using the Green's function, to the moment method to compute the scattering form 2-D structures.

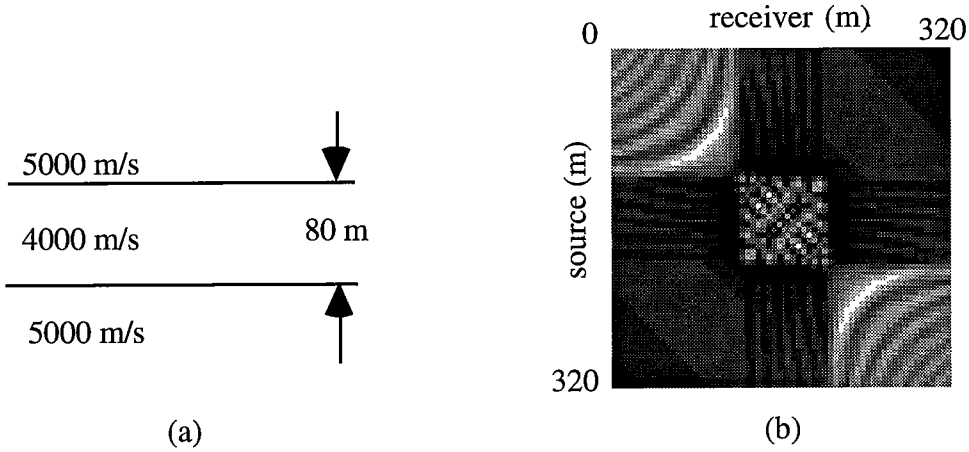

Fig. 10. (a) Three layer model. (b) The amplitude of the frequency response of the calculated Green's function (Frequency=400 Hz).

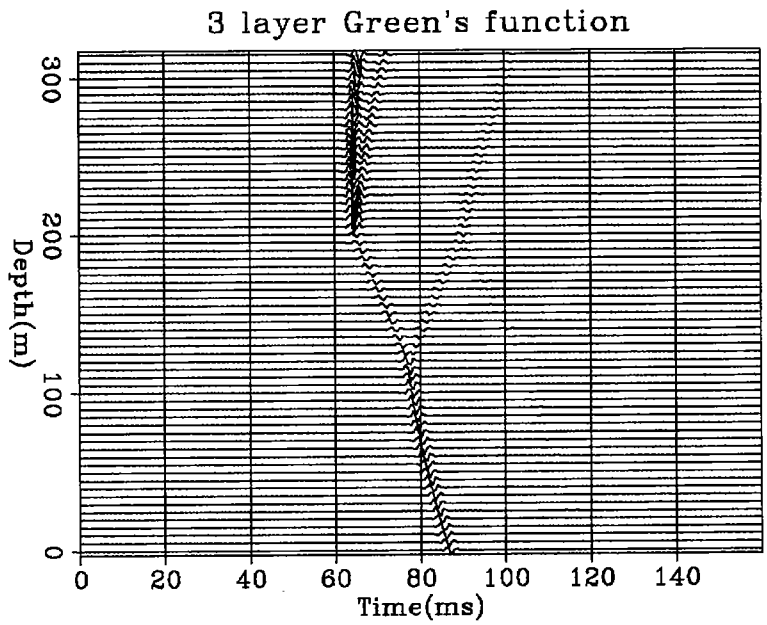

Fig. 11. The time domain Green's function of three layer model.
The reflection and transmission are consistent with theoretical analysis.

SAMPLE RESULTS OF SCATTERING FROM 2-D STRUCTURE

On inserting the proper representation for $G^l(r,r')$ into equation (6), which is rewritten here as

$$u_{jk} + \sum_{i,m} g^l(j,k,i,m) f(r_{im}) u_{im} = G^l(r_{jk}),$$

where $g^l(j,k,i,m) = \int_{s_{im}} G^l(r_{jk}) d^2r$, and $G^l(r_{jk})$ is Green's function for layered background, we can calculate the scattering field from a 2d model as indicated in Figure 12 (a). The amplitude of the frequency response with the sample model is shown in Figure 12 (b) and the corresponding scattered field in the time domain is shown in Figure 13.

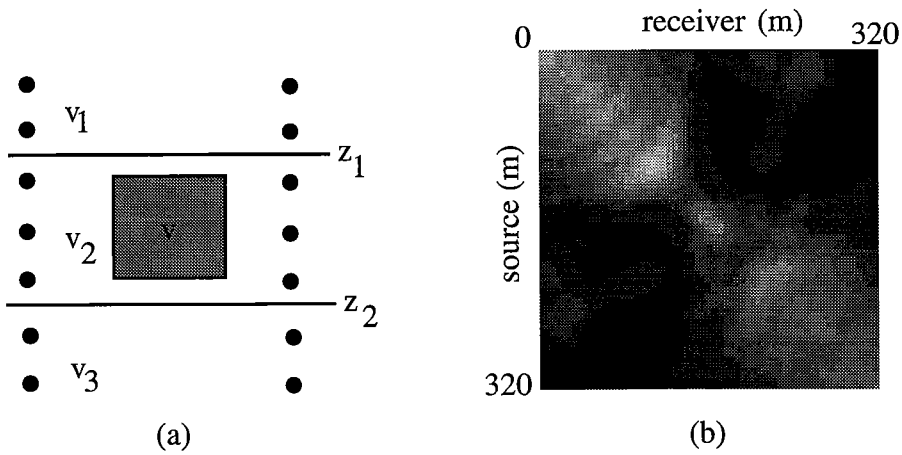

Fig. 12 (a) 2-D model forward scattering model, v1=4000, v2=3000 v3=3500 and v=3600 (m/s). (b) The amplitude of the frequency response at frequency=500 Hz

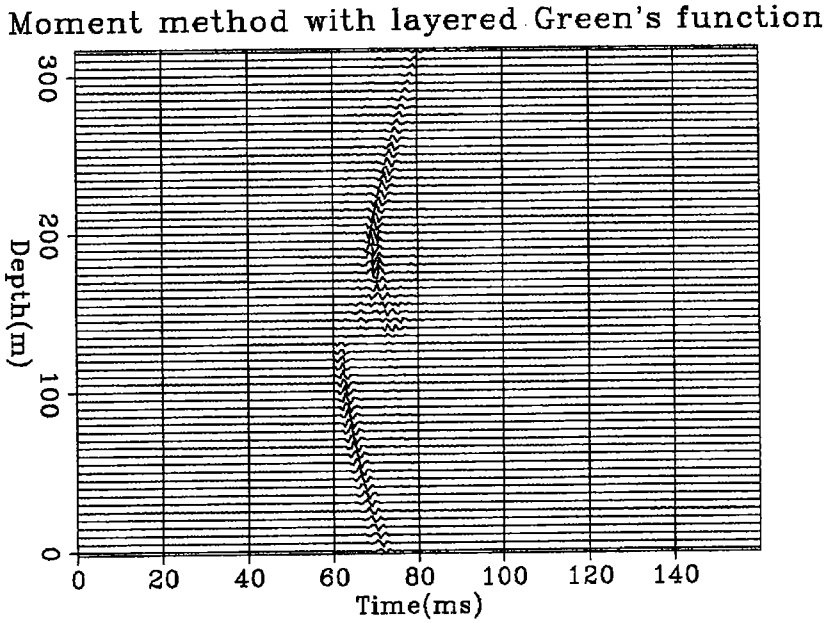

Fig. 13 Scattered field from the model in figure 12 using the moment method with layered Green's function.

CONCLUSIONS

With the layered Green's function, the calculations using the moment of method become much more efficient in some situations, because only relatively small scatterers needed to be discretized. The layered Green's function can be calculated with a Fourier transform technique. This forward scattering calculation provides a useful tool for migration or inversion in the frequency domain.

ACKNOWLEDGMENT

The paper was edited by Sonya Williams and Nicholas Smalley. The author is grateful for their help.

REFERENCES

Bathe, K. J., 1982. Finite element procedures in engineering analysis, Englewoodd Cliffs, NJ: Prentice Hall, Inc.

Brekhovskikh, L. and Lysaanov Yu., 1982. Fundamentals of Ocean Acoustics, Spring-Verlag Berlin Heidelberg, New York.

Chew, W. C. 1990. Waves and fields in inhomogeneous media. New York: Van Nostrand Reinhold

Richmond J. H. , 1965. Scattering by a dielectric cylinder of arbitrary cross section shape, IEEE trans. Antennas Propagat. vol. Ap-14, pp. 334-341

PAPER J

REFLECTION IMAGING USING RICCATI EQUATIONS

Guan Y. Wang

ABSTRACT

In investigating wave propagation in a stratified medium, the concept of reflection and transmission play important roles and often lead to a simplified and intuitive picture of wave propagation in inhomogeneous media. When we image properties of the medium, rather than calculating the wave field, using equations governing reflection function instead of the wave equation may have certain computational advantages. We derive the Riccati equations of an arbitrary incident angle directly from physical equations. By applying the single reflection approximation to the integral representation of the Riccati equations, we are able to reconstruct reflection coefficient profiles with Fourier transform techniques. We also derived a recursive relation with which we can map the reconstructed reflection coefficient profile onto a velocity profile.

INTRODUCTION

For the scalar field produced by a time harmonic point source in a stratified inhomogeneous medium, the reduced wave equation can be written as

$$\Delta p + k^2(z)p = -\delta(z - z_0)\delta(r) / 2\pi r \qquad (1)$$

If we consider a finite volume of the medium, we shall obtain the exact solution by three well known methods, which lead to three different representations of p. These are the method of normal modes, the method of Hankel transform, and the method of multiple scattering. These representations can be transformed into one another by using contour integration and residual evaluation, the binomial expansion and Poisson summation formula (Keller, 1977, Brekhovskikh, 1982). However, these representation are very complicated and are inconvenient for inverse problems. We know that when a plane wave falls on a boundary between two media of different properties, it is split into a transmitted wave

proceeding into second medium and a reflected wave propagated back into the first medium. Very often we do not seek the field itself in the medium but some other characteristic quantity, such as the reflection coefficient. Therefore, instead of using the reduced wave equation, it may have some computational advantages to directly use original physical equations. These coupled first order differential equations can be combined to Riccati equations which are first order but often nonlinear differential equations. In the following sections we first derive the Riccati equations for an arbitrary incident angle and their integral representations, and then apply single reflection approximation to the integral representation to reconstruct the reflection coefficient profile with Fourier transform techniques. We also discussed upgoing and downgoing waves separation and the mapping from the reflection coefficient profile to the velocity profile.

RICCATI EQUATIONS OF ARBITRARY INCIDENT ANGLE

Consider that waves propagate in the region $z_0 < z < L$ characterized by a wave number which is positive and varying continuously with z. Let this region extend from z_0 to $-\infty$ with a constant value k_0, and from L to ∞ with another constant value k_1 for the wave number as shown in Figure 1.

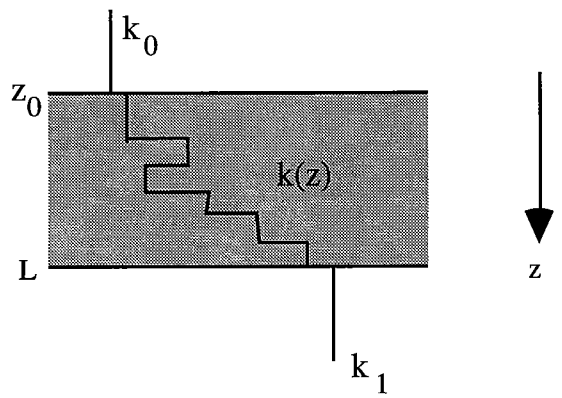

Fig.1. Wave number profile of inhomogeneous layer

Starting from the continuity equation and Euler equation:

$$\frac{\partial p}{\partial t} + c^2 \nabla \cdot v = 0, \tag{2}$$

and $$\frac{\partial v}{\partial t} + c^2 \nabla p = 0, \tag{3}$$

the following wave equations in the different regions can be derived as

$$(\Delta + k^2(z))p = 0, \qquad z_0 < z < L$$

$$(\Delta + k_0^2)p = 0, \qquad z < z_0$$

and $$(\Delta + k_1^2)p = 0. \qquad z > L$$

We know the solution to these wave equations corresponding to reflected and transmitted waves. However, instead of the wave equation, we like to arrive at the differential equations governing reflection function or transmission function directly from equation (2) and (3). We will see later this may result in certain computational advantages.

Assume the solution to above wave equation consists of upgoing and downgoing waves, then the pressure field and velocity field can be written as

$$p(x,z) = [u(z) + d(z)]e^{i\xi x}, \tag{4}$$

and $$v_z(x,z) = \frac{\beta(z)}{\omega}[-u(z) + d(z)]e^{i\xi x}, \tag{5}$$

where *u(z)* and *d(z)* represent upgoing and downgoing waves. The factor $e^{-i\omega t}$ is omitted. Notice that the expression (5) is true only under the condition of $(k(z))' << 1$ which implies the weak reflection of the medium (Harris, 1994). Let $\frac{\partial}{\partial t} = -i\omega$, then equations (2) and (3) become

$$\frac{\partial v_z(x,z)}{\partial z} = i\frac{\beta^2(z)}{\omega} p(x,z), \tag{2'}$$

and $$\frac{\partial p}{\partial z} = i\omega v_z(x,z). \tag{3'}$$

From equation (2') and (3') we arrive at

$$-u' + d' = i\beta(u + d) - \frac{\beta'}{\beta}(-u + d), \tag{6}$$

and

$$u' + d' = i\beta(-u + d). \tag{7}$$

Add equation (6) to equation (7) we obtain

$$d' = i\beta d - \frac{\beta'}{2\beta}(-u + d). \tag{8}$$

Subtracting equation (6) from equation (7) results in

$$u' = -i\beta u + \frac{\beta'}{2\beta}(-u + d). \tag{9}$$

By multiplying u to equation (8) and d to equation (9), we obtain

$$du' = -i\beta ud + \frac{\beta'}{2\beta}(-ud + d^2), \tag{10}$$

and $$ud' = i\beta ud - \frac{\beta'}{2\beta}(-u^2 + ud). \tag{11}$$

Subtracting equation (10) from (11) we have

$$\frac{du' - ud'}{d^2} = -2i\beta u / d + \frac{\beta'}{2\beta}(1 - u^2 / d^2),$$

or

$$R'(z) = -2i\beta(z)R(z) + \gamma(z)(1 - R^2(z)), \tag{12}$$

where $R(z) = u(z) / d(z)$ is defined as reflection function, the vertical wave number $\beta = k(z)\cos\theta(z)$ and the reflection coefficient over a fine layer or an effective interface

$\gamma = \frac{\beta'}{2\beta}$. Equation (12) is called Riccati equation governing reflection function which is a first order but nonlinear differential equation.

INTEGRAL REPRESENTATION OF REFLECTION FUNCTION

By noticeing that $\exp(2i\int_{z_0}^{z}\beta(z')dz')$ is an integrating factor for Riccati equation (12), the Riccati equation can be solved as the following:

$$\frac{d}{dz}[R(z)\exp(2i\int_{z_0}^{z}\beta(z')dz')] = \gamma(1-R^2)\exp(2i\int_{z_0}^{z}\beta(z')dz') \qquad (12')$$

where z_0 is a arbitrary reference point. With boundary condition $R(z)\to 0$ as $z\to\infty$, and integrating equation (12') from z to infinity, we obtain the integral representation of the reflection function

$$-R(z)\exp(2i\int_{z_0}^{z}\beta(z')dz') = \int_{z}^{\infty}\gamma(1-k^2(z))\exp(2i\int_{z_0}^{z}\beta(z')dz')dz$$

Let $\varphi(z) = 2\int_{z_0}^{z}\beta(z')dz'$. The above representation is simplified as

$$R(z)e^{i\varphi(z)} = -\int_{z}^{\infty}\gamma(z)(1-R^2(z))e^{i\varphi(z)}dz. \qquad (13)$$

From the integral representation (13) we can see the physical significance of reflection function $R(z)e^{i\varphi(z)}$. It represents the ratio between complex amplitude of up and down waves and the phase variation due to propagation. At an effective interface, or over a fine layer, the reflection function degenerates to the form of the conventional reflection coefficient for a single interface, that is

$$-e^{-i\varphi(z)}\int_{z_n}^{z_{n+1}}\gamma(z)e^{i\varphi(z)}dz = -e^{-i\varphi(z)}\frac{\beta_{n+1}-\beta_n}{\beta_{n+1}+\beta_n}. \qquad (14)$$

Note that the equation (13) is for the half space problem by which we mean that the incident field is illuminated at the top of the inhomogeneous layer as shown in figure 1. For the incident wave inside the layer, i.e. "the whole space problem", we can denote the reflection function results from contributions above and below the receiver depth as

$$R^{+}(z_g)e^{i\varphi(z_s,z_g)} = -\int_{z_g}^{\infty} \gamma(z')(1-R^2(z'))e^{i\varphi(z',z_s)}dz \tag{15}$$

$$-R^{-}(z_g)e^{i\varphi(z_s,z_g)} = -\int_{-\infty}^{z_g} \gamma(z')(1-R^2(z'))e^{i\varphi(z',z_s)}dz \tag{16}$$

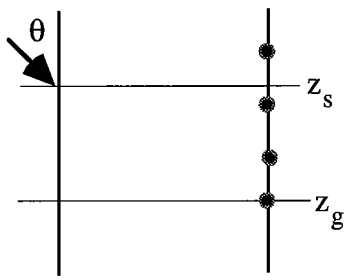

Fig. 2. Incident depth and receiver depth

For a given incident depth z_S and receiver depth z_g, see figure 2, equation (15) and (16) can be combined into one equation which is

$$R(z_g)e^{i\varphi(z_s,z_g)} = -\int_{-\infty}^{\infty} \gamma(z')(1-R^2(z))e^{i\varphi(z',z_s)}dz. \tag{17}$$

where we have used the same notation of "half space " for that of "whole space" without confusion.

UP AND DOWN WAVE SEPARATION

In order to get separated upgoing and downgoing waves from recorded data, we assume that all sources lies in the region $x < 0$ and that the medium is homogeneous for $x \geq 0$ (Devaney, 1986), the wave field can be expressed as a superposition of up and down plane waves

$$p(x,z,t)=\frac{1}{4\pi^2}\int_{-\infty}^{\infty}d\omega\int_{-\infty}^{\infty}dk_z[U(k_z,\omega)e^{i(k\cdot r-\omega t)}+D(k_z,\omega)e^{-i(k\cdot r+\omega t)}], \tag{18}$$

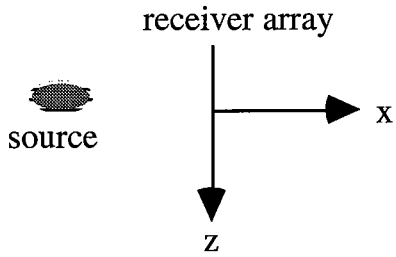

Fig. 3. Geometry of upgoing and downgoing wave separation.
The receiver array lies along the z-axis

where the wave vector $k=k_x\hat{x}+k_z\hat{z}=\sqrt{(\omega/v)^2-k_z^2}\,\hat{x}+k_z\hat{z}$. Equation (18) expressed the wave field as a spectrum of up and down plane waves in the right half space. Amplitudes of U and D components in equation (13) can be determined from the total field recorded by the array $p(x=0,z,t)$. To show this we take the Fourier transform of p in z and t at $x=0$

$$U(k_z,\omega)+D(k_z,\omega)=\int_{-\infty}^{\infty}dz\int_{-\infty}^{\infty}dtp(x=0,z,t) \tag{19}$$

Similarly, we take the Fourier transform of derivative of p in z direction:

$$ik_z[U(k_z,\omega)-D(k_z,\omega)]=\int_{-\infty}^{\infty}dz\int_{-\infty}^{\infty}dt\frac{\partial p(x=0,z,t)}{\partial z}. \tag{20}$$

From equation (19) and (20) we can solve for the spectrum U and D. The reflection function is then expressed as the ratio between the upgoing wave and downgoing wave:

$$R(z)e^{i\varphi(z)}=\frac{Ue^{ik\cdot r-i\omega t}}{De^{-ik\cdot r-i\omega t}}=\frac{U}{D}e^{2ik_z z} \tag{21}$$

REFLECTION IMAGING WITH SINGLE REFLECTION APPROXIMATION

Considering the phase factor in equation (17) consists of two parts, one is linear and the other is nonlinear, i.e.

$$\phi(z', z_s) = [\beta' + \beta''(z')]z'$$

where β' is the constant vertical wave number and $\beta''(z')$ is space variant local vertical wave number which can be considered as the cause of phase modulation in wave propagating in the medium. By neglecting $R^2(z)$ in the integrand of equation (17), i.e. only single reflection is taken into account, we have

$$\tilde{R}(\beta') = -\int_{-\infty}^{\infty} \gamma(z') e^{i[\beta' + \beta''(z')]z'} dz', \tag{22}$$

where $\tilde{R}(\beta') = R(z_g) e^{i\phi(z_s, z_g)}$. Since the wave number in equation (22) is spatially variant we call $\tilde{R}(\beta')$ the modified spectrum of $\gamma(z')$. In order to evaluate the function $\gamma(z')$ by the Fourier transform we look at the d.c. component of the spectrum

$$\tilde{R}(0) = -\int_{-\infty}^{\infty} \gamma(z') e^{i\beta''(z')z'} dz'. \tag{23}$$

If we multiply the complex conjugate of equation (23) to (22) we have

$$\tilde{R}(\beta')\tilde{R}^*(0) = -\int_{-\infty}^{\infty} \gamma(x) e^{-i\beta''(x)x} dx \int_{-\infty}^{\infty} \gamma(y) e^{i[\beta' + \beta''(y)]y} dy. \tag{24}$$

Under the condition that the $\gamma(z')$ is localized, i.e. the autocorrelation length of the γ function is small. Therefore equation (24) is reduced to

$$\tilde{R}(\beta)\tilde{R}(0) = -L\int_{-\infty}^{\infty} N(x) e^{i\beta' x} dx, \tag{25}$$

where $N(x) = \gamma(x)\gamma(x)$, and L is the length of integration. From equation (25) we can see that $\tilde{R}(k_s^{'})\tilde{R}^*(0)$ is proportional to spectrum of N(x). N(x) can be found by taking the inverse Fourier transform of $\tilde{R}(\beta')\tilde{R}^*(0)$.

VELOCITY RECOVERY FROM REFLECTION COEFFICIENTS

In the above section, we found the reflection coefficient γ which is a function both velocity and propagation angle, i.e.

$$\gamma(z) = \frac{\beta'(z)}{2\beta(z)}, \tag{26}$$

where $\beta(z) = k(z)\cos\theta(z)$. The velocity can be found by using equation (26) together with Snell's law. Integrating equation (26) over a layer, we have

$$\int_{\beta(z)}^{\beta(z+\Delta z)} \frac{d\beta}{\beta} = \int_{z}^{z+\Delta z} 2\gamma(z)dz,$$

or

$$\beta(z+\Delta z) = \beta(z)e^{2[\gamma(z+\Delta z)-\gamma(z)]}.$$

Therefore

$$v(z+\Delta z) = \frac{\cos\theta(z+\Delta z)}{\cos\theta(z)} v(z)e^{2[\gamma(z+\Delta z)-\gamma(z)]}. \tag{27}$$

Apply Snell's law

$$v(z+\Delta z) = \frac{\sin\theta(z+\Delta z)}{\sin\theta(z)} v(z) \tag{28}$$

to equation (27) we obtain the following recursive relation to recovery velocity

$$v(z+\Delta z) = v(z) / \sqrt{e^{4[\gamma(z+\Delta z)-\gamma(z)]}\cos^2\theta(z) + \sin^2\theta(z)}. \tag{29}$$

CONCLUSIONS

Directly from physical equations such as the continuity equation and Euler's equation we derived Riccati equation governing the reflection function and its integral representation for an arbitrary incident angle. With the reflection function and its integral representation to perform imaging has advantages over with wave equation. Because by using reflection function we can avoid to use the scattered field, as we did when we used the wave equation, which is difficult to obtain in practice.

ACKNOWLEDGMENT

The paper was edited by Nicholas Smalley. The author is grateful for his help.

REFERENCES

Bellman R. and Vasudevan R. Wave propagation an invariant imbedding approach, D. Reidel Publishing Company, 1986

Brekhovskikh, L. and Lysaanov Yu., 1982. Fundamentals of Ocean Acoustics, Spring-Verlag Berlin Heidelberg, New York.

Devaney A. J., Aplane-wave decomposition for elastic wave fields applied to the separation of p-waves and s-waves in vector seismic data, Geophysics, 1986

Harris J. Lecture notes on wave phenomenon, 1994

Keller J. and Papadakis S. Wave propagation and underwater acoustics, Springer-Verlag, 1977

PAPER K

CALCULATION OF DIRECT ARRIVAL TRAVELTIMES BY THE EIKONAL EQUATION

Le-Wei Mo

ABSTRACT

We present a traveltime calculation scheme based on the eikonal equation that calculates the traveltimes of direct arrivals from a point source. In typical earth models, critical refractions, diffractions and reflections are weak. Most of the energy radiated by the source is contained in the direct arrivals. Direct arrivals are thus generally the most energetic events in a time evolving wavefield. Our scheme successfully computes the traveltimes of direct arrivals and is computationally efficient. The method is presented in two dimensions.

INTRODUCTION

Wave propagation in medium, in high frequency asymptotics, can be described by the WKBJ Green function, which consists of traveltimes and amplitudes. The traveltimes satisfy the eikonal equation that relates the gradient of the traveltimes to slowness of the model. The amplitudes satisfy the transport equations. In this paper, we will address the problem of solving the eikonal equation for direct arrival traveltimes. One method of solving the eikonal equation is the method of characteristics (Cerveny et al., 1977; Zauderer, 1989). The ray equations are derived from the eikonal equation, whose solutions are raypaths or the characteristic curves of the eikonal equation. Because the raypaths are local, wave propagation along rays is thus intuitive and easy to understand. This explains why the application of ray tracing is so popular and well published. However, ray tracing has its limitations and disadvantages as pointed out by some authors (Vidale, 1988). Seismic depth migration, and many other applications require traveltimes on a uniform grid. If these traveltimes are computed by ray tracing, computation cost is immense (Zhang, 1993). We would rather solve the eikonal equation directly for traveltimes on a uniform grid.

Reshef and Kosloff (1986) first formulated finite-difference scheme to solve the eikonal equation for traveltimes on a uniform grid by extrapolating the depth gradient of traveltimes. Vidale (1988, 1990) formulated a finite-difference scheme in Cartesian coordinates that

solves the eikonal equation progressing outward from an "expanding square" for traveltimes of first arriving waves from a point source. His scheme can quickly fill in traveltimes in a uniform grid, and is by far the fastest method of computing traveltime. However, Vidale's scheme encounters stability problems, e.g., calculating the square root of a negative number. Qin et al. (1992) propose an alternate of Vidale's scheme, i.e., progressing outward from an "expanding wavefront." Qin et al.'s scheme solves some of the stability problems of Vidale's algorithm. But searching for the global minimum to start computation at each step makes their scheme very computation costly. Podvin and Lecomte (1991) dissect wave propagation in a cell into all possible modes of transmission, diffraction and head waves, resulting in a stable scheme of traveltime calculation. In their parallel implementation of traveltime calculation, each grid point of a velocity model is associated with a processor. All the processors simultaneously update the traveltimes at the associated grid point. However, traveltime calculation is a bad candidate for parallel computation. The parallel implementation does not effectively use computational power because, during the computation, most of the processors away from the wavefront perform useless operations. Van Trier and Symes (1991) and Zhang (1993) formulated traveltime calculation in polar coordinates by extrapolating the gradients of traveltimes. In their schemes, traveltime computation has the contradiction of dense sampling near the source and coarse sampling far away from the source. And mapping the slowness and traveltime fields to and from polar coordinates gives additional cost to their schemes. As a matter of fact, efficiency of a traveltime computation scheme also depends on the computer architecture. But Vidale's scheme requires the least number of algebraic operations.

The common shortcoming of the above finite-difference traveltime calculation schemes is that they all explicitly or implicitly calculate traveltime of first arriving waves, which may carry little energy and are quite weak, e.g., head waves and diffractions. In this paper, we propose a traveltime calculation scheme that aims at calculating the traveltimes of direct arrivals from a point source. In typical earth models, diffraction and reflection effects are weak. Most of the energy radiated by the source is contained in the direct arrivals. Direct arrivals are thus generally the most energetic events in a time evolving wavefield. First, we analyze why we prefer direct arrival traveltimes to first arriving traveltimes in tomography and migration imaging. Then we present our scheme of calculating direct arrival traveltimes. Finally, we show several numerical examples of calculating direct arrival traveltimes. Our scheme successfully computes the traveltimes of direct arrivals and is computationally efficient. The method is presented in two dimensions.

WHY DIRECT ARRIVAL TRAVELTIMES

Figure 1(b) shows the snapshot wavefield at 0.16 seconds of a two layer velocity model of Figure 1(a). The wavefield is simulated by the finite-difference solution to the scalar wave equation. The source is at the upper left corner. The source wavelet is the first derivative of the Gaussian function. For this model, head wave is generated and part of its travel path is the boundary separating the slow and the fast medium. The head wave is a boundary wave, and carries very little energy. Figure 1(c) is the common shot gather or history wavefield of receivers at the right edge of Figure 1(b). From Figure 1(b) and (c), we see that the first arrival - head wave, travels ahead of the direct arrival and is much weaker than the direct arrival. If the traveltimes of the head wave in the slow medium were used for transmission traveltime tomography, the slow velocity medium would be inverted as an erroneous high velocity medium. And reflections that are used by migration to image velocity discontinuities are not generated by the first arrival head wave. Thus traveltimes of the first arrival - head wave, are not suited for transmission traveltime tomography and migration imaging. Instead, traveltimes of direct arrivals should be used. Overlay on Figure 1(b) and (c) are the direct arrival traveltimes computed by our finite-difference scheme of solving the eikonal equation. The direct arrival traveltimes closely match the first breaks of the direct arrivals computed by finite-difference wave equation modeling.

RAY TRACING

Figure 2 is a two layer velocity model. The lower medium has higher velocity. By ray tracing, the incidence ray at point *C* is in critical incidence and generates a creeping ray along the boundary. The incidence rays to the left of point *C*, e.g., at point *A*, are in pre-critical incidence and generate refracted waves in the lower medium. The incidence rays to the right of point *C*, e.g., at point *B*, are in post-critical incidence, and total reflection occurs. For post-critical incidence rays, the symptoms are the sine of the refraction angle is greater than *1* and the incidence wavefront in the slow medium and the creeping wavefront in the fast medium are discontinuous across the interface. Transmission ray tracing can be performed for pre-critical incidence rays to the left of point *C*. However, transmission ray tracing can not be performed for post-critical incidence rays to the right of point *C*. That is, transmission ray tracing is performed only until total reflection occurs, or until the sine of the refraction angle is greater than *1*.

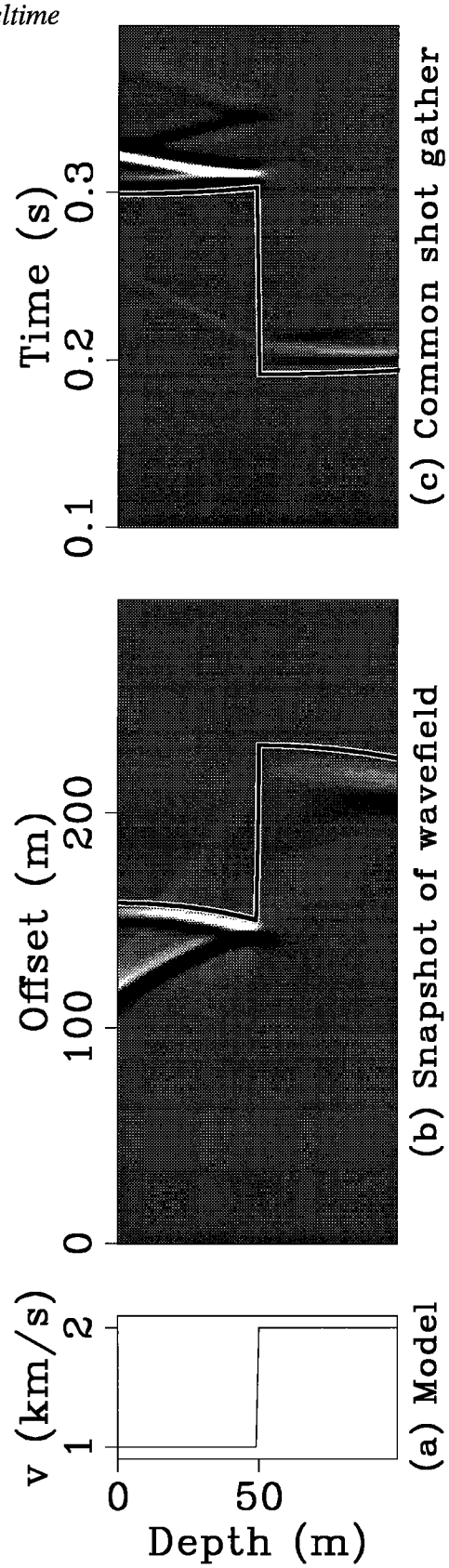

Figure 1: (a) is the velocity. In (b), source is at the upper left corner. (c) is the common shot gather with receivers at the right edge (b).

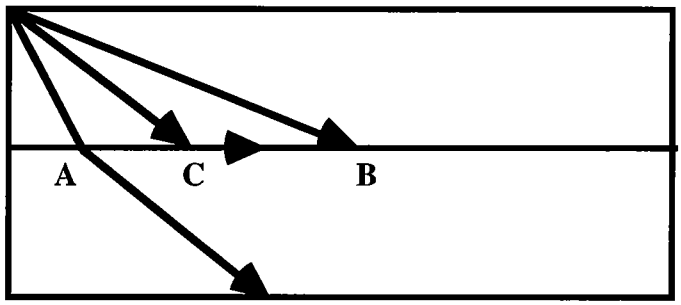

Figure 2: Incidence ray at point *C* is in critical incidence. Incidence ray at *A* (*B*) is in pre-critical (post-critical) incidence.

SOLVING THE EIKONAL EQUATION

In a two dimensional medium, the traveltime of wave propagation is governed by the eikonal equation, which relates the gradient of traveltimes to the slowness of the medium,

$$\left(\frac{\partial t}{\partial x}\right)^2 + \left(\frac{\partial t}{\partial z}\right)^2 = s^2(x,z) \tag{1}$$

where *(x,z)* is spatial coordinate, *t* is traveltime, *s(x,z)* is slowness. We parameterize the medium by square cells, with mesh spacing *h*, Figure 3. In a localized cell of Figure 3, when traveltimes at three corners *a*, *b* and *c* are known, the traveltime at the fourth corner --- *d* can be found by finite-difference method based on the assumption of local plane wave. We use the centered finite-difference (Vidale, 1988) to approximate the two differential terms in equation (1)

$$\frac{\partial t}{\partial x} = \frac{1}{2h}\left(t_b + t_d - t_a - t_c\right) \tag{2}$$

and

$$\frac{\partial t}{\partial z} = \frac{1}{2h}\left(t_c + t_d - t_a - t_b\right) \tag{3}$$

Substituting equations (2) and (3) into equation (1) gives

$$t_d = t_a + \sqrt{2(hs)^2 - (t_b - t_c)^2} \tag{4}$$

where h is mesh spacing, s is the slowness inside the cell with the grid indexes of corner d, t_a, t_b, t_c and t_d are the traveltimes at the corners a, b, c and d. Finite-differences in equations (2) and (3) have second order of numerical accuracy.

Equation (4) can only be used for traveltime calculation at pre-critical incidence. At post-critical incidence, the problem is to compute the square root of a negative number. But setting the negative number inside the square root to zero (Vidale, 1988, 1990) does not conform to physics. When geometrical ray theory is valid and the wavefronts are continuous across an interface, the time difference between diagonal nodes of a square cell is at most $\sqrt{2}hs$, where h is the mesh spacing of the cell and s is the slowness inside the cell. Thus there are three equivalent symptoms of post-critical incidence, the sine of the refraction angle being greater than *1*, wavefronts being discontinuous across an interface and the time difference between diagonal nodes of a square cell being greater than $\sqrt{2}hs$. Thus in solving the eikonal equation, the term inside the square root of equation (4) is negative at post-critical incidence. If corners a and b lie in a horizontal direction and wave travels from a to b, then corners a and b are in the slow velocity medium, and corners c and d are in the high velocity medium. In geometric ray theory, the direct arrival to corner d is a creeping ray from corner c to corner d. The traveltime at corner d is then computed as

$$t_d = t_c + hs \tag{5}$$

If corners a and b lie in a vertical direction and wave travels from a to b, the direct arrival to corner d is a creeping ray from corner b to corner d. The traveltime at corner d is then computed as

$$t_d = t_b + hs \tag{6}$$

We have described the traveltime computation at a localized cell. Next, we describe the arrangement of computation patterns.

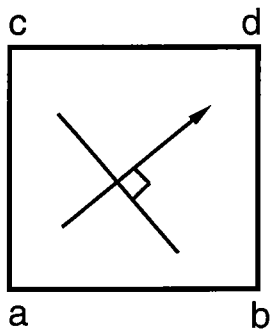

Figure 3: In a square cell with constant slowness *s*, wave propagates from corner *a* to corner *d* through corners *b* and *c*. *Traveltime* is larger at corner *b* than at corner *a*.

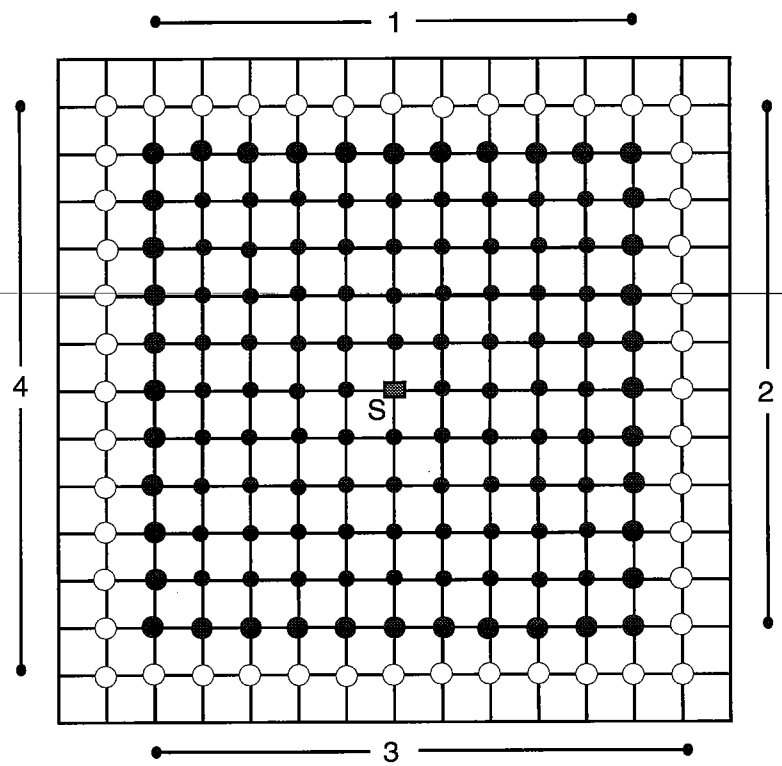

Figure 4: **S** is the source grid point. Traveltime computations proceed sequentially on the four sides.

Computation pattern

Traveltime computation is initialized by assuming straight ray paths in a constant velocity square surrounding the source point. We found the radius of $5h$ to be a generally good choice for the initialization square. Traveltime computations are then carried out by expanding squares around the source point, as the computation layout in Figure 4. The filled circles indicate grid points that have had their traveltimes calculated. We are to use the traveltimes at the boundary ring of grid points, large filled circles, to compute traveltimes of grid points at an outer ring, the hollow circles. The inductive scheme for calculating a new ring of traveltimes is now described. Computations proceed sequentially on the four sides, as shown in Figure 4. To initialize computation at a side, the points in the inner side are examined in a loop from one end to the other to locate the point with local minimum traveltime. Using one-sided finite-difference stencil, the traveltime of the point outside the point with local minimum traveltime is computed as

$$t_c = t_a + \sqrt{(hs)^2 - (t_b - t_a)^2} \tag{7}$$

where t_C is the time to be found, t_a is the local minimum traveltime in the inside row, t_b is the traveltime of the neighboring grid point at the source side, s is the slowness at point c. However, if the term inside the square root of equation (7) is negative, the traveltime at point c is computed as

$$t_c = t_a + hs \tag{8}$$

At the next stage, equation (4) is applied to compute traveltimes.

In application of equation (4), the propagation direction of local plane wave does not come in play. The traveltimes at the three corners a, b and d can also be used to compute the traveltime at corner c because of the assumption of local plane wave. Equations (5) and (6) are then changed by computing the right hand side unknown traveltime from the left hand side known traveltime. However, it is easy to program calculation from small traveltimes to large traveltimes, i.e., in a upwind format.

Consider calculating traveltimes at side *1* (top) of Figure 4. Application of equation (4) is carried out in three loops. The first loop progresses from the left end to the lateral

location of the source. Then the second loop progresses from the right end to the left end. Finally the third loop progresses from the lateral location of the source to the right end. During each loop, calculation starts at each local minimum traveltime point and progresses until a local maximum traveltime point is reached. Similar traveltime calculations are carried out sequentially for the other three sides.

EXAMPLE

Figure 5(a) is a more complicated 1-D velocity model. Figure 5(b) shows the traveltime contours of direct arrivals with the source at the upper left corner. All the possible direct arrivals in 1-D medium are correctly modeled. It has transmission from high velocity medium to low velocity medium, transmission and creeping boundary wave from low velocity medium to high velocity medium, and overturning waves in medium with linear increasing velocities.

A POSTERIORI RAY TRACING

After traveltimes are found for all the grid points, raypath from any receiver grid point back to the source can be traced by following the steepest descent direction through the traveltime field. The raypath is guaranteed to end at the source point as the source point has the smallest traveltime. Figure 6 shows the ray paths traced from the right edge of the model back to the source using the traveltime map of Figure 5(b).

DISCUSSIONS

In this traveltime calculation scheme, the velocity model is parameterized as constant velocity cells. For one-dimensional velocity medium, it is perfect. For two-dimensional velocity medium, dipping interfaces are represented by stairways.

As seen in Figure 1, the calculated direct arrival traveltimes closely overlay the waveforms of wave equation modeling. We are confident that the direct arrival traveltimes calculated by our scheme are accurate up to the spatial and temporal sampling requirements.

The computational cost of this scheme at each grid point is to evaluate equation (7). For a model of realistic size, say 250,000 grid points, computational time is just a few seconds at a present workstation with computation speed of Mflops/s. Also traveltime computations are carried out in a few well defined loops as explained in the section of computation pattern, this traveltime computation scheme can easily put into a vector computer.

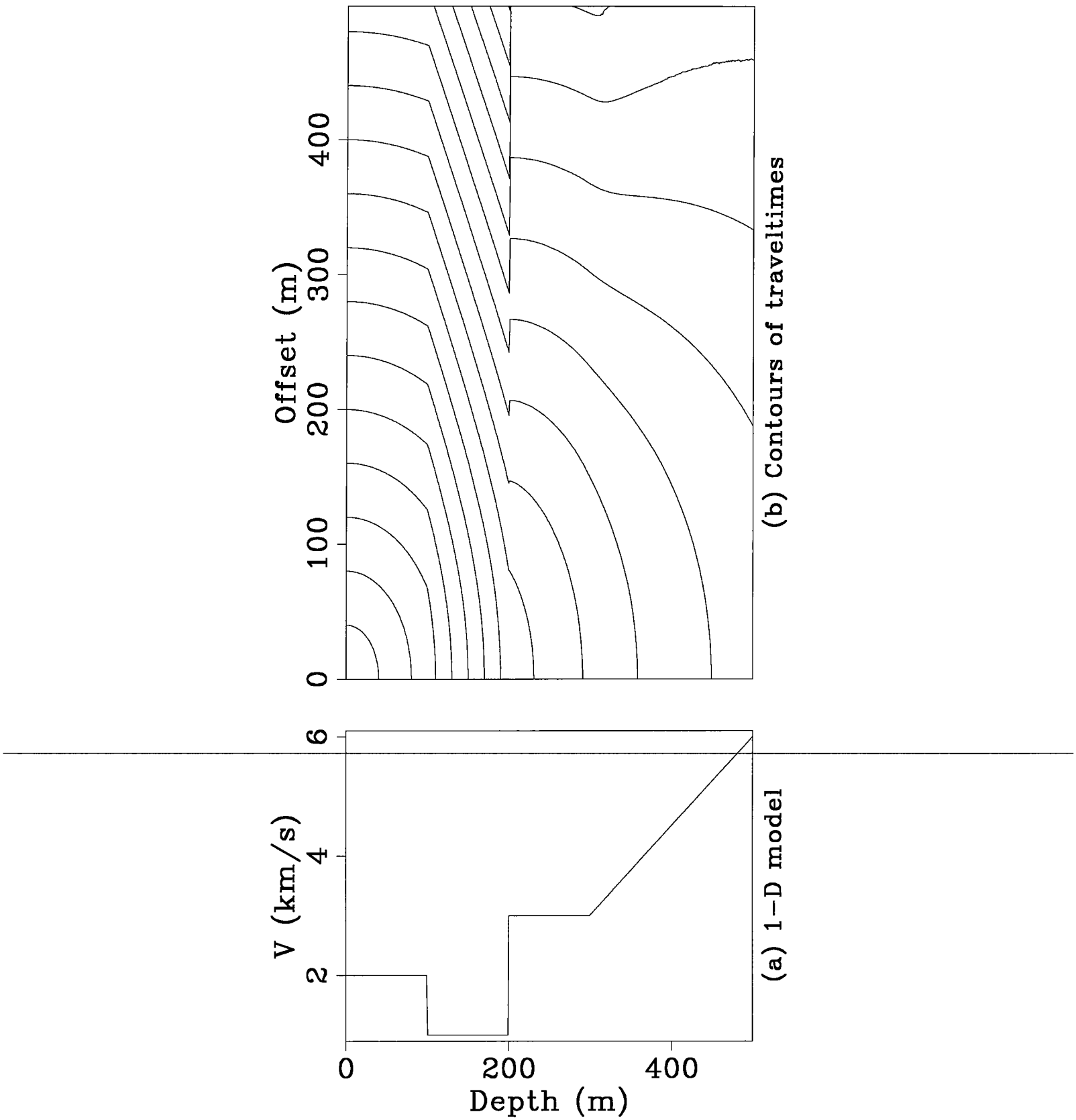

Figure 5: (a) is velocity model. (b) is the contours of direct arrival traveltimes.

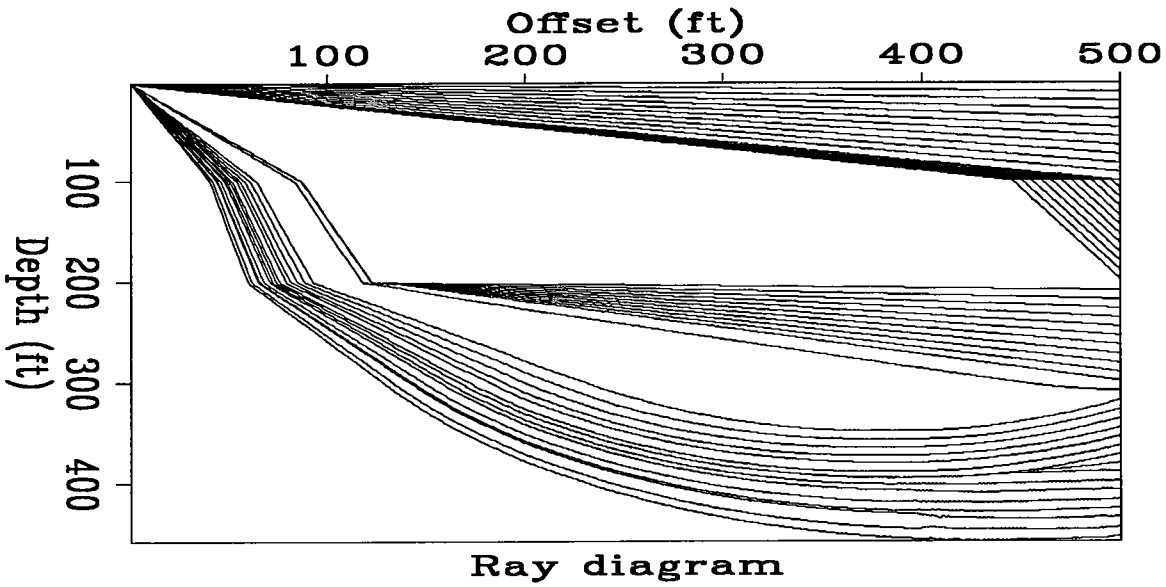

Figure 6: Raypaths from the right edge back to the source using the traveltime map of Figure 5(b).

CONCLUSIONS

Our new scheme of finite-difference solving the eikonal equation successfully computes the traveltimes of direct arriving waves. The accuracy in computed traveltimes is good up to the spatial and temporal sampling requirements. Direct arrivals are usually the most energetic event in a time evolving wavefield. Traveltimes of direct arrivals will be very useful in both transmission traveltime tomography and migration imaging.

REFERENCES

Cerveny, V., Molotkov, I. A., and Psencik, I., 1977, Ray method in seismology: Karlova Univerzita, Prague.

Podvin, P., and Lecomte, I., 1991, Finite difference computation of traveltimes in very contrasted velocity models: a massively parallel approach and its associated tools: Geophys. J. Int., **105**, 271–284.

Qin, F., Luo, Y., Oslen, K. B., Cai, W., and Schuster, G. T., 1992, Finite-difference solution of the eikonal equation along expanding wavefronts: Geophysics, **57**, 478–487.

Reshef, M., and Kosloff, D., 1986, Migration of common-shot gathers: Geophysics, **51**, 324–331.

Van Trier, J., and Symes, W. W., 1991, Upwind finite-difference calculation of traveltimes: Geophysics, **56**, 812–821.

Vidale, J., 1988, Finite-difference calculation of travel times: Bull. Seism. Soc. Am., **78**, no. 6, 2062–2076.

Vidale, J., 1990, Finite-difference calculation of travel times in 3-D: Geophysics, **55,** 521–526.

Zauderer, R., 1989, Partial Differential Equations of Applied Mathematics: John Wiley and Sons.

Zhang, L., 1993, Imaging by the wavefront propagation method: Ph.D. thesis, Stanford University.

PAPER L

SEISMOGRAM SYNTHESIS FOR RADIALLY MULTI-LAYERED MEDIA USING THE GENERALIZED R/T COEFFICIENTS METHOD

Youli Quan

ABSTRACT

A new method based on generalized reflection and transmission coefficients is proposed to calculate the waves in radially multi-layered media. The method is used to simulate full waveform sonic logs in cemented and cased boreholes and crosswell seismic profiles in situations where we need to consider borehole effects. Our formulations are renormalized; therefore, they are more stable and efficient than previous methods for numerical computation. The new formulations are tested by comparing our numerical results with available previous work, showing excellent agreement.

INTRODUCTION

Sonic logging in cased boreholes is useful for evaluating the quality of the cement job. Also, effort is being made to measure the formation properties from full waveform sonic logs run in cased boreholes. A cased borehole and any near borehole alteration can be modeled as a radially layered medium. Study of waves in a radially layered medium is useful for understanding and interpreting full waveform sonic logs. Tubman et al. (1984) used the Thomson-Haskell method for modeling the cased borehole. We propose a new approach using generalized reflection and transmission (R/T) coefficients to solve this problem. The generalized R/T coefficients method is widely used in modeling the elastic waves in vertically layered media because of its computational stability and efficiency over the Thomson-Haskell method, especially for high frequency problems (see, e.g., Luco & Apsel, 1983; Kennett, 1983; Chen, 1993). Yao & Zheng (1985) derived a set of formulas for computing synthetic seismograms in radially layered borehole environments using the generalized R/T coefficient method, but they did not conduct numerical tests to check their

---

This paper is a joint work with Xiaofei Chen of Department of Earth Sciences, USC

formulation. We derive a set of alternative formulations which are more stable and efficient than the previous methods for numerical computation. First, We introduce the concepts of modified and generalized reflection and transmission (R/T) matrices for the radially layered media and derive a recursive scheme to calculate them. Then, we determine the wave fields using the R/T matrices. To check the formulation, we compare our calculated results with those of Cheng and Toksoz (1981) for a two-layer open borehole model, of Tubman (1984) for a four-layer cased hole model. The comparison shows a good agreement. Quan et al. (1994) used this method to investigate acoustic attenuation logging and geometrical spreading of the P head wave in boreholes with mudcake and invaded zone.

GOVERNING EQUATIONS AND THEIR GENERAL SOLUTIONS

The radially multi-layered model considered in this study is shown in Figure 1. The first layer ($r < r^{(1)}$) is fluid. For this axially symmetrical problem, there only exist *P* and *SV* waves, i.e., the displacement can be written as

$$\mathbf{u} = \nabla\phi + \nabla \times (\mathbf{e}_\theta \psi). \tag{1}$$

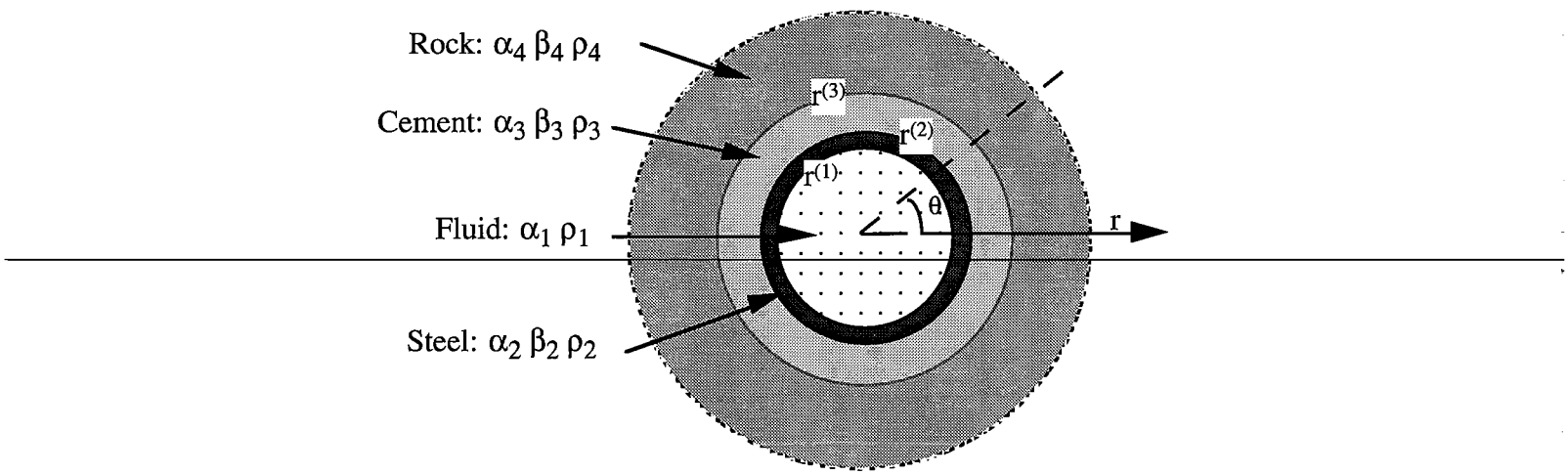

Figure 1. A radially multi-layered model.

Substituting Eqn (1) into the elastodynamic equation in the frequency domain we obtain

$$\frac{\partial^2\phi^{(j)}}{\partial r^2} + \frac{1}{r}\frac{\partial\,\phi^{(j)}}{\partial r} + \frac{\partial^2\phi^{(j)}}{\partial z^2} + k_\alpha^{(j)2}\phi^{(j)} = F(\omega)\frac{\delta(r)\delta(z)}{2\pi r}\delta_{j1}, \tag{2a}$$

$$\frac{\partial^2\psi^{(j)}}{\partial r^2}+\frac{1}{r}\frac{\partial\psi^{(j)}}{\partial r}-\frac{\psi^{(j)}}{r^2}+\frac{\partial^2\psi^{(j)}}{\partial z^2}+k_\beta^{(j)2}\psi^{(j)}=0, \tag{2b}$$

for $r^{(j-1)}<r<r^{(j)}$, $j=1,2,...,N$, (define $r^{(0)}=0$). In Equation (1), $k_\alpha^{(j)}=\omega/\alpha^{(j)}$, $k_\beta^{(j)}=\omega/\beta^{(j)}$, $F(\omega)$ is the source spectrum, α and β are *P*-wave and S-wave velocities, respectively. In the $k-\omega$ domain, the solutions of Eqns (2a) and (2b) are

$$\tilde{\phi}_k^{(j)}(r)=c_{p_-}^{(j)}e^{iv_\alpha^{(j)}(r^{(j)}-r)}\overline{H}_o^{(2)}(v_\alpha^{(j)}r)+c_{p_+}^{(j)}e^{iv_\alpha^{(j)}(r-r^{(j-1)})}\overline{H}_o^{(1)}(v_\alpha^{(j)}r), \tag{3}$$

$$\tilde{\psi}_k^{(j)}(r)=c_{s_-}^{(j)}e^{iv_\beta^{(j)}(r^{(j)}-r)}\overline{H}_1^{(2)}(v_\beta^{(j)}r)+c_{s_+}^{(j)}e^{iv_\beta^{(j)}(r-r^{(j-1)})}\overline{H}_1^{(1)}(v_\beta^{(j)}r), \tag{4}$$

where $v_\alpha^{(j)}=\sqrt{k_\alpha^{(j)2}-k^2}$, $\mathrm{Im}\{v_\alpha^{(j)}\}>0$, $v_\beta^{(j)}=\sqrt{(k_\beta^{(j)})^2-k^2}$, $\mathrm{Im}\{v_\beta^{(j)}\}>0$, and j =2,3, ..., N, N+1. $\overline{H}_n^{(1)}(x)=e^{-ix}H_n^{(1)}(x)$ and $\overline{H}_n^{(2)}(x)=e^{ix}H_n^{(2)}(x)$ are the first and second kind *renormalized* Hankel functions of n^{th} order, respectively. $c_{p_-}^{(j)}, c_{p_+}^{(j)}, c_{s_-}^{(j)}$ and $c_{s_+}^{(j)}$ are unknowns, where "+" refers to outgoing waves and "-" refers to incoming waves. Instead of the usual Hankel functions, we used the renormalized Hankel functions whose asymptotic behavior for *large argument* is very gentle for expressing our solutions. For j = 1, in the fluid-filled borehole, we have

$$\begin{aligned}\tilde{\phi}_k^{(1)}(r)&=cJ_o(v_\alpha^{(1)}r)-\frac{i}{8\pi}F(\omega)H_o^{(1)}(v_\alpha^{(1)}r)\\&=c_-^{(1)}e^{iv_\alpha^{(1)}(r^{(1)}-r)}\overline{H}_o^{(2)}(v_\alpha^{(1)}r)+(c_+^{(1)}+s_+)e^{iv_\alpha^{(1)}r}\overline{H}_o^{(1)}(v_\alpha^{(1)}r)\end{aligned} \tag{5}$$

where

$$c_+^{(1)}=c_-^{(1)}e^{iv_\alpha^{(1)}r^{(1)}} \quad \text{and} \quad s_+=-\frac{i}{8\pi}F(\omega). \tag{6}$$

Using above potential solutions we obtain the displacements and stresses in the cylindrical layers (j > 1) as

$$\begin{bmatrix}\tilde{u}_k^{(j)}(r)\\ \tilde{v}_k^{(j)}(r)\\ \tilde{\sigma}_k^{(j)}(r)\\ \tilde{\tau}_k^{(j)}(r)\end{bmatrix}=\begin{bmatrix}e_{11}^{(j)}(r) & e_{12}^{(j)}(r) & e_{13}^{(j)}(r) & e_{14}^{(j)}(r)\\ e_{21}^{(j)}(r) & e_{22}^{(j)}(r) & e_{23}^{(j)}(r) & e_{24}^{(j)}(r)\\ e_{31}^{(j)}(r) & e_{32}^{(j)}(r) & e_{33}^{(j)}(r) & e_{34}^{(j)}(r)\\ e_{41}^{(j)}(r) & e_{42}^{(j)}(r) & e_{43}^{(j)}(r) & e_{44}^{(j)}(r)\end{bmatrix}\begin{bmatrix}c_{p_-}^{(j)}\\ c_{s_-}^{(j)}\\ c_{p_+}^{(j)}\\ c_{s_+}^{(j)}\end{bmatrix}, \tag{7}$$

where

$$e_{11}^{(j)} = -\nu_\alpha^{(j)} \overline{H}_1^{(2)}(\nu_\alpha^{(j)} r) e^{i\nu_\alpha^{(j)}(r^{(j)}-r)}, \qquad e_{12}^{(j)} = -ik\overline{H}_1^{(2)}(\nu_\beta^{(j)} r) e^{i\nu_\beta^{(j)}(r^{(j)}-r)},$$

$$e_{13}^{(j)} = -\nu_\alpha^{(j)} \overline{H}_1^{(1)}(\nu_\alpha^{(j)} r) e^{i\nu_\alpha^{(j)}(r-r^{(j-1)})}, \qquad e_{14}^{(j)} = -ik\overline{H}_1^{(1)}(\nu_\beta^{(j)} r) e^{i\nu_\beta^{(j)}(r-r^{(j-1)})},$$

$$e_{21}^{(j)} = ik\overline{H}_o^{(2)}(\nu_\alpha^{(j)} r) e^{i\nu_\alpha^{(j)}(r^{(j)}-r)}, \qquad e_{22}^{(j)} = \nu_\beta^{(j)} \overline{H}_o^{(2)}(\nu_\beta^{(j)} r) e^{i\nu_\beta^{(j)}(r^{(j)}-r)},$$

$$e_{23}^{(j)} = ik\overline{H}_o^{(1)}(\nu_\alpha^{(j)} r) e^{i\nu_\alpha^{(j)}(r-r^{(j-1)})}, \qquad e_{24}^{(j)} = \nu_\beta^{(j)} \overline{H}_o^{(1)}(\nu_\beta^{(j)} r) e^{i\nu_\beta^{(j)}(r-r^{(j-1)})},$$

$$e_{31}^{(j)} = 2\mu^{(j)}[\Omega^{(j)} \overline{H}_o^{(2)}(\nu_\alpha^{(j)} r) + \nu_\alpha^{(j)} \overline{H}_1^{(2)}(\nu_\alpha^{(j)} r)/r] e^{i\nu_\alpha^{(j)}(r^{(j)}-r)},$$

$$e_{32}^{(j)} = -ik\mu^{(j)} \nu_\beta^{(j)}[\overline{H}_o^{(2)}(\nu_\beta^{(j)} r) - \overline{H}_2^{(2)}(\nu_\beta^{(j)} r)] e^{i\nu_\beta^{(j)}(r^{(j)}-r)},$$

$$e_{33}^{(j)} = 2\mu^{(j)}[\Omega^{(j)} \overline{H}_o^{(1)}(\nu_\alpha^{(j)} r) + \nu_\alpha^{(j)} \overline{H}_1^{(1)}(\nu_\alpha^{(j)} r)/r] e^{i\nu_\alpha^{(j)}(r-r^{(j-1)})},$$

$$e_{34}^{(j)} = -ik\mu^{(j)} \nu_\beta^{(j)}[\overline{H}_o^{(1)}(\nu_\beta^{(j)} r) - \overline{H}_2^{(1)}(\nu_\beta^{(j)} r)] e^{i\nu_\beta^{(j)}(r-r^{(j-1)})},$$

$$e_{41}^{(j)} = -2ik\mu^{(j)} \nu_\alpha^{(j)} \overline{H}_1^{(2)}(\nu_\alpha^{(j)} r) e^{i\nu_\alpha^{(j)}(r^{(j)}-r)},$$

$$e_{42}^{(j)} = 2\mu^{(j)} \Omega^{(j)} \overline{H}_1^{(2)}(\nu_\beta^{(j)} r) e^{i\nu_\beta^{(j)}(r^{(j)}-r)},$$

$$e_{43}^{(j)} = -2ik\mu^{(j)} \nu_\alpha^{(j)} \overline{H}_1^{(1)}(\nu_\alpha^{(j)} r) e^{i\nu_\alpha^{(j)}(r-r^{(j-1)})},$$

$$e_{44}^{(j)} = 2\mu^{(j)} \Omega^{(j)} \overline{H}_1^{(1)}(\nu_\beta^{(j)} r) e^{i\nu_\beta^{(j)}(r-r^{(j-1)})},$$

---

and, $\Omega^{(j)} = k^2 - \frac{1}{2} k_\beta^{(j)2}$ and $r^{(j-1)} < r < r^{(j)}$. For the first layer, i.e., the liquid layer, we have

$$\begin{bmatrix} \tilde{u}_k^{(1)}(r) \\ \tilde{\sigma}_k^{(1)}(r) \end{bmatrix} = \begin{bmatrix} e_{11}^{(1)}(r) & e_{12}^{(1)}(r) \\ e_{21}^{(1)}(r) & e_{22}^{(1)}(r) \end{bmatrix} \begin{bmatrix} c_{p-}^{(1)} \\ c_{p+}^{(1)} \end{bmatrix}, \tag{8}$$

where

$$e_{11}^{(1)} = -\nu_\alpha^{(1)} \overline{H}_1^{(2)}(\nu_\alpha^{(1)} r) e^{i\nu_\alpha^{(1)}(r^{(1)}-r)}, \qquad e_{12}^{(1)} = -\nu_\alpha^{(1)} \overline{H}_1^{(1)}(\nu_\alpha^{(1)} r) e^{i\nu_\alpha^{(1)} r},$$

$$e_{21}^{(1)} = -\lambda^{(1)} k_\alpha^{(1)2} \overline{H}_0^{(2)}(\nu_\alpha^{(1)} r) e^{i\nu_\alpha^{(1)}(r^{(1)}-r)}, \qquad e_{22}^{(1)} = -\lambda^{(1)} k_\alpha^{(1)2} \overline{H}_0^{(1)}(\nu_\alpha^{(1)} r) e^{i\nu_\alpha^{(1)} r}$$

and $c_{p-}^{(1)} = c_-^{(1)}$, $c_{p+}^{(1)} = c_+^{(1)} + s_+$.

R/T MATRICES AND SOLUTION SYNTHESIS

In the preceding section, we obtained the general solutions with unknowns, $c_{p_-}^{(j)}, c_{p_+}^{(j)}, c_{s_-}^{(j)}$ and $c_{s_+}^{(j)}$ for j = 2, 3, ..., N+1, and $c_{-}^{(1)}$. These unknowns can be determined by imposing boundary conditions at each interface. For the first interface (liquid-solid boundary), the boundary conditions are

$$\begin{bmatrix} \tilde{u}_k^{(1)}(r^{(1)}) \\ \tilde{\sigma}_k^{(1)}(r^{(1)}) \end{bmatrix} = \begin{bmatrix} \tilde{u}_k^{(2)}(r^{(1)}) \\ \tilde{\sigma}_k^{(2)}(r^{(1)}) \end{bmatrix} \tag{9}$$

and

$$0 = \tilde{\tau}_k^{(2)}(r^{(1)}). \tag{10}$$

For the j^{th} interface (j = 2, 3,..., N) which is solid-solid boundary, we have

$$\begin{bmatrix} \tilde{u}_k^{(j)}(r^{(j)}) \\ \tilde{v}_k^{(j)}(r^{(j)}) \\ \tilde{\sigma}_k^{(j)}(r^{(j)}) \\ \tilde{\tau}_k^{(j)}(r^{(j)}) \end{bmatrix} = \begin{bmatrix} \tilde{u}_k^{(j+1)}(r^{(j)}) \\ \tilde{v}_k^{(j+1)}(r^{(j)}) \\ \tilde{\sigma}_k^{(j+1)}(r^{(j)}) \\ \tilde{\tau}_k^{(j+1)}(r^{(j)}) \end{bmatrix}. \tag{11}$$

To effectively determine the unknowns for each layer, we introduce the generalized reflection and transmission (R/T) matrices and derive their explicit expressions by using the above boundary conditions.

Modified R/T matrices

The modified R/T matrices for solid-solid interfaces are defined in the relations

$$\begin{aligned} \mathbf{c}_-^{(j)} &= \mathbf{R}_{+-}^{(j)}(\mathbf{c}_+^{(j)} + \delta_{1j}s_+) + \mathbf{T}_-^{(j)}\mathbf{c}_-^{(j+1)} \\ \mathbf{c}_+^{(j+1)} &= \mathbf{T}_+^{(j)}(\mathbf{c}_+^{(j)} + \delta_{1j}s_+) + \mathbf{R}_{-+}^{(j)}\mathbf{c}_-^{(j+1)}, \end{aligned} \quad \text{for } j=1, 2, ..., N, \tag{12}$$

where $\mathbf{c}_{\pm}^{(j)} = [c_{p\pm}^{(j)}, c_{s\pm}^{(j)}]^{\mathrm{T}}$ and $\mathbf{R}_{+-}^{(j)}$, $\mathbf{R}_{-+}^{(j)}$, $\mathbf{T}_{+}^{(j)}$ and $\mathbf{T}_{-}^{(j)}$ are the modified R/T matrices for the j-th interface. Substituting Eqn (7) into Eqn (11), then comparing with Eqn (12) we obtain

$$\begin{bmatrix} \mathbf{R}_{+-}^{(j)} & \mathbf{T}_{-}^{(j)} \\ \mathbf{T}_{+}^{(j)} & \mathbf{R}_{-+}^{(j)} \end{bmatrix} = \begin{bmatrix} e_{11}^{(j)}(r^{(j)}) & e_{12}^{(j)}(r^{(j)}) & -e_{13}^{(j+1)}(r^{(j)}) & -e_{14}^{(j+1)}(r^{(j)}) \\ e_{21}^{(j)}(r^{(j)}) & e_{22}^{(j)}(r^{(j)}) & -e_{23}^{(j+1)}(r^{(j)}) & -e_{24}^{(j+1)}(r^{(j)}) \\ e_{31}^{(j)}(r^{(j)}) & e_{32}^{(j)}(r^{(j)}) & -e_{33}^{(j+1)}(r^{(j)}) & -e_{34}^{(j+1)}(r^{(j)}) \\ e_{41}^{(j)}(r^{(j)}) & e_{42}^{(j)}(r^{(j)}) & -e_{43}^{(j+1)}(r^{(j)}) & -e_{44}^{(j+1)}(r^{(j)}) \end{bmatrix}^{-1}$$
$$\times \begin{bmatrix} -e_{13}^{(j)}(r^{(j)}) & -e_{14}^{(j)}(r^{(j)}) & e_{11}^{(j+1)}(r^{(j)}) & e_{12}^{(j+1)}(r^{(j)}) \\ -e_{23}^{(j)}(r^{(j)}) & -e_{24}^{(j)}(r^{(j)}) & e_{21}^{(j+1)}(r^{(j)}) & e_{22}^{(j+1)}(r^{(j)}) \\ -e_{33}^{(j)}(r^{(j)}) & -e_{34}^{(j)}(r^{(j)}) & e_{31}^{(j+1)}(r^{(j)}) & e_{32}^{(j+1)}(r^{(j)}) \\ -e_{43}^{(j)}(r^{(j)}) & -e_{44}^{(j)}(r^{(j)}) & e_{41}^{(j+1)}(r^{(j)}) & e_{42}^{(j+1)}(r^{(j)}) \end{bmatrix}, \tag{13}$$

for $j = 2, 3,..., N$. Similarly, from Eqns (8), (9) and (10), we find

$$\begin{bmatrix} \mathbf{R}_{+-}^{(1)} & \mathbf{T}_{-}^{(1)} \\ \mathbf{T}_{+}^{(1)} & \mathbf{R}_{-+}^{(1)} \end{bmatrix} = \begin{bmatrix} e_{11}^{(1)}(r^{(1)}) & -e_{13}^{(2)}(r^{(1)}) & -e_{14}^{(2)}(r^{(1)}) \\ e_{21}^{(1)}(r^{(1)}) & -e_{33}^{(2)}(r^{(1)}) & -e_{34}^{(2)}(r^{(1)}) \\ 0 & -e_{43}^{(2)}(r^{(1)}) & -e_{44}^{(2)}(r^{(1)}) \end{bmatrix}^{-1}$$
$$\times \begin{bmatrix} -e_{12}^{(1)}(r^{(1)}) & e_{11}^{(2)}(r^{(1)}) & e_{12}^{(2)}(r^{(1)}) \\ -e_{22}^{(1)}(r^{(1)}) & e_{31}^{(2)}(r^{(1)}) & e_{32}^{(2)}(r^{(1)}) \\ 0 & e_{41}^{(2)}(r^{(1)}) & e_{42}^{(2)}(r^{(1)}) \end{bmatrix}. \tag{14}$$

Generalized R/T matrices

The generalized R/T matrices, $\hat{\mathbf{R}}_{+-}^{(j)}$ and $\hat{\mathbf{T}}_{+}^{(j)}$, are defined via following relations:

$$\begin{cases} \mathbf{c}_{+}^{(j+1)} = \hat{\mathbf{T}}_{+}^{(j)}(\mathbf{c}_{+}^{(j)} + \delta_{j1}\mathbf{s}_{+}) \\ \mathbf{c}_{-}^{(j)} = \hat{\mathbf{R}}_{+-}^{(j)}(\mathbf{c}_{+}^{(j)} + \delta_{j1}\mathbf{s}_{+}) \end{cases} \quad \text{for } j = 1,2,.....,N. \tag{15}$$

Substituting Eqn (16) into Eqns (12) and (13) and rearranging them, we obtain a recursive relation

$$\begin{cases} \hat{\mathbf{T}}_{+}^{(j)} = [\mathbf{I} - \mathbf{R}_{-+}^{(j)}\hat{\mathbf{R}}_{+-}^{(j+1)}]^{-1}\mathbf{T}_{+}^{(j)} \\ \hat{\mathbf{R}}_{+-}^{(j)} = \mathbf{R}_{+-}^{(j)} + \mathbf{T}_{-}^{(j)}\hat{\mathbf{R}}_{+-}^{(j+1)}\hat{\mathbf{T}}_{+}^{(j)} \end{cases} \quad \text{for } j = \text{N, N-1, ..., 2,1,} \tag{16}$$

where $\mathbf{I}$ is the unit matrix. Eqn (16) provides an efficient recursive scheme to calculate the generalized R/T matrices from the modified R/T matrices. Our formulations are numerically more stable than the previous methods (e.g., Tubman et al, 1984 and Yao & Zheng, 1985)

because of the use of the renormalized Hankel functions and the renormalization factors $e^{iv_{\alpha,\beta}^{(j)}r^{(j)}}$ and $e^{-iv_{\alpha,\beta}^{(j)}r^{(j-1)}}$.

Solution synthesis

Having the generalized R/T matrices, we can compute the unknowns $\mathbf{c}_{\pm}^{(j)}$ for any layer. Thus, we can compute the displacements and stresses for any layer. In a sonic logging problem, we are interested in the stress waves in the fluid-filled borehole where the normal stress is

$$\begin{aligned}\tilde{\sigma}_k^{(1)}(r) &= e_{21}^{(1)}(r)c_-^{(1)} + e_{22}^{(1)}(r)(c_+^{(1)} + s_+) \\ &= \lambda^{(1)}k_\alpha^{(1)2}\left[\frac{2J_o(v_\alpha^{(1)}r)e^{iv_\alpha^{(1)}r^{(1)}}\hat{R}_{+-}^{(1)}}{\hat{R}_{+-}^{(1)}e^{iv_\alpha^{(1)}r^{(1)}} - 1} - H_o^{(1)}(v_\alpha^{(1)}r)\right]s_+. \qquad (17)\end{aligned}$$

Taking inverse Fourier transforms over k and ω, we obtain the solution in spatial and time domains as

$$\begin{aligned}\sigma^{(1)}(r,z,t) = \frac{\rho^{(1)}}{4\pi}\int_{-\infty}^{+\infty}\omega^2 F(\omega)e^{-i\omega t}\{\int_{-\infty}^{+\infty} i\frac{J_o(v_\alpha^{(1)}r)e^{iv_\alpha^{(1)}r^{(1)}}\hat{R}_{+-}^{(1)}}{1-\hat{R}_{+-}^{(1)}e^{iv_\alpha^{(1)}r^{(1)}}}e^{ikz}dk \\ + \frac{1}{R}e^{ik_\alpha^{(1)}R}\}d\omega. \qquad (18)\end{aligned}$$

where, $R = \sqrt{r^2 + z^2}$.

NUMERICAL IMPLEMENTATION

The discrete wave-number technique (Bouchon & Aki, 1977) and FFT are used to numerically evaluate the $k-\omega$ integral in Eqn (18). A complete program package is written to implement our new algorithm. To check the validity of our formulation and program, we test a two-layer open hole model chosen from Cheng and Toksoz (1981) and a four-layer cased borehole model chosen from Tubman et al. (1984). The spectrum of source function is described by

$$F(\omega) = \frac{1}{\omega^2}\frac{8\alpha\omega_o(\alpha - i\omega)}{[(\alpha - i\omega)^2 + \omega_o^2]^2},$$

and attenuation is introduced through complex velocity defined by

$$v(\omega) = v(\omega_{ref})[1 + \frac{1}{\pi Q}\log(\frac{\omega}{\omega_{ref}}) - \frac{i}{2Q}],$$

where Q is the quality factor for either P-wave or S-wave, and v is either P-wave velocity or S-wave velocity.

The seismograms computed by the generalized R/T matrix method are shown in Figures 2 and 3. Figures 4 and 5 are taken from the papers mentioned above, respectively. Comparisons of our result with theirs show very good agreement. The model parameters used in Figures 2 and 4 are shown in Table 1. The parameters of the source function are: $\omega_o=2\pi$ x15000Hz and $\alpha= 0.5\omega_o/\pi$. The source-receiver separation is 2.44 m. For Figures 3 and 5, the model is referred to Figure 1 whose parameters are given in Table 2. The source-receiver separation is 3.048m. The parameters of the source function are: $\omega_o=2\pi$ x 13000Hz and $\alpha=0.5\omega_o/\pi$.

Layer	r (cm)	α (km/s)	β (km/s)	ρ (g/cm^3)	Q_p/Q_s
Fluid	10.2	1.83	–	1.2	∞
formation	∞	5.94	3.05	2.3	∞

Table 1. Model parameters used for Figures 2 and 4.

Layer	r (cm)	α (km/s)	β (km/s)	ρ (g/cm^3)	Q_p	Q_s
Fluid	4.7	1.68	–	1.2	20	–
Casing	5.72	6.1	3.35	7.5	1000	1000
Cement	10.2	2.82	1.73	1.92	40	30
Formation	∞	4.88	2.6	2.16	60	60

Table 2. Model parameters used for Figures 3 and 5.

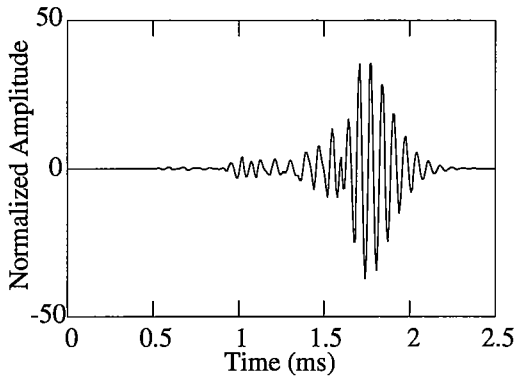

Figure 2. Seismogram calculated by the generalized R/T coefficients method using a *two-layer* open hole model.

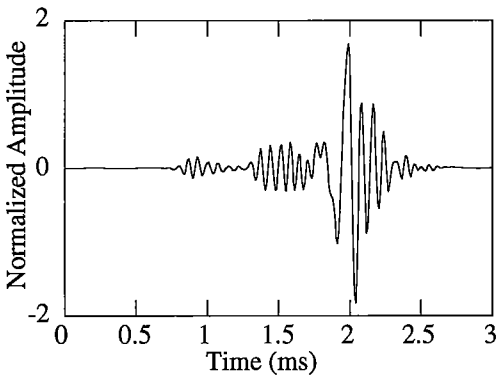

Figure 3. Seismogram calculated by the generalized R/T coefficients method using a *four-layer* open hole model.

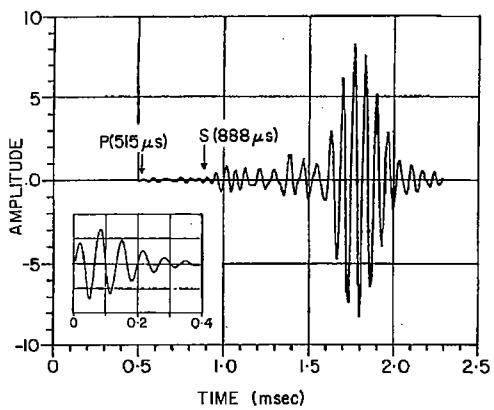

Figure 4. Seismogram taken from Page 1047 in Cheng & Toksoz (1981) for comparison with Figure 2.

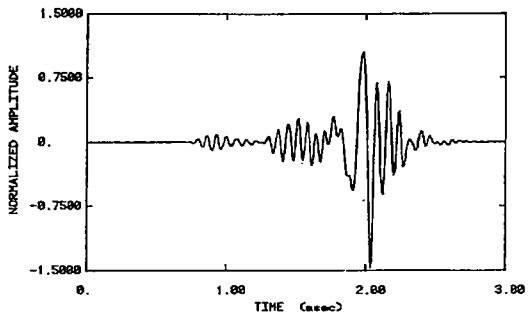

Figure 4. Seismogram taken from Page 1055 in Tubman (1984) for comparison with Figure 3.

CONCLUSIONS

An approach based on generalized reflection and transmission coefficients is developed to calculate waves in radially layered media. The renormalized Hankel functions and the renormalization factors are introduced to make the numerical procedure more stable. Aside from the examples presented in the previous section, we have also successfully simulated crosswell seismic profiles and the open hole with invaded zone using this method.

ACKNOWLEDGMENT

The author would like to thank Steven Bacharach for editing this paper.

REFERENCES

Bouchon, M. and Aki, K., 1977, Discrete wavenumber presentation of seismic-source wave fields: Bull. Seism. Soc. Am, **67**, 259-277.

Chen, X., 1993, A systematic and efficient method of computing normal modes for multilayered half-space: Geophys. J. Int, **115**, 391-409.

Cheng, C. H. and Toksoz, M. N., 1981, Elastic wave propagation in a fluid-filled borehole and synthetic acoustic logs: Geophysics, **46**, 1042-1053.

Kennett, B.L.N, 1983, *Seismic wave propagation in stratified media*: Cambridge University Press, New York.

Luco, J.E. and Apsel, R.J., 1983, On the Green's function for a layered half-space, Part I: Bull. Seism. Soc. Am., **73**, 909-929.

Quan, Y, Harris, J. M. & Chen, X. F., 1994, Acoustic attenuation logging using centroid frequency shift and amplitude ratio methods: A numerical study: Abstract of the 64th SEG annual meeting.

Tubman, K. M., Cheng, C. H. and Toksoz, M. N., 1984, Synthetic full waveform acoustic logs in cased boreholes: Geophysics, **49**, 1051-1059.

Yao, Z. and Zheng, T., 1985. The generalized reflection-transmission coefficient method in acoustic well logging, Acta Geophysics Sinica (in Chinese), **28**, 510-518.

PAPER M

ACOUSTIC ATTENUATION LOGGING USING THE CENTROID FREQUENCY SHIFT AND AMPLITUDE RATIO METHODS: A NUMERICAL STUDY

Youli Quan

ABSTRACT

The centroid frequency shift method is proposed to estimate seismic attenuation from full waveform acoustic logs. This approach along with the amplitude ratio method is applied to investigate the attenuation properties of the *P* head wave in fluid-filled boreholes. The generalized reflection and transmission coefficients method is used to perform forward modeling. We suggest an empirical formula to describe the frequency-dependent geometrical spreading of the *P*-wave in a borehole. We simulate a more realistic borehole by including a mudcake and an invaded zone which are modeled by a large number of radially symmetric thin layers. The numerical tests show that the invaded zone exhibits a very strong influence on the attenuation measurement.

INTRODUCTION

Many efforts have been made to estimate the seismic attenuation from sonic logs. Existing methods include amplitude ratio, spectral ratio, partition coefficients and full waveform inversion (Paillet and Cheng 1991). We propose another method which is based on centroid frequency shift. The centroid frequency shift method has been applied to crosswell seismic attenuation (Quan & Harris, 1993). In crosswell profiling this method measures the spectral centroid difference between incident and transmitted waves and uses this difference to estimate the attenuation (1/Q). For the full waveform logging we take the advantage of multiple receivers and measure the spectral centroid difference of P-waves between two or more receivers for attenuation estimation. In acoustic logs the first arrival is a P head wave refracted from the borehole wall. In order to understand the

---

** This paper is a joint work with Xiaofei Chen of Department of Earth Sciences, USC*

attenuation property of the head wave in boreholes and provide a guide to in situ measurement, we use the generalized reflection and transmission coefficients method (Chen, et al., 1994) to model waves in boreholes, We then apply the centroid frequency shift method along with the amplitude ratio method for inversion. This approach is tested with numerical simulations.

FORWARD MODELING

In the sonic logging problem, we measure stress waves in a fluid-filled borehole where the normal stress $p^{(1)}$ is given by calculating a k-ω integral (Chen et al., 1994):

$$p^{(1)}(r,z,t)=\frac{\rho^{(1)}}{4\pi}\int_{-\infty}^{+\infty}\omega^2 F(\omega)e^{-i\omega t}\{\int_{-\infty}^{+\infty} i\frac{J_o(\nu_\alpha^{(1)}r)e^{i\nu_\alpha^{(1)}r^{(1)}}\hat{R}_{+-}^{(1)}}{1-\hat{R}_{+-}^{(1)}e^{i\nu_\alpha^{(1)}r^{(1)}}}e^{ikz}dk+\frac{1}{R}e^{ik_\alpha^{(1)}R}\}d\omega. \qquad (1)$$

where, $R=\sqrt{r^2+z^2}$, z = source-receiver offset, r = the distance of receiver from borehole center, $\rho^{(1)}$ = fluid density, $\hat{R}_{+-}^{(1)}$ = the generalized reflection coefficient calculated from Eqn (16) in (Chen et al., 1994), $F(\omega)$ = source spectrum, and $\nu_\alpha^{(1)}=\sqrt{(\omega/\alpha^{(1)})^2-k^2}$ with $\alpha^{(1)}$ = P-wave velocity in the fluid. The superscript is the layer number, and the first layer is fluid-filled borehole. The discrete wave-number technique and FFT are used to evaluate Eqn (1). In our simulation the spectrum of source function $F(\omega)$ corresponding to displacement is described by (Tsang and Rader, 1979)

$$F(\omega)=\frac{1}{\omega^2}\frac{8\alpha\omega_o(\alpha_s-i\omega)}{[(\alpha_s-i\omega)^2+\omega_o^2]^2}$$

with $\omega_o = 2\pi \times 14000$ Hz and $\alpha_s = 0.5\ \omega_o/\pi$. The attenuation is introduced through complex velocity defined by (Aki and Richards, 1980)

$$v(\omega)=v(\omega_o)[1+\frac{1}{\pi Q}\log(\frac{\omega}{\omega_o})-\frac{i}{2Q}], \qquad (2)$$

where Q is the quality factor for either P-wave or S-wave, and v is either P-wave velocity or S-wave velocity.

ATTENUATION ESTIMATION FORM SONIC LOGGING

The first arrival in full waveform sonic logs is a P head wave. We separate it from later arrivals using a time window. We use this first arrival to estimate P-wave attenuation (1/Q). The magnitude of recorded wave spectrum $R_{i+1}(f)$ at r= 0 and z=z_{i+1} is written as (see Figure 1)

$$R_{i+1}(f) = \frac{R_i(f)}{G_i} G_{i+1} \exp[-\alpha_{oi} f(z_{i+1} - z_i)], \tag{3}$$

where G represents geometrical spreading, and

$$\alpha_{oi} = \pi/(v_i Q_i) \tag{4}$$

is the intrinsic seismic attenuation coefficient. In general, the velocity v_i and attenuation coefficient α_{oi} vary with depth z_i. In our model, we consider radial variation but no vertical variation. The subscript "i" indicates the i^{th} receiver in a receiver array. As noticed by some authors (e.g., Page 144 in Paillet and Cheng, 1991), the geometrical spreading of this refracted head wave is highly frequency dependent. But how the geometrical spreading depends on frequency is not clear. In this study we assume that

$$G_{i+1} = G(f, z_{i+1}) \sim \frac{\exp(-\alpha_g f z_{i+1})}{z_{i+1}^p} \tag{5}$$

where α_g is an attenuation coefficient related to frequency-dependent geometrical spreading, and p is the power of "true" geometric spreading factor. Combining Eqns (3) and (5) we have

$$R_{i+1}(f) = (\frac{z_i}{z_{i+1}})^p R_i(f) \exp[-f(\alpha_g + \alpha_{oi})(z_{i+1} - z_i)] \tag{6}$$

We will empirically determine α_g and p from numerical simulation for a given borehole structure. We use two techniques to estimate the intrinsic attenuation coefficient α_o. The first one is frequency shift method (Quan and Harris, 1993). In this method we define the spectral centroid of $R_i(f)$ to be

$$f_i = \frac{\int f R_i(f) df}{\int R_i(f) df}, \tag{7}$$

and its variance to be

$$\sigma_i^2 = \frac{\int (f - f_i)^2 R_i(f) df}{\int R_i(f) df}. \tag{8}$$

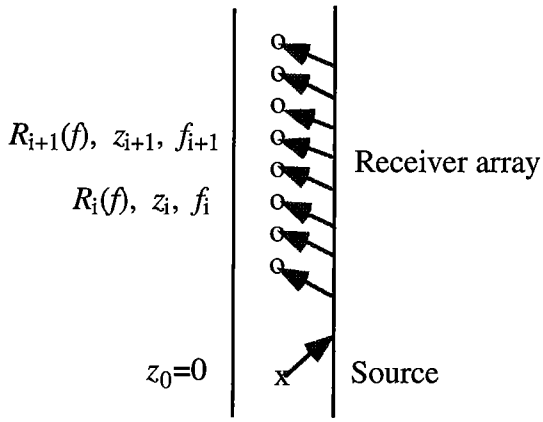

Figure 1. Sonic log geometry. $R_i(f)$ is the signal spectrum at the i^{th} reciver, z_i is the receiver depth and f_i is the centroid frequency of $R_i(f)$ defined in Eqn (7).

Then, the intrinsic attenuation coefficient α_{oi} at depth z_i can be obtained from following equation

$$\alpha_{oi} = \frac{1}{\sigma_i^2} \frac{\Delta f_i}{\Delta z_i} - \alpha_g. \tag{9}$$

where $\Delta f_i = f_i - f_{i+1}$ is the frequency down-shifting between two receivers, and $\Delta z_i = z_{i+1} - z_i$. Another method is based on the amplitude ratio. Rearranging Eqn (6) and taking the logarithm we obtain

$$\alpha_{oi} = \frac{1}{f \Delta z_i} \log[\frac{R_i(f) z_i^p}{R_{i+1}(f) z_{i+1}^p}] - \alpha_g. \tag{10}$$

In the next section we use Eqns (9) and (10) to estimate the attenuation coefficient α_{oi} from synthetic seismograms obtained for the sonic log geometry.

NUMERICAL SIMULATIONS

Simple boreholes

Let us first consider a simple open borehole whose model parameters are shown in Figure 2. Using Eqn (1) we obtain the seismograms in Figure 3. Then we perform a Fourier transform to the first arrival (*P*-wave) that is just covered by a short time window and use Eqn (7) to calculate the spectral centroid (Curve A in Figure 4). Changing the Q_p value in Figure 2 to Q_p = 80 and Q_p =120 we obtain Curves B and C, respectively. We then use Eqn (9) (frequency shift method) and Eqn (10) (amplitude ratio method) to estimate Q_p values. The slope of the centroid frequency curves carries information about Q_p.

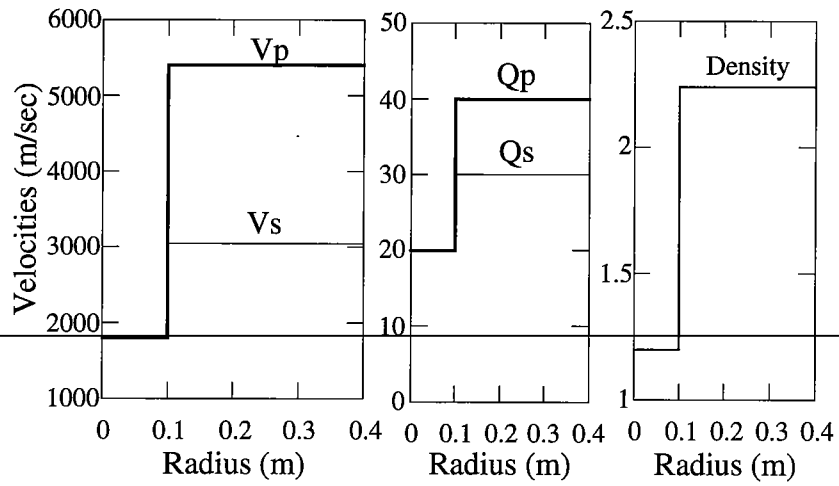

Figure 2. A simple fluid-filled open borehole.
The radius of the borehole is 0.1 m.

If we ignore the effect of frequency-dependent spreading ($\alpha_g = 0$), then from Eqns (9) (frequency shift method only) we estimate $\tilde{Q}_p$= 37, 69, and 95 which correspond to the given values Q_p = 40, 80, and 120, respectively. Here, Eqn (4) is used to convert α_o into Q. Obviously, the estimated $\tilde{Q}_p$'s are systematically smaller than the given Q_p's. If we do not ignore the effect of frequency-dependent spreading and find α_g from a measurement then use it as correction for all the measurements, we obtain the *corrected*

$\tilde{Q}_p$= 40, 82, and 120. The correction $\alpha_g = \pi/(vQ_g)$ with $Q_g = 450$ is found by solving Eqn (9) from a single measurement.

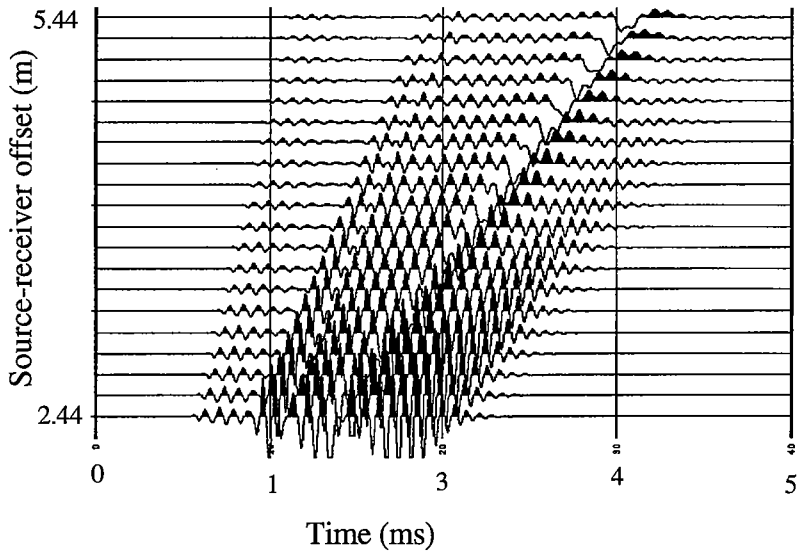

Figure 3. Synthetic seismograms in a simple borehole shown in Figure 1.

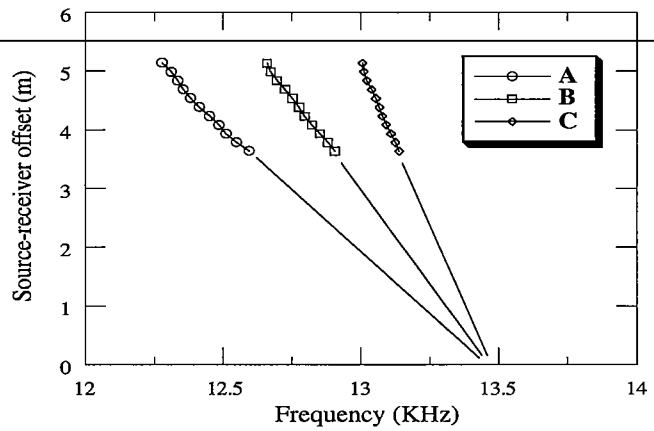

Figure 4. Centroid frequency picks corresponding to Q_p=40 (Curve A), Q_p=80 (Curve B) and Q_p=120 (Curve C).

Let us now consider the same synthetic data using the amplitude ratio method. Choosing the same value of α_g obtained above and setting power p in Eqn (10) to be 0.87, we obtain the estimated $\tilde{Q}_p$= 40, 80 and 119, respectively. If we set α_g = 0 and p = 1, equivalent to the conventional amplitude ratio method (e.g., Cheng et al, 1982), we obtain $\tilde{Q}_p$= 43, 93, and 148, respectively.

Boreholes with Mudcake and Invaded Zone

The borehole model shown in Figure 2 is idealized. We design a more realistic model which consists of a fluid-filled borehole, a mudcake and an invaded zone. Since the modeling algorithm can efficiently handle an arbitrary number of radial layers, we use ten thin layers to model the invaded zone (Figure 5). The Q_p of the invaded zone varies from 35 to 40. Figure 6 shows the seismograms calculated using this model. For a closer comparison we pick out the first traces (nearest source-receiver offset) from Figures 3 and 6 and plot them together in Figure 7. The mudcake and invaded zone exhibit a significant effect on the wave trains. The amplitude of the first arrival (P-wave) becomes relatively higher when the invaded zone is present. The attenuation study in the following paragraph shows more detailed effects of the invaded zone.

We also change the Q_p of the invaded zone in Figure 6 to be 75-80 and calculate another data set. Using Eqn (9) (frequency shift method) with α_g = 0, we obtain the estimated $\tilde{Q}_p$= 16.5 and 16.7, which correspond to the given values of Q_p = 35-40 and 75-80, respectively. If we use Eqn (10) (amplitude ratio method) with α_g = 0 and p = 1, then the estimated $\tilde{Q}_p$= 78 and 747, which again correspond to the given values of 35-40 and 75-80, respectively. However, if we choose α_g = 0 and p = 0.6 in Eqn (10), we obtain the estimated $\tilde{Q}_p$= 41 and 78 which are very close to the predicted values. These experiments show that the geometrical spreading in a borehole with an invaded zone is more complex than in a simple borehole. We can not simply use p = 1 in Eqn (5) to describe the geometrical spreading effects in a complex borehole. The frequency-dependent term $\exp(-\alpha_g f z_{i+1})$ in Eqn (5) may be too simple, since we could not find a single correction α_g to recover all the estimated $\tilde{Q}_p$'s to the predicted values.

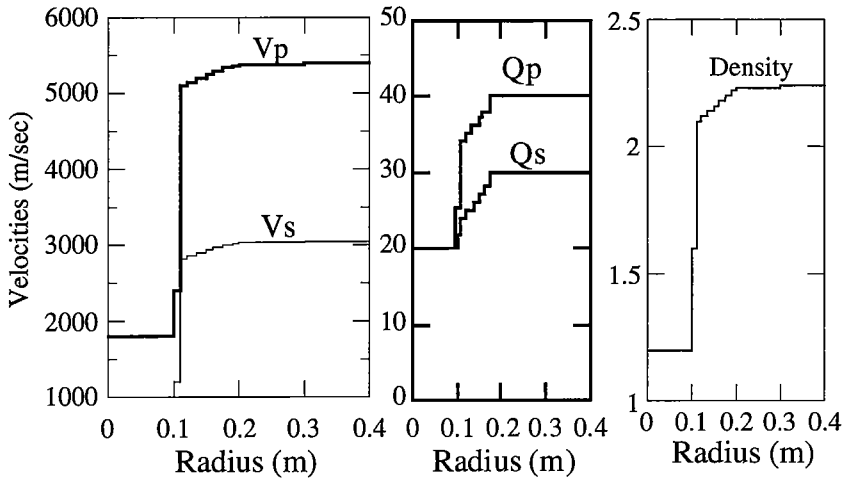

Figure 5. A borehole with mudcake and invaded zone.

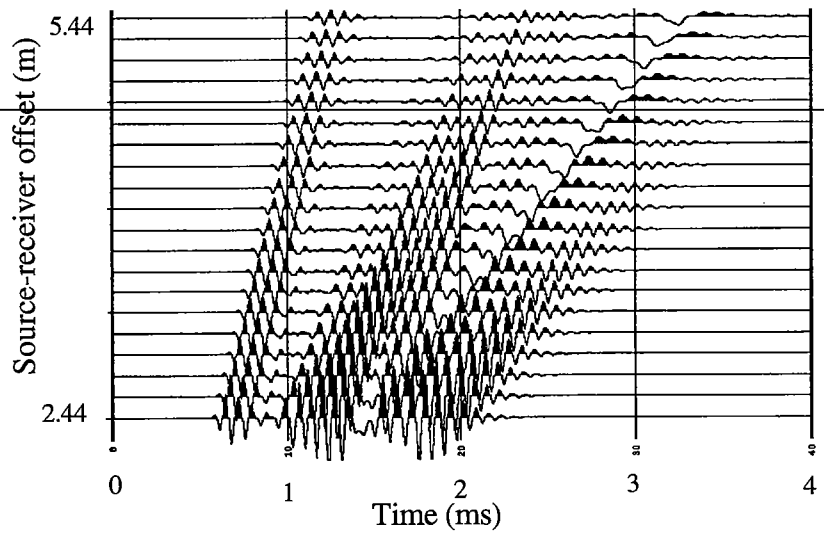

Figure 6. Synthetic seismograms in a complicated open borehole

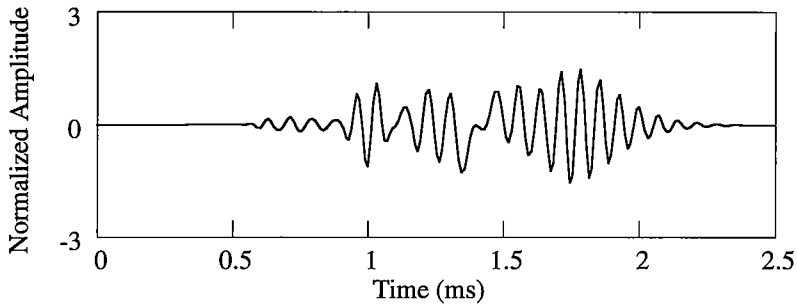

(a) A trace from a simple open borehole.

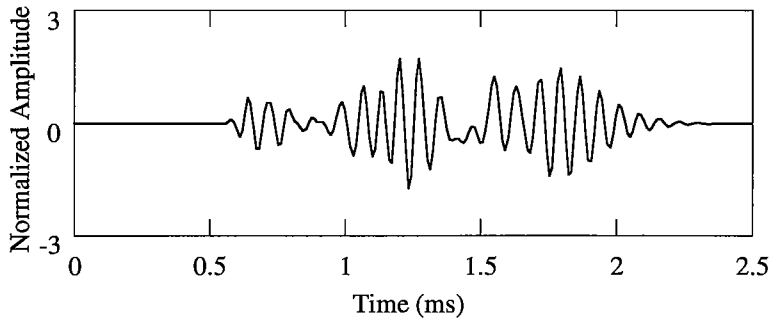

(b) A trace from an invaded open borehole.

Figure 7. Comparison of seismograms calculated from simple and complicated boreholes.

DISCUSSIONS

The examples in the previous section indicate the attenuation property of *P*-waves. The estimated results, more or less, are affected by window length and window types used to calculate attenuation. For the purpose of reducing the effect of window length and the contamination of later wave trains we only use the seismograms for source to receiver separation greater than 3.5 m in Figures (3) and (6).

The frequency shift method is strongly affected by α_g, the attenuation coefficient related to the frequency-dependent geometrical spreading (see Eqn (5) for definition). It is independent of the "true' geometrical spreading factor $1/z^p$.

The test on the borehole with an invaded zone shows that if we set $\alpha_g = 0$ and $p = 1$, the Q_p value estimated from centroid frequency shift method (Eqn 9) is too small, and the Q_p value estimated from amplitude ratio method (Eqn 10) is too large. The amount of the difference between them may carry information about borehole structures, for example, the depth of the invaded zone.

CONCLUSIONS

The generalized reflection/transmission coefficients method is applied to numerically investigate seismic wave attenuation in simple boreholes and complicated boreholes with invaded zones. In order to measure the intrinsic attenuation we need to remove the geometrical spreading effect which is complex and highly frequency-dependent. If we use the frequency shift method for a simple borehole, we can introduce a simple geometrical spreading factor to do the correction. For a complicated borehole we need more work to figure out the correction term. For the amplitude ratio method the power p in geometrical spreading factor $1/z^p$ can be different from 1.

ACKNOWLEDGMENTS

The author would like to thank Mark Van Schaack for helpful discussions about practical considerations of mudcake and invaded zone. The author also would like to thank Steven Bacharach for editing this paper.

REFERENCES

Aki, K, and Richards, P., G., 1980, *Quantitative Seismology, Theory and Methods*: W.H. Freeman and Co., San Francisco.

Chen, X. F., Quan, Y. and Harris, J. M., 1994, Seismogram synthesis for radially Multi-layered media using the generalized reflection/transmission coefficients method: Expanded Abstracts of the 64th SEG annual meeting.

Cheng, C. H., Toksöz, M. N. and Willis, M. E., 1982, Determination of in situ attenuation from full waveform acoustic logs: J.G.R., **87**, No B7, 5477-5484.

Paillet, L. and Cheng, C. H., 1991, *Acoustic Waves in Boreholes*: CRC Press, Inc.

Quan, Y. & Harris, J. M., 1993, Seismic attenuation tomography based on centroid frequency shift: Expanded Abstracts of the 63rd SEG annual meeting.

Tsang, L. and Rader, D., 1979, Numerical evaluation of the transient acoustic waveform due to a point source in a fluid-filled borehole: Geophysics, **44**, No. 10, 1706-1720.

PAPER N

A TEST ON SEISMIC ANISOTROPY AND SCALE EFFECTS IN FINELY LAYERED MEDIA

Youli Quan

ABSTRACT

Wave properties in a layered medium depend on the ratio of wavelength to layer thickness. If this ratio is large enough, the medium behaves as a transversely isotropic material. If the ratio is small, scattering and dispersion are present. This report gives numerical simulations using seismogram synthesis for vertically layered media, and examines the results with the theoretical formula.

INTRODUCTION

A very common rock formation is the finely layered sedimentary deposit, e.g., Devine test site. This layered formation exhibits a transversely isotropic feature if the wave length is long compared with the thicknesses of the layers. When the wave length is close to the dimensions of the layers, the layering shows a heterogeneous property, and scattering is present. The terminology *scale effect* refers to the behavior of waves in media with different wavelength to layer-thickness ratios (R). A model with a large R is calculated to study the transverse isotropy, and the averaged elasticity for long wavelength (Backus, 1962) is used to predict the anisotropic velocities. Then a model with a small R is simulated to test the scattering and dispersive effects. These two models have the same average material contents.

TRANSVERSE ISOTROPY AND SCATTERING

VESPA (a software of seismogram synthesis for vertically layered media) is used to simulate the transverse isotropy in finely layered media (see Figure 1). The model consists of 300 layers each with thickness of 10 cm. In this example a limestone-sandstone sediment is simulated. The ratio of wave length to layer thickness is greater

than 30, which satisfies the long wave approximation. A horizontal line (Survey H) and a vertical line (Survey V) are placed in the model to study the direction-dependent properties of waves.

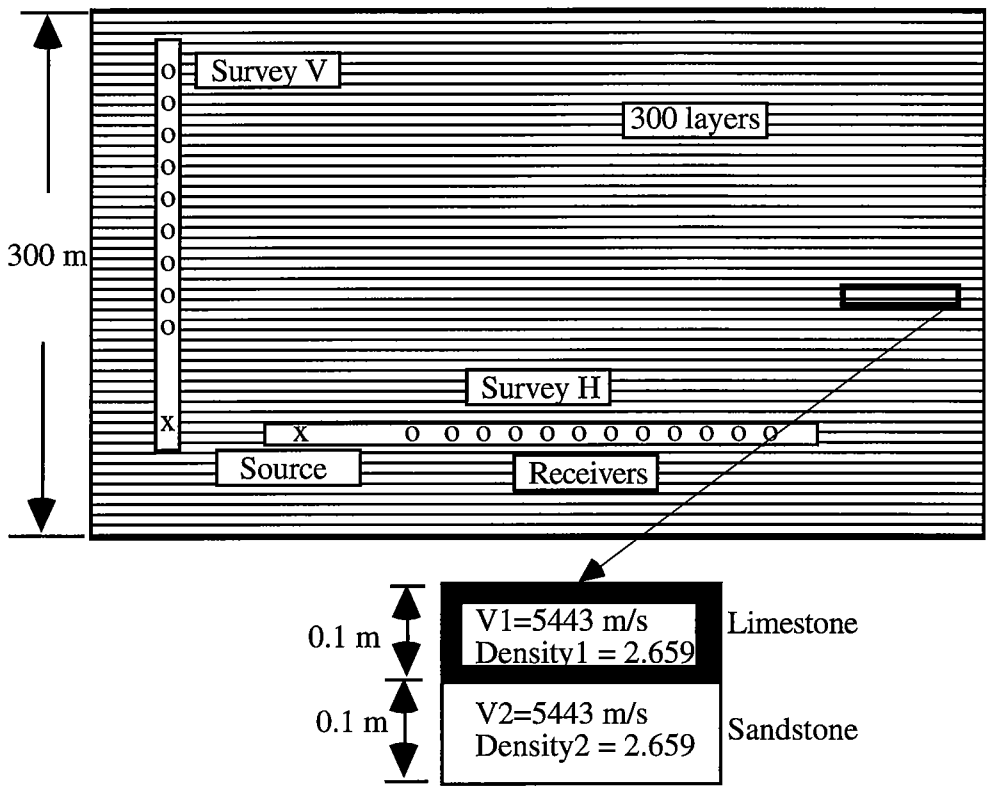

Figure 1. Model used for transversely isotropic simulation. It is made up of periodically stacked limestone and sandstone. The thickness *d* of each layer is 0.1 m. VESPA is used for forward modeling. The frequency band is 100-1000 Hz. The minimum wave length $\lambda_{min}=V_{min}/f_{min}$ = 3m. The ratio $R = \lambda_{min}/d$ = 30 meets the long wave approximation. Survey H and Survey V have the same source-receiver offsets, from 6m to 25 m.

Figure 2 shows the seismograms recorded in the two directions. I pick the travel times of P waves and show them in Figure 3. From the travel time curves, we find a horizontal velocity V_h=4514 m/s and a vertical velocity V_V=3521 m/s. The relative change $(V_h-V_v)/V_v$=28 %. The average velocity $V_m=2V_1V_2/(V_1+V_2)$, where V_1= 5443 m/s is velocity of the limestone and V_2=2949 m/s is the velocity of sandstone. Plugging in V_1 and V_2 we get V_m=3825 m/s. It can be seen that $V_v<V_m<V_h$. That means we can not use this simply averaged velocity for this medium.

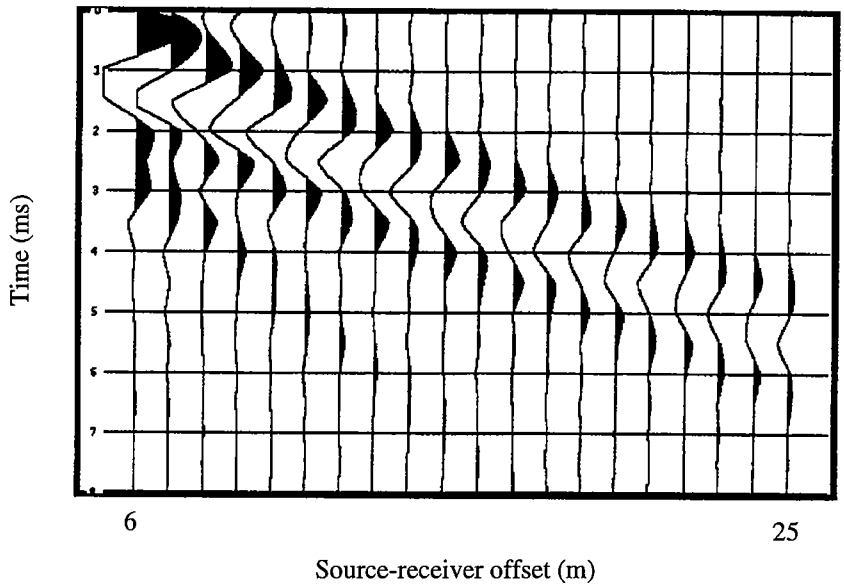

(a) Waves propagating in horizontal direction recorded in survey H

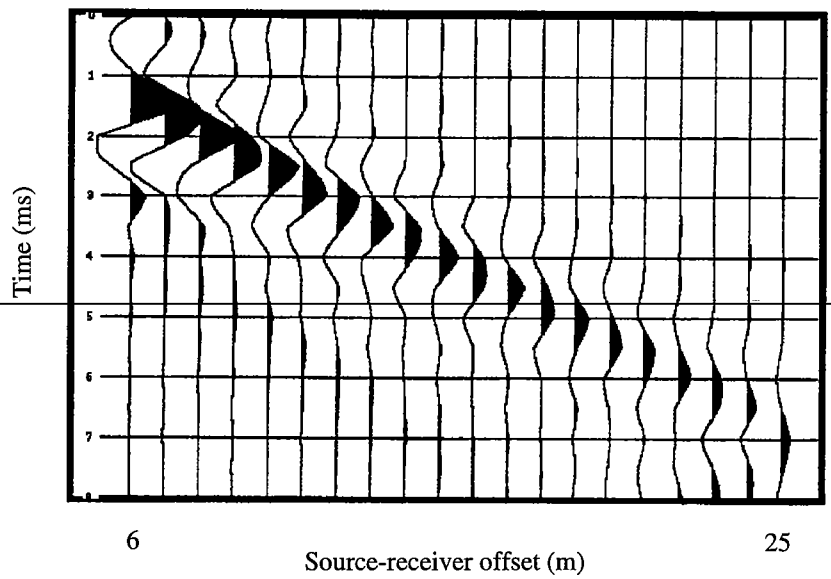

(b) Waves propagating in vetical direction recorded in survey V

Figure 2. Seismograms caculated by VESPA for the model with layer thickness of 0.1 meter.

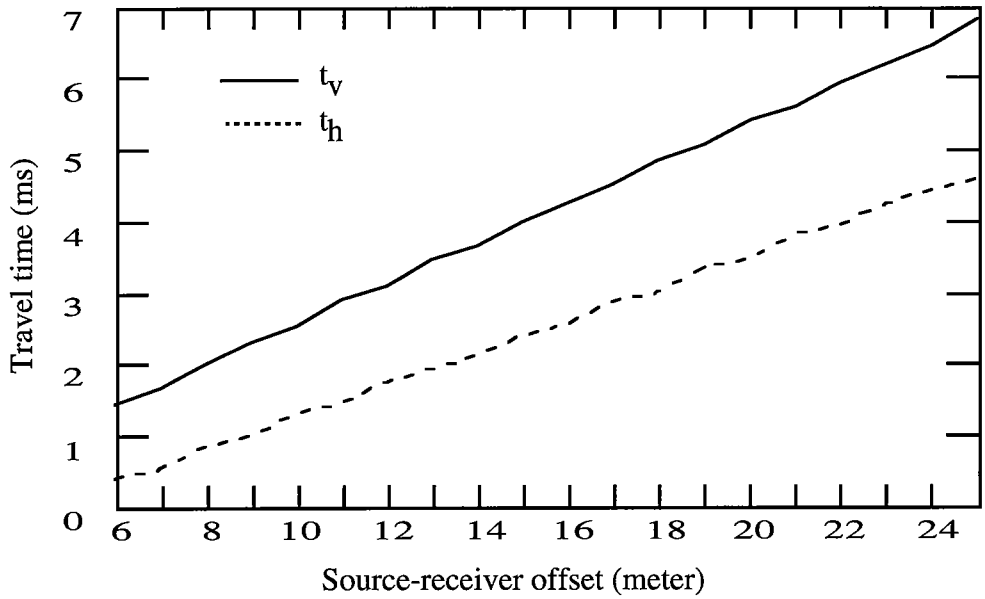

Figure 3. Travel times of waves in vertical direction (t_V) and horizontal direction (t_h), which correspond to the Survey V and Survey H shown in Figure 1. From these travel times we obtain the vertical velocity V_V=3521 m/s, and V_h=4514 m/s. Here, $(V_h-V_V)/V_V$=28%. Note that the medium used consists of limestone with V1=5443 m/s and sandstone with V_2=2949 m/s.

We can theoretically predict V_h and V_v from the averaged elastic modulus for the long-wave approximation (Backus, 1962; Carcione et al., 1991). Let M be a modulus. The averaged modulus $\overline{M}$ in the horizontal direction (see Figure 4) is given by

$$\overline{M} = \frac{1}{2}(M_1 + M_2). \tag{1}$$

The averaged density is

$$\overline{\rho} = \frac{1}{2}(\rho_1 + \rho_2). \tag{2}$$

The averaged velocity can be calculated by

$$\overline{V}_h = \sqrt{\frac{\overline{M}}{\overline{\rho}}} = \sqrt{\frac{\rho_1 V_1^2 + \rho_2 V_2^2}{\rho_1 + \rho_2}}. \tag{3}$$

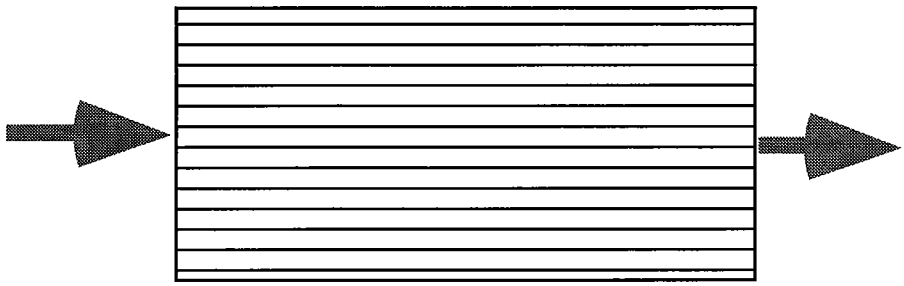

Figure 4. Waves in horizontal direction

The averaged modulus in the vertical direction (see Figure 5) is given by

$$\overline{M} = \frac{2M_1M_2}{M_1 + M_2},, \tag{4}$$

$$\overline{\rho} = \frac{1}{2}(\rho_1 + \rho_2). \tag{5}$$

and

$$\overline{V}_v = \sqrt{\frac{\overline{M}}{\overline{\rho}}} = \sqrt{\frac{2}{\rho_1 + \rho_2}\frac{2\rho_1 V_1^{\,2}\rho_2 V_2^{\,2}}{\rho_1 + \rho_2}} \tag{6}$$

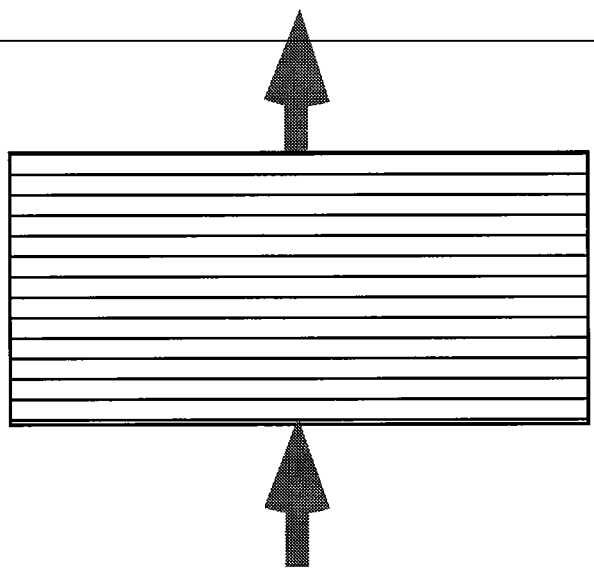

Figure 5. Waves in vertical direction.

Applying Eqns (3) and (6) to Survey H and Survey V we can obtain the theoretical velocities in horizontal and vertical directions. The theoretical prediction and the numerical result shown in Figure 6 are very close.

Theoretical Prediction:	Numerical Result:
V_h = 4468 m/sec	V_h = 4514 m/sec
V_v = 3582 m/sec	V_v = 3521 m/sec

Figure 6. Comparison of theoretical and numerical anisotropic velocities in finely layered medium under the condition of long wave approximation.

For the purpose to examine the scale effects I only change the layer thickness from 0.1 meter to 1.0 meter and re-calculate the seismograms for Survey H and Survey V. This does not change the average material contents of the medium. But the wavelength to layer-thickness ratio R is changed from 30 to 3. The calculated seismograms for R = 3 are shown in Figure 7. It can be seen that strong dispersion appears in Figure 7a. The scattering in the form of coda waves is present in Figure 7b. Comparing Figure 7 with Figure 2 we can see that these waves exhibit very different features for large R and small R. In the case of small R we can not use Eqns (3) and (6), since the condition of the long wavelength is not satisfied.

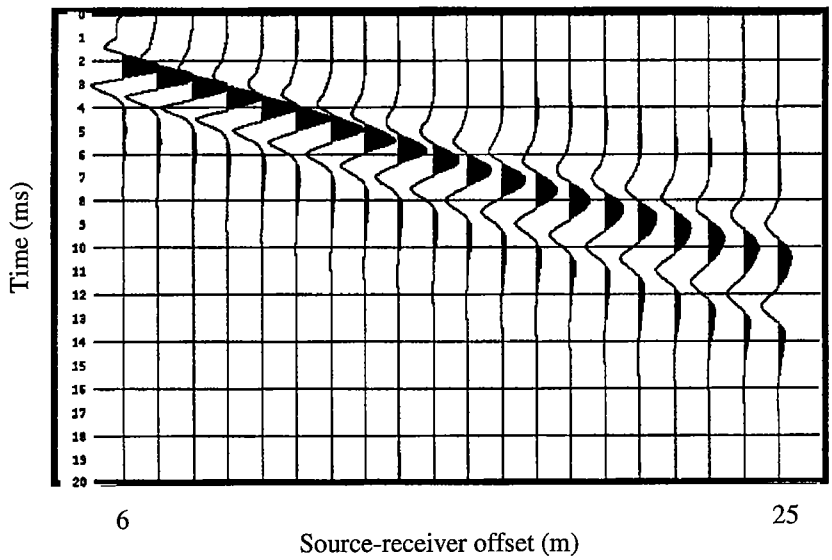

(a) Waves propagating in horizontal direction recorded in survey H

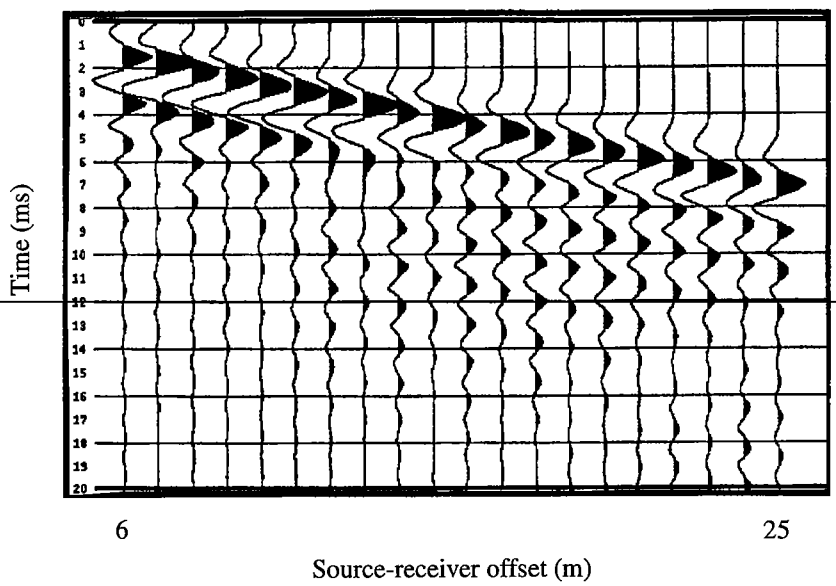

(b) Waves propagating in vetical direction recorded in survey V

Figure 7. Seismograms caculated by VESPA for the model with layer thickness of 1 meter.

CONCLUSIONS

The scale effects of waves in finely layered media are evident. The wave behavior is controlled by the ratio of wavelength to layer-thickness (or more generally, the period of the media). If this ratio (R) is large enough (for instance, $R > 20$), the medium behaves as a transversely isotropic material, and the vertical and horizontal velocity can be found by simple formulas which are based on the long wave average. If the ratio R is small (for instance, $R < 5$) strong scattering will be present, and the medium behaves as a heterogeneous dispersive material.

ACKNOWLEDGMENT

The author would like to thank Nicholas Smalley for editing this paper.

REFERENCES

Backus, G. E., 1962, Long-wave elastic anisotropy produced by horizontal layers: J. Geophysics, Res., **67**, 4427-4440.

Carcione, J. M., Kosloff, D. and Behle, A., 1991, Long-wave anisotropy in stratified media: A numerical test: Geophysics, 56, 245-254.

PAPER O

ANALYZING DIFFRACTIONS AND REFLECTIONS BY WAVE EQUATION MODELING

Le-Wei Mo

ABSTRACT

In this paper, we show an example of synthesizing reflection from diffractions. It is accomplished by solving the velocity-density acoustic wave equation by Fourier transform method or, as it is often called, the pseudospectral method. It is shown that as discrete diffractors are lined up, their diffractions collapse to a reflection.

INTRODUCTION

In the simulation carried out in this paper, we concern with the acoustic wave equation,

$$\frac{\partial}{\partial x}\left(\frac{1}{\rho}\frac{\partial P}{\partial x}\right)+\frac{\partial}{\partial y}\left(\frac{1}{\rho}\frac{\partial P}{\partial y}\right)=\frac{1}{c^2\rho}\frac{\partial^2 P}{\partial^2 t}+S$$

where $P(x,y,t)$ represents the pressure, ρ(x,y) the density, $c(x,y)$ the wave velocity, and $S(x,y,t)$ the source term which equals the divergence of the body force divided by the density.

In numerically solving the acoustic wave equation (1), we apply a highly accurate method -- the pseudospectral method (Kosloff and Baysal, 1982). The spatial derivatives are calculated by Fourier transforms. The time derivative is calculated by a second order finite-difference. By this method, the spatial derivatives are calculated exactly, the only numerical error comes from the temporal finite-differencing. We choose the time sampling interval to be sufficiently small that the Courant number is less than 0.1, then modeling by this method is considered to be exact.

MODELING EXAMPLES

Figure 1 shows the modeling geometry. Source *S* is at the left well. Receivers are at the right well. The medium is homogeneous, with a constant velocity of 18,000 ft/s and density 3 g/cm^3. The source wavelet is the first derivative of the Gaussian function with a dominant frequency of 500 Hz (Alford et al., 1974). The two wells are separated by ten wavelengths. Diffractors are put at the middle between the two wells by changing the velocity of the nodes to be 9,000 ft/s and density 2 g/cm^3. The lengths of the aligned diffractors to modeled are quarter, half, one, one and half, two, four, eight, and ten wavelengths.

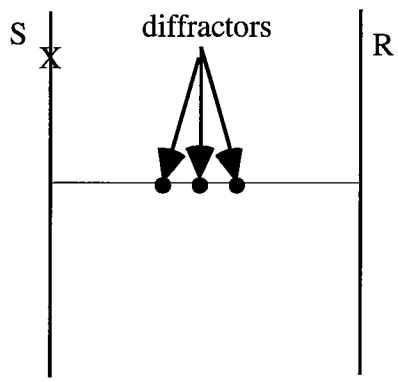

Figure 1 Modeling geometry. Diffractors are created by changing the velocity and density at the designated nodes.

Figures 2 and 3 show the modeling results of the different diffractor dimensions. Figure 2 shows that when the dimension of the diffractor is less than or equal to one wavelength, its modeling responses are in the forms of diffractions. Figure 3 shows that as the dimension of the diffractors is increasing to be larger than one, its modeling responses tend to be the reflection, i.e., the diffraction responses of the individual diffractors collapse to a reflection.

CONCLUSIONS

The relationship between reflection and diffraction has been analyzed by an accurate numerical wave equation modeling. When the dimension of the diffractor is less than or equal to one wavelength, its modeling responses are in the form of diffractions. As the dimension of the diffractors is increasing to be larger than one, its modeling responses tend to be the reflection, i.e., the diffraction responses of the individual diffractors collapse to a reflection.

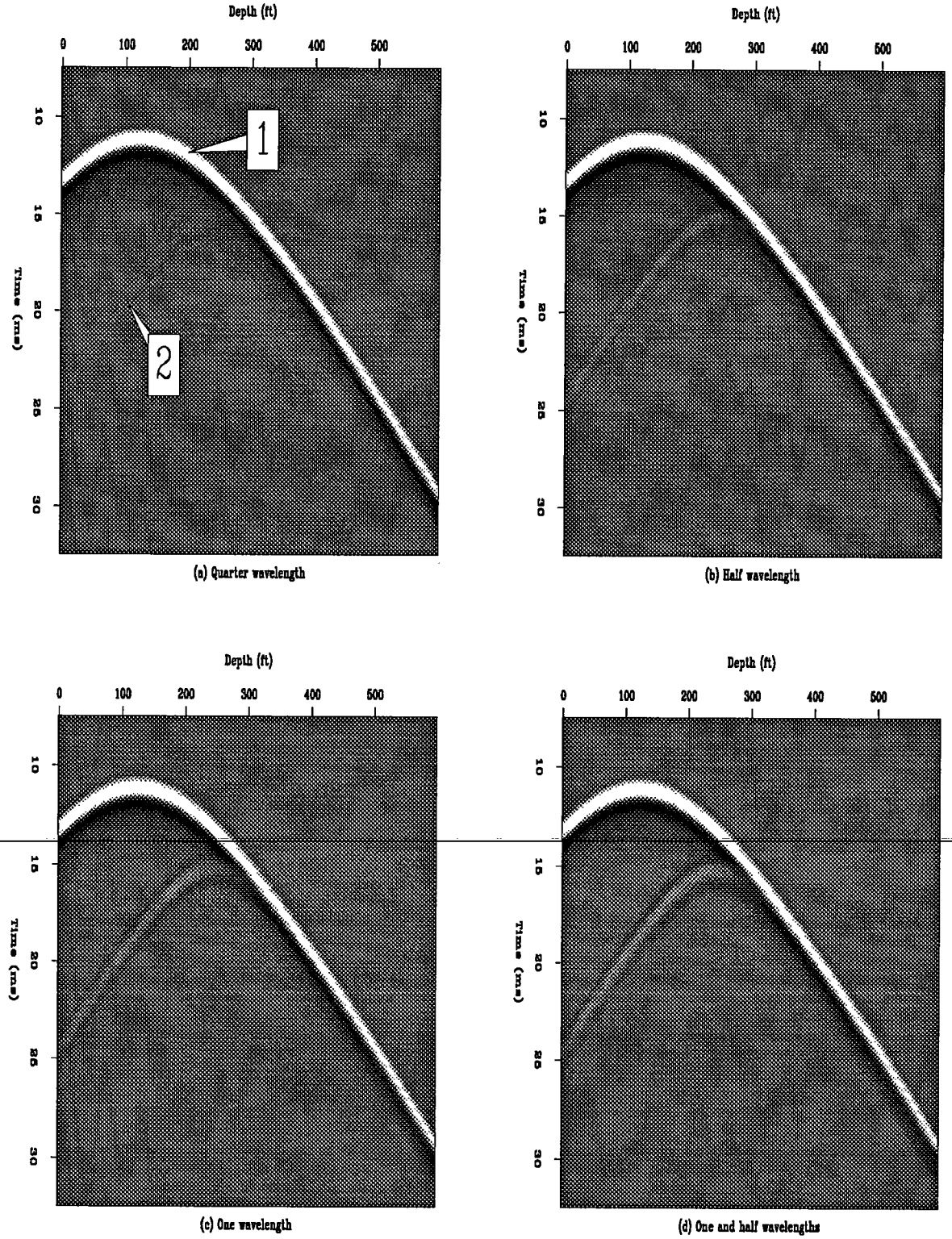

Figure 2 Modeling results when the lengths of the diffractors are quarter, half, one, one and half wavelengths.In (a), 1 is the direct arrival, 2 the diffraction. Similar event identifications apply to (b), (c), and (d).

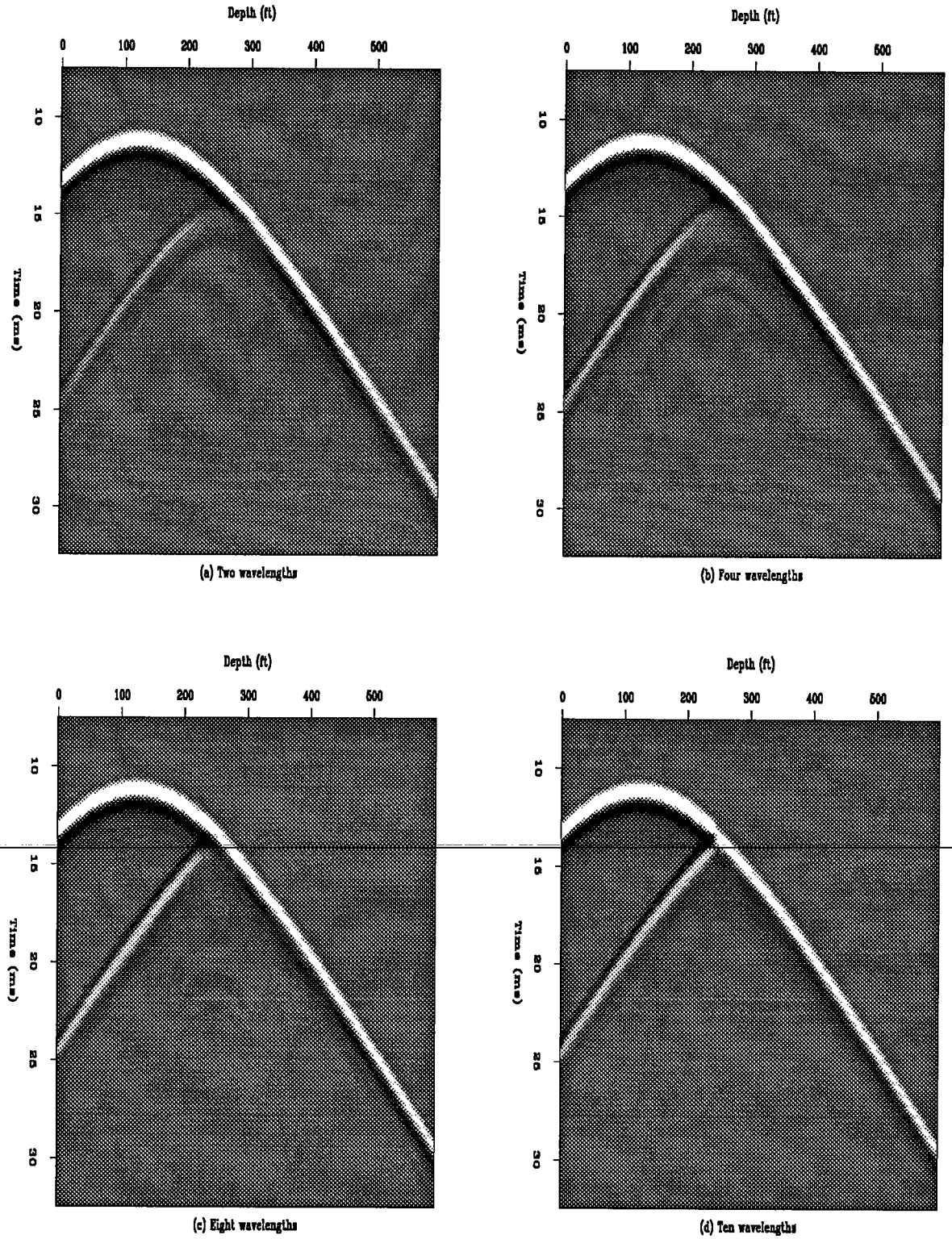

Figure 3 Modeling results when thelengths of the diffractors are two, four, eight, and ten wavelengths.The distance between the two wells is ten wavelengths.As the dimension of the diffractors is increasing to be larger than one, its modeling responses tend to be the reflection.

REFERENCES

Alford, R. M., Kelly, K. R., and Boore, D. M., 1974, Accuracy of finite-difference modeling of the acoustic wave equation:Geophysics, **39**, 834--842.

Cerjan, C., Kosloff, D., Kosloff, R., and Reshef, M., 1985, A nonreflecting boundary condition for discrete acoustic and elastic wave equations: Geophysics, **50**, 705--708.

Kosloff, D., and Baysal, E., 1982,Forward modeling by a Fourier method:Geophysics, **47**, 1402--1412.

PAPER P

NONLINEAR MULTI-FREQUENCY WAVE EQUATION INVERSION

Jerry M. Harris and Feng Yin

ABSTRACT

A method of nonlinear wave equation inversion using multiple frequencies is developed. The method sequentially inverts low to high signal frequencies of the wave field. First, the low frequencies are used to reconstruct the low spatial wavenumbers of the heterogeneities. Then, higher frequencies are used to reconstruct higher spatial wavenumbers. A subspace method is used to minimize the misfit between the observed *total* wave field and the corresponding theoretical synthetic wave field. The gradient of the misfit function, the rate of change of the gradient, and a regularization factor are used to find the optimum search direction to the solution of inverse problem. It is not necessary to assume weak scattering, e.g., Born or Rytov, nor is it necessary to remove the incident field before inversion as required in linear diffraction tomography. These advantages make this method more flexible than linear diffraction tomography. Tests on synthetic data show that the method is effective in reconstructing velocities with up to 15% variation and that the inversion is stable and more precise than single frequency wave equation methods. These advantages are available with not much penalty of computation effort or time.

INTRODUCTION

Transmission travel time methods based on ray equation are the most often used methods in seismic inversion, because they are robust in field data applications (Dines and Lytle 1979; Wong. Hurley and West, 1983). Yet these methods can only give the low wavenumber components of the heterogeneous media. In order to derive higher resolution, some aspects of the full wave field, e.g., reflections, must be used.

In wave equation tomography, there are two types of methods: one is analytic inversion method, another is non-linear iterative method. In the analytic method, the Born or Rytov weak scattering approximation i s made in order to derive the analytic inversion formula.

The perturbation of velocity to be inverted cannot be very large (Devaney, 1984, Harris, 1987, Wu, et al, 1987). Non-linear iterative wave equation tomography methods are better for large contract velocity (Torantola, 1987, Pratt, 1990, Yin, et al, 1993). Nonlinear methods have three main parts: (1) the forward calculation, (2) calculation of the Frechét derivative, and (3) the method of updating the model. In addition, we can implement the inversion in time domain or in frequency domain. In time domain, Torantola (1984, 1987, Mora, 1987) applied a back-propagation method to the difference field computed between the observed waveform and calculated waveform to invert for the media elastic parameters. Since the full waveform is used in this method, reconstruction is improved, but it requires a large amount of memory and computer time to implement

Inversions using the full waveform can also be implemented in frequency domain also. We can select different frequencies according to the resolution requirement. We expect the low frequencies to provide the low spatial wavenumber components of the media, and the high frequencies to provide the high wavenumbers. We can invert for a broad range of velocity scales from multi-frequency wave fields, thereby creating an inversion that is stable over the entire range while raising the resolution of the reconstruction step by step with frequency. In addition, scattering is strongest for heterogeneities comparable in size to the wavelength; therefore, each frequency of the multi-frequency decomposition is maximally sensitive to different scales of the heterogeneity spectrum.

In this paper, we describe a nonlinear, multi-frequency, and multi-grid wave equation inversion method based on the 2-D acoustical wave equation. In our method, the low frequency components in the waveform are first used to invert for the low wavenumber components of the media. A bi-linear interpolation method is used to interpolate the low frequency reconstruction to smaller cells or a finer grid. Then, higher frequency components of the waveform are used to invert the velocity on the finer grid, and so on until the velocities at the smallest grid are reconstructed.

When solving the nonlinear inverse problem, our goal is to reduce the value of the misfit function which describes the mismatch between the observed total wave field data and the corresponding synthetically calculated data below a threshold determined by the errors in the observations. We use the moment method to calculate the synthetic fields. In this way, our method does not require the removal of the incident wave field before inversion. This is important in field applications for empirically we do not know the incident field. The objective function for inversion is quadratic, thus its first and second derivatives are required to minimize it. In this work, we use the subspace method (Skilling, 1984; Kennet and Williamson, 1987) to minimize the quadratic misfit function involving

second derivatives to the model and to avoid the inversion of large matrices. At each step in the iteration we use a local quadratic approximation to the misfit function and three directions are used to find a path towards the minimum. These three directions are the gradient of the misfit function, a regularization term, and the direction of the rate of change of the gradient. To prevent unreasonable behavior of the model parameters, some form of regularization condition on the model is imposed. We applied our method to the crosswell geometry to conduct a forward and inverse simulation. The results show that our multi-frequency and multi-grid method gives a better reconstruction for velocity than the single frequency method without much penalty in computation time.

THE ACOUSTICAL SCATTERING SOLUTION

In order to implement the nonlinear wave equation inversion, we should have a good and robust method of forward modeling for waves in inhomogeneous media. Starting from the wave equation in the frequency domain,

$$\nabla^2 U(\mathbf{r},\omega)+\frac{\omega^2}{V^2}U(\mathbf{r},\omega)=-S(\omega)\delta(\mathbf{r}-\mathbf{r}_S) \tag{1}$$

where $\mathbf{r}$=(x, z) is a spatial position in the imaging region, $\mathbf{r}_s=(x_s,z_s)$ is the source position, ω is an angular frequency and $U(r,\omega)$ is the pressure field in the imaging region, and V is the velocity field. Taking $U(\mathbf{r},\omega)=U^{in}(\mathbf{r},\omega)+U^{sc}(\mathbf{r},\omega)$, $V^{-2}(\mathbf{r})=V_0^{-2}(\mathbf{r})-m(\mathbf{r})V_0^{-2}(\mathbf{r})$, where $V_0(\mathbf{r})$ is the velocity of the background, we derive an integral equation corresponding to Eqn. (1) as follows:

$$U(\mathbf{r},\omega)=U^{in}-\int_{\Omega}k_0^2(\mathbf{r}')\mathrm{U}(\mathbf{r},\omega)m(\mathbf{r})\mathrm{G}(\mathbf{r}_g,\mathbf{r}')d\mathbf{r}' \tag{2}$$

where Ω is the image area, $\mathbf{r}_g=(x_g,y_g)$ and $k_0=\omega/V_0(\mathbf{r})$. We divide the image region into N pixels, then, $\Omega=\Omega_1\cap\Omega_2\cap\cdots\cap\Omega_N(\Omega_i\cup\Omega_j=0,i=j)$. Assuming m_i is the value of m($\mathbf{r}$) at pixel Ω_i. By the moment method, Eqn. (2) can be discretized to give

$$\mathbf{F}\cdot\mathbf{a}=\mathbf{b} \tag{3}$$

where

$$\mathrm{F}_{ij}=\delta_{ij}+\iint_{\Omega_i}k_0^2G(|\mathbf{r}-\mathbf{r}'|,n_b)m(\mathbf{r}')d\mathbf{r}' \tag{4}$$

and **a** is the unknown column vector whose elements are the discretized total field U_i, **b** is a vector whose elements are the discretized value of the incident field U_i^{in} in the imaging region. The solution of this equation solves the forward modeling problem. By the same method, we can also obtain the Green's function $G(\mathbf{r_g},\mathbf{r})$ by putting a point source at the receiver position $\mathbf{r}_g$ and applying the reciprocity principle. Because $U(\mathbf{r})$ is dependent on $m(\mathbf{r})$, Eqn. (2) is a non-linear system in $m(\mathbf{r})$. In order to derive an analytic inversion solution, various linearized methods based on the Born approximation have been derived (Wu and Toksoz, 1987, Harris, 1987, and Harris and Wang, 1993). Next, we will solve the inverse problem by using a non-linear iterative method.

NON-LINEAR ITERATIVE INVERSION

Suppose that the observed wave field is $U^0(\mathbf{r}_s,\mathbf{r}_s,\omega_l)$ $(1\le s\le S, 1\le g\le G, 1\le l\le L)$. We wish to use these observed data to determine a model M=$(m_1,m_2,\cdots,m_N)$ from which the corresponding calculated wave field matches the observed wave field. Therefore, we should have a measure of fit, that is, we should establish a measure for assessing the degree of mismatch between the observed data and synthetic data. We choose the squared L_2 norm of the observed and calculated data, that is, our goal is to minimize the function

$$J(M)=\tfrac{1}{2}\sum_s\sum_g\sum_l \|U^o(r_s,r_g,\omega_l)-U^c(r_s,r_g,\omega_l)\|^2=\text{minimum} \qquad (5)$$

where U^o and U^c are measured field data and calculated field data, respectively. The wave equation inverse problem in crosswell geometry is not only nonlinear, but extremely non unique, that is, ill-posed. In order to derive a stable solution of the inverse problem and prevent unrealistic behavior of the model parameters, we impose some form of regularization condition to Eqn. (5) as follows:

$$Q(\mathbf{M})=\tfrac{1}{2}\sum_s^S\sum_g^G\sum_l^L \|U^o(r_s,r_g,\omega_l)-U^c(r_s,r_g,\omega_l)\|^2+\lambda H(\mathbf{M})=\text{minimum} \qquad (6)$$

where H(M) is the regularization term, e.g., a smoothing operator. Then, we use steepest gradient method, conjugate gradients. Eqn. (6) is quadratic function, therefore, not only the first derivative, but also the second derivative are required. A subspace method (Kennet, etc., 1987, Skilling, et al, 1987) in which the Hessian matrix is used will be utilized to solve equation (6) in our paper.

In the subspace method, the current model is updated by a small model perturbation which is determined in a small subspace, that is

$$\mathbf{M}^{(q+1)} = \mathbf{M}^{(q)} + \Delta\mathbf{M}^{(q)} \tag{7}$$

$$\Delta\mathbf{M}^{(q)} = x_1\mathbf{e}_1 + x_2\mathbf{e}_2 + x_3\mathbf{e}_3 \tag{8}$$

where $\mathbf{e}_1, \mathbf{e}_2$ and $\mathbf{e}_3$ are the basis of the subspace, and they are

$$(\mathbf{e}_1)_i = \frac{\partial J}{\partial m_i},\ (\mathbf{e}_2)_i = \frac{\partial H}{\partial m_i},\ (\mathbf{e}_3)_i = \sum_k \frac{\partial^2 J}{\partial m_i \partial m_k}\frac{\partial Q}{\partial m_k} \tag{9}$$

and x_1, x_2 and x_3 can be determined by the subspace method (Skilling,1984, Kennet, et al, 1987).

We can see that one of main points of the inversion step is the calculation of the Frechét derivative and the second derivative of the quadratic function. After the wave fields are calculated in the current background media, the total wave field at receiver array can be expressed as

$$U^c(\mathbf{r}_s, \mathbf{r}_g, \omega) = U^{in}(\mathbf{r}_s, \mathbf{r}_g, \omega) + \sum_j A_{ji} m_i \quad (j = 1, \mathrm{L}\ , G \cdot S) \tag{10}$$

where

$$A_{ji} = -\iint_{\Omega_i} k_0^2 U^c(\mathbf{r}_s, \mathbf{r}', \omega) G(\mathbf{r}_g, \mathbf{r}', \omega) d\mathbf{r} \tag{11}$$

Therefore, the Frechét derivative for inversion and the second derivative of the objective function can be easily expressed as

$$\frac{\partial J}{\partial m_i} = \sum_l^{SGL} R(A_{li}) \cdot \left[R(U_l^c) - R(U_l^o)\right] + I(A_{li}) \cdot \left[I(U_l^c) - I(U_l^o)\right] \tag{12}$$

$$\frac{\partial^2 J}{\partial m_i \partial m_k} = \sum_l^{SGL} [R(A_{li}) \cdot R(A_{lk}) + I(A_{li}) \cdot R(A_{lk})] \tag{13}$$

where R and I means taking real part and imaginary part. S, G, and L are the total number of the discrete sources, receivers, and frequencies.

Because analytical formulas for the Frechét derivative can be obtained for our numerical method, we use them to invert the model by non-linear iterative methods of Eqns. (7) - (8). In addition, when we reconstruct the velocity, three overlapping grids are used to implement the reconstruction. The velocities at the largest grid spacing are reconstructed first, then the velocities at the middle grid, and finally at the smallest grid. Therefore, the following problem should be solved by subspace method:

$$Q(\mathbf{M}_1) = \tfrac{1}{2}\sum_{s}^{S}\sum_{g}^{G}\sum_{l}^{L_1} \| U^O(r_S, r_g, \omega_l) - U^C(r_S, r_g, \omega_l) \|_2 + \lambda H(\mathbf{M}_1) = \text{minimum} \qquad (14)$$

$$Q(\mathbf{M}_2) = \tfrac{1}{2}\sum_{s}^{S}\sum_{g}^{G}\sum_{l}^{L_2} \| U^O(r_S, r_g, \omega_l) - U^C(r_S, r_g, \omega_l) \|_2 + \lambda H(\mathbf{M}_2) = \text{minimum} \qquad (15)$$

$$Q(\mathbf{M}_3) = \tfrac{1}{2}\sum_{s}^{S}\sum_{g}^{G}\sum_{l}^{L_2} \| U^O(r_S, r_g, \omega_l) - U^C(r_S, r_g, \omega_l) \|_2 + \lambda H(\mathbf{M}_3) = \text{minimum} \qquad (16)$$

where $\mathbf{M}_1, \mathbf{M}_2$ and $\mathbf{M}_3$ are the model vectors for the first, the second grid and third grid, respectively. L_1, L_2 and L_3 are the numbers of frequencies used in the first, second and third grids. After the velocities on smallest grid are reconstructed, the inversion stops.

INVERSION WITH SYNTHETIC DATA

Fig. 1 is a model for the crosswell geometry. The velocities in each region is shown. The minimum velocity is 5000 m/s, the maximum 5750 m/s, and the range of the variation is 15%. In the forward calculation, the image region is divided into 20×50 pixels, where the width of each pixel is 2 m. We select six frequencies from 100 Hz to 225 Hz in steps of Δf =25 Hz. The forward wave field is produced by Eqn. (10). In the inversion step, the image region is divided into three grids. The number of pixels in the first, second and third grid are 10×25, 14×35 and 20×50, respectively. Two frequencies of 100 Hz to 125 Hz were used for the first grid, four frequencies of 100 to 175 Hz for the second grid, and six frequencies of 100 Hz to 225 Hz for the third grid. Fig. 2 gives the reconstruction results

using multiple frequencies and the multiple grids with the non-linear wave equation method. The three frequency bands used 12, 8, and 6 iterations, respectively. Fig. 3 is the reconstruction result using single frequency of 225 Hz for 20×50 pixels. Comparing Figs. 2 and 3, we can see that the velocity in each region of Fig. 2 is more homogeneous than that of Fig. 3, that is the multi-frequency results are more accurate with fewer artifacts.

CONCLUSIONS

In this paper we have presented a non-linear multi-frequency inversion method of wave equation tomography. Our goal is to reduce the value of the misfit function which describes the mismatch between the observed total wave field data and the corresponding calculated data below a threshold determined by the errors in the observations. This goal is implemented by a subspace method. This method is a powerful technique which does not have the limitations of linear diffraction tomography. It does not require the removal of the incident field before inversion. When multi-frequency wave equation is applied to crosswell imaging, the precision of reconstruction is better than the single frequency method and the time for inversion is not significantly increased.

ACKNOWLEDGMENTS

This work is supported by the Seismic Tomography Project of Stanford University, a research consortium sponsored by companies of the oil and gas industry.

REFERENCES

Devaney. A.J., Geophysical diffraction tomography, IEEE Transaction on Geoscience and Remote Sensing, GE-22,3-13,1984

Harris, J.M., Diffraction tomography imaging with arrays of line sources and detectors, IEEE Trans. Geoscience Remote Sensing, Vol. Ge-25, No.4, 448-455, 1987.

Harris, J.M. and Guan Y. Wang, Diffraction tomography for inhomogeneities in a layered background media,Expanded abstract of 1993 SEG annual meeting, 49-52.

Kennet, B.L.N. and Williamson, P.R., 1987, Subspace methods for large scale non-linear inverse problems involving multiple parameter classes, Geophysical Journal, Vol. 94, 237-247, 1988.

Mora, P., Elastic wavefield inversion and the adjoint operation for the elastic wave equation, Mathematical Geophysics, Edited by N.J. Vlaar, G.Nolet, M.J.R. Wortel & S.A.P.L. Cloetingh, 1988 by D. Reidel Publishing Company.

Skilling, J., and Bryan, R.K., Maximum entropy image reconstruction: general algorithm, Mon. Not. R. Astr. Soc.., 211, 111-124, 1984.

Pratt, R. Gerhard and Worthington, M.H., Inverse theory applied to multi-source cross-hole tomography. Part 1:Acoustic wave equation method, Geophysical Prospecting 38, 287-310.1990

Tarantola, A., The seismic reflection inverse problem. In: Inverse Problems of Acoustic and Elastic Waves: Santosa, F., Pao, Y.H., Symes,W. and Hoolland, Ch.(eds.), Society of Industrial and Applied Mathematics, Philadelphia, 1984.

Tarantola, A., Inverse problem theory: Methods for data fitting and parameter Estimation, Elsevier Science Publishers Co.,1987

Yin F. and Wang, J.S., Wave equation tomography using maximum entropy, Expanded abstract of 1992 SEG annual meeting, 1050-1053

Wu, R. and Toksöz, M.N., Diffraction tomography and multisource holography applied to seismic imaging, Geophysics 52, 11-25, 1987

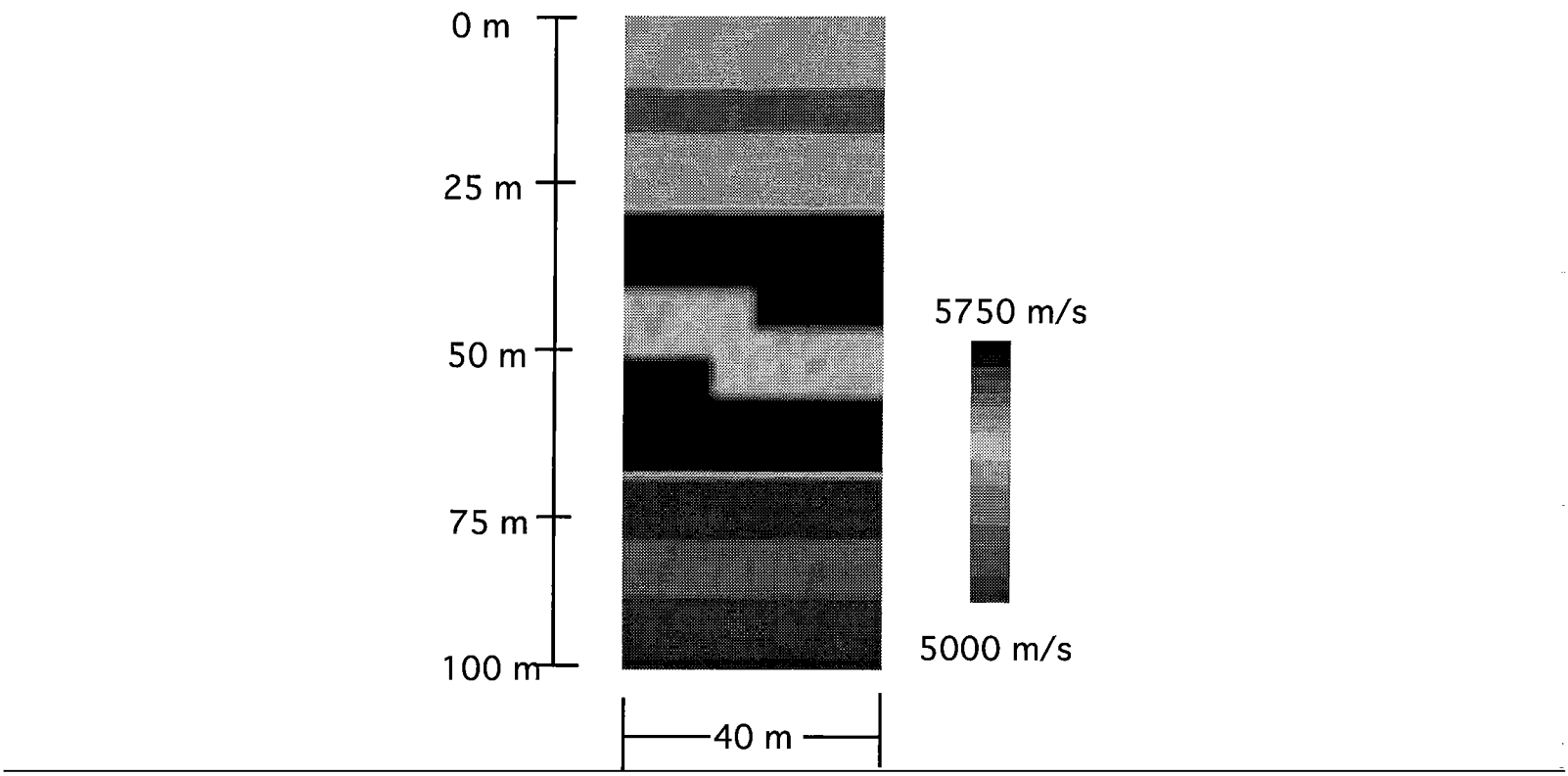

Fig. 1. The synthetic velocity model.

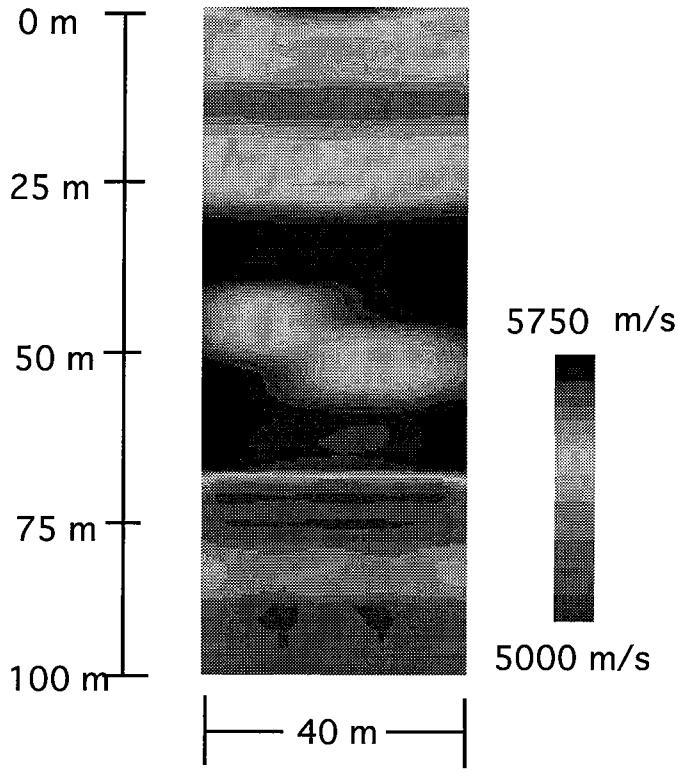

Fig. 2. Multiple frequency (six frequencies from 100- 225 Hz) inversion result derived by nonlinear wave equation inversion tomography.

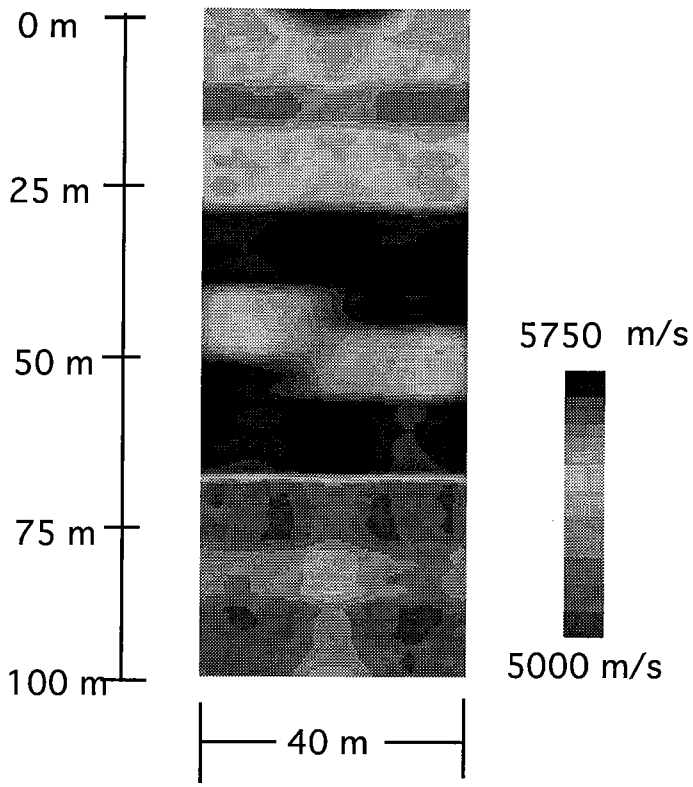

Fig. 3. Single frequency inversion result derived by nonlinear wave equation tomography after 25 iterations.

PAPER Q

TOMOGRAPHY AND TOMOGRAPHIC MIGRATION USING RAY THEORY

Jerry M. Harris and Feng Yin

ABSTRACT

In this paper, we present wavefield tomography methods based on asymptotic ray theory. We introduce the concept of the wavefield tomography operator and compare it with traditional tomography methods. When the scattered fields, after being processed by a correlation procedure, are operated on with the tomography operator, we get an image of the velocity perturbation relative to a velocity background. If instead we input separated up-going and down-going reflection data into our tomography operator, we can get an image of reflectivity. With this general idea, we can develop and use tomographic reconstruction operators and algorithms not only for velocity inversion, but also for migration imaging. In the last part of this paper, we present simulation results and an example using real crosswell reflection field data. The results confirm that the algorithms are useful for crosswell imaging.

INTRODUCTION

Wave equation tomography is increasingly finding a place in crosswell data processing. Wave equation tomography methods, based on full wave theory, can be implemented in the time domain or in the frequency domain. In frequency domain, there is a very large matrix that occupies extremely large computer memory to be inverted (Harris and Yin, 1994). In the time domain, forward and back propagation computations cost too much CPU time (Tarantola, 1984) and also occupy significant computer memory. In addition, when the frequency is very high, we must sample the imaging region into many pixels or nodes and calculate the fields and Green's functions at this fine scale. To avoid these problems, wave equation inversion methods using asymptotic ray theory have been introduced (Beylkin, 1985, Miller, et. al., 1987, Yin, 1993).

The methods described herein are based on the full wave theory. We use a L_2 norm objective function derived for multiple frequencies for the observed wavefield minus the calculated wavefield. Then, we can use a Frechét derivative of this objective function to update the velocity relative to a background medium as in the paper by Harris and Yin (1994). Due to some disadvantages of full wave theory tomography as we mentioned above, we prefer to use asymptotic ray theory which is not only suitable for velocity inversion but also for migration imaging. With ray theory, the phase of the Green's function in the background medium can be calculated accurately and we do not need to compute the fields many pixel locations or nodes, e.g. as with moment methods and finite difference methods. This advantage is very important in field data applications.

By applying the geometrical optical approximation and inverse Fourier transform to the Frechét derivative of our L_2 norm objective function, we obtain the Frechét derivative represented by wavefield data in time domain and use this function for velocity inversion. In order to understand the physical meaning of this function for inversion, we compare the result with traditional traveltime tomography. We find that the Frechét derivative corresponds to simple backprojection tomography (BPT) as it is applied to traveltime data (Herman, 1980). In traveltime BPT, traveltime data are backprojected into the image region along raypaths, but in this case, the scattering data are backprojected into the image region along isochronic lines. We call this procedure the tomographic operator, and accordingly the Frechét derivative is the local linearized BPT tomographic wavefield operator. In this way, we can develop many wavefield tomography operators for inversion. In this paper, we consider only the SIRT operator.

In addition, from the Fréchét derivative, we can see that a correlation process on the wavefield data is required. This is one of the main characteristics in these methods. If we omit this correlation term, we must separate up-going and down-going wave before the tomographic operator is applied to the wavefield. Otherwise, the image will be contain many artifacts because of mispositioning of waveforms at the boundaries of heterogeneities.

We find that if we input the scattering field data into our tomography operators, we can get velocity perturbation image; therefore, we call this procedure *wavefield tomography.* If we input the separated up-going and down-going reflection data, or reflection data after being processed by a correlation procedure, we obtain as image which is similar to that obtained from migration; therefore, we call this image *tomographic migration.* We applied our algorithms to synthetic data and field crosswell data. The results show that these methods are extremely useful.

WAVEFIELD TOMOGRAPHY AND TOMOGRAPHIC MIGRATION

The goal of the non-linear wave equation tomography is to minimize the L_2 norm objective function:

$$J(m)=\frac{1}{2}\sum_{\omega}^{\Omega}\sum_{g}^{G}\sum_{s}^{S}\|u^{o}(r_g,r_s,\omega)-u^{c}(r_g,r_s,\omega)\|_2 \qquad (1)$$

where u^O and u^C are the observed and calculated wavefield in frequency domain, ω and s and g denote the frequency and source and receiver locations, and

$$u^{o}(\mathbf{r},\omega)-u^{c}(\mathbf{r},\omega)=-\omega^2 S(\omega)\int_V \tilde{u}^{c}(\mathbf{r}',\omega)m(\mathbf{r}')G(\mathbf{r}_g,\mathbf{r}',\omega)d\mathbf{r}', \qquad (2)$$

where $m(\mathbf{r})=\dfrac{\delta c_0(\mathbf{r})}{c_0^3(\mathbf{r})}$, $c_0(\mathbf{r})$ is the velocity in the background media. The wavefield in this background medium is $u^c(\mathbf{r})=S(\omega)\,\tilde{u}^c$, where $S(\omega)$ is the spectrum of the source function. The Frechét derivative can be derived as

$$\frac{\partial J}{\partial m}=-\sum_{\omega,s,g}\omega^2[S(\omega)\tilde{u}^{c}(\mathbf{r},\mathbf{r}_s)G(\mathbf{r},\mathbf{r}_g)]^{+}\delta u(\mathbf{r}_s,\mathbf{r}_g,\omega) \qquad (3)$$

where $\delta u = u^o - u^c$, + denotes conjugate. Then, we can use above derivative to update the background model as following

$$c^{(q+1)}=c^{(q)}+\alpha\frac{\partial J}{\partial m}. \qquad (4)$$

We have implemented the above method as in the paper (Harris and Yin, 1994). However, the total field $\tilde{u}^c(\mathbf{r},\mathbf{r}_s,\omega)$ must be evaluated for each frequency. Because our method is derived in the frequency domain, it is non-local in space and thus requires much computer time and memory to implement. To avoid these computation problems, we applied geometrical optical and the Born approximation to implement our method in the time domain. In the time domain, the finite speed of propagation of waves is used to restrict the domain of influence at an image point.

Using geometrical optics, the Born approximation, and the inverse Fourier transform, the above expression for Frechét derivative can be written as

$$\frac{\partial J}{\partial m} = \sum_{s,g} \sum_{s,g} [a(\mathbf{r}_s, \mathbf{r}, \mathbf{r}_g)] \delta \bar{\bar{u}}(\mathbf{r}_s, \mathbf{r}_g, \tau(\mathbf{r}_s, \mathbf{r}, \mathbf{r}_g)) \quad (5)$$

where

$$\delta \bar{\bar{u}} = \dot{S}(-t) * \dot{S}(t) * \overline{\delta u}(\mathbf{r}_s, \mathbf{r}_g, \tau(\mathbf{r}_s, \mathbf{r}, \mathbf{r}_g)) \quad (6)$$

$$\delta \bar{u}(\mathbf{r}_s, \mathbf{r}_g, t) = \int_V m(\mathbf{r}') u^c(\mathbf{r}', \mathbf{r}_s, t) * G(\mathbf{r}_g, t | \mathbf{r}', 0) d\mathbf{r}' \quad (7)$$

where $a(\mathbf{r}_s, \mathbf{r}, \mathbf{r}_g) = A(\mathbf{r}, \mathbf{r}_s) A(\mathbf{r}, \mathbf{r}_g)$, $\tau(\mathbf{r}_s, \mathbf{r}, \mathbf{r}_g) = T(\mathbf{r}, \mathbf{r}_s) + T(\mathbf{r}, \mathbf{r}_g)$, and A and T satisfy the transport and eikonal equations, respectively. Using the geometrical optics approximation, we have

$$\overline{\delta u}(\mathbf{r}_s, \mathbf{r}_g, t) = \int_V m(\mathbf{r}') a(\mathbf{r}_g, \mathbf{r}', \mathbf{r}_s) \delta(t - \tau(\mathbf{r}_g, \mathbf{r}', \mathbf{r}_s) d\mathbf{r}' \quad (8)$$

From equations (5)-(6), we can see that a correlation procedure must be applied to the source function in wavefield tomography in order to obtain a zero phase time function $W(t)=\dot{S}(-t) * S(t)$; therefore, the convolution between W(t) and $\overline{\delta u}(\mathbf{r}_s, \mathbf{r}_g, t)$ does not change the phase of $\overline{\delta u}(\mathbf{r}_s, \mathbf{r}_g, t)$. and it is not necessary to separate the down-going wavefield from the up-going wavefield in wavefield tomography method. This separation step is usually required in cross-hole migration. In addition, although the forward calculation of the wavefield requires accurate computation of u^c and updating the model using equation (4) is done repeatedly, we can reach the goal of velocity inversion when the function J(m) tends to zero. We can also conduct one iteration inversion for imaging a velocity perturbation under the linear assumption, using equation (5).

After we compare equation (5) with simple traveltime backprojection tomography (BPT), we find that equation (5) is almost the same as traveltime BPT except for the weight. In traveltime BPT, we backproject the traveltime along the ray path. In wavefield imaging, we backproject the wavefield $\delta \bar{\bar{u}}(\mathbf{r}_s, \mathbf{r}_g, t)$ along isochronic lines with the specified weight. So we call the right hand side of equation (5) the BPT wavefield tomography operator. Whenever it acts on the wavefield $\delta \bar{\bar{u}}(\mathbf{r}_s, \mathbf{r}_g, t)$, we can get the velocity perturbation. The forward operator corresponding to this tomography operator is

$$\bar{\bar{\delta}} u(\mathbf{r_s}, \mathbf{r_g}, t) = \int_V \frac{\partial J}{\partial m} a(\mathbf{r_g}, \mathbf{r}', \mathbf{r_s}) \delta(t - \tau(\mathbf{r_g}, \mathbf{r}', \mathbf{r_s}) d\mathbf{r}' \quad (9)$$

In order to improve the image resolution, we can also modify the weight when we backproject the wavefield $\delta\bar{\bar{u}}(\mathbf{r}_s,\mathbf{r}_g,t)$ along isochronic lines and develop other methods to invert for function $f(\mathbf{r})=\frac{\partial J}{\partial m}$. Next, we will develop SIRT wavefield tomography to invert for function $f(\mathbf{r})$ as follows.

Considering the k^{th} isochronic plane $I(t_k)$, the equation (9) can be discretized as

$$d_k = \sum_n c_{kn} \cdot f_n \tag{10}$$

where

$$c_{kn} = \sum_m a(l_{km}) \cdot \rho_{nkm} \cdot \Delta s \tag{12}$$

where d_k is the k^{th} sampling point of the wavefield $\delta\bar{\bar{u}}(\mathbf{r}_s,\mathbf{r}_g,t)$, $a(l_{km})$ is the value of the amplitude $a(\mathbf{r}_g,\mathbf{r}',\mathbf{r}_s)$ at the point l_{km}, ρ_{nkm} is the pulse basis function, Δs is the integral step. Then, we have the following SIRT iterative form for $f(\mathbf{r})$

$$f_n^{(q+1)} = f_n^{(q)} + \beta \sum_k \frac{c_{kn}}{\sum_n c_{kn}^2} (d_k - \sum_n c_{kn} \cdot f_n) / z_n \tag{13}$$

where, β is a damping factor, z_n is the non-zero numbers of c_{kn} $(1 \le k \le L \cdot S \cdot R)$. We call the above inversion method the SIRT wavefield tomography operator. To use this operator, we must know the isochronic lines in the background media for distribution of $f(\mathbf{r})$ along it.

The BPT and SIRT wavefield tomography operators for velocity perturbation are obtained next. By comparing the inverse Radon transform(IRT) method(Miller, 1987) with traditional traveltime tomography, we know that the method corresponds to the convolution filtered backprojection tomography method for traveltimes. For wavefield data, this would become IRT tomography wavefield operator. When we input the scattering data into each tomography operator, we can output the velocity perturbation related to the current background. All of the above methods are fast and accurate inversions.

But as we know, sometime, we are not only interested in velocity inversion, but also in geometry in the imaging region. Next we will extend our tomography operators to invert for geometry in the imaging region.

If we omit the correlation procedure in above inversion equations, and directly input the raw reflection data into our BPT wavefield tomography operator, we have

$$\frac{\partial J}{\partial m} = \sum_{s,g} [a(\mathbf{r}_s, \mathbf{r}, \mathbf{r}_g)] ref(\mathbf{r}_s, \mathbf{r}_g, \tau(\mathbf{r}_s, \mathbf{r}, \mathbf{r}_g)]. \tag{14}$$

Also, if we don't separate down-going and up-going wave and use equation (14) to backproject the reflection data into model space directly, we will obtain many artifacts for the reflectivity of a given layer. This is because reflections from opposite directions take opposite signs when viewed from above or below the layer (Hu, 1988). If we modify equation (14) as follow

$$\frac{\partial J^{up}}{\partial m} = \sum_{s,g} a(\mathbf{r}_s, \mathbf{r}, \mathbf{r}_g) ref^{up}(\mathbf{r}_s, \mathbf{r}_g, \tau(\mathbf{r}_s, \mathbf{r}, \mathbf{r}_g)) \tag{15}$$

$$\frac{\partial J^{down}}{\partial m} = \sum_{s,g} a(\mathbf{r}_s, \mathbf{r}, \mathbf{r}_g) ref^{down}(\mathbf{r}_s, \mathbf{r}_g, \tau(\mathbf{r}_s, \mathbf{r}, \mathbf{r}_g)) \tag{16}$$

then, we can get the migration image which represents reflectivity. This means if we input up-going or down-going wavefield into our wavefield tomography operator, we can get a migration image so we call the procedure tomographic migration. The operators are first developed for velocity inversion, but we apply them to reflection data to get the geometry image. We use Fig. 1 to show how the wave tomography operators for velocity inversion compare with migration imaging.

SYNTHETIC AND REAL DATA TESTS

A synthetic model for crosswell imaging is presented in Fig. 2. We placed 40 sources in the left hole and 40 receivers in the right hole. We then use a ray method to produce the scattering field data and use our BPT operator to get the velocity perturbation picture as shown in Fig. 3. Next, we place three sources on the surface and locate 40 receivers in left hole and 40 receivers in the right hole. If we don't correlate the scattering data, using the time function $\dot{S}(-t)$, and use our BPT and SIRT operators, we get the results shown in Fig. 4 and Fig. 5, respectively. These represent geometry images of the scattering region. From Fig. 5, we can see if we also put sources on the bottom and don't correlate with the time function $\dot{S}(-t)$, and input the scattering field excited by both the top and bottom sources, we will get a null picture, i.e., the top and bottom data will cancel.

CONCLUSIONS

In order to obtain a high resolution inversion image and save computation time and computer memory, two wavefield tomography operators using asymptotic ray theory have been developed. Through demonstration with a synthetic example and the field data example, we believe that our methods will become very useful tools not only for velocity inversion but also for migration imaging. Next we will apply our BPT and SIRT wavefield tomography operators to real scattering field data for velocity perturbation inversion.

ACKNOWLEDGMENTS

This work is supported by the Seismic Tomography Project of Stanford University, a research consortium sponsored by companies of the oil and gas industry. The second author would like to thank Nicholas Smalley for his help in obtaining the up-going and down-going wavefields for the Devine data set, and Youli Quan and Mark Van Schaack for their help in processing and plotting pictures with computer network of STP.

REFERENCES

Harris, J.M. and Feng Yin, Nonlinear-frequency wave equation inversion, in 1994 STP report

Herman, G.T., Imaging reconstruction from projections, Academic Press, New York,

Lazaratos, Spyros K., et. al., High resolution imaging with crosswell reflection data, Seismic tomography project, Vol. 2, No.1, 1991

Hu, L.Z, McMechan, G.A. and Harris, J.M., Acoustic prestack migration of cross-hole data, Geophysics, 53, 1015-1023, 1988

Miller D., Oristaglio, M., and Beylkin, G., 1987, A new slant on seismic imaging: Migration and integral geometry: Geophysics, 52, 943-964.

Tarantola, A., The seismic reflection inversion problem. In: Inverse problems of Acoustic and Elastic Waves: Santosa, F., Pao, Y.H.., Symes, W. and Holland, Ch.(eds.), Society of Industrial and Applied Mathematics, Philadelphia, 1984.

Yin Feng, Geophysical diffraction tomography using waveform as projection, 63th Ann. Intern. SEG. Mtg.., Expanded Abstracts:57-59, 1993.

Yin F., B.L. Gu and Y. Wei, Ray tracing tomography for cross-hole exploration, Chinese Journal of Geophysics, Vol. 34, No. 4, 667-666, 1991.

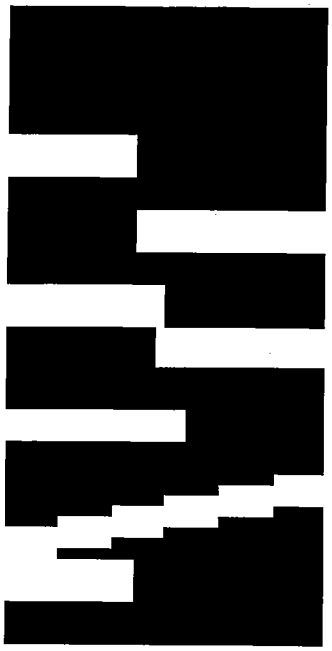

Figure 2:A scattering model for computer simulation.

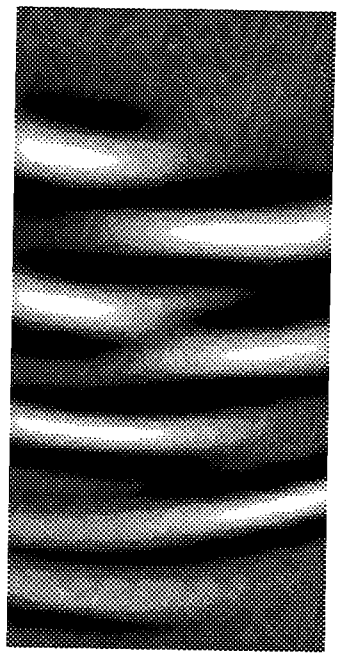

Figure 3: Velocity perturbation image by SIRT wave field tomography operator

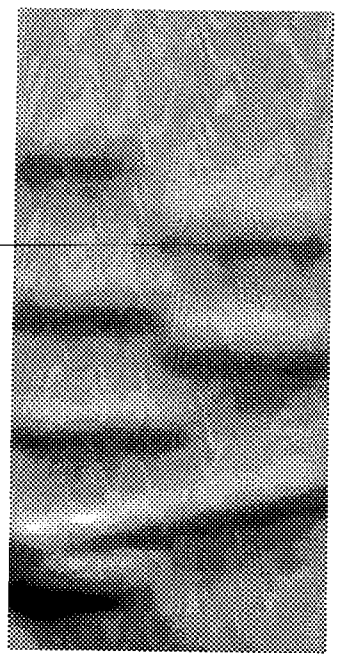

Figure 4: Geometry image of the scattering region by BPT wave field tomography operator

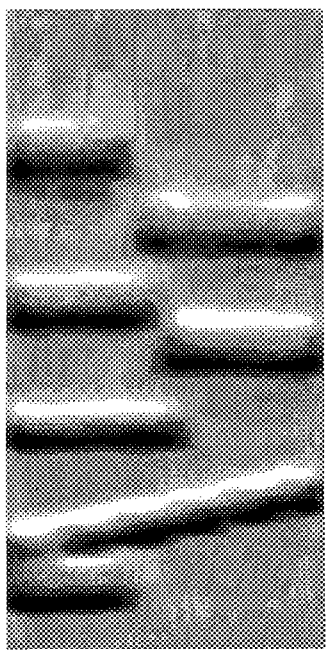

Figure 5: Geometry imaging of the scattering Region by SIRT wave field tomography operator

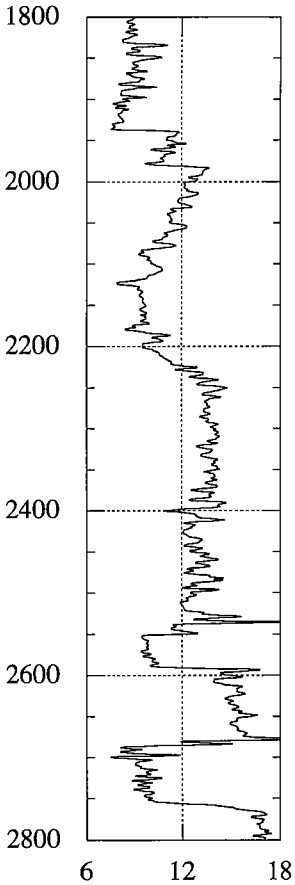

Figure. 6: Sonic log

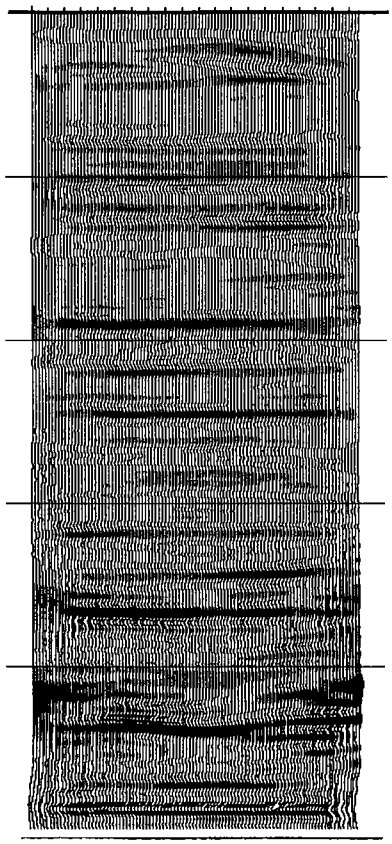

Figure 7: Reflection imaging by our BPT wave field tomography operator using Devine dataset

Figure 8: Traveltime tomography

PAPER R

WAVEFORM TOMOGRAPHY FOR TWO PARAMETERS IN ELASTIC MEDIA

Feng Yin

ABSTRACT

In this paper, we developed one waveform tomography method for P velocity and density inversion in elastic media. Starting from the elastic wave equation, we derived one P wave equation which includes the scattered terms of P-wave to P-wave conversion and S-wave to P-wave conversion. By discretizing the scattering integral equation corresponding to this equation directly, we can obtain one equation corresponding to each point on the waveform. The result of this formulation is a very large system of algebraic equations that is solved using ART and SIRT. The results of computational simulation applied to cross-hole geometry show that our method is valid when the velocity and density perturbation is not very large. Next we will extend this method to heterogeneous media and apply it to real field data.

INTRODUCTION

Recently, the wave equation tomography methods based on acoustical wave equation have been applied to the real cross-hole data (Harris and Wang,1993). Therefore, these methods become more attractive in the inversion field. But, there are many complicated wave events contained in seismogram data, e.g., S wave, mode converted wave, Rayleigh waves, etc. , which can not be described by an acoustical equation. However, each of the different events provides useful information about the subsurface compressional and shear wave velocities and all these events can be modeled well by the elastic wave equation. Therefore, we should develop the inversion methods based on elastic wave equation to obtain more physical parameters of the media. In elastic wave equation inversion studies, one method is to find the parameters (P- and S-wave velocities and density) that minimize the square error between the wavefield

computed using this model and the observed wavefield (Tarantola, 1984; Mora, 1986). But in this method, the seismogram must be calculated by solving the 2D elastic wave equation numerically in each iteration, therefore, the computation of this method is very costly. In order to simplify the inverse problem, some researchers considered a one dimensional inverse problems (Norton and Testard, 1988) and obtained a better inversion solution. However, the media of the earth usually are two dimensional, and in this case, this method is unvalid. Additionally, some only used the SH wave in their inversion method (Hooshyer and Weglein, 1986). In this case, the equation for inversion can be reduced to a scalar equation, but the SH wave is independent of P wave and SV wave, and therefore, the SH wave can only invert shear modulas and density. In order to obtain Lamé parameters and density in two dimensional elastic media effectively, we should develop the inversion methods based on the P wave equation.

In this paper, starting from the 2D isotropic inhomogeneous elastic wave equation, the scattering theory in weak inhomogenous media is studied. We also establish a scalar P wave equation which includes the scattered terms of P-wave to P-wave conversion and S-wave to P-wave conversion. From this equation, a scattering integral equation in the frequency domain is derived. Under the Born and geometrical optical approximation, we show how the time-domain scattered fields can be related to density and velocity perturbations through a generalized Radon transform. Therefore, time-domain P-wave scattered fields can be used as projection data to relate each point in the scattered waveform to the elastic parameters. The result of this formulation is a very large system of algebraic equations that is solved using ART and SIRT. The algorithm is tested on numerically simulated data generated for the cross-hole geometry of sources and receivers. The test results illustrate the ease of implementation and robustness of the method.

THEORY OF P WAVE SCATTERING IN WEAK INHOMOGENEOUS MEDIA

From 2D isotropic inhomogeneous elastic wave equation, we have

$$\frac{\partial^2 \mathbf{u}}{\partial t^2} = c_p^2 \nabla(\nabla \cdot \mathbf{u}) - c_s^2 \nabla \times (\nabla \times \mathbf{u}) + \frac{1}{\rho}\left[(\nabla\lambda)\nabla \cdot \mathbf{u} + (\nabla\mu)\cdot(\nabla\mathbf{u}) + (\nabla\mathbf{u})\cdot(\nabla\mu)\right] \quad (1)$$

where $\mathbf{u}=\mathbf{u}(\mathbf{x},t)$, it is displacement field, c_p, c_s are velocity of P wave and S wave, μ, λ, ρ are shear modula, Lame parameter and density of elastic media.

Assuming that the background is homogeneous and its elastic parameters are $c_{p0}^2, c_{s0}^2, \lambda_0, \mu_0, \rho_0$, and corresponding perturbation parameters due to heterogeneities are $\delta c_p^2, \delta c_s^2, \delta\lambda, \delta\mu,$ and $\delta\rho$, we have

$$c_p^2 = c_{p0}^2 + \delta c_p^2, \qquad c_s^2 = c_{s0}^2 + \delta c_s^2,$$

$$\lambda = \lambda_0 + \delta\lambda, \qquad \mu = \mu_0 + \delta\mu, \tag{2}$$

$$\text{and } \rho = \rho_0 + \delta\rho.$$

Putting equation(2) into equation (1), we have

$$\frac{\partial^2 \mathbf{u}}{\partial t^2} = c_{p0}^2 \nabla(\nabla \cdot \mathbf{u}) - c_{s0}^2 \nabla \times (\nabla \times \mathbf{u}) + \mathbf{B}, \tag{3}$$

where

$$\mathbf{B} = \delta c_p^2 \nabla(\nabla \cdot \mathbf{u}) - \delta c_s^2 \nabla \times (\nabla \times \mathbf{u}) + \frac{1}{\rho_0}[(\nabla\delta\lambda)(\nabla\mathbf{u}) + (\nabla\delta\mu)\cdot(\nabla\mathbf{u}) + (\nabla\mathbf{u})\cdot(\nabla\delta\mu)]. \tag{4}$$

By defining

$$\Phi = \nabla \cdot \mathbf{u}(\mathbf{x}, t) \tag{5}$$

and taking divergence of both sides of equation (3), we have

$$\frac{\partial^2 \Phi}{\partial t^2} - c_{p0}^2 \nabla^2 \Phi = \nabla \cdot \mathbf{B} \tag{6}$$

where

$$\nabla \cdot \mathbf{B} = \nabla \cdot [(2\delta c_p^2 + \frac{\delta\rho}{\rho_0} c_{p0}^2)] \nabla\Phi - (\delta c_p^2 + \frac{\delta\rho}{\rho_0} c_{p0}^2) \nabla^2 \Phi$$

$$-\nabla \cdot [(2\delta c_s^2 + c_{s0}^2 \frac{\delta\rho}{\rho_0}) \nabla \times (\nabla \times \mathbf{u})] \tag{7}$$

in which the second derivative of $\delta\lambda, \delta\mu$ and $\delta\rho$ with respect to space position are omitted due to the weak inhomogeneous media assumption.

By taking the Fourier transform over time t on both sides of equation (7), we derive the equation in frequency domain,

$$\nabla^2\tilde{\Phi}+k_{p0}^2\tilde{\Phi}=-\frac{1}{c_{p0}^2}\nabla\cdot\tilde{\mathbf{B}}, \tag{8}$$

where $\tilde{\Phi}$ and $\tilde{\mathbf{B}}$ are the Fourier transform of Φ and $\mathbf{B}$ with respect to time t.

By defining

$$b_1(\mathbf{x})=2\delta c_p^2/c_{p0}^2+\delta\rho/\rho_0\ , \tag{9}$$

$$b_2(x)=\delta c_p^2/c_{p0}^2+\delta\rho/\rho_0\ , \tag{10}$$

$$b_3(x)=2\delta c_s^2/c_{p0}^2+c_{s0}^2/c_{p0}^2\frac{\delta\rho}{\rho_0}, \tag{11}$$

,

therefore, equation (8) can be recast as

$$\nabla^2\tilde{\Phi}+k_{p0}^2\tilde{\Phi}=-\nabla\cdot[b_1(\mathbf{x})\nabla\tilde{\Phi}]+b_2(x)\nabla^2\tilde{\Phi}+\nabla\cdot[b_3(x)\nabla\times(\nabla\times\mathbf{u})] \tag{12}$$

In the right hand side of above equation, there are three terms, the first two terms belong to the scattering sources of P to P wave, the third term comes from the S wave to P wave conversion due to the inhomogeneous perturbation in elastic media.

Let

$$\tilde{\Phi}=\tilde{\Phi}_{in}+\tilde{\Phi}_{sc}\ , \tag{13}$$

where $\tilde{\Phi}_{in}$ is the incident field in the background media, which satisfies

$$\nabla^2\tilde{\Phi}_{in}+k_{p0}^2\tilde{\Phi}_{in}=s(\omega)\delta(\mathbf{x}-\mathbf{x}_s)\ . \tag{14}$$

In this equation $s(\omega)$ is source function, $\mathbf{x}_s$ is the position of the source, and the scattering field $\tilde{\Phi}_{sc}$ can be expressed as

$$\begin{aligned}\tilde{\Phi}_{sc}(\mathbf{x},k_{p0})=-S(\omega)\cdot\int_{\Omega}d\mathbf{x}'\{&\nabla\cdot(b_1(\mathbf{x}')\nabla\tilde{\Phi})-b_2(\mathbf{x}')\nabla^2\tilde{\Phi}\\&-\nabla\cdot[b_3(\mathbf{x}')\nabla\times(\nabla\times\mathbf{u})]\}\mathrm{G}(\mathbf{x},\mathbf{x}',\mathrm{k}_{p0})\end{aligned} \tag{15}$$

where $\mathrm{G}(\mathbf{x},\mathbf{x}',\mathrm{k}_{p0})$ is the Green function, which satisfies

$$\nabla^2 G_0 + k_{p0}^2 G_0 = \delta(\mathbf{x} - \mathbf{x}') \tag{16}$$

From equation (15), we know that the scattering fields are produced by three perturbation parameters. Next we will develop one waveform tomography method to invert for parameters $b_1(\mathbf{x})$ and $b_2(x)$. For $b_3(x)$ inversion, the S wave scattering problem should be consider, it will be studied in the future.

WAVEFORM TOMOGRAPHY METHOD FOR P VELOCITY AND DENSITY

In our imaging method, the P wave point source is used to illuminate the object region. Then, applying the Born approximation to equation (15), the total field $\tilde{\Phi}$ and $\mathbf{u}$ in the integral equation (15) can be replaced by incident field $\tilde{\Phi}_{in}$ and $\mathbf{u}_{in}$, where $\mathbf{u}_{in}$ is displacement field of incident P wave. Therefore, $\nabla \times \mathbf{u}$=0 in equation (15), and the third term is omitted. Notice that $\tilde{\Phi}_{in}$ satisfies equation (14),. Therefore, the second term in equation (15) can be simplified as

$$-\int dx' b_2(x') \nabla^2 \tilde{\Phi}_{in} G(\mathbf{x}, \mathbf{x}', k_{p0}^2) = k_{p0}^2 \int dx' b_2(x') \tilde{\Phi}_{in} G(\mathbf{x}, \mathbf{x}', k_{p0}^2) \,. \tag{17}$$

Under the Born approximation, equation (15) can be expressed as

$$\tilde{\Phi}_{sc}(\mathbf{x}, k_{p0}) = -S(\omega) \cdot \int_{\Omega} d\mathbf{x}' \{\nabla \cdot (b_1(\mathbf{x}') \nabla \tilde{\Phi}_{in}) + k_{p0}^2 b_2(\mathbf{x}') \tilde{\Phi}_{in}\} G(\mathbf{x}, \mathbf{x}', k_{p0}^2) \tag{18}$$

Applying the geometrical optical approximation, we have

$$\tilde{\Phi}_{sc}(\mathbf{x}, k_{p0}) = -S(\omega) \cdot \int_{\Omega} d\mathbf{x}' \{\nabla \cdot (b_1(\mathbf{x}') \nabla A(\mathbf{x}', \mathbf{x}_s) e^{-i\omega T(\mathbf{x}', \mathbf{x}_s)})$$

$$+ k_{p0}^2 b_2(\mathbf{x}') A(\mathbf{x}', \mathbf{x}_s) e^{-i\omega T(\mathbf{x}', \mathbf{x}_s)}\} \cdot A(\mathbf{x}, \mathbf{x}') e^{-i\omega T(\mathbf{x}, \mathbf{x}')} \cdot \frac{c_0}{i\omega} \,, \tag{19}$$

where the amplitude A and travel time T satisfy the transport equation and eikonal equation, respectively.

By using Green's theorem in the plane and assuming that b_1 and b_2 =0 on the boundary of the imaging region, we have

$$\tilde{\Phi}_{sc}(\mathbf{x},k_{p0}) = i\omega S(\omega)\int_{\Omega} d\mathbf{x}' a(\mathbf{x},\mathbf{x}',\mathbf{x}_s)(b_1(\mathbf{x}')\cdot\cos(\theta)+b_2(\mathbf{x}'))e^{-i\omega\tau(\mathbf{x},\mathbf{x}',\mathbf{x}_s)} \quad (20)$$

where

$$a(\mathbf{x},\mathbf{x}',\mathbf{x}_s) = A(\mathbf{x}',\mathbf{x}_s)A(\mathbf{x},\mathbf{x}')/c_0, \quad (21)$$

$$\tau(\mathbf{x},\mathbf{x}',\mathbf{x}_s) = T(\mathbf{x}',\mathbf{x}_s)+T(\mathbf{x},\mathbf{x}') . \quad (22)$$

and θ is the angle between $\nabla T(\mathbf{x}',\mathbf{x}_s)$ and $\nabla T(\mathbf{x},\mathbf{x}')$.

Taking the inverse Fourier transform of both sides of equation (22), we obtain the scattering field in time domain as

$$\Phi_{sc}(\mathbf{x},t) = W(t) * \int_{\Omega} d\mathbf{x}' a(\mathbf{x},\mathbf{x}',\mathbf{x}_s)(b_1(\mathbf{x}')\cdot\cos(\theta)+b_2(\mathbf{x}'))\delta(t-\tau(\mathbf{x},\mathbf{x}',\mathbf{x}_s))$$

$$= W(t) * \int_{I(\tau)} a(\mathbf{x},\mathbf{x}',\mathbf{x}_s)(b_1(\mathbf{x})\cos(\theta)+b_2(\mathbf{x}))ds \quad (23)$$

where $W(t)=S'(t)$, convolution is denoted by *. The above equation is called a generalized Radon transform. I(τ) is an isochronic plane with a fixed time τ, from which the perturbation parameters can be related to the waveform. For each point on the waveform, we can derive one equation for inversion. For each pair of source and receiver $(\mathbf{x},\mathbf{x}_s)$, all the isochronic lines can cover the object region. when the spatial position of the source or receiver is moved, the direction of set of isochronic lines belonging to the same pair of source and receiver $(\mathbf{x},\mathbf{x}_s)$ is changed. Therefore, the projection in different direction can be derived, and we can use the waveform as a projection to invert for the elastic parameters.

Considering kth isochronic plane $I(t_k)$, equation (23) can be discetized as

$$d_k = W_k * \sum_m a(l_{km})\cdot(b_2(l_{km})\cos(\theta_{km})+b_1(l_{km}))\Delta s \quad (1\le k\le K, 1\le m\le M) \quad (24)$$

where $d_k = \Phi_{sc}(\mathbf{x},\mathbf{x}_s,t_k)$, $W_k = W(t_k)$, $K = L\times S\times R$, L, S and R are the total number of sampling points on the waveform, source and receiver, l_{km} is the length of kth isochronic line from the first point to mthpoint , M is the total numbers of the integral step along mth isochronic line, $a(l_{km})$, $b_1(l_{km})$ and $b_2(l_{km})$ are the values of $a(\mathbf{x},\mathbf{x}',\mathbf{x}_s)$, $b_1(\mathbf{x}')$ and $b_2(\mathbf{x}')$ at l_{km}, θ_{km} is the value of θ at point l_{km}, and Δs is the integral step. The object region is divided into $I\times J$ pixels. When the coordinate of l_{km} satisfies,

$i\Delta x \le x \le (i+1)\Delta x$, $i\Delta z \le z \le (i+1)\Delta z$, where Δx and Δz are the width of pixel in x and z direction, $1 \le i \le I$, $1 \le j \le J$.

By defining

$$\rho_{nkm} = \begin{cases} 1 & when \quad n = (j-1) \times J + i \\ 0 & when \quad n \ne (j-1) \times J + i \end{cases} \tag{25}$$

we have

$$b_1(l_{km}) = \sum_n \rho_{nkm} \cdot b_{1n} \qquad (1 \le n \le I \times J) \tag{26}$$

$$b_2(l_{km}) = \sum_n \rho_{nkm} \cdot b_{2n} \qquad (1 \le n \le I \times J), \tag{27}$$

where b_{1n} and b_{2n} are the values of $b_1(\mathbf{x}')$ and $b_2(\mathbf{x}')$ at n^{th} pixel. Puting equations (25)-(27) into equation (24), we have

$$d_k = W_k * \sum_n (c_{1kn} \cdot b_{1n} + c_{2kn} \cdot b_{2n}) \tag{28}$$

where

$$c_{1kn} = \sum_m a(l_{km}) \cdot \rho_{nkm} \cdot \Delta s \tag{29}$$

$$c_{2kn} = \sum_m a(l_{km}) \cdot \rho_{nkm} \cdot \cos(\theta_{km}) \cdot \Delta s \tag{30}$$

Let

$$g_{kn} = \begin{cases} c_{1kn} & when \quad 1 \le n \le I \times J \\ c_{2kn} & when \quad I \times J \le n \le 2 \times I \times J \end{cases} \tag{31}$$

$$f_{kn} = \begin{cases} b_{1n} & when \quad 1 \le n \le I \times J \\ b_{2n} & when \quad I \times J \le n \le 2 \times I \times J \end{cases} \tag{32}$$

Then equation (28) can be written as

$$d_k = W_k * \sum_n^{2IJ} g_{kn} \cdot f_n \tag{33}$$

Let

$$h_{kn} = \sum W_{k-l} g_{\ln} \qquad (1 \le l \le L) \tag{34}$$

then equation (33) can be written as

$$d_k = \sum_{n}^{2IJ} h_{kn} \cdot f_n \tag{35}$$

From equation (35), we can invert for P velocity and density using the waveform as the projection. In order to solve equation (35) effectively, the algorithms ART and SIRT are used to solve equation (35) to get the fast execution speed of the inversion. Then we have the following ART and SIRT iterative form:

$$f_n^{(q+1)} = f_n^{(q)} + \alpha \frac{h_{kn}}{\sum_n h_{kn}^2} (d_k - \sum_n h_{kn} \cdot f_n) \tag{36}$$

$$f_n^{(q+1)} = f_n^{(q)} + \beta \sum_k \frac{h_{kn}}{\sum_n h_{kn}^2} (d_k - \sum_n h_{kn} \cdot f_n) / z_n \tag{37}$$

where α, β are the weight factors, z_n is the non-zero numbers of h_{kn} $(1 \le k \le L \cdot S \cdot R)$.

By the above methods, the waveform can be used as the projection to invert for the parameters $b_1(x)$ and $b_2(x)$, and the P velocity and density can be obtained from them.

COMPUTATION SIMULATION

Now we apply the above method to the cross-well imaging system. At first, three sources are located on the surface to illuminate the imaging region, and for each source, 20 receivers located in the left well at x=-50m and 20 receivers located in right well at x=50m are used to receive the signal, respectively, Then 10 sources located in left well are used to illuminate the imaging region, and 20 receivers located in right well are used to receive the signal. The depth of the well is 200m. The source function we used is a ricker wavelet, the center frequency is 200 Hz. The imaging region is divided into 20 by 20 pixels, where he width of each pixel is 3 meters. Figure 1 and figure 2 are the P velocity and density perturbation models for the reconstruction test. The parameters of the background are: c_{p0} = 2500 m/s, ρ_0=2.3 g/cm^3 .The perturbation of P velocity and density are 10% with respect to the background values. Figure 3 and figure 4 are the

inverted results of P reconstruction and density by SIRT. Figure 5 and figure 6 are the reconstruction results of P velocity and density by ART. From figure 4 and figure 6, we can see the vertical resolution is not high in this imaging geometry. This is because there are not enough projections in the vertical direction. From the reconstruction results, we can see that the tomography results derived by SIRT are better than that by ART.

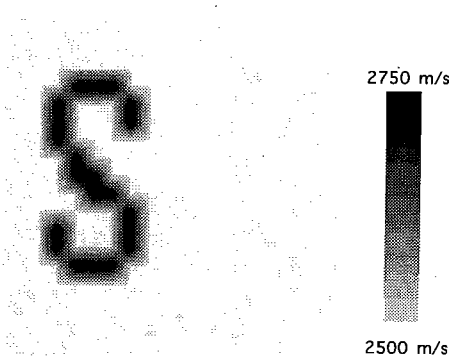

Figure 1. The synthetic P wave velocity model

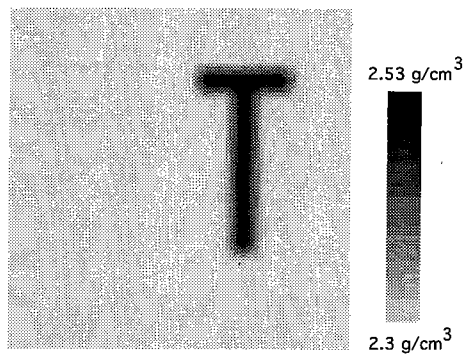

Figure 2. The synthetic density model

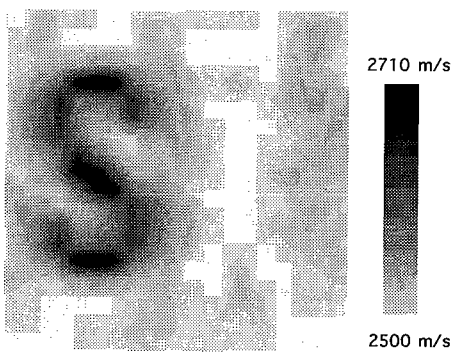

Figure 3. P velocity reconstructed result by SIRT method

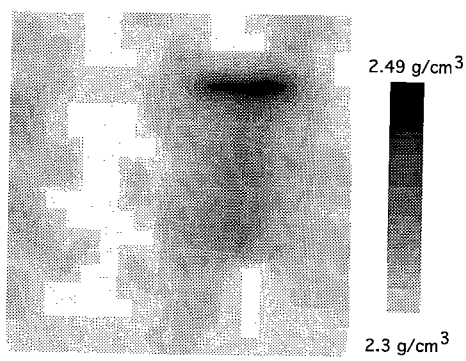

Figure 4. Density reconstructed result by SIRT

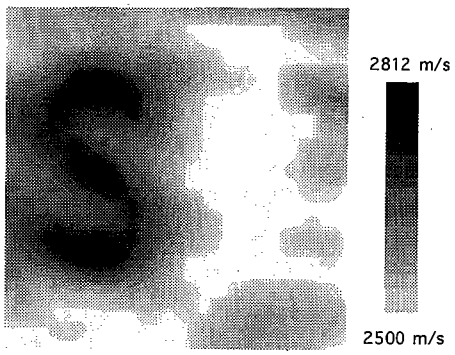

Figure 5. P velocity reconstructed result by ART method

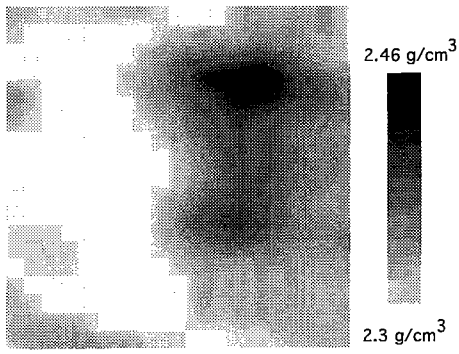

Figure 6. Density reconstructed result by ART

CONCLUSIONS

A new waveform tomography for P velocity and density in elastic media is put forward in this paper. Although the elastic wave equation inversion is a very complicated mathematics problem; this problem can be simplified immensely. Under the Born and geometrical optics approximation when starting from P wave equation, the waveform data can be related to the perturbation of P velocity and density by a generalized Radon transform. For each point on the waveform, discretizing this Radon transform can lead to one equation for these two parameters. Then back projection methods ART and SIRT are used to solve such a huge system. The numerical results show that this method is very robust to reconstruct P velocity and density. Although the Born approximation in real data application is limited, the main structure in the media can be estimated by use of it.

ACKNOWLEDGMENTS

This work is supported by the Seismic Tomography Project of Stanford University and a research consortium of the oil and gas industry. The author thanks Sonya Williams for her help in typing this paper and Nicholas Smalley for editing this paper.

REFERENCES

Harris, J. M. and G. Wang, Diffraction tomography for inhomogeneities in a layered background medium, Sixty-Third Annual Meeting and International Exposition of Society of Exploration Geophysicists, Expanded Abstracts, 49-52, 1993.

Hooshyar, M.A. and A.B. Weglein, Inversion of the two-dimensional SH elastic wave equation for the density and shear modulus, J.Acoust. Soc.Am., 78, 1280, 1986.

Norton, S.J. and L.R. Testard, Reconstruction of one-dimensional inhomogeneneities in elastic modulus and density using acoustical dimensional resonances, J.Acousti. Soc. Am., 79(4), 932-942,1988.

Miller, D., M. Oristaglio, and G. Beylkin, A new slant on seismic imaging: Migration and integral geometry, Geophysics, 57,7, 943-946, 1984.

Mora, P., Elastic wavefield inversion and adjoin operator for the elastic wave equation, in: Mathematical Geophysics, p.117-137, Edited by N. J. Valaar, G. Nolet, M.J.R. Wortel & S.A.P.L. Cloetingh, 1988 by P. Reidel Publishing Company.

Tarantola,A., 1984, The seismic reflection inverse problem, Inverse Problems of Acoustic and Elastic waves, edited by F. Santosa, Y.H.Dao, W.Symes and Ch. Holland, SIAM, Philadelplia.

PAPER S

DIFFRACTION TOMOGRAPHY USING MULTISCALE FOURIER TRANSFORMS

Guan Y. Wang

ABSTRACT

To overcome the difficulty resulting from a strongly non-uniform medium, a variable background is chosen to maintain a weak contrast between the scatterers and the background so that the single scattering approximation is still valid. Assuming that the amplitude variation of the wave field, due to propagation, is less than the phases, the Green's function of variable background can be treated as the Green's function associated with a constant reference background modified by a phase distortion function. The spectrum of the scattering field is expressed as a planar integral of harmonic oscillators. Each oscillator possesses an amplitude consisting of the scattering potential and a nonlinear phase. The phase factor is further expanded into Fourier series. The inverse Fourier transform applied to the filtered spectrum of the measurements is equivalently applied to each harmonic component in the series which results in multiscale images. The complete image is obtained, via Mobius transform, with those multiscale images.

INTRODUCTION

The image reconstructed with the ray tomography has the resolution only on the scale of first Fresnel zone even for full aperture. When a higher resolution result is required, such as in reservoir imaging, other wave phenomena should also be utilized in addition to transmission traveltimes. The resolution of the reconstruction with diffraction tomography is about one wavelength. The existing diffraction tomographic inversions are mainly based on plane wave expansion and Fourier transform techniques for uniform background medium (Devaney, 1982, Harris, 1987, Wu and Toksoz, 1987). Such methods are simple to implement but do not work well when the background medium is strongly non-uniform. One way to overcome the problem of the strong inhomogeneity of the medium is to apply the distorted Born approximation (Devaney, et al. 1983). This consists

of adopting a variable background to maintain a weak contrast between the perturbation and the background medium. However, under the distorted Born approximation, the difficulty is not only how to find the Green's function associated with the variable background but also the Green's function generally has little use for utilizing Fourier transform techniques to reconstruct images. This is why most proposed algorithms dealing with variable background are restricted to some special case. For example, the case of 1-D medium in which the problem is greatly simplified (Dickens, 1992, Huan, 1992).

By introducing a reference medium and the WKBJ Green's functions, and assuming the amplitude variations due to the variation of the background is less the phases, we reformulate the inverse scattering problem of an arbitrary 2-D host medium such that the spectrum of the scattered field is expressed as a planar integral of harmonic oscillators. The oscillator possesses an amplitude which consists of the scattering potential and a nonlinear phase. In order to utilize Fourier transform reconstruction techniques, the phase factor is expanded into Fourier series. The inverse Fourier transform applied to the spectrum of the measurements is equivalently applied to each harmonic component in the series which leads to the construction of the images with different scales. The complete image is combined, via Mobius inversion, from those components with different scales. The reconstruction algorithm is essentially the same as that of Fourier diffraction tomography for a constant host medium, except that we first construct the images with different scales and then combine them together.

SPECTRUM OF SCATTERED FIELD FROM A HARMONIC OSCILLATOR MODEL

For a variable background medium, the scattered field generated by an inhomogeneity perturbed over a variable background can be written as

$$u^{sc}(s,g) = \int o(r)u(r,s)\tilde{G}(g,r)dr \qquad (1)$$

where $\tilde{G}$ is the Green's function of the background. With distorted Born approximation, the equation (1) is liberalized as

$$u^{sc}(s,g) = \int o(r)\tilde{G}(r,s)\tilde{G}(g,r)dr \qquad (2)$$

Generally, it is difficult to find the Green's $\tilde{G}$ function associated with the variable background. By introducing the Green's functions of a constant reference background, we can rewrite equation (2) as

$$u^{sc}(s,g) = \int o(r) \frac{\tilde{G}(r,s)\tilde{G}(g,r)}{G(r,s)G(g,r)} G(r,s)G(g,r)dr, \tag{3}$$

where $G(r,s)$ and $G(g,r)$ are the Green's functions associating with the reference background. By replacing the Green's functions in $\frac{\tilde{G}(r,s)\tilde{G}(g,r)}{G(r,s)G(g,r)}$ with corresponding WKBJ forms,

$$\tilde{G}(r,r') = A(r,r')e^{-i\theta(r,r')} \text{ and } G(r,r') = \frac{1}{|r-r'|} e^{-ik\cdot|r-r'|},$$

and neglecting the variation of the amplitude due to the variation of the background, i.e., assuming

$$\frac{A(r,s)}{|r-s|} \approx 1, \text{ and } \frac{A(g,r)}{|g-r|} \approx 1,$$

we have

$$\frac{\tilde{G}(r,s)\tilde{G}(g,r)}{G(r,s)G(g,r)} \approx e^{i\phi(r)}, \tag{4}$$

where $\phi(r)$ is the phase distortion resulting from the "variation" of the background medium. Substituting (4) into equation (3) leads to

$$u^{sc}(s,g) = \int o(r)e^{i\phi(r)}G(r,s)G(g,r)dr. \tag{5}$$

We can see that equation (5) is the same as in the case of the uniform background medium, except that the integrand is modified by a phase distortion function. In a 2-D medium with a line source, the Green's function is the Hankel function of first kind and zero order, i.e.,

$$G(r,r') = \frac{i}{4} H_0^{(1)}(\bar{k}|r-r'|).$$

Taking the Fourier transform of equation (5) over s and g , which is decomposing the cylindrical wave into plane waves, we have

$$u^{sc}(k_s,k_g)4\gamma_s\gamma_g e^{-i(\gamma_s d_s+\gamma_g d_g)} = \int o(r)e^{-ik(r)\cdot r}dr, \qquad (6)$$

where d_S, - d_g is the separation between source and receiver well, $\gamma_s = \sqrt{\bar{k}^2 - k_s^2}$ and $\gamma_g = \sqrt{\bar{k}^2 - k_g^2}$. $\bar{k} = (\bar{k}_x, \bar{k}_z) = (\gamma_g - \gamma_s, k_s + k_g)$ is the wave vector in the reference medium. The resultant wave vector $k(r) = \bar{k}(1 - \frac{\Delta v(r)}{\bar{v}})$, where $\Delta v(r)$ is the variation on the top of the reference medium $\bar{v}$. The equation (6) states that the spectrum of the scattered field is generated equivalently by an "harmonic oscillator" $o(r)e^{-ik(r)\cdot r}$ located at each image point. The oscillator possesses the amplitude o*(r)* and the nonlinear phase $\phi(r) = k(r)\cdot r$.

RECONSTRUCTION WITH MULTISCALE FOURIER TRANSFORMS

Equation (6) is not a conventional Fourier type integral, since the resultant wave vector *k(r)* is spatially variant. We can not directly reconstruct the scattering potential function *o(r)* via the inverse Fourier transform. One way to overcome this difficulty is to expand phase function $p(x,z) = e^{i[k_x(x,z)x + k_z(x,z)z]}$ into a Fourier series with $\bar{k}$ as the fundamental wave number, and then treat each harmonic separately. Notice that *p(x,z)* is defined in the rectangle region $0 \le x \le L,\ 0 \le z \le H$. If we extend p(x,z) into a periodic odd function with periods of L and H in the horizontal and vertical directions respectively, i.e.,

$$odd(x,z) = \begin{cases} p(x,z) & 0 \le x \le L,\ 0 \le z \le H \\ -p(-x,z) & -L \le x < 0,\ 0 \le z \le H \\ -p(x,-z) & 0 \le x \le L,\ -\mathrm{H} \le z < 0 \\ p(-x,-z) & -L \le x < 0,\ -\mathrm{H} \le z < 0, \end{cases}$$

and

$$odd(x+2L,z) = odd(x,z)$$
$$odd(x,z+2H) = odd(x,z), \qquad x,z \in (-\infty,\infty)$$

then the finite sine transform of *odd(x,z)* can be written as

$$P(m,n) = \frac{4}{L \times H} \int_0^L \int_0^H p(x,z) \sin(\bar{k}_x mx) \sin(\bar{k}_z nz) dxdz,$$

where L and H are the width and height of the image domain respectively. With the above definitions, we can expand p(x,z) as

$$p(x,z) = \sum_{m,n=1}^{\infty} P(m,n) \sin(\bar{k}_x mx) \sin(\bar{k}_z nz). \tag{7}$$

Substituting expansion (7) into equation (6) and interchanging the order of the summation and integration we obtain

$$\begin{aligned} &u^{sc}(k_s,k_g) 4\gamma_s \gamma_g e^{-i(\gamma_s d_s + \gamma_g d_g)} = \\ &\sum_{m,n=1}^{\infty} P(m,n) \int o(x,z) \sin(\bar{k}_x mx) \sin(\bar{k}_z nz)\} dxdz. \end{aligned} \tag{8}$$

From equation (8) we can see that the filtered spectrum of the measurement on the left side of the equation is related to a series of weighted multiresolution potential spectra on the right side. Taking the inverse Fourier transform to both sides of equation (8) we obtain

$$\begin{aligned} &FT^{-1}\{u^{sc}(k_s,k_g) 4\gamma_s \gamma_g e^{-i(\gamma_s d_s + \gamma_g d_g)} |J(\bar{k};k_s,k_g)|\} = \\ &\sum_{n=1}^{\infty} \frac{P(m,n)}{-4} \{o(\frac{x}{m},\frac{z}{n}) - o(\frac{-x}{m},\frac{z}{n}) - o(\frac{x}{m},\frac{-z}{n}) + o(\frac{-x}{m},\frac{-z}{n})\}, \end{aligned} \tag{9}$$

where $J(\bar{k};k_s,k_g)$ is the Jacobean transformation from $(\bar{k}_x,\bar{k}_z)$ to (k_s,k_g). Notice that the average value of the image is not computed correctly by the finite algorithm, since it will evaluate the spectrum at the origin as zero. The D.C. component of the image is restored by computing it directly form the data as $4u^{sc}(0,0)e^{-i\bar{k}L} / L \times H$.

In the case of a constant background medium, equation (9) would be the reconstructed scattering potential function. Now, after the inverse Fourier transform is applied to equation (9), instead of the potential function itself, a summation of multiscale components of the potential function is reconstructed. The role of the harmonic indexes m and n is that of the scale lengths in the Wavelet transforms. Consequently, the component $o(\frac{x}{m},\frac{z}{n})$ is an image with a specific scale. With large scale length, i.e., small m and n,

$o(\frac{x}{m},\frac{z}{n})$ provides a global view, while small scales, i.e., large m and n, $o(\frac{x}{m},\frac{z}{n})$ provide increasingly detailed views of smaller subsets of the image. The remaining problem is to invert equation (9), i.e., to combine those multiscale images into a complete image.

MULTISCALE INVERSION VIA MOBIUS TRANSFORM

We want to invert the scattering potential function $o(x,z)$ using equation (9), which can be rewritten as

$$d(x,z)=\frac{-1}{4}\sum_{m,n=1}^{\infty}\frac{P(m,n)}{mn}o(\frac{x}{m},\frac{z}{n}), \tag{10}$$

where $d(x,z)=FT^{-1}\{u^{sc}(k_s,k_g)4\gamma_s\gamma_g e^{-i(\gamma_s d_s+\gamma_g d_g)}|J(\bar{k};k_s,k_g)|\}$. Losing no generality, we have assumed $o(x,z)=-o(-x,z)=-o(x,-z)=o(-x,-z)$ in equation (9). According to Mobius inversion theorem (Hardy, 1979, Chen, N. 1989), if

$$F(x)=\sum_{n=1}^{\infty} f(\frac{x}{n}) \tag{11}$$

then

$$f(x)=\sum_{n=1}^{\infty}\mu(n)F(\frac{x}{n}), \tag{12}$$

where Mobius function

$$\mu(n)=\begin{cases}1 & \text{n = 1}\\ (-1)^r & \text{n include r distinct prime factors}\\ 0 & \text{otherwise.}\end{cases}$$

Applying Mobius transform (12) to equation (10) we obtain the complete image of the scattering potential

$$o(x,z)=\frac{-4}{P(1,1)}\sum_{m,n=1}^{\infty}\frac{\mu(m)\mu(n)}{mn}d(\frac{x}{m},\frac{z}{n}). \tag{13}$$

Note that $\left| d(\frac{x}{m},\frac{z}{n}) / mn \right| \le \frac{const.}{mn}$. Therefore, the series (13) is absolutely convergent. Equation (13) can be explicitly written as

$$o(x,z) = \frac{-4}{P(1,1)} \sum_{m,n=1}^{\infty} \frac{\mu(m)\mu(n)}{mn} \times \int u^{sc}(k_s,k_g) 4\gamma_s\gamma_g e^{-i(\gamma_s d_s + \gamma_g d_g)} |J(\bar{k};k_s,k_g)| e^{i(\bar{k}_x \frac{x}{m} + \bar{k}_z \frac{z}{n})} dk_s dk_g \tag{14}$$

which states that the potential function is reconstructed by summing a series of multiscale inverse Fourier transforms of the filtered spectra of the measurement.

It is convenient to use $u^{sc}(k_S,k_g,\omega/n)$ instead of $u^{sc}(nk_S,nk_g,\omega)$ in the computation. It can be show that $u^{sc}(k_S,k_g,\omega/n) = u^{sc}(nk_S,nk_g,\omega)$. Thus,

$$o(x,z) = \frac{-4}{P(1,1)} \sum_{m,n=1}^{\infty} \frac{\mu(m)\mu(n)}{mn} \times n\int u^{sc}(nk_s,nk_g,\omega) 4\hat{\gamma}_s\hat{\gamma}_g e^{-i(\hat{\gamma}_s d_s + \hat{\gamma}_g d_g)} |J(\bar{k};nk_s,nk_g)| e^{i(\bar{k}_x \frac{x}{m} + \bar{k}_z z)} dk_s dk_g \tag{15}$$

and

$$o(x,z) = \frac{-4}{P(1,1)} \sum_{m,n=1}^{\infty} \frac{\mu(m)\mu(n)}{mn} \times n\int u^{sc}(k_s,k_g,\frac{\omega}{n}) 4\hat{\gamma}_s\hat{\gamma}_g e^{-i(\hat{\gamma}_s d_s + \hat{\gamma}_g d_g)} |J(\bar{k};k_s,k_g)| e^{i(\bar{k}_x \frac{x}{m} + \bar{k}_z z)} dk_s dk_g \tag{16}$$

CONCLUSIONS

We have presented a formulation of diffraction tomography for variable background medium which relates the filtered spectrum of the measurement to multiscale spectra of the scattering potential resulting from the Fourier expansion of the spatially variant phase function. The potential function is recovered from multiscale components via Mobius inversion. As well as the applicability to strongly non-uniform medium, the method can be easily implemented and is computationally efficient, since the algorithm is similar to what is used in a constant background medium.

ACKNOWLEDGMENT

I would like thank Lewei Mo for providing the finite difference modeling code, and Youli Quan and Nicholas Smalley for their valuable comments and suggestions. The paper was edited by Nicholas Smalley. The author is grateful for his help.

REFERENCE

Chen, Nan-xian, 1989, Modified Mobius Inverse Formula and its application in physics, Physical review letters, 64, 11.

Devaney A. J., Oristaglio, 1983, Inversion procedure for inverse scattering within the distorted-wave Born approximation: Phys. Rev. Letters 51, 237

Devaney, A. J., 1984, Geophysical diffraction tomography, IEEE trans. Geosci. remote, GE-22, 3-13.

Dickens, T. A., 1992, Study of diffraction tomography for layered backgrounds: SEG expanded abstract.

Hardy, G. H. and Wright, E. M., 1979, An introduction to the theory of numbers: Oxford University Press, Oxford, 5th ed.

Harris, J. M. 1987, Diffraction tomography with arrays of discrete sources and receivers: IEEE trans. Geosci. remote, GE-25(4), 448-455.

Huan, L., Wu, R. 1992, Multifrequency backscattering tomography: extension to the case of vertical varying background: SEG expanded abstract.

Wu, R. and Toksoz, M. N. 1987, Diffraction tomography and multi-source holography applied to seismic imaging: Geophysics, 52, 11-25.

PAPER T

DIFFRACTION TOMOGRAPHIC INVERSION: FIELD DATA STUDY

Guan Y. Wang

ABSTRACT

The field data from McElroy and King Mountain test sites are studied using diffraction tomographic inversion techniques. The diffraction tomography methods with uniform and stratified background media are applied to single frequency wave fields. In the reconstructed scattering potential and velocity images, the fine scale structures and subtle dips are apparent but absent in the traveltime tomogram. The results show that diffraction and scattering inversion techniques have enormous potential in subsurface characterization and delineation with comparison to the transmission tomography.

INTRODUCTION

Small changes of velocities superimposed on large stratified variations is of interest to reservoir imaging. The general theory of diffraction indicates that diffraction tomography has the potential to achieve maximum spatial resolution and minimum image distortion for crosswell seismic data. In this paper we study the field data from McElroy and King Mountain test sites in West Texas using diffraction tomographic inversion techniques. Although powerful, the applications of the diffraction inversion methods are successful only if the heterogeneity represents small deviations from background, and if the correlation lengths of these deviations are large compared to a wavelength. With these limitations in mind, we use diffraction tomography in conjunction with traveltime tomography. Traveltime tomography does not explicitly depend upon any assumption about the scale, the strength of the variations in the inhomogeneity, and yields velocities from virtually any starting model. The resulting images then can be adequately used as reference velocities or the background model for diffraction tomography. We also account for variable background velocity using the distorted Born approximation to make the reconstruction more accurate.

The paper is divided into two sections. In the first section, the methodology used for the inversion is described briefly. The reconstructed images of McElroy and King Mountain are presented in section two with the detail discussions and comparison. The results illustrate the enormous potential of scattering and diffraction inversion techniques to usefully address reservoir delineation and characterization problems.

METHODOLOGY DESCRIPTIONS

Since diffraction tomography is used to deal with scattered effects, a background or host medium model is needed to calculate the illuminating field. This is difficult for a real experiment since the host medium is not known. Our intention is that traveltime and diffraction tomography should be used in conjunction with each other to provide high resolution images. Ray tomography does not explicitly depend upon any assumption about the scale, the strength of the variations in the inhomogeneity, and yields velocities from virtually any starting model. The resulting images then can be adequately used as reference velocities or the background model for diffraction tomography. It can be shown that ray tomography is a special case of diffraction tomography. Therefore, this complementary nature of two processes is justified. We apply the method of diffraction tomography for a stratified background medium (Harris and Wang, 1993) to field data from the McElroy field in West Texas.

In real data, the source functions and coupling factors are unknown. Instead of directly estimating them, the source function and coupling factors are eliminated by normalizing the amplitude of the wave field at the nearest offset receiver position according to the corresponding geometrical spreading. The amplitudes of the wave field at the rest of receiver positions are normalized relative to the one at the nearest offset. The rationale is that the diffraction tomography does not necessarily require good amplitude information to be effective, even though its performance would be enhanced by good amplitude information. The phase of Fourier transforms carries essential information about the object. A shift of an object in the space leads to a shift of the phase in Fourier wavenumber domain.

We are aware that multiple frequency reconstruction could enhance the quality of the image. It would be ideal to stack coherently to enhance desired features, and incoherently to get rid of unwanted distortions. But a coherent multi-frequency stacking may involve data stretching and interpolation in the wave number domain and it is difficult to apply when the background medium is inhomogeneous. In other words, a simply addition of the images obtained with different frequencies will not necessary improve the reconstruction. In fact, the strength of the image will change dramatically with change of the

frequency. Therefore, simple addition of the images would degrade the quality of the image. In this study we consider single frequency inversion.

In an ideal situation in which the source and receiver lines are extended to infinity, the maximum vertical wave number is $2\pi/\Delta$ and the maximum horizontal wave number is one wavelength that is approximately 10 ft. If the spatial sampling interval Δ is 2.5 ft (one quarter of the wavelength), then the best resolution of the image would be 2.5 in the vertical direction and 10 ft in horizontal direction. Due to the limited aperture and relatively low frequency, the wave numbers in both vertical and horizontal directions can not reach these maximum values and the reconstructed image is blurred. The resolution of the reconstructed images is reduced. Taking into consideration both of resolution limits and the distortion effect of limited aperture, the resolution of the image can be estimated as approximately half the wavelength or 5 ft in vertical direction and one and one half wavelength, or 15 ft in horizontal direction respectively.

McELROY FIELD DATA INVERSION

We apply the algorithm for a layered background medium to the field data from McElroy test site at West Texas. The measurement geometry is shown in figure 1. For the 185 ft well separation, both the source and receiver spacing were 2.5 ft apart. For the 600 ft well separation, the sources and receivers' intervals are 5 ft. According to prior known geological information, the reservoir is located at the depth between 2850 ~ 2950.

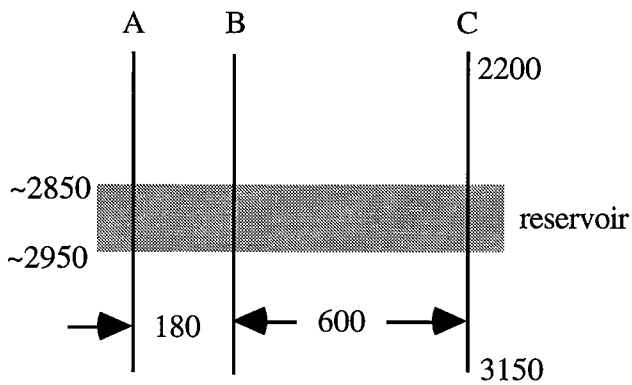

Fig. 1. The well locations of the McElroy field survey

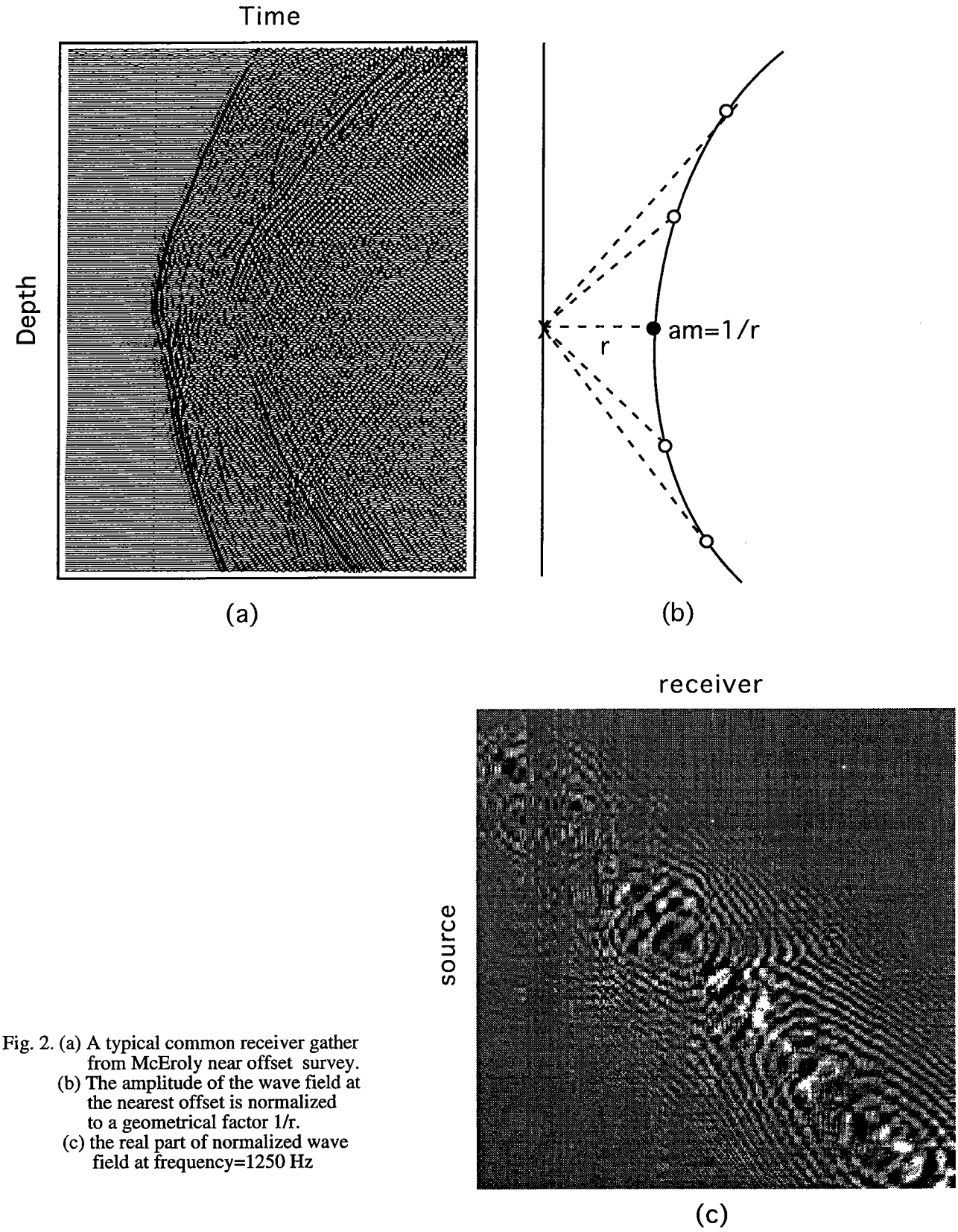

Fig. 2. (a) A typical common receiver gather from McEroly near offset survey.
(b) The amplitude of the wave field at the nearest offset is normalized to a geometrical factor 1/r.
(c) the real part of normalized wave field at frequency=1250 Hz

A typical common receiver gather is plotted in figure 2 (a). A traveltime tomogram (figure 3) of the field data is used to create a 1-D background model for the inversion. In the field experiment, the data is recorded at 202 receiver and 202 source positions. For convenience, the source line and receiver line is padded with zeros to form a 256 by 256 matrix and then Fourier transformed to the wave number domain (figure 2c).

The images are reconstructed with the data at frequency 1400 Hz and the results are shown in figure 4. From the scattering potential image and velocity image one can identify the internal structure of the reservoir. Notice that although the reservoir zone can be seen, its internal structure is not resolved by traveltime tomogram. This is not surprising, because in essence, with the traveltime tomography one reconstructs the low frequency components of the inhomogeneity. With the diffraction tomography one recovers the higher frequency components. Most of the structures in the reconstructed images here are comparable to those with crosswell reflection imaging and migration techniques (Larazators, et al., Mo, et al., 1992).

The inversion results of the McElroy far offset data are shown in figure 5. From the scattering potential image and velocity image, we can see the improvement of the resolution compared to the traveltime tomogram, especially around the reservoir area. Notice that although the resolution is lower, the far offset images can still be tied to the near offset images, see figure 6.

KING MOUNTAIN FIELD DATA INVERSION

A well was drilled with the target being a prolific "carbonate mound". A second well offset 630 ft from the first missed the target. It is desirable to know the lateral and vertical extents of this carbonate mount so that a horizontal step-out well could be drilled (Langan, 1994). The survey geometry is shown in figure 7. Notice that both the receiver well (M13) and the source well (M35) are deviated wells that may greatly influence the inversion results. In this study, we account for well deviation in traveltime inversion but not in diffraction inversion.

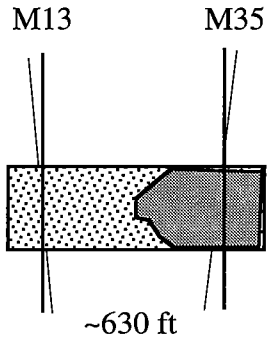

Fig. 6. The well locations of the King Montain field survey. Both the receiver and source well are deviated.

Unlike the situation at McElroy test site, the sonic log and transmission tomography study indicate that the low frequency component of the velocity field at King Mountain test site has two dimensional characteristics. A stratified background medium is no longer applicable. Because of non-uniform background, it is impossible to choose a single velocity to calculate the background field. On the other hand, if we can treat the diffraction theory of a constant velocity as an approximation to a general theory, including variable background velocity in the algorithm is important. In other words, we use the algorithm of the diffraction for constant background velocity, but replace the velocity with a variable one. Actually, this procedure is a good approximation to a rigorous diffraction algorithm for a variable background (Wang, 1994).

The inversion results are show in figure 8. The vertical and lateral extents of the reef are apparent in the traveltime tomogram. The scattering potential image and the velocity image not only match the sonic log better but also revel some structure features which are absent in the traveltime tomogram. However, we believe these results are still primary due to the nature of an incomplete inversion theory and without accounting for well deviation.

CONCLUSIONS

We have shown how crosswell direct wave traveltime and scattering are combined to image the internal structure of a West Texas carbonate reservoir. The high resolution images result from the complement nature of the direct wave field and scattered fields. We believe our results illustrate the enormous potential of scattering and diffraction tomographic inversions to usefully address reservoir delineation and characterization problems.

ACKNOWLEDGMENT

I want thank Mark Van Schaack for his valuable comments and suggestions. The paper was edited by Sonya Williams and Nicholas Smalley. The author is grateful for their help.

REFERENCES

Mo, L., and Harris, J. 1993, Migration of crosswell seismic data: field data case, STP-93 Paper L.

Lazaratos, S. K., 1993, Crosswell reflection imaging: Ph. D. dissertation: Department of Geophysics, Stanford University

Langan, R. 1994, private communication.

Harris J. and Wang. G., 1993 Diffraction tomography for inhomogeneties in a layered background medium, STP-93 paper M

Wang, G. and Harris J., 1994, Diffraction tomography using multiscale Fourier transform, STP-94 Paper

STP INFORMATION

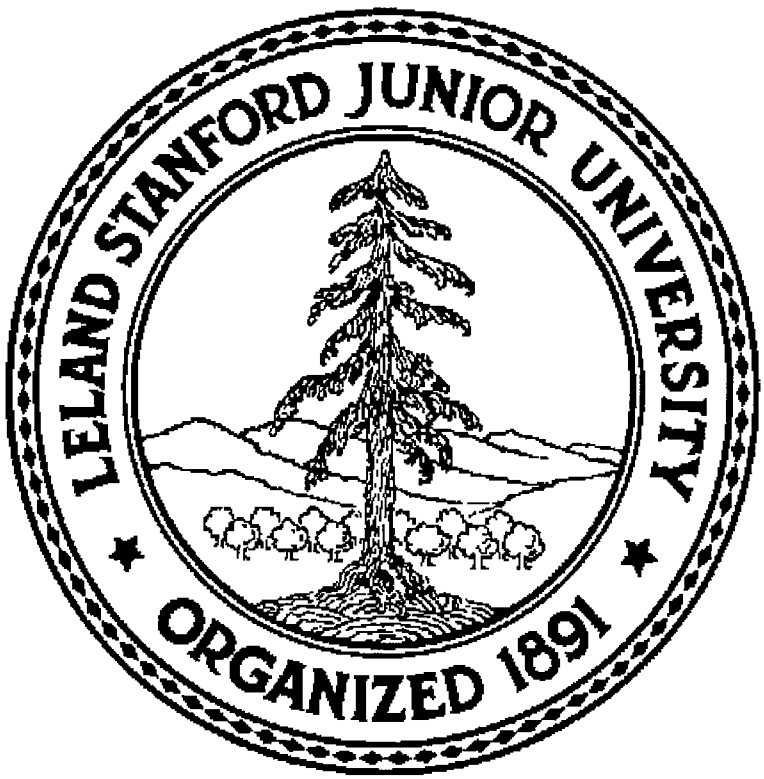

STP COMPUTER HARDWARE RESOURCES

WORKSTATIONS, TERMINALS and MACINTOSHES

DECalpha station 3000/400	96 Mb RAM, 1.0 Gb disk
DECalpha station 3000/400 (2)	48 Mb RAM, 1.0 Gb disk
DECstation 5000/240	80 Mb RAM, 1.0 Gb disk
DEC station 5000/240	64 Mb RAM, 6.1 Gb disk
DECstation 5000/240	48 Mb RAM, 3.0 Gb disk
DECstation 5000/200	32 Mb RAM, 2.0 Gb disk
DECstation 3100	24 Mb RAM, 200 Mb disk
Sun 4/150	8 Mb RAM, 200 Mb disk
Sun 3/60	8 Mb RAM, 200 Mb disk

2 - 14" color NCD X terminals
3 - 16" monochrome NCD X terminals
1 - 16" NH color terminal
3 - Macintoshes

PERIPHERALS

2 - 8mm Exabyte tape drives
1 - TK50 tape drive
1 - HP ScanJet Plus
2 - Laserwriter Plus
1 - HP Deskjet color printer

STP DIRECTORY

Name:	**Phone:**	**Electronic Mail:** (@pangea.stanford.edu)
Faculty:		
Jerry M. Harris	(415) 723-0496	harris
Post Doc:		
Feng Yin	(415) 725-4369	feng
Graduate Students:		
Steven Bacharach	(415) 723-4469	steven
Le-wei Mo	(415) 723-9410	mo
Youli Quan	(415) 723-9410	quan
Nicholas Smalley	(415) 723-9410	smalley
Mark Van Schaack	(415) 723-9410	mvs
Guan Yong Wang	(415) 723-9410	gywang
Administrator		
Sonya N. Williams	(415) 723-1099	sonya
Tomography Laboratory	(415) 723-9410	
Seismic Tomography Fax	(415) 725-2032	
Stanford University Fax	(415) 723-0010	
Stanford University Telex	348402 STANFORD STNU	

RESEARCH PERSONNEL

Jerry M. Harris received his M.S. degree (1974) in electrical engineering from the California Institute of Technology. From 1974 to 1977, he was with the Communications Satellite Corporation working millimeter wave scattering and attenuation in the troposphere. He returned to Caltech and finished the Ph.D. in 1980. After graduation from Caltech, he joined Exxon Production Research Company where he worked on adaptive signal processing and scattering of seismic waves. In 1982, he initiated Exxon's crosswell tomography project in Long Range Research. In 1984, he joined the Standard Oil Company to lead development of the seismic tomography project. Dr. Harris joined the faculty at Stanford University in 1988 as Associate Professor of Geophysics. His current research interests include experimental methods in seismology and electromagnetics for imaging and measurement of in-situ rock properties, crosswell tomography, and general topics involving wave physics and signal processing.

Steven Bacharach received his B.A. in 1992 in geophysics from the University of California, Berkeley. He is a Ph.D. candidate in geophysics. His research interests are joint seismic and hydraulic modelling and environment geophysics.

Le-Wei Mo received a B.A. in applied geophysics from Changchun College of Geology in 1985. From 1986 to 1987 he studied in the Master's program, Computer Science Department, at Fudan University. From 1988 to 1999, he worked for the Beijing Computer Center, Ministry of Geology and Mineral Resources. He received his M.S. in computer application from Fudan University in 1990. He worked for Stanford Exploration Project as a research assistant from February 1991 to September 1992. He joined the Seismic Tomography Project in September 1992 and is currently working towards a Ph.D. in geophysics. His research interests include signal processing, seismic wave modeling and imaging.

Youli Quan received his B.S. in 1982 from the University of Science and Technology of China, and his M.S. in 1986 from the Institute of Geophysics, Chinese Academy of Sciences, and is presently a Ph.D. student at Stanford University. He worked for the Institute of Geophysics, Chinese Academy of Sciences from 1986 to 1989.

Nicholas Smalley received his B.S. in Geophysics from Texas A&M in 1989. He is a Ph.D. candidate in Geophysics. His research interests are crosswell reflector imaging and migration. He is a member of the Society of Exploration Geophysicists.

Mark Van Schaack received his B.S. in geophysical engineering from the Colorado School of Mines in 1985. He joined Schlumberger Wireline Services in 1985 and spent his next four years working in Syria, Egypt, and Sudan as a Field Engineer. In 1989, Mark went to work as a Research Associate for the University of California, Santa Barbara's Institute for Crustal Studies. His work at ICS included the processing of several surface seismic lines shot in the Southeastern Sierra Nevada's. He has been a graduate student at Stanford University since 1990 and is currently working toward his Ph.D. in geophysics.

Guan Yong Wang received his B.S. in geophysics from the Geological Institute of Changchun. From 1982 to 1983, he worked as a geophysicist for Shanxi Geological Survey (China). He received his M.S. in geophysics from the Graduate School of Academia Sinica in 1986. From 1986 to 1989, he was a research geophysicist with the Institute of Geology, State Seismological Bureau in China. He received a M.E. in engineering geoscience in 1991 from the University of California at Berkeley. He joined the Seismic Tomography Project in September 1991, and is currently working towards a Ph.D. in geophysics.

Feng Yin received his B.S. degree (1982) and M.S. (1984) in electrical engineering from the Nanjing Institute of Technology. From 1984 to 1986, he was with Beijing Vacuum Electronics Institute working with laser scattering and spectroscopy technology. He received his Ph.D in electrical engineering from Southeast University (China). After graduation from SU, he joined their Department of Physics as an associate professor from 1990 to 1993. In 1993, he worked as a visiting scholar in geophysics at the Institute of Karlsruhe University (Germany). In October of 1993, he joined the Seismic Tomography project as a post-doctoral fellow. His current research interests include seismic tomography, migration and wave propagation in inhomogeneous media, and inverse scattering problems.

STP 1994 SPONSORS

Henry Tan
Amoco Production Company
P.O. Box 3385
Tulsa, OK 74102

Yoshiro Ishii
Japan National Oil Corporation
1-2-2, Hamada
Mihama, Chiba-City
260 Japan

Robert Langan
Chevron Petroleum Technology Company
P.O.Box 446
La Habra, CA 90633-0446

Joseph Gallagher
Phillips Petroleum Company
570G Plaza Office Building
Bartlesville, OK 74004

John Queen
Conoco Inc.
P.O. Box 1267
Ponca City, OK 74602-1267

R. L. LeRoy
Noranda Technology Centre
240 boulevard Hymus
Pointe-Claire, Quebec
Canada H9R 1G5

Sen T. Chen
Exxon Production Research Company
P.O. Box 2189
Houston, Texas 77252

Danny R. Melton
Texaco Inc.
P.O. Box 770070
Houston, Texas 77215-0070

Yumio Iwaki
Japex Geosciences Institute, Inc.
Akasaka Twin Tower East Wing -3rd Floor
2-17-22 Akasaka, Minato-ku
Tokyo 107, Japan

Timothy Anderson
Unocal Corporation
P.O. Box 76
Brea, CA 92621

Dennis O'Brien
Advance Geophysical Corporation
7409 Alton Court, Suite 100
Englewood, CO 80111

James L. Peters
Union Pacific Resources Co.
P.O. Box 7
Fort Worth, TX 76101-0007

Sergio Zarantonello
Fujitsu America
3055 Orchard Drive
San Jose, CA 95134-2022